

Comet Formation in the Framework of Streaming Instability

Von der Fakultät für Elektrotechnik, Informationstechnik, Physik
der Technischen Universität Carolo-Wilhelmina zu Braunschweig

zur Erlangung des Grades eines
Doktors der Naturwissenschaften (Dr. rer. nat.)

genehmigte Dissertation

von Sebastian Lorek

aus Neumarkt i.d.OPf.

eingereicht am: 15.09.2017

Disputation am: 19.12.2017

1. Referentin oder Referent: Prof. Dr. Jürgen Blum
2. Referentin oder Referent: Prof. Dr. Cornelis P. Dullemond

Druckjahr: 2018

Bibliografische Information der Deutschen Nationalbibliothek

Die Deutsche Nationalbibliothek verzeichnet diese Publikation in der Deutschen Nationalbibliografie; detaillierte bibliografische Daten sind im Internet über <http://dnb.d-nb.de> abrufbar.

Dissertation an der Technischen Universität Braunschweig,
Fakultät für Elektrotechnik, Informationstechnik, Physik

ISBN 978-3-944072-62-3

uni-edition GmbH 2018

<http://www.uni-edition.de>

© Sebastian Lorek



This work is distributed under a
Creative Commons Attribution 3.0 License

Printed in Germany

Contents

Zusammenfassung	11
Summary	13
1 Introduction	15
1.1 Historical overview of comet exploration	15
1.2 Characteristics of comets	16
1.2.1 Source regions of comets	16
1.2.2 Properties of the nucleus	17
1.2.3 Coma and tail of comets	19
1.3 The formation of comets	19
1.3.1 Dust growth in the solar nebula	20
1.3.2 Streaming instability	21
1.3.3 Comet formation by gravitational instability	22
1.3.4 Alternative hypotheses for the formation of comets	23
1.4 Motivation and structure of the thesis	25
2 Model of the solar nebula	27
2.1 The minimum mass solar nebula	27
2.2 Turbulence	28
2.3 Dust in protoplanetary disks	29
2.3.1 Aerodynamic drag on solid aggregates	30
2.3.2 The Stokes number	31
2.3.3 Relative velocities between dust and gas	32
3 Collision model	35
3.1 Dust properties	35
3.1.1 Material properties of the monomers	35
3.1.2 Material properties of dust aggregates	36
3.2 Collision velocities of dust aggregates	37
3.2.1 Brownian motion	37
3.2.2 Turbulence induced collision velocities	38
3.2.3 Differential drift of aggregates	38
3.2.4 Total collision velocity	39
3.3 The outcome of dust aggregate collisions	39
3.3.1 Sticking and bouncing	40
3.3.2 Fragmentation, erosion, and mass transfer	40

3.3.3	The change of the aggregate mass	41
3.3.4	Material and collision properties of water ice	42
3.4	The porosity of dust aggregates	42
3.4.1	Porosity change in sticking collisions	43
3.4.2	Compression in bouncing collisions	44
3.4.3	Porosity change in fragmentation, erosion, and mass transfer	47
3.4.4	Non-collisional compression of porous aggregates	47
3.5	Aggregates of mixed composition	48
3.5.1	Composition and density	48
3.5.2	Collision model for aggregates of mixed composition	49
3.6	Caveats of the collision model	53
3.6.1	Homogeneously mixed aggregates	53
3.6.2	Combining collision outcome with porosity	53
3.6.3	Bouncing of porous aggregates	54
4	Monte Carlo modelling of dust coagulation	55
4.1	The Smoluchowski equation for coagulation	55
4.2	Numerically solving the Smoluchowski equation	56
4.2.1	Direct numerical integration	56
4.2.2	Monte Carlo methods	56
4.3	The representative particle method	57
4.3.1	Collision rates and time of the next collision	57
4.3.2	Particles involved in the collision	58
4.3.3	Change of particle properties	58
5	Local growth of aggregates in the solar nebula	61
5.1	Initial conditions for the simulations	62
5.1.1	Coagulation model	62
5.1.2	Collision model	64
5.2	Results of aggregate growth simulations	65
5.2.1	Nominal case: aggregate growth at 30 au	66
5.2.2	Parameter study for aggregate growth	73
5.2.3	Caveats	82
5.2.4	Summary of aggregate properties	84
6	Aggregate compression during the gravitational collapse of pebble clouds	89
6.1	Gravitational collapse of a pebble cloud	89
6.2	Initial conditions for the simulations	91
6.2.1	Pebble cloud model and collision model	91
6.2.2	Coefficient of restitution of aggregates	92
6.2.3	Summary of the initial conditions	92
6.3	Results of pebble cloud collapse simulations	93
6.3.1	Collision types during collapse	93
6.3.2	Compression of aggregates	96
6.3.3	Formation of comet-like planetesimal	98

7	Implications for the formation of comets	107
7.1	Local formation of comets at large heliocentric distance	107
7.2	Implications from the comparison with observations of cometary pebbles	108
7.2.1	Compression of millimetre-sized aggregates	108
7.2.2	Post-collapse aggregate sizes in the nominal case	114
7.2.3	Post-collapse aggregate sizes in the parameter study	115
7.2.4	Preferred solar nebula conditions for comet formation	118
7.3	Formation of comets from comet-like planetesimals	119
7.3.1	Formation of substructure by clustering of aggregates	120
7.3.2	Rotation of pebble clouds	120
7.3.3	Presence of fractal aggregates	121
8	Conclusion	123
	Bibliography	125
	Publications	143
	Acknowledgements	145
	Curriculum vitae	147

List of Figures

1.1	Inclination as function of semi-major axis of comets.	17
1.2	Image of comet 103P/Hartley 2	18
3.1	Compression curve of granular water ice from laboratory experiments.	45
3.2	Compression curve for dust and ice aggregates.	46
3.3	Collision outcome map for compact aggregate collisions	51
3.4	Collision outcome map for porous aggregate collisions	52
5.1	Sketch of the simulation domain.	63
5.2	Aggregate properties as function of time in the nominal case.	67
5.3	Mass distribution function in the nominal case; 0.1 μm sized monomers, dust-to-ice ratio of 5.	68
5.4	Mass distribution function in the nominal case; 1 μm sized monomers, dust-to-ice ratio of 5.	68
5.5	Mass distribution function and residuals in the nominal case; 0.1 μm sized monomers.	71
5.6	Mass distribution function and residuals in the nominal case; 1 μm sized monomers.	72
5.7	Aggregate properties as function of time: different heliocentric distances.	74
5.8	Aggregate properties as function of time: weaker and stronger turbulence.	75
5.9	Aggregate properties as function of time: varying gas surface density.	76
5.10	Aggregate properties as function of time: dispersing solar nebula.	77
5.11	Aggregate properties as function of time: varying the sticking properties.	78
5.12	Aggregate properties as function of time: bouncing only for compact aggregates.	79
5.13	Aggregate mass versus heliocentric distance.	81
6.1	Collision velocity as function of pebble cloud density: initial volume-filling factor of 10^{-2} , dust-to-ice ratio of 5.	95
6.2	Collision types as a function of planetesimal density: initial volume-filling factor of 10^{-2} , dust-to-ice ratio of 5.	96
6.3	Mass distribution function during pebble cloud collapse: initial volume-filling factor of 10^{-2} , dust-to-ice ratio of 5.	97
6.4	Volume-filling factor of aggregates as a function of initial volume-filling factor.	98
6.5	Volume-filling factor of aggregates as a function of initial volume-filling factor: pure dust and ice, initial volume-filling factors $10^{-3} - 0.4$	99

List of Figures

6.6	Aggregate packing as function of pebble cloud density: very low-mass pebble cloud.	101
6.7	Aggregate packing as function of pebble cloud density: low-mass pebble cloud.	102
6.8	Aggregate packing as function of pebble cloud density: intermediate-mass pebble cloud.	103
6.9	Aggregate packing as function of pebble cloud density: high-mass pebble cloud.	104
7.1	Collision velocity as function of pebble cloud density: aggregate radius 0.45 mm, 0.1 μm monomers, initial volume-filling factor of 1.2×10^{-2} , dust-to-ice ratio of 5 at 30 au.	109
7.2	Mass distribution function during pebble cloud collapse: aggregate radius 0.45 mm, 0.1 μm monomers, initial volume-filling factor of 1.2×10^{-2} , dust-to-ice ratio of 5 at 30 au.	110
7.3	Aggregate packing as function of pebble cloud density: aggregate radius 0.45 mm, 0.1 μm monomers, initial volume-filling factor of 1.2×10^{-2} , dust-to-ice ratio of 5 at 30 au.	112
7.4	Mass distribution function during pebble cloud collapse: aggregate radius 0.36 mm, 0.1 μm monomers, initial volume-filling factor of 1.8×10^{-1} , dust-to-ice ratio of 5 at 5 au.	113
7.5	Aggregate packing as function of pebble cloud density: aggregate radius 0.36 mm, 0.1 μm monomers, initial volume-filling factor of 1.8×10^{-1} , and dust-to-ice ratio of 5 at 5 au.	115
7.6	Post-collapse aggregate radius versus heliocentric distance.	116
7.7	Post-collapse aggregate radius for parameter study at 30 au.	117

List of Tables

3.1	Parameters for the dust and ice compression curves.	47
5.1	Simulation parameters used in the nominal run.	62
5.2	Overview of model designs used in parameter study.	80
5.3	Maximum mass and mass at St_{\min} for $0.1 \mu\text{m}$ sized monomers.	85
5.4	Maximum mass and mass at St_{\min} for $1 \mu\text{m}$ sized monomers.	86
5.5	Aggregate growth for different model settings.	87
6.1	Initial conditions for simulations of pebble cloud collapse.	93
6.2	Volume-weighted mean filling factor of aggregates for all simulations.	100
7.1	Aggregate properties at different planetesimal densities at 30 au.	111
7.2	Aggregate properties at different planetesimal densities at 5 au.	114
7.3	Pre- and post-collapse aggregate radii.	119

Vorabveröffentlichungen der Dissertation

Teilergebnisse dieser Dissertation wurden mit Genehmigung der Fakultät für Elektrotechnik, Informationstechnik, Physik, vertreten durch den Mentor der Arbeit, Prof. Dr. Jürgen Blum, in den unten gelisteten Artikeln und Konferenzbeiträgen vorab veröffentlicht. Erlaubnis zur Verwendung von Abbildungen und Tabellen aus den Artikeln wurde gewährt von: Astronomy & Astrophysics, ©ESO.

Publikationen

S. Lorek, P. Lacerda, and J. Blum, *Local growth of dust- and ice-mixed aggregates as cometary building blocks in the solar nebula*, A&A, 611, A18, doi: 10.1051/0004-6361/201630175, 2018, March

S. Lorek, B. Gundlach, P. Lacerda, and J. Blum, *Comet formation in collapsing pebble clouds. What cometary bulk density implies for the cloud mass and dust-to-ice ratio*, A&A, 587, A128, doi: 10.1051/0004-6361/201526565, 2016, March

Konferenzbeiträge

S. Lorek, P. Lacerda, J. Blum, *Comet formation in collapsing pebble clouds: Pebble formation*, Department of Planetary Science/European Planetary Science Congress Joint Meeting, Pasadena, California, USA, 2016, October (*Poster*)

S. Lorek, P. Lacerda, J. Blum, B. Gundlach, *Size matters? Monomer size and transition from fractal to compact ice aggregates*, Wilhelm und Else Heraeus Seminar *How primitive are comets?*, Bad-Honnef, Germany, 2016, April (*Poster*)

S. Lorek, P. Lacerda, B. Gundlach, and J. Blum, *Compression of Pebbles in Collapsing Pebble Clouds*, Planet Formation and Evolution Workshop, Duisburg-Essen, Germany, 2016, March (*Oral*)

S. Lorek, P. Lacerda, B. Gundlach, and J. Blum, *Compression of Pebbles in Collapsing Pebble Clouds and the Dust-to-Ice ratio*, European Planetary Science Congress (EPSC), Nantes, France, 2015, October (*Oral*)

Zusammenfassung

Die Körper im Sonnensystem bildeten sich vor etwa 4.6 Gyr in der protoplanetaren Scheibe um die junge Sonne. Kollisionen zwischen anfänglich submikrometer großen Staub- und Eiskörnern führten zu Wachstum und der Entstehung größerer Teilchen, Planetesimalen und letztendlich Planeten. Man vermutet, dass Kometen diejenigen kilometergroßen eishaltigen Planetesimale sind, die nicht zum Wachstum größerer Objekte beigetragen und bis heute überlebt haben.

Es ist bislang nur unzureichend verstanden, wie Körper zu Größen größer als etwa Millimeter bis Dezimeter anwachsen können, da elastische Kollisionen und Fragmentation Wachstum bei diesen Größen beendet. Strömungsinstabilität, die durch die Kopplung zwischen Gas und millimeter- bis dezimetergroßen Staubteilchen mittels Reibung entsteht, ist ein vielversprechender Mechanismus, um diese Lücke zu schließen (Youdin and Goodman 2005). Diese Instabilität erzeugt lokal hohe Staubdichten, die auf Grund der Eigengravitation kollabieren und Planetesimale im Größenbereich Kilometer bis einige hundert Kilometer erzeugen (Johansen et al. 2007).

Kometen besitzen eine hohe Porosität (70% – 80%), eine geringe Zugfestigkeit ($\lesssim 150$ Pa) und eine geringe Dichte etwa 0.5 g cm^{-3} (z.Bsp. Sierks et al. 2015). Hochauflösende Aufnahmen der freiliegenden Oberfläche einer Wand auf dem Kometen 67P/Tschurjumow-Gerassimenko zeigen millimeter- bis zentimetergroße Staubteilchen, von denen man glaubt, dass sie die ursprünglichen Bauteile des Kometen sind (Poulet et al. 2016). Planetesimalentstehung durch Strömungsinstabilität sagt genau diese Eigenschaften vorher.

Diese Dissertation untersucht die Entstehung von Kometen im Kontext der Strömungsinstabilität. Das Wachstum von Staubteilchen im solaren Urnebel wird modelliert, um die Eigenschaften der Staubteilchen, die die Strömungsinstabilität auslösen, zu bestimmen. Simulationen des Gravitationskollapses einer Wolke aus porösen Staubteilchen sollen zum einen klären, wie sich die Eigenschaften der Staubteilchen während des Kollapses ändern, und zum anderen, ob ein Planetesimal, der auf diese Weise entsteht, kometenähnliche Eigenschaften aufweist.

Folgende Ergebnisse wurden erhalten: Staubteilchen mit den richtigen aerodynamischen Eigenschaften, um die Strömungsinstabilität auszulösen, haben bei einer für die Entstehung von Kometen typischen Entfernung zur Sonne von 5 bis 30 Astronomischen Einheiten (AU) Größen im Bereich $\sim 3 \text{ mm} \lesssim a \lesssim 7 \text{ mm}$ und Volumenfüllfaktoren (der mit Materie gefüllte Bruchteil des Gesamtvolumens) von etwa $\phi \approx 10^{-2} - 10^{-1}$. Die Entstehung von Planetesimalen mit kometenähnlichen Eigenschaften aus diesen porösen Staubteilchen benötigt Wolken mit einer Masse $\gtrsim 2.6 \times 10^{20} \text{ g}$ (entspricht einem Planetesimal von $\sim 100 \text{ km}$ Durchmesser) und ein relatives Verhältnis von Staub zu Eis von etwa 3 – 10. Dieses Ergebnis ist im Einklang mit numerischen Simulationen

zur Planetesimalentstehung durch Strömungsinstabilität (Schäfer et al. 2017) und mit den beobachteten Staub zu Eis Verhältnissen von Kometen (Fulle et al. 2017). Weiterhin sind die Größen der Staubteilchen nach dem Gravitationskollaps im Einklang mit den Staubteilchen, die auf 67P/Tschurjumov-Gerassimenko beobachtet wurden (Poulet et al. 2016). Strömungsinstabilität stellt daher einen brauchbaren Mechanismus für die Entstehung von Kometen dar.

Summary

The bodies of the solar system formed 4.6 Gyr ago in the protoplanetary disk around the young protosun. Starting with submicrometre-sized dust and ice grains, collisions and coalescence led to the formation of aggregates, planetesimals, and eventually planets. Comets are believed to be the kilometre-sized icy planetesimals that were not accreted into larger bodies and have survived until today.

It is poorly understood how bodies manage to grow to sizes larger than about millimetre to decimetre because bouncing and fragmentation terminate growth well below kilometres. Streaming instability arising from the coupling between the gas and millimetre- to decimetre-sized dust aggregates via drag is a promising mechanism to bridge this gap (Youdin and Goodman 2005). The instability produces locally high dust densities which collapse due to self-gravity and form planetesimals in the size range kilometres to a few hundred kilometres (Johansen et al. 2007).

Comets are highly porous (70% – 80%) fragile (tensile strength $\lesssim 150$ Pa) objects with low bulk density (~ 0.5 g cm⁻³) (e.g. Sierks et al. 2015). High resolution images of the exposed surface of a wall on 67P/Churyumov-Gerasimenko revealed millimetre- to centimetre-sized aggregates which are believed to represent the building blocks from which the comet formed (Poulet et al. 2016). Planetesimal formation through streaming instability predicts objects with these characteristic properties.

This thesis investigates the formation of comets in the framework of the streaming instability. Aggregate growth in the solar nebula is modelled to find the specific properties of the aggregates that eventually trigger the streaming instability. Simulations of the gravitational collapse of a cloud of porous aggregates (pebble cloud) are conducted to address the questions how aggregate properties change during the collapse and whether or not the resulting planetesimal has the properties of a comet.

The following results are obtained: between 5 and 30 astronomical units (au) - typical heliocentric distances for comet formation - aggregates with the right aerodynamic properties for streaming instability have sizes in the range ~ 3 mm $\lesssim a \lesssim 7$ mm and volume-filling factors (the fraction of the volume filled with solid material) of $\phi \approx 10^{-2} - 10^{-1}$. The formation of a planetesimal with comet-like properties from these porous aggregates requires pebble clouds with a mass $\gtrsim 2.6 \times 10^{20}$ g (equivalent to a planetesimal of diameter ~ 100 km) and a dust-to-ice ratio in the range 3–10. This is consistent with numerical simulations of planetesimal formation through streaming instability (Schäfer et al. 2017) and the observed dust-to-ice ratios of comets (Fulle et al. 2017). Furthermore, the sizes of the aggregates after collapse are consistent with aggregates observed on comet 67P/Churyumov-Gerasimenko (Poulet et al. 2016). This renders streaming instability as a viable mechanism for comet formation.

1 Introduction

1.1 Historical overview of comet exploration

The understanding of comets has changed dramatically throughout history (Festou et al. 2004). Being considered as atmospheric phenomena by the ancient Greek philosophers and as evil omens in the middle ages, the picture was repainted with the rediscovery of comet 1P/Halley. The orbit of the comet was determined and its return predicted by English astronomer Edmond Halley (1656-1742) in 1705. About 53 years later in 1758, German astronomer Johann Georg Palitzsch (1723-1788) successfully rediscovered 1P/Halley on its predicted orbit, thereby proving the validity of Newton's general law of gravitation.

Later, in the 19th and at beginning of the 20th century, the development of new tools, such as spectroscopy in the visual wavelength range, allowed scientists to gain some information about the physical properties of comets. It was discovered that the light of comets was scattered sunlight. However, it was not until the 1950s when the foundations of modern cometary science were established. Whipple published his "icy conglomerate" model (Whipple 1950, 1951), Oort proposed a spherical reservoir of comets at heliocentric distances $\gtrsim 10^4$ astronomical units (au), known today as the Oort cloud (Oort 1950), and Biermann discovered the physical process shaping the ion tail of a comet (Biermann 1951).

In the 1980s, the study of comets reached a new level. The Giotto spacecraft flew by comet 1P/Halley as the comet approached perihelion in 1986. The nucleus of a comet was seen for the first time and an overwhelmingly large amount of data was collected: images of the nucleus showing surface features, measurements of dust sizes, confirmation of the silicate-rich composition of dust grains, but also grains rich in C, H, O, and N (known today as "CHONs"), composition of coma gas with H₂O representing 85% of the gas phase mass, and magnetic fields (Gringauz et al. 1986; Keller et al. 1986; Kissel et al. 1986b,a; Krankowsky et al. 1986; McDonnell et al. 1986; Keller et al. 1988).

Flybys of two more comets, 19P/Borrelly and 81P/Wild 2 by the Deep Space 1 and Stardust spacecraft in 2001 and 2004, respectively, added more high resolution images of comet nuclei. The samples of cometary dust from comet Wild 2 that were returned to Earth by the Stardust spacecraft contributed to understand the formation and mixing processes of dust in the solar nebula (McKeegan et al. 2006; Zolensky et al. 2006).

While these spacecraft could only probe the surface and the coma of the comets, the Deep Impact mission to comet 9P/Tempel 1 in 2005 could probe the inside. An

impactor with a mass of 370 kg was carried along with the spacecraft and was released to hit the surface with a velocity of $\sim 10.2 \text{ km s}^{-1}$ on 4 July 2005. The impact produced a crater and excavated material from the comet's interior. The composition of the material could be measured revealing a much higher dust content than previously expected (Küppers et al. 2005; Sunshine et al. 2007). The flyby of 103P/Hartley 2 by the Deep Impact spacecraft as part of NASA's EPOXI mission showed a peanut-shaped nucleus with most of the ejected gas being composed of CO_2 (A'Hearn et al. 2011).

The current peak of space missions to comets was reached in 2014, when the Rosetta spacecraft, launched in 2004, reached comet 67P/Churyumov-Gerasimenko (67P hereafter) after a journey of 10 years and followed the comet along its orbit for almost 2 years until end of mission in September 2016. During this time, the scientific camera systems on board took high resolution images of the surface showing morphological features of the surface, the shape of the nucleus, patches of ice, cliffs and overhangs, jets and outbursts (Sierks et al. 2015; Thomas et al. 2015). Other instruments of the scientific payload investigated the composition of the coma gas and the D/H ratio of the comet, the structure and composition of dust, and subsurface temperatures (Altwegg et al. 2015; Capaccioni et al. 2015; Fulle et al. 2016b; Gulikis et al. 2015; Rotundi et al. 2015; Rubin et al. 2015). The Philae lander was dispatched in November 2014 to land on the surface and to perform in situ measurements. Although the planned and final destination of the lander deviated, high resolution images of exposed cometary material and radar measurements could be obtained allowing for a glimpse into the comet interior (Kofman et al. 2015; Poulet et al. 2016).

1.2 Characteristics of comets

1.2.1 Source regions of comets

During the dynamical evolution of the solar system, comets were placed in different cometary reservoirs until being sent back to the inner solar system by gravitational perturbations due to passing stars, molecular clouds, or the planet Neptune (Levison 1996).

The Oort cloud surrounds the solar system at heliocentric distances beyond $5 \times 10^4 \text{ au}$ (Oort 1950; Tremaine 1993) and is the reservoir of long-period comets (LPCs) with orbital periods longer than 200 yr. These objects enter the inner solar system on highly eccentric, almost parabolic, orbits with semi-major axes larger than $\sim 10^4 \text{ au}$. The distribution of orbital planes of LPCs is nearly isotropic (see Fig. 1.1)

The Kuiper belt and scattered disk outside the orbit of Neptune (Edgeworth 1949; Kuiper 1951; Jewitt and Luu 1993) is the source region of short-period comets (SPCs) with orbital periods shorter than 200 yr. In contrast to LPCs, the orbital planes of short-period comets are nearly aligned with the ecliptic plane (see Fig. 1.1). Short-period comets that are gravitationally perturbed by Jupiter such that their aphelion (the point of the orbit that is farthest away from the Sun) is at approximately the orbital distance of Jupiter at $\sim 5.2 \text{ au}$ are named Jupiter-family comets (JFCs). The orbital periods of JFCs are typically shorter than 20 yr.

The modern classification of cometary orbits is based on the Tisserand parameter

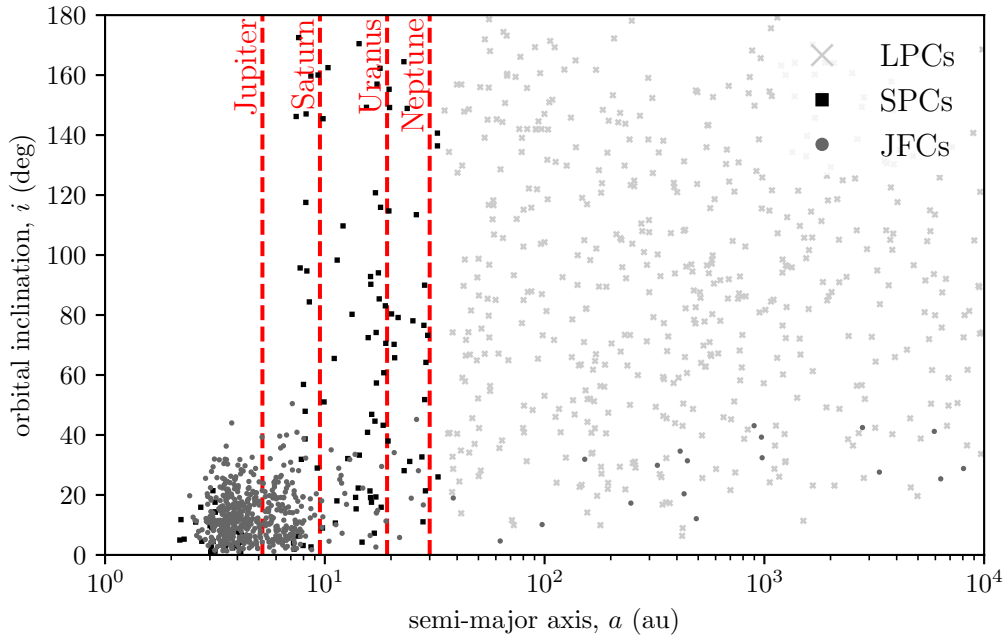


Figure 1.1: Inclination as function of semi-major axis of comets. The different symbols show different groups of comets: long period comets (LPCs \times) with orbital periods > 200 yr ($\mathcal{T} < 2$), short period comets (SPCs \blacksquare) with orbital periods < 200 yr ($\mathcal{T} > 2$), and Jupiter family comets (JFCs \bullet) as a group of SPCs with orbital periods < 20 yr ($2 < \mathcal{T} < 3$). The dashed red vertical lines mark the semi-major axes of the giant planets (Jupiter, Saturn, Uranus, and Neptune). (Credit: JPL Small-Body Database)

with respect to Jupiter

$$\mathcal{T} = \frac{a_J}{a} + 2 \sqrt{(1 - e^2) \frac{a}{a_J} \cos i}. \quad (1.1)$$

In this parameter, a , e , and i are semi-major axis, eccentricity, and inclination of the orbit of the comet and a_J is the semi-major axis of the orbit of Jupiter (Levison 1996). In the circular restricted three-body problem of the Sun, Jupiter, and a massless test particle, the Jacobi constant is a conserved quantity. The Tisserand parameter is an approximation to this constant. \mathcal{T} relates orbital energy and angular momentum of the comet.

In the new classification scheme for comets proposed by Levison (1996) nearly isotropic comets (LPCs) have $\mathcal{T} < 2$, whereas ecliptic comets (SPCs) have $\mathcal{T} > 2$. The ecliptic comets are subdivided into comets with $2 < \mathcal{T} < 3$ on orbits crossing the orbit of Jupiter (JFCs) and comets with $\mathcal{T} > 3$ on orbits which do not cross the orbit of Jupiter. Encke-type comets orbit inside, whereas Chiron-type comets orbit outside Jupiter.

1.2.2 Properties of the nucleus

Cometary nuclei are solar system bodies with typical sizes in the range 1 km – 10 km (Lamy et al. 2004; A'Hearn 2011; Kokotanekova et al. 2017). Most of the cometary

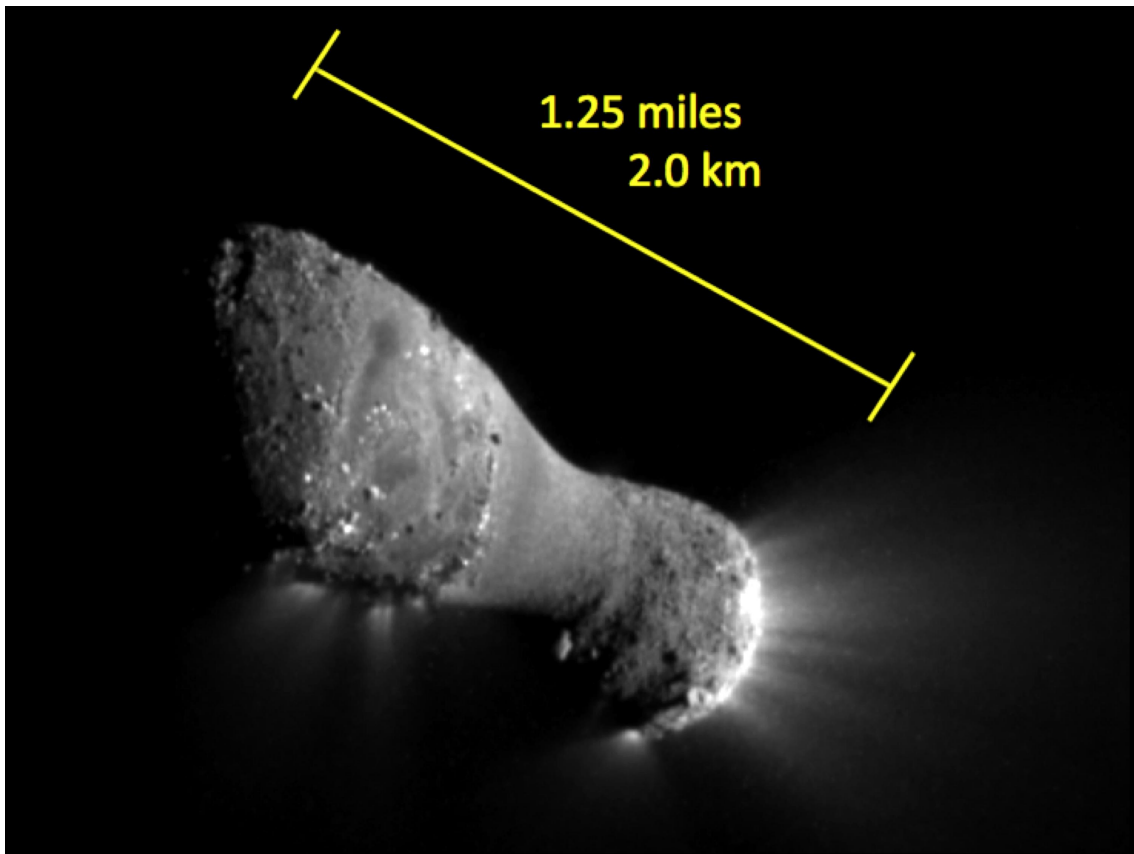


Figure 1.2: Image of comet 103P/Hartley 2 taken with the Medium Resolution Instrument (MRI) of the Deep Impact spacecraft in flyby during EPOXI mission. (Credit: NASA/JPL-Caltech/UMD)

nuclei visited by spacecraft (1P/Halley, 9P/Tempel 1, 19P/Borrelly, 67P/Churyumov-Gerasimenko, 103P/Hartley 2) have a bilobate structure (see Fig. 1.2 of Hartley 2).

The nucleus is a mixture of refractory silicate and carbonaceous dust, organics, and ices of different volatiles, mainly H_2O , CO , and CO_2 (Fernandez and Jockers 1983; Kissel et al. 1986b,a; Krankowsky et al. 1986; Mumma and Charnley 2011; Capaccioni et al. 2015; Rubin et al. 2015; Fulle et al. 2017). The mass ratio of dust to ice (hereafter dust-to-ice ratio) is typically $\gtrsim 1$ (Keller 1989; Sykes and Walker 1992; Küppers et al. 2005). For comet 67P, the Rosetta spacecraft measured a value of ~ 5 (Rotundi et al. 2015; Fulle et al. 2017).

The bulk density of comets is very low, typically 0.5 g cm^{-3} , only half the density of water ice (Blum et al. 2006; A'Hearn 2011; Sierks et al. 2015; Pätzold et al. 2016). For objects composed of refractory dust and ices, this implies an extremely high porosity of 70% – 80% (Blum et al. 2006; Kofman et al. 2015; Sierks et al. 2015; Pätzold et al. 2016; Fulle et al. 2017).

Additionally, the tensile strength of cometary material, that is the resistance of the material to stresses tearing them apart, is extremely low (Blum et al. 2006). This is known from the break-up of comets, for example of comet D/1993 F2 Shoemaker-Levy 9 which was disrupted due to tidal forces during a close encounter with Jupiter in 1992 and impacted the planet in 1994 (Boehnhardt 2004). An upper limit on the

tensile strength of 150 Pa could be derived from different morphological features on the surface of comet 67P (Groussin et al. 2015).

1.2.3 Coma and tail of comets

When the solar irradiation gradually heats up the deep-frozen subsurface material of the comet, volatile species sublime, stream away from the comet surface, and thereby drag along refractory micrometre- to millimetre-sized dust grains. The small nucleus develops a tenuous atmosphere of dust and gas extending 10^4 km to 10^5 km into space and forms a tail with lengths of 10^7 km to 10^8 km.

Comet tails have two, not necessarily aligned, components: a dust tail and an ion tail. The molecules of the cometary gas in the coma are dissociated and ionised by the solar radiation. Interactions between the particles of the solar wind and the magnetic field lines frozen into the solar wind accelerate the ions away from the comet and radially away from the Sun thereby producing the ion tail (Biermann 1951). On the other hand, dust particles are pushed away from the nucleus by radiation pressure. At heliocentric distances larger than the comet's, the Keplerian velocity is lower and the dust grains lack behind the orbital position of the comet leading to the bent structure of the dust tail (Finson and Probst 1968; Fulle 2004).

While coma and tails may appear brightly on the night sky, the small nucleus remains hidden to the naked eye. In the past years, this was the case for several comets. Most notably the comets C/1996 B2 Hyakutake in 1996, C/1995 O1 Hale-Bopp in 1997, C/2006 P1 McNaught in 2007, and C/2011 W3 Lovejoy in 2011. All of them could be spotted on the night sky by the visual observer for weeks and, in case of Hale-Bopp, even several months. For this reason, these comets were dubbed as the great comets of 1996, 1997, 2007, and 2011, respectively.

1.3 The formation of comets

When the solar system formed about 4.6 Gyr ago from a dusty gas disk around the young protosun (the solar nebula hereafter), submicrometre-sized dust and ice grains collided and coalesced to form aggregates, planetesimals, and finally planets. Comets, which are in this context just icy planetesimals, are remnants from this phase. As their volatile content suggests, comets must have formed beyond the ice line which separates the warm part of the disk where only refractory material was present from the cold part where ices of different volatiles prevailed. D/H-ratios (Altwegg et al. 2015) and volatile content of comets, for example the detection of N_2 in the coma of comet 67P (Rubin et al. 2015), place the formation region to heliocentric distances larger than ~ 5 au.

However, the formation of comets, and planetesimals in general, is still poorly understood. The main factor which controls the growth from submicrometre-sized grains to larger aggregates and planetesimals is the collision velocity. The collision velocity, on the other hand, is determined by the size-dependent coupling between solid bodies and the gas of the solar nebula. Accordingly, as aggregates grow their

collision velocities are changing which will lead to different collision outcomes (Blum and Wurm 2008; Güttler et al. 2010; Windmark et al. 2012a).

1.3.1 Dust growth in the solar nebula

Sub-micrometre-sized dust and ice grains are well-mixed with the solar nebula gas. The collisions are driven by Brownian motion which arises on a microscopic level from the collisions between the gas molecules and the refractory grains leading to energy equipartition between the two components (Ossenkopf 1993). Collision velocities due to Brownian motion are typically slower than cm s^{-1} . At these low speeds, the colliding aggregates stick where they hit without restructuring (hit-and-stick) and grow to highly porous fractal aggregates with sizes of $10 \mu\text{m}$ to $100 \mu\text{m}$ (Kempf et al. 1999).

The size distribution in the Brownian motion-driven growth phase remains narrow and growth is due to collisions between similar-sized aggregates. This characterises ballistic cluster-cluster aggregation (BCCA), which is one of two modes of aggregate growth. The second one is ballistic particle-cluster aggregation (BPCA), in which aggregates grow by addition of single grains onto a larger target. BPCA is characteristic of a system with a wide or bimodal size distribution as being established later on when fragmentation replenishes small aggregates. In contrast to BCCA, BPCA produces more compact, spherical, and non-fractal aggregates (Blum 2006).

As aggregates grow their dynamical behaviour changes. The aggregates sediment towards the disk midplane at a terminal velocity given by the balance between the vertical component of solar gravity and gas friction. On a timescale of $\sim 10^3 \text{ yr}$ inside $\sim 10 \text{ au}$ sedimentation reduces the thickness of the dust disk significantly to $\sim 1.7\%$ of the typical thickness of the gas disk (Dullemond and Dominik 2004). Because larger aggregates settle faster than smaller ones, the larger aggregates would grow to sizes in the millimetre to centimetre range by sweeping up the small ones (Dullemond and Dominik 2005).

Brownian motion becomes unimportant for larger masses and while small aggregates follow the flow of the solar nebula gas, larger aggregates develop relative motion to the gas. The aggregates couple to the turbulent motion of the gas on different scales which leads to higher collision velocities up to several m s^{-1} for aggregates of centimetre to decimetre in size (Cuzzi and Hogan 2003; Ormel and Cuzzi 2007). Highest collision velocities are obtained between aggregates with large size ratio. While a small projectile is dragged along with the gas flow, the large target moves with almost Keplerian speed. The relative velocity between the aggregates are as high as several tens of m s^{-1} .

The high collision velocities not only end fractal growth due to restructuring and compression of the aggregates, but also pose a problem to aggregate growth. Instead of sticking together, aggregates colliding at speeds higher than m s^{-1} erode or fragment and growth stops (Blum and Münch 1993; Dominik and Tielens 1997; Blum and Wurm 2008). At 1 au this limits the maximum size of aggregates from centimetre to less than metre.

Modelling of dust growth in protoplanetary disks around T Tauri stars has revealed that fragmentation is indeed necessary to explain the spectral energy distribution (SED) of these disks. Without fragmentation of larger aggregates replenishing a population

of small grains, the optical depth is quickly reduced. The excess emission in the infrared emitted from the dust heated by stellar radiation seen in the SED would vanish within 1 Myr. This is inconsistent with the typical lifetime of these disks of $\lesssim 10$ Myr (Dullemond and Dominik 2005).

However, even before erosion or fragmentation set in, bouncing collisions of submillimetre- to centimetre-sized aggregates lead to no net gain of mass (Zsom et al. 2010).

Windmark et al. (2012a) suggest a scenario for overcoming this “bouncing barrier”: a population of centimetre-sized “lucky” aggregates which may form due to subsequent low-velocity collisions (Windmark et al. 2012b) sweeps up the $100 \mu\text{m}$ -sized aggregates which are stuck at the bouncing barrier. Because the mass ratio of the collision partners is high, the small projectile fragments on impact and thereby deposits some of its mass on the target. This mass-transfer effect is, however, a very slow process due to the low projectile mass. It takes 1 Myr to grow a 100 m-sized body at 3 au.

On top of these collisional processes, millimetre- to metre-sized aggregates are effectively removed from the local formation regions by radial drift (Weidenschilling 1977a).

Because of that, the growth of larger bodies up to kilometre-sized planetesimals – and thus comets – simply through aggregation is effectively prevented making alternative formation mechanisms necessary.

1.3.2 Streaming instability

A hypothesis for the formation of planetesimals is to avoid the challenging intermediate size regime between metres and kilometres. The discovery of streaming instability in turbulent protoplanetary disks made it possible (Youdin and Goodman 2005; Johansen et al. 2007). This process makes use of the millimetre- to decimetre-sized aggregates, the typical sizes at which growth stops due to bouncing and fragmentation. These aggregates couple to the turbulent gas flow depending on their Stokes number.

The Stokes number (St) is the ratio of the stopping time of the aggregate (τ_s) and the orbital timescale (Ω_K^{-1}). Within one stopping time, the aggregate loses its momentum relative to the gas because of drag. While for $St \ll 1$ the aggregate is tightly coupled to the gas flow effectively moving with the gas, for $St \gg 1$ the aggregate is decoupled from the gas and moves with Keplerian speed, experiencing a headwind due to the gas. The intermediate range, $St \sim 1$, is interesting for the streaming instability.

Protoplanetary disks typically have vertically integrated solid-to-gas ratios (hereafter metallicity, Z) of 1% (Hayashi 1981; Williams and Best 2014). The ratio of the volumetric mass densities of dust (ρ_d) and gas (ρ_g) in the disk midplane (hereafter mass loading, ρ_d/ρ_g) is typically much lower than unity. When the turbulent motion of the gas, however, locally concentrates the aggregates in pressure maxima such that the mass loading exceeds unity, an instability is triggered (Youdin and Goodman 2005; Johansen et al. 2014).

Because the drag force between aggregates and gas acts in both ways, the accumulated aggregates accelerate the gas towards Keplerian velocity, thereby reducing the velocity difference to the gas. This slows down radial drift of the accumulated aggregates (Nakagawa et al. 1986). The slowing down of drift is enhanced by material

drifting into the already accumulated material which increases the mass loading. This positive feedback causes the instability to develop and to accumulate more aggregates. The mass loading rapidly increases to $10^2 - 10^3$ times its initial value. When the accumulated material fills its own Hill radius, self-gravity keeps the material together.

In the classical three-body problem of the Sun, a planet, and a massless test particle, the Hill radius defines the sphere around the planet inside which the test particle is gravitationally bound to the planet. This means the planet's gravity is stronger than Keplerian shear and tidal forces from the Sun. In the context of streaming instability, the role of the planet is replaced by the combined mass of the accumulated dust.

Gravitational collapse of the cloud of aggregates (hereafter pebble cloud) then forms planetesimals in the size range of kilometres to several hundreds of kilometres (Johansen et al. 2007; Nesvorný et al. 2010; Wahlberg Jansson and Johansen 2014; Schäfer et al. 2017).

Numerical studies of the onset of streaming instability show that the minimum Stokes number for which the instability occurs depends on the metallicity, for example $St \approx 0.1$ for $Z \approx 1.5\%$ (Carrera et al. 2015; Yang et al. 2017). A higher metallicity allows streaming instability to occur at lower Stokes numbers at the expense of longer timescales required before the instability sets in. A fixed value of $St = 0.1$ translates to an aggregate sizes in the range 20 cm to 0.7 mm between 1 au and 30 au, respectively, because the Stokes number depends not only on the aggregate size, but also on heliocentric distance through the surface density of the gas.

1.3.3 Comet formation by gravitational instability

Planetesimal formation through streaming instability is interesting in the context of comet formation, because it predicts highly porous, low density objects with very low tensile strength (Blum et al. 2014).

There are two sources contributing to the high porosity: the porosity of the aggregates constituting the building blocks of the planetesimal and the porosity due to the arrangement of aggregates within the planetesimal. The porosity of the aggregates is $\gtrsim 60\%$ depending on the compression experienced during formation (Zsom et al. 2010) and gravitational collapse of the cloud. The arrangement of aggregates adds another 40% porosity, because of the random packing of a narrow size distribution of approximately spherical aggregates (Skorov and Blum 2012; Fulle and Blum 2017). The final porosity of the planetesimal is then $\sim 70\%$ or higher. High porosity and dust-to-ice ratio larger than unity combine to give the low bulk density.

The gravitational collapse of the accumulated aggregates is a sequence of bouncing collisions (Blum et al. 2014; Wahlberg Jansson and Johansen 2014). The aggregates gradually lose energy and eventually stick together. Because the velocity at which millimetre- to decimetre-sized aggregates stick is low (of the order mm s^{-1}), the contact area at which the aggregates stick together is small. The porosity of the individual aggregates reduces the contact area even more. The result is a loosely packed layer with extremely low tensile strength, with values down to 1 Pa for millimetre-sized dust aggregates (Skorov and Blum 2012). For comparison, the collision and coalescence of aggregates produces objects with only 60% porosity and tensile strengths of the order 10^3 Pa and higher (Blum et al. 2006, 2014).

Aggregates in the size range between 3 mm to 1.6 cm were observed on comet 67P with the Comet Infrared and Visible Analyser (CIVA) camera on board the Philae lander of the Rosetta spacecraft (Poulet et al. 2016). The unplanned landing location of the lander turned out to be valuable, because it allowed imaging of an exposed wall not covered by cometary dust showing substructure of cracks and granular components. The millimetre-sized granular structures cannot have formed recently due to processes on the comet, because their size distribution is very different from other cometary material, such as boulders or dust in the coma. This led to the conclusion that CIVA imaged the very building blocks – millimetre- to centimetre-sized aggregates reminiscent of pebbles on a beach – of the comet. This fits very well with the picture of comets formed through gravitational collapse of material concentrated through the streaming instability. Furthermore, the observational constraint allows for the first time the direct comparison of numerical models of aggregate growth in the solar nebula with material of remnant and mostly unprocessed planetesimals.

1.3.4 Alternative hypotheses for the formation of comets

Besides streaming instability which continues at the point where growth of larger bodies is stopped by bouncing and fragmentation, there are other hypotheses for the formation of comets.

Porous growth of icy planetesimals

Increasing porosity in combination with the sticking properties of ice may form kilometre-sized icy planetesimals (Okuzumi et al. 2012; Kataoka et al. 2013b). While porosity significantly slows down radial drift and increases the growth rate of aggregates, the sticking properties of ice shift the maximum size of aggregates to larger values and may even prevent fragmentation. The rapid growth is a consequence of the aerodynamical coupling of aggregates with radii exceeding the mean free path of the molecules of the gas. The growth rate in this regime depends on aggregate size and larger aggregates grow faster, eventually faster than they would drift towards the Sun. Planetesimals would form locally as highly porous icy bodies with densities as low as $10^{-3} \text{ g cm}^{-3}$. Self-gravity then compresses these bodies to densities of $\sim 0.1 \text{ g cm}^{-3}$ (Kataoka et al. 2013b).

However, the porous growth scenario relies on the assumption that ice erodes or fragments only at very high collision velocities exceeding 60 ms^{-1} (Wada et al. 2013; Krijt et al. 2015). Realistic values for the onset of erosion of granular ice aggregates have recently been found to be around 15 ms^{-1} (Gundlach and Blum 2015). Furthermore, the collisional growth produces planetesimals with a tensile strength of typically $\gtrsim 10^3 - 10^4 \text{ Pa}$ (Blum et al. 2006, 2014) which is too high for comets. Furthermore, the condition that porosity accelerates growth is satisfied only at heliocentric distances $\lesssim 10 \text{ au}$. Farther out in the disk, radial drift still prohibits the formation of kilometre-sized planetesimals.

Comets as collisional fragments of planetesimals

The Nice model (Gomes et al. 2005; Morbidelli et al. 2005; Tsiganis et al. 2005) describes the evolution of the outer solar system and the formation of the Kuiper belt.

When the solar system formed, the orbits of the giant planets were closer together than today. The orbit of the outermost planet was inside 17 au. A disk of icy planetesimals, the transplanetary disk, extended from outside the orbits of the planets ($\gtrsim 17$ au) to ~ 30 au. The crossing of the mutual 1:2 mean motion resonance (integer ratio of the orbital periods) of Jupiter and Saturn ~ 700 Myr after formation of the planets created a dynamical instability in which the planets got their current orbits and the Kuiper belt formed from scattered planetesimals of the transplanetary disk (Tsiganis et al. 2005).

Morbidelli and Rickman (2015) and Rickman et al. (2015) estimated that a comet-sized body must have had at least one catastrophic collision on average. They therefore argue that comets are the collisional fragments of larger primordial planetesimals that formed in the transplanetary disk.

Unless comets escaped all catastrophic collision from formation until today, the collisional fragment scenario requires that collisions preserve the material properties of cometary nuclei, for example the high porosity and low tensile strength, or the bilobate shape (Rickman et al. 2015). Furthermore, pristine fractal dust aggregates contribute a significant fraction to cometary dust (Fulle et al. 2015; Mannel et al. 2016). Fulle and Blum (2017) showed that stresses exerted during catastrophic impacts would destroy any fractal aggregates which contradicts the collisional origin of comets.

Comets as primordial rubble piles

Based on observations of comet 67P and numerical simulation of comet formation conducted by Weidenschilling (1997), Davidsson et al. (2016) outline a comprehensive formation scenario for comets. The authors propose that comets are primordial rubble piles which formed at heliocentric distances in the range 15 au – 30 au due to the hierarchical aggregation of icy material.

While settling slowly to the midplane of the disk, submicrometre-sized grains grow to typically millimetre- to centimetre-sized bodies, the largest having sizes up to decimetres. The sticking properties of ice (Gundlach and Blum 2015) and collisions in which one of the collision partners fragments and transfers mass to the target (Windmark et al. 2012a) allow aggregates to overcome the regime of bouncing collision and metre-sized boulders to grow by sweeping up the smaller centimetre-sized aggregates.

Weidenschilling (1997) argues for differential drift as the dominant contribution to the collision velocity. Because drift velocities decrease for boulders with sizes larger than metres, collision velocities also decrease which prevents fragmentation and favours growth. By systematic accretion of bodies which are 3 – 6 times smaller than the growing body, kilometre-sized comets eventually form after a few Myr.

The slow growth of comets in this model prevents thermal alteration due to the radioactive decay of ^{26}Al because small bodies lose heat more efficiently than big ones. Therefore, comets remain at low temperatures which retains volatile components (CO , CO_2). The low collision velocities furthermore guarantee the formation of bodies with

high porosity, low bulk density, low tensile strength, and substructure on the metre scale.

However, a severe threat to this hierarchical growth model is radial drift of metre-sized boulders (Weidenschilling 1997; Davidsson et al. 2016) at large heliocentric distances. Bodies of this size drift significant distances in the disk within short timescales and are eventually accreted by the protosun before kilometre-sized comets can form (Weidenschilling 1977a). Turbulence adds a significant contribution to the collision velocity (Ormel and Cuzzi 2007). Furthermore, laboratory experiments and numerical modelling of aggregate growth have shown that fragmentation and erosion efficiently limits the maximum size of aggregates to less than metres (Blum and Wurm 2008; Güttler et al. 2010; Windmark et al. 2012a; Krijt et al. 2015).

1.4 Motivation and structure of the thesis

The aim of this thesis is to shed light on the process of comet formation in the context of planetesimals formed through gravitational collapse of dust and ice aggregates accumulated by the streaming instability. The following questions are addressed:

- What are the material properties (mass, size, porosity) of the aggregates that trigger the streaming instability?
- Does the gravitational collapse of a cloud of porous aggregates form planetesimals with comet-like properties?
- What are the implications for comet formation?

To answer the first question, local simulations of aggregate growth in the solar nebula are conducted to find the maximum size aggregates can locally reach making use of a laboratory-based collision model.

The second question is addressed by simulating the gravitational collapse of an ensemble of porous aggregates to find the combinations of composition, cloud mass, and initial porosity which lead to comet-like planetesimals.

Finally, the last question is tackled by combining the answers obtained for the two previous question with observational evidence of millimetre-sized cometary building blocks recently observed on comet 67P/Churyumov-Gerasimenko.

The thesis is organised as follows: In Chapters 2, 3, and 4 the solar nebula model, the collision model, and the representative particle method – the methodological backbone of the simulations – are discussed. In Chapter 5 the simulations of aggregate growth are presented. The gravitational collapse simulations are discussed in Chapter 6. In Chapter 7, implications for comet formation are drawn. Chapter 8 concludes the thesis with a summary.

2 Model of the solar nebula

The growth of aggregates takes place in the gaseous environment of protoplanetary disks. These disks form naturally around stars as a consequence of angular momentum conservation during the gravitational collapse of protostellar clouds of cold molecular gas (Shu et al. 1987). A description of such a protoplanetary disk needs to contain the density distributions of gas and dust, the temperature profile, and the turbulent state of the gas. The disk model affects the dynamics of the dust and hence the growth of aggregates. In this chapter, a technical description of the disk model used in this thesis and the dust dynamics is given.

2.1 The minimum mass solar nebula

The protoplanetary disk around the Sun in which the planets were born is the solar nebula. Using the structure of the solar system, the properties of the solar nebula were reconstructed by spreading the mass of each planet augmented by H and He until solar composition is reached in an annulus centred at the planet's current orbit (Weidenschilling 1977b; Hayashi 1981). The total mass of the solar nebula in units of the mass of the Sun ($M_{\odot} = 1.9891 \times 10^{33}$ g) was found to be between $0.01 M_{\odot}$ and $0.07 M_{\odot}$ with a surface density $\Sigma_g \propto r^{-3/2}$ between the planets Venus and Neptune, where r is the heliocentric distance (Weidenschilling 1977b). Later work using the same method revised the value of the surface density and established the minimum mass solar nebula (hereafter MMSN) as a protoplanetary disk containing the minimum amount of material required for the formation of the planets of the solar system (Hayashi 1981). The gas surface density profile of the MMSN is

$$\Sigma_g = 1700 \text{ g cm}^{-2} \times \left(\frac{r}{\text{au}} \right)^{-3/2}, \quad (2.1)$$

which amounts to a total mass of nebular gas of $0.013 M_{\odot}$ in the planetary domain between 0.35 au and 36 au. Observations of protoplanetary disks around other stars reveal similar masses in the range $10^{-4} M_{\odot}$ to $10^{-1} M_{\odot}$ (Williams and Best 2014).

Making the assumptions that solar irradiation is the only heating mechanism and that the disk emits the absorbed radiation as a block body, the temperature (T) of the MMSN is that of a passive disk, being vertically isothermal and varying with heliocentric distance only,

$$T = 280 \text{ K} \times \left(\frac{r}{\text{au}} \right)^{-1/2}. \quad (2.2)$$

While the MMSN temperature structure is in general a good first assumption, the true temperature structure of protoplanetary disks is more complicated and determined by the wavelength-dependent opacity of the dust. The vertical temperature structure is not isothermal, but consists of a cold midplane layer, a warm surface layer above the midplane, and a hot atmosphere (Dutrey et al. 2014; Armitage 2015).

Chiang and Goldreich (1997) analysed the temperature structure of a passive disk (no accretion) in radiative equilibrium around a T Tauri star by considering the hydrostatic equilibrium and the radiative transfer of dust and gas, which also allows dust and gas to have different temperatures, in a self-consistent way. They found that solar irradiation heats the dust of the upper layer of the disk to temperatures higher than that of a black body. This is because the dust absorbs more radiation in the visible wavelength regime than it emits in the infrared. The warm layer extends from the disk surface down to a depth where the disk becomes opaque for radiation in the visible wavelength regime (that is the optical depth of the dust in the visual (τ_v) reaches unity). The black body radiation emitted by the warm dust in the infrared penetrates deeper into the disk and heats the disk until it becomes also opaque in this wavelength regime ($\tau_{\text{IR}} = 1$). Even farther down, thermal balance sets the temperature which is the same for dust and gas. Chiang and Goldreich (1997) found that for a star with mass $M_\star = 0.5 M_\odot$, radius $R_\star = 2.5 R_\odot$ (solar radius $R_\odot = 6.96 \times 10^{10}$ cm), and effective temperature $T_\star = 4000$ K, the temperature of the disk midplane is $T_{\text{mid}} = 150 \text{ K} (r/\text{au})^{-3/7}$.

In addition to irradiation by the central star, the release of gravitational potential energy due to mass accretion linked to the disk's viscous evolution (Lynden-Bell and Pringle 1974) provides another heating mechanism.

In the remainder of this thesis, Eq. 2.2 is used for the disk temperature.

The vertical density structure of a protoplanetary disk is determined by hydrostatic equilibrium. The volumetric mass density of the disk is a Gaussian,

$$\rho_g = \frac{\Sigma_g}{\sqrt{2\pi}h_g} \exp\left(-\frac{z^2}{2h_g^2}\right), \quad (2.3)$$

where z is the height above (or below) the midplane, $h_g = c_s/\Omega_K$ is the pressure scale height defined as the ratio of sound speed (c_s) and Keplerian frequency ($\Omega_K = \sqrt{GM_\odot/r^3}$, where $G = 6.674 \times 10^{-8} \text{ cm}^3 \text{ g}^{-1} \text{ s}^{-2}$ is the gravitational constant). The mean molecular weight (μ) of a gas at temperature T consisting of different species whose partial pressures add up to the total pressure is the harmonic mean of the atomic mass numbers (A) weighted by the fractional abundance (f) of the respective species $\mu = \left(\sum_i f_i/A_i\right)^{-1}$. This results in $\mu \approx 2.3$ for an ideal gas of nominal disk composition of 75% H_2 and 25% He. The equation of state connecting pressure (p), gas density, and temperature is $p = k_B T \rho_g / (\mu m_{\text{H}})$, where $k_B = 1.38 \times 10^{-16} \text{ erg K}^{-1}$ is the Boltzmann constant and $m_{\text{H}} = 1.66 \times 10^{-24} \text{ g}$ is the atomic mass unit. The sound speed follows from $c_s^2 = \partial p / \partial \rho_g \propto r^{-1/2}$.

2.2 Turbulence

Protoplanetary disks are turbulent environments. Energy input on the largest scales cascades down to smaller scales until being dissipated as heat due to molecular friction.

Turbulence is necessary to account for the viscous evolution of protoplanetary disks which cannot be explained by molecular viscosity alone (Armitage 2010).

It is generally assumed that the magneto-rational instability (MRI) is the dominant mechanism which produces turbulence (Balbus and Hawley 1991). MRI acts in regions of the protoplanetary disk where the ionisation fraction of the gas (the ratio of number densities of electrons and gas) is sufficiently high. Gammie (1996) derived that the heliocentric distance- and temperature-dependent ionisation fraction should be $\gtrsim 10^{-13}$ (at 1 au) for MRI to work. A lower ionisation fraction would imply a higher resistivity (diffusivity) of the plasma for which the magnetic field lines can no longer be considered as frozen into the fluid, which is a requirement for the MRI mechanism.

Two gas parcels at heliocentric distances r_i and $r_o (\geq r_i)$ are coupled via magnetic fields. The differential rotation of the protoplanetary disk shears the gas parcels apart. The spring-like behaviour of magnetic fields slows down the inner parcel which loses angular momentum and moves closer in. The opposite happens for the outer gas parcel. This situation is unstable giving rise to turbulence.

Other sources of turbulence are hydrodynamic processes. The radial temperature gradient of a protoplanetary disk leads to vertical shear giving rise to vertical shear instability (VSI). Although protoplanetary disks are stable against radial convection, non-aligned pressure and density gradients give rise to the subcritical baroclinic instability (SBI) (Armitage 2015).

Shakura and Sunyaev (1973) introduced the so-called α -parameter to quantify the angular momentum transport due to turbulence. It can be described with a turbulent viscosity defined as $\eta_t = \rho_g v_t L$, where v_t is the typical velocity of turbulent eddies and L is the typical length scale of the turbulent eddy. For subsonic turbulence, the velocity of the turbulent eddy must be lower than the sound speed, $v_t \leq c_s$. The maximum size of a turbulent eddy is the pressure scale height of the disk, h_g . The turbulent viscosity is then $\eta_t = \alpha \rho_g c_s h_g$ with $\alpha < 1$. For protoplanetary disks with turbulence due to MRI, VSI, or SBI the turbulent strength is found to be $\alpha \sim 10^{-3}$ (Cuzzi et al. 2005; Armitage 2015).

2.3 Dust in protoplanetary disks

Protoplanetary disks contain refractory dust and volatiles frozen out as ice, both typically referred to as “dust”. The surface density of dust in the MMSN is

$$\Sigma_d = \begin{cases} 7.1 \text{ g cm}^{-2} \times \left(\frac{r}{\text{au}}\right)^{-3/2} & r < 2.7 \text{ au} \\ 30 \text{ g cm}^{-2} \times \left(\frac{r}{\text{au}}\right)^{-3/2} & r \geq 2.7 \text{ au} \end{cases} \quad (2.4)$$

(Hayashi 1981). The sudden increase of surface density is due to condensation of water ice outside the ice line at 2.7 au where the temperature falls below 170 K, the condensation temperature of water ice for MMSN conditions. With decreasing temperatures at larger heliocentric distances more volatile species freeze out. For example, CO_2 condenses below 80 K, CO below 25 K, and O below 24 K. From the surface density of dust follows that the metallicity is typically of the order 1%, which agrees with the metallicity of the interstellar medium (ISM) as well as disks around other stars which have metallicities in the range 5×10^{-3} to 0.5 (Williams and Best 2014).

The vertical density structure of the dust is determined by settling towards the disk's midplane due to the vertical component of the solar gravity and turbulent diffusion (Dubrulle et al. 1995). The volumetric mass density is well approximated by a Gaussian,

$$\rho_d = \frac{\Sigma_d}{\sqrt{2\pi}h_d} \exp\left(-\frac{z^2}{2h_d^2}\right), \quad (2.5)$$

with the scale height of the dust being dependent on the coupling between gas and dust via the Stokes number (see Sect. 2.3.2) and diffusion through turbulence via α

$$h_d = h_g \left[1 + \frac{\text{St}}{\alpha} \frac{1 + 2\text{St}}{1 + \text{St}} \right]^{-1/2} \quad (2.6)$$

(Dubrulle et al. 1995; Carballido et al. 2006; Youdin and Lithwick 2007). The efficient stirring of dust with $\text{St} \lesssim \alpha$ opposes sedimentation and puffs up the dust disk which leads to a scale height $h_d \approx h_g$. On the other hand, dust with $\text{St} \gtrsim \alpha$ sediments towards the midplane leading to $h_d \lesssim h_g$ and the formation of a dense midplane layer.

2.3.1 Aerodynamic drag on solid aggregates

The gas of the protoplanetary disk is pressure supported in radial direction. The pressure force partially balances gravity leading to a sub-Keplerian rotation velocity of the gas, $v_g = (1 - \eta)v_K$, with pressure gradient

$$\eta = -\frac{1}{2} \left(\frac{c_s}{v_K} \right)^2 \frac{\partial \log(\rho_g c_s^2)}{\partial \log r} = 1.8 \times 10^{-3} \left(\frac{r}{\text{au}} \right)^{1/2} \quad (2.7)$$

being of the order 1% at 30 au (Weidenschilling 1977a; Nakagawa et al. 1986); $v_K = \Omega_K r$ is the Keplerian velocity.

The motion of solid aggregates embedded in the disk is not pressure supported, but coupled to the gas via aerodynamic forces. The stopping time of the aggregates is defined as

$$\tau_s = \frac{m\Delta v}{F_D}, \quad (2.8)$$

characterising the timescale on which the aggregate loses its momentum relative to the gas.

The drag force $F_D = (1/2) C_D \rho_g A \Delta v^2$ depends on the geometrical cross section of the aggregate (A), the gas density (ρ_g), and the relative velocity between aggregate and gas (Δv). C_D is a dimensionless drag coefficient. There are different drag regimes depending on the ratio (a/λ) of aggregate size and mean free path of the gas molecules and the Reynolds number (Re) of the gas flow across the aggregate (Weidenschilling 1977a). The mean free path $\lambda = \mu m_H / (\rho_g A_{\text{mol}})$ is the typical length molecules travel without hitting other molecules. $A_{\text{mol}} = 2 \times 10^{-15} \text{ cm}^2$ is the collisional cross section of the gas molecules (75% H_2 and 25% He). The Reynolds number is $\text{Re} = 2a\Delta v/\nu$, comparing inertial forces acting on the aggregate with frictional forces, where $\nu = (1/2)\lambda v_{\text{thm}}$ is the molecular viscosity and $v_{\text{thm}} = \sqrt{8/\pi}c_s$ is the thermal velocity of the molecules.

The Epstein regime applies for aggregates smaller than the gas mean free path ($\lambda/a > 4/9$) and the drag coefficient is

$$C_D = \frac{8v_{\text{thm}}}{3\Delta v}. \quad (2.9)$$

In the Epstein regime, the drag force is due to molecules colliding elastically with the solid aggregate. Momentum is transferred between the molecules and the aggregates and the aggregate is decelerated (Epstein 1924).

For larger aggregates ($\lambda/a < 4/9$), there are three regimes depending on the Reynolds number

$$C_D = \begin{cases} 24 \text{Re}^{-1} & \text{Re} < 1, \\ 24 \text{Re}^{-0.6} & 1 < \text{Re} < 800, \\ 0.44 & \text{Re} > 800. \end{cases} \quad (2.10)$$

The first regime is the Stokes regime, the second is non-linear drag, and the third regime is the quadratic drag regime. In contrast to the Epstein regime, the drag arises from the hydrodynamical flow of gas across the aggregate. In the Stokes regime, the drag force reduces to the well-know formula for a solid sphere of radius a and cross section $A = \pi a^2$ moving through a viscous fluid at velocity Δv : $F_D = 6\pi\eta a\Delta v$, where $\eta = \nu\rho_g$ is the dynamic viscosity.

2.3.2 The Stokes number

The dimensionless Stokes number,

$$\text{St} = \tau_s \Omega_K, \quad (2.11)$$

compares the stopping time to the orbital timescale. Aggregate and gas are tightly coupled for $\text{St} \ll 1$ meaning that the aggregate follows the gas flow. On the other hand, aggregate and gas are decoupled for $\text{St} \gg 1$. The aggregate moves with almost Keplerian velocity but experiences a constant headwind of magnitude ηv_K as a consequence of which the aggregate slowly spirals towards the Sun (Adachi et al. 1976; Weidenschilling 1977a). The marginal coupling for $\text{St} \approx 1$ aggregates gives rise to dynamical effects like the streaming instability (Youdin and Goodman 2005; Johansen et al. 2007).

From the definition of the stopping time and the drag coefficient presented in Sect. 2.3.1, the Stokes numbers in the Epstein and the Stokes regime are

$$\text{St} = \begin{cases} \frac{3\pi}{8} \frac{m}{A\Sigma_g} & \lambda/a > 4/9 \quad (\text{Epstein}), \\ \frac{3\pi}{8} \frac{m}{A\Sigma_g} \frac{4}{9} \frac{a}{\lambda} & \lambda/a < 4/9 \quad (\text{Stokes}). \end{cases} \quad (2.12)$$

Here, m , a , and A are the mass, the radius, and the geometrical cross section of the aggregate. Σ_g and λ are the surface density and the mean free path of the gas.

2.3.3 Relative velocities between dust and gas

Radial and azimuthal drift of the aggregates with respect to the gas are consequences of the aerodynamic coupling. Small aggregates ($St \ll 1$) are forced to sub-Keplerian speeds. Because of the lack of pressure support, the sub-Keplerian motion leads to an inward directed net force acting on the aggregate and resulting in radial drift towards the Sun. Large aggregates ($St \gg 1$) move with nearly Keplerian speed. The gas flow provides a constant headwind of magnitude ηv_K and the drag force reduces the orbital energy of the aggregate leading to inward drift.

The respective drift velocities are

$$\Delta v_r = \frac{-2\Delta v_{hw}}{St + St^{-1}} \quad (2.13)$$

for radial drift and

$$\Delta v_\phi = \frac{-\Delta v_{hw}}{1 + St^2}. \quad (2.14)$$

for azimuthal drift relative to a Keplerian orbit (Weidenschilling 1977a; Armitage 2010, 2015).

The disk headwind velocity $\Delta v_{hw} = v_K - (1 - \eta)v_K$ is the difference between the gas velocity and the Keplerian velocity of the aggregate. The azimuthal drift of the aggregate relative to the gas is hence $\Delta v'_\phi = \Delta v_{hw} - \Delta v_\phi$.

Turbulence produces relative motion between aggregates and gas. The turbulent motion of the gas stirs the aggregates leading to a relative velocity of magnitude

$$\Delta v_t = c_s \sqrt{\frac{\alpha(1 - Re_t^{-1/2})}{(1 + St)(St + Re_t^{-1/2})}} St, \quad (2.15)$$

where $Re_t = \alpha c_s h_g / \nu$ is the turbulent Reynolds number defined as the ratio of turbulent viscosity ($\alpha c_s h_g$) and molecular viscosity (ν) (Cuzzi and Hogan 2003; Ormel and Cuzzi 2007).

For typical disk conditions, turbulent viscosity is orders of magnitudes higher than molecular viscosity and hence $Re_t \ll 1$. Turbulent stirring increases with aggregate size $\propto \sqrt{St}$ due to the coupling to larger eddies and approaches the limiting value $\sqrt{\alpha} c_s$ given by the velocity of the largest eddies (Cuzzi and Weidenschilling 2006).

Drift and turbulent stirring add up to the total relative velocity of the aggregate with respect to the gas

$$\Delta v = \sqrt{\Delta v_t^2 + \Delta v'_\phi{}^2 + \Delta v_r^2}. \quad (2.16)$$

While radial and azimuthal drift are systematic velocities with a clear direction, turbulent stirring has random direction as turbulence is assumed to be isotropic.

Brownian motion is energy equipartition between the gas molecules and the aggregates. The velocity distribution function is described by a Maxwell-Boltzmann distribution with mean value of the velocity of

$$\Delta v_{BM} = \sqrt{\frac{8k_B T}{\pi m}} \quad (2.17)$$

(Ossenkopf 1993). Small aggregates are in the Epstein regime or the Stokes regime where $F_{\text{drag}} \propto \Delta v$ instead of $\propto \Delta v^2$. The Stokes number is independent of the relative motion between aggregate and gas, and the contribution from Brownian motion is unimportant. Large aggregates are not affected by Brownian motion because the velocity decreases with mass $\propto m^{-1/2}$. For this reason, it is safe to neglect Brownian motion as a contribution to the relative velocity.

In the non-linear and the quadratic drag regimes Δv and St need to be determined self-consistently via iteration, because Δv is a function of the Stokes number and vice versa. However, this only plays a role for large particles and does not affect the early stage of aggregate growth.

3 Collision model

The backbone of any numerical modelling of aggregate growth in protoplanetary disks or aggregate collisions during gravitational collapse of a pebble cloud is a collision model for binary collisions between aggregates. Depending on the material properties and the collision velocity of the aggregates, the collision model predicts the outcome of the collision. Numerical and laboratory studies revealed a variety of different outcomes ranging from sticking to fragmentation (Blum and Wurm 2008; Wada et al. 2008; Güttler et al. 2010; Windmark et al. 2012a). This chapter gives a technical description of the collision model used in the simulations.

3.1 Dust properties

3.1.1 Material properties of the monomers

Aggregate growth is a hierarchical process starting with monomers as the smallest unit. Monomers have radius a_0 and are made of either silicate dust or water ice with grain densities of $\rho_d = 3 \text{ g cm}^{-3}$ and $\rho_i = 1 \text{ g cm}^{-3}$, respectively.

Collisions between aggregates create, restructure, or break contacts between the constituent monomers. Two monomers in contact are connected by adhesive van der Waals forces. Therefore, this adhesive force needs to be overcome for starting restructuring. The rolling friction force (F_{roll}) is the threshold force above which the contact changes irreversibly due to a rolling motion of the two spheres. The other mechanisms that are able to move the contact irreversibly are sliding and twisting of the two spheres. However, sliding and twisting require more energy than rolling which is hence the dominant source of aggregate restructuring (Dominik and Tielens 1997).

$F_{\text{roll}} = 6\pi\gamma\delta$ is a material property and depends on the surface energy (γ) and the critical displacement (δ) for the onset of rolling (Dominik and Tielens 1995; Krijt et al. 2014). The values of γ and δ are somewhat uncertain. However, F_{roll} can be measured in the laboratory with time resolved observations of restructuring events of aggregates (Heim et al. 1999). Using similar measurements Gundlach et al. (2011a) find $F_{\text{roll}} = 114.8 \times 10^{-5} \text{ dyn}$ for $a_0 = 1.45 \mu\text{m}$ ice grains, while $F_{\text{roll}} = 12.1 \times 10^{-5} \text{ dyn}$ for $a_0 = 0.75 \mu\text{m}$ SiO_2 grains. The difference of roughly a factor of 10 reflects the higher surface energy of ice due to H_2O being a polar molecule causing stronger van der Waals forces at contact.

The rolling energy $E_{\text{roll}} = (1/2)F_{\text{roll}}\pi a_0$ is the energy that is needed to roll two monomers in contact by a quarter of their circumference $\pi a_0/2$ (Dominik and Tielens 1997). Krijt et al. (2014) found that the rolling friction force scales with monomer

radius $\propto a_0^{2/3}$ because the critical displacement is a fraction of the contact radius of two viscous spheres, which is given by JKR-theory (Johnson et al. 1971) to be $a_{\text{eq}} = [9\pi\gamma a_0^2 / (8\mathcal{E})]^{1/3}$, where \mathcal{E} is the reduced modulus of elasticity combining Young's modulus and Poisson ratio describing the material response to deformation. With the measured values for the rolling friction force and the scaling with monomer size, the respective rolling energies for silicate dust and water ice are

$$E_{\text{roll}} = \begin{cases} 1.4 \times 10^{-8} \left(\frac{a_0}{0.75 \mu\text{m}} \right)^{5/3} \text{ erg} & (\text{dust}), \\ 2.6 \times 10^{-7} \left(\frac{a_0}{1.45 \mu\text{m}} \right)^{5/3} \text{ erg} & (\text{ice}). \end{cases} \quad (3.1)$$

3.1.2 Material properties of dust aggregates

An aggregate of mass m and characteristic radius a (Mukai et al. 1992) is an agglomerate of N monomers. Mass and radius are linked through a mass-radius relation

$$m \propto a^{D_f}, \quad (3.2)$$

where D_f is the fractal dimension in the range $D_f = 1 \dots 3$. A spherical aggregate has $D_f = 3$, a flat plain-like aggregate has $D_f = 2$, and a chain-like aggregate has $D_f = 1$ (Blum et al. 2006).

There are two basic types of aggregates: highly porous fractal aggregates that form through ballistic cluster-cluster aggregation (BCCA) and spherical porous non-fractal aggregates that form through ballistic particle-cluster aggregation (BPCA). BCCA is characteristic for a system with a narrow size distribution. Collisions take place between similar-sized aggregates and the fractal aggregates that form have a fractal dimension of $D_f \approx 2$. On the other hand, BPCA is characteristic for a system with a wide or bimodal size distribution. Aggregates grow by addition of single grains onto the larger target and the aggregates. This process produces spherical aggregates with fractal dimension of $D_f = 3$.

The volume-filling factor of the aggregate is defined as the ratio of the volume filled with matter, given by the total volume of monomers (NV_0), and the effective volume of the aggregate ($V = 4\pi a^3/3$)

$$\phi = \frac{NV_0}{V}. \quad (3.3)$$

Porosity is related to the volume-filling factor via $\mathcal{P} = 1 - \phi$, quantifying the amount of void space within the aggregate. A volume-filling factor of $\phi = 1$ characterises a solid sphere without void space. On the other hand, an aggregate with 90% porosity has a volume-filling factor of $\phi = 0.1$. Because the monomers are assumed to be solid spheres without substructure they have $\phi = 1$, while aggregates have $\phi < 1$ in general.

The geometrical cross section (A) of the aggregate determines the strength of aerodynamic coupling to the solar nebula gas. For a solid sphere, the geometrical cross section is simply πa^2 . However, naively assuming that for porous aggregates $A = \pi a^2$ would result in a geometrical cross section that increases faster than the total cross section of the constituent monomers, because the fractal dimension of aggregates that

form due to Brownian motion driven coagulation is $D_f \approx 1.9$ (Kempf et al. 1999). For fractal aggregates, the number of constituent monomers scales with aggregate radius $N \propto a^{D_f}$ (see Eq. 3.2 for $N = m/m_0$). For this reason, the geometrical cross section is $A \propto N^{2/D_f} \approx N^{1.05}$, while the total cross section of monomers is $A \propto N$. To solve this, Minato et al. (2006) numerically measured the geometrical cross section of aggregates formed through BCCA and provided an empirical formula for the geometrical cross section given by

$$\frac{A_{\text{BCCA}}}{\pi a_0^2} = \begin{cases} 12.5N^{0.685} \exp(-2.53/N^{0.0920}) & N < 16 \\ 0.352N + 0.566N^{0.862} & N \geq 16. \end{cases} \quad (3.4)$$

For aggregates formed through BPCA with fractal dimension of $D_f \approx 3$, the cross section is

$$A_{\text{BPCA}} \approx \pi a^2 \quad (3.5)$$

because of the spherical shape of the aggregate. Okuzumi et al. (2009) combine the different cross-sections to construct a formula for the geometrical cross section of a porous aggregate

$$A = \left(\frac{1}{A_{\text{BCCA}}} + \frac{1}{\pi a^2} - \frac{1}{\pi a_0^2 N^{2/D_f}} \right)^{-1}. \quad (3.6)$$

In the BCCA-limit, where $\pi a^2 \gg A_{\text{BCCA}}$, Eq. 3.6 reduces to A_{BCCA} . In the BPCA-limit, where $A_{\text{BCCA}} \gg \pi a^2$, the formula recovers A_{BPCA} . For a porous aggregate with fractal dimension $2 \lesssim D_f \lesssim 3$, the geometrical cross section will be in between the limiting cases due to the correction term $(\pi a_0^2 N^{2/D_f})^{-1}$.

A physical collision between two aggregates with radii a_1 and a_2 , respectively, takes place if the mutual distance is less than $a_1 + a_2$. For this reason, $\pi(a_1 + a_2)^2$ is the collisional cross section of the two aggregates.

3.2 Collision velocities of dust aggregates

The relative velocities of aggregates are linked to their aerodynamic coupling to the gas given by the underlying protoplanetary disk model. Collisions between aggregates are driven by Brownian motion, turbulence, and relative drift. The vertical component of the Sun's gravity forcing aggregates to settle towards the mid-plane of the protoplanetary disk adds a vertical velocity component. In the mid-plane, however, the vertical settling velocity is zero.

3.2.1 Brownian motion

Brownian motion due to elastic collisions between gas molecules and aggregates is a stochastic process which leads to a relative velocity of magnitude

$$\Delta v_{\text{BM}} = \sqrt{\frac{8k_B T (m_1 + m_2)}{\pi m_1 m_2}} \quad (3.7)$$

between two aggregates of masses m_1 and m_2 , respectively. Brownian motion increases for higher gas temperature, because the faster thermal motion of molecules renders collisions more energetic leading to higher velocities of the individual aggregates. On the other hand, Brownian motion decreases with increasing aggregate mass because the relative momentum of the light gas molecules decreases.

3.2.2 Turbulence induced collision velocities

Ormel and Cuzzi (2007) calculate relative velocities of aggregates due to turbulence and provide closed form expressions for collisions between two aggregates with Stokes numbers St_1 and St_2 ($St_2 \leq St_1$).

Small aggregates tightly coupled to the gas ($St_{1,2} < Re_t^{-1/2}$) have stopping times shorter than the typical decay time of a turbulent eddy. The aggregate adjusts to the gas motion of the eddy. This means that two aggregates with the same Stokes number trapped in the same eddy will have the same systematic motion and hence zero relative velocity.

In an intermediate regime for aggregates with $Re_t^{-1/2} < St_1 < 1$, stopping times are longer than the eddy turn-over time. Therefore, aggregates experience random velocity kicks by the eddies. Even for two aggregates with the same Stokes number, the kicks are different in magnitude and direction and the collision velocity is non-zero.

Heavy aggregates with $St_1 > 1$ have stopping times longer than the turn-over time of the largest eddies ($\sim \Omega_K^{-1}$). As a consequence, the aggregates still experience random kicks by turbulent eddies that cause non-zero collision velocities, but the magnitude of these kicks decreases for increasing size.

In summary, the turbulent collision velocities in the three different regimes are

$$\Delta v_t^2 = \alpha c_s^2 \begin{cases} \frac{St_1 - St_2}{St_1 + St_2} \left(\frac{St_1^2}{St_1 + Re_t^{-1/2}} - \frac{St_2^2}{St_2 + Re_t^{-1/2}} \right) & St_1, St_2 < Re_t^{-1/2} \\ \left[2y_a - (1 + \beta) + \frac{2}{1 + \beta} \left(\frac{1}{1 + y_a} + \frac{\beta^3}{y_a + \beta} \right) \right] St_1 & Re_t^{-1/2} < St_1 < 1, \\ \frac{1}{1 + St_1} + \frac{1}{1 + St_2} & St_1 > 1 \end{cases} \quad (3.8)$$

where $y_a = 1.6$ and $\beta = St_1/St_2$.

The highest collision velocities due to turbulence of the order $\sqrt{\alpha} c_s \sim 55 \text{ m s}^{-1}$ at 1 au are reached for aggregates with $St_1 \approx 1$ and $St_1 \gg St_2$. As the sound speed decreases with increasing distance to the Sun, turbulent collision velocities for fixed Stokes number are highest in the inner disk. Because the Stokes number depends on aggregate size and the outward decreasing surface density of the gas ($\Sigma_g \propto r^{-3/2}$), aggregates colliding with a fixed velocity are smaller for larger heliocentric distance.

3.2.3 Differential drift of aggregates

Differential radial and azimuthal drift lead to non-zero velocity collisions between aggregates with different Stokes numbers given by

$$\Delta \bar{v}_r = |\Delta v_r(St_1) - \Delta v_r(St_2)|, \quad (3.9)$$

$$\Delta \bar{v}_\phi = |\Delta v_\phi(St_1) - \Delta v_\phi(St_2)|. \quad (3.10)$$

Here, Δv_r and Δv_ϕ are the velocities given in Eqs. 2.13 and 2.14.

Collision velocities due to relative drift are highest for two aggregates with very different Stokes numbers, for example $St_1 \gg St_2$. In this case, collision velocities are of the order $\eta v_K \sim 60 \text{ m s}^{-1}$ for nominal disk conditions, which holds throughout the disk because $\eta \propto r^{1/2}$ and $v_K \propto r^{-1/2}$ cancel the dependence on heliocentric distance.

3.2.4 Total collision velocity

The total collision velocity between aggregates 1 and 2, respectively, is given by the sum of the squares of the individual contributions

$$\Delta v = \sqrt{\Delta v_{\text{BM}}^2 + \Delta v_t^2 + \Delta \bar{v}_r^2 + \Delta \bar{v}_\phi^2}. \quad (3.11)$$

While drift is systematic motion, Brownian motion and turbulence are velocity contributions with random direction.

3.3 The outcome of dust aggregate collisions

The amount of energy which is dissipated within the aggregate in a collision is given by the collision energy,

$$\Delta E = \frac{1}{2} (1 - \varepsilon^2) \frac{m_1 m_2}{m_1 + m_2} \Delta v^2. \quad (3.12)$$

This is the energy used for rearranging and breaking contacts between monomers resulting in fragmentation and/or compression. The coefficient of restitution (ε) is 0 for purely inelastic collision (sticking) and 1 for purely elastic collision. For collisions that lead to bouncing and dissipate only part of the energy, the coefficient of restitution is in the range $0 < \varepsilon < 1$.

Collisions between dust aggregates have a broad spectrum of possible outcomes. Depending on collision velocities and masses of the involved aggregates, sticking, bouncing, fragmentation, mass transfer, and erosion were observed in the laboratory (Güttler et al. 2010). Sticking leads to growth of porous aggregates. While hit-and-stick collisions build up fractal aggregates, sticking collisions at higher velocities also lead to compression of the aggregates terminating fractal growth. Bouncing collisions do not contribute to the growth of aggregates, even though negligible amounts of mass may be transferred between the bouncing aggregates. Already fractured aggregates may fragment as a result of bouncing collisions. Mass transfer describes the process where a small projectile colliding with a large target fragments and deposits some of its mass on the target. Finally, erosion takes place when the small projectile produces a crater on the target thereby excavating mass which is lost from the target.

Mass transfer and erosion usually occur simultaneously and whether the aggregate gains or loses mass is determined by the net effect of both processes. While mass transfer and erosion leave most of the target intact, fragmentation globally destroys the colliding aggregates thereby producing a distribution of fragments.

The transition between all these different collision types is expressed by threshold velocities above which a collision leads to a different outcome. This is reasonable,

because more energy is dissipated within the aggregate for higher collision velocities. As a results more contacts can be restructured or broken eventually leading to erosion or fragmentation. Windmark et al. (2012a) compiled the results of a large number of available laboratory experiments to extract these threshold velocities and to construct a collision model for dust aggregates. The thresholds are found to be power laws in mass, $\Delta v \propto m^q$.

3.3.1 Sticking and bouncing

For sticking and bouncing collisions the slope is $q = -5/18$ (Thornton and Ning 1998) and the threshold velocities depend on the projectile mass (m_p) as

$$\Delta v_{\text{stick}} = \left(\frac{m_p}{3.0 \times 10^{-12} \text{ g}} \right)^{-5/18} \text{ cm s}^{-1}, \quad (3.13)$$

$$\Delta v_{\text{bounce}} = \left(\frac{m_p}{3.3 \times 10^{-3} \text{ g}} \right)^{-5/18} \text{ cm s}^{-1}, \quad (3.14)$$

(Weidling et al. 2012).

Below the sticking threshold ($\Delta v \leq \Delta v_{\text{stick}}$), collisions between aggregates result in sticking. Whether this is hit-and-stick growth without restructuring or sticking with compression depends on ΔE and the rolling energy (see porosity model below).

Above the bouncing threshold ($\Delta v \geq \Delta v_{\text{bounce}}$), collisions result in bouncing. There is no net gain in mass in this regime, but porous aggregates are compressed.

Collision velocities in the range $\Delta v_{\text{stick}} < \Delta v < \Delta v_{\text{bounce}}$ result in either sticking or bouncing with a certain sticking probability $0 < P_{\text{stick}} < 1$. The sticking probability is assumed to be a logarithmic probability distribution of the functional form

$$P_{\text{stick}} = 1 - \frac{\log_{10}(\Delta v / \Delta v_{\text{stick}})}{\log_{10}(\Delta v_{\text{bounce}} / \Delta v_{\text{stick}})} \quad (3.15)$$

(Windmark et al. 2012a). The ratio $\Delta v_{\text{bounce}} / \Delta v_{\text{stick}}$ is independent of mass. However, for given collision velocity Δv , the sticking threshold decreases with increasing projectile mass. Therefore, P_{stick} decreases for increasing projectile mass rendering sticking less likely for larger projectiles.

3.3.2 Fragmentation, erosion, and mass transfer

A collision between aggregates with high mass ratio ($m_t \gg m_p$) will not result in the global fragmentation of the target, because the collision energy is deposited locally at the impact site of the projectile. The small projectile, however, will fragment thereby eroding mass from or depositing mass onto the target. On the other hand, for similar masses ($m_t \approx m_p$), the collision energy is distributed equally between target and projectile leading to the fragmentation of both bodies.

For this reason, fragmentation is best modelled in the centre of mass (cms) frame, where the mass ratio of target and projectile determines how the collision energy is

distributed between the colliding bodies (Windmark et al. 2012a). The velocities of target and projectile in the centre of mass frame are

$$\Delta v_{p,\text{cms}} = \frac{\Delta v}{1 + m_p/m_t}, \quad \Delta v_{t,\text{cms}} = \frac{\Delta v}{1 + m_t/m_p}. \quad (3.16)$$

The collision energy available for the body to fragment is given by the cms-velocity. Thus, comparing the cms-velocity to the threshold velocity of fragmentation allows to determine whether the body fragments or not.

For fragmentation, the slope of the power law is $q = -0.16$ (Beitz et al. 2011) and less steep than for sticking and bouncing and the threshold velocity is

$$\Delta v_{\text{frag}} = \left(\frac{m_{p,t}}{3.67 \times 10^7 \text{ g}} \right)^{-0.16} \text{ cm s}^{-1}. \quad (3.17)$$

The normalisation constants follow from laboratory experiments (Beitz et al. 2011) and the mass is either the mass of the projectile (m_p) or of the target (m_t). Fragmentation occurs if $\Delta v_{\text{cms}} > \Delta v_{\text{frag}}$.

3.3.3 The change of the aggregate mass

Once the collision type is set, the new mass of the aggregates can be determined. While sticking and bouncing are simple, because the new mass is either the sum of the aggregate masses (sticking) or unchanged (bouncing), fragmenting collisions are more complicated, because the amount of material removed (or added, for mass transfer) needs to be determined. Quantitative expressions can be found in the literature compiling the results of laboratory experiments of dust aggregate collisions (Güttler et al. 2010; Windmark et al. 2012a).

In general, fragmentation produces a largest remnant and a distribution of fragments. The relative mass of the largest remnant is found from the relation

$$\mu_{\text{lr}} = 3.27 \left(\frac{m}{1 \text{ g}} \right)^{-0.068} \left(\frac{\Delta v}{1 \text{ cm s}^{-1}} \right)^{-0.43}, \quad (3.18)$$

which applies for target and projectile by using the respective mass and cms-velocity (Windmark et al. 2012a). The mass of the largest remnant is hence $m_{\text{lr}} = \mu_{\text{lr}} m$. The number density of fragments is a power law distribution $n(m)dm \propto m^{-9/8} dm$ (Blum and Münch 1993; Güttler et al. 2010).

Global fragmentation of both aggregates occurs if $\mu_{\text{lr},p} < 1$ and $\mu_{\text{lr},t} < 1$. Both target and projectile fragment into a largest remnant and a distribution of fragments.

On the other hand, if $\mu_{\text{lr},p} < 1$ and $\mu_{\text{lr},t} \geq 1$, only the projectile fragments and the target is left mostly intact or gains mass indicating erosion or mass transfer, respectively. The amount of mass transferred from projectile to target ($\epsilon_{\text{acc}} m_p$) found in laboratory experiments is expressed in terms of a velocity dependent accretion efficiency

$$\epsilon_{\text{acc}} = -6.8 \times 10^{-3} + 2.8 \times 10^{-4} \frac{13 \text{ cm s}^{-1}}{\Delta v_{\text{frag}}} \frac{\Delta v}{1 \text{ cm s}^{-1}}, \quad (3.19)$$

which is at most 0.5 (Beitz et al. 2011; Windmark et al. 2012a). Similarly, the degree of erosion in terms of the projectile mass is found to be

$$\frac{m_{\text{er}}}{m_{\text{p}}} = 9.3 \times 10^{-6} \left(\frac{m_{\text{p}}}{m_0} \right)^{0.15} \frac{\Delta v}{1 \text{ cm s}^{-1}} - 0.4 \quad (3.20)$$

(Teiser and Wurm 2009; Schr apler and Blum 2011; Windmark et al. 2012a). The net effect of mass transfer and erosion $\Delta m = \epsilon_{\text{acc}} m_{\text{p}} - m_{\text{er}}$ determines whether the aggregate gains ($\Delta m > 0$) or loses mass ($\Delta m < 0$). Therefore, the mass of the target changes to $m_{\text{t}} + \Delta m$, while the projectile mass is reduced by $\epsilon_{\text{acc}} m_{\text{p}}$. Because the projectile fragments, the mass that is not deposited on the target ($m_{\text{p}} - \epsilon_{\text{acc}} m_{\text{p}}$) is distributed among a largest remnant and a power law distribution of fragments.

3.3.4 Material and collision properties of water ice

The threshold velocities given by Eqs. (3.13), (3.14), and (3.17) are valid for silicate dust aggregates. However, water is ubiquitous in the universe, from molecular clouds to protoplanetary disks. In the outer solar system, water ice frozen out on small silicate grains is expected to contribute much to the solid material. Furthermore, water ice is the major volatile component of comets. Because H_2O is a polar molecule, the surface energy of water ice is higher compared to silicate dust making sticking more efficient and fragmentation more difficult (Dominik and Tielens 1997; Wada et al. 2007; Gundlach et al. 2011a; Aumatell and Wurm 2014).

While laboratory experiments with silicate dust aggregates are relatively easy to do, experiments with ices are much more challenging. The experiment must be conducted at low temperatures to prevent the ice from melting. Therefore, experimental data on collisions of icy aggregates is still sparse, but first results are already available (Gundlach et al. 2011a; Gundlach and Blum 2015). Experiments with ice aggregates composed of micrometre-sized ice grains indicate that sticking is possible for velocities of up to 9.6 m s^{-1} , while erosion sets in for velocities $\gtrsim 15.3 \text{ m s}^{-1}$ (Gundlach and Blum 2015). This is ~ 10 times higher than for silicate dust. Therefore as a good first approximation, the threshold velocities for sticking, bouncing, and fragmentation of dust can be scaled up by a factor 10 to obtain the corresponding thresholds for ice.

3.4 The porosity of dust aggregates

The porosity of the aggregates is an integral part of the collision model as it has been shown to be important for aggregate growth (Ormel et al. 2007; Okuzumi et al. 2012; Kataoka et al. 2013b). While sticking collisions build up highly porous aggregates no matter whether restructuring is taken into consideration, the cumulative effect of bouncing collisions once they set in result in strong compression of the aggregates up to a maximum value. Although it can be expected that the violent process of fragmentation changes the volume-filling factor, the effect should be restricted to the impact location.

3.4.1 Porosity change in sticking collisions

The porosity model of Okuzumi et al. (2012) describes the porosity change of aggregates in sticking collisions with compression.

A hit-and-stick collision of two aggregates with volumes V_1 and $V_2 (\leq V_1)$, respectively, without compression creates a new aggregate with volume

$$V_{1+2,HS} = V_1 + V_2 + V_{\text{void}}, \quad (3.21)$$

where V_{void} is the volume of void space added in the collision. Okuzumi et al. (2009) calculate V_{void} by numerically studying the growth history of porous aggregates and find

$$V_{\text{void}} = \min \left[0.99 - 1.03 \ln \left(\frac{2}{V_1/V_2 + 1} \right), 6.94 \right] V_2. \quad (3.22)$$

In the BCCA limit of $V_1 \approx V_2$, the additional void space created is $0.99V_2$ and Eq. 3.21 reduces to $V_{1+2} \approx 3V_1$. From the fractal law, $N \propto a^{D_f}$, follows a fractal dimension of the new aggregate of $D_f = 3 \log 2 / \log 3 \approx 1.9$, which is the expected value for BCCA. In the BPCA limit of $V_1 \gg V_2$, the volume of the new aggregate is $V_{1+2} = V_1 + V_2 + 6.94V_2 \gtrsim V_1$, which is derived considering that BPCA leads to a porosity of 0.874 (Kozasa et al. 1993). For any other volume ratio V_1/V_2 , the void volume takes a value in between the limiting cases and the resulting aggregate will have a fractal dimension $1.9 \lesssim D_f \lesssim 3$.

With compression starting when the collision energy exceeds the rolling energy ($\Delta E \gtrsim E_{\text{roll}}$), the voids in the newly created aggregate are partially crushed. Wada et al. (2008) and Suyama et al. (2008) found that for head-on collisions of equal-sized aggregates ($V_1 = V_2$) the volume of the new aggregate in the limit $\Delta E \gg E_{\text{roll}}$ is

$$V_{1+2} = \left[\frac{(3/5)^5 \Delta E}{N_{1+2}^5 b E_{\text{roll}} V_0^{10/3}} + (2V_1^{5/6})^{-4} \right]^{-3/10}, \quad (3.23)$$

where $b = 0.15$ is a dimensionless fitting parameter and V_0 is the volume of a monomer (Wada et al. 2008).

Equations 3.21 and 3.23 are limiting cases for $\Delta E \ll E_{\text{roll}}$ and $\Delta E \gg E_{\text{roll}}$, respectively. Suyama et al. (2012) provide an updated analytic formula to also take the intermediate case ($\Delta E \sim E_{\text{roll}}$) into account. Therefore, a sticking collision with collisional compression produces a new aggregate with volume

$$V_{1+2} = \begin{cases} \left[\left(1 - \frac{\Delta E}{3bE_{\text{roll}}} \right) V_{1+2,HS}^{5/6} + \frac{\Delta E}{3bE_{\text{roll}}} (V_1^{5/6} + V_2^{5/6}) \right]^{6/5} & V_{1+2,HS}^{5/6} > V_1^{5/6} + V_2^{5/6}, \\ & \Delta E < 3bE_{\text{roll}} \\ \left[\frac{(3/5)^5 (\Delta E - 3bE_{\text{roll}})}{N_{1+2}^5 b E_{\text{roll}} V_0^{10/3}} + (V_1^{5/6} + V_2^{5/6})^{-4} \right]^{-3/10} & V_{1+2,HS}^{5/6} > V_1^{5/6} + V_2^{5/6}, \\ & \Delta E > 3bE_{\text{roll}} \\ \left[\frac{(3/5)^5 \Delta E}{N_{1+2}^5 b E_{\text{roll}} V_0^{10/3}} + V_{1+2,HS}^{-10/3} \right]^{-3/10} & V_{1+2,HS}^{5/6} < V_1^{5/6} + V_2^{5/6} \end{cases}, \quad (3.24)$$

(Okuzumi et al. 2012). The coefficient of restitution in ΔE is $\varepsilon = 0$, because the aggregates stick.

3.4.2 Compression in bouncing collisions

Aggregates which do not stick but bounce off each other are compressed. The compression is given by the compression curve of the respective material describing the response of the volume-filling factor to the applied pressure.

Compression experiments with silicate dust

Blum and Schr apler (2004), Blum et al. (2006), and G uttler et al. (2009) performed compression experiments with silica aggregates as cosmic dust analogues. In these experiments, dust samples were produced by the random ballistic deposition method (Blum and Schr apler 2004). The samples have an initial volume-filling factor of $\phi = 0.15$. An unidirectional pressure was applied and the volume-filling factor as function of the pressure was measured.

According to G uttler et al. (2009), the compression curve can be approximated by an analytic function of the form

$$\phi(p) = \phi_2 - \frac{\phi_2 - \phi_1}{\exp\left(\frac{\log_{10} p - \log_{10} p_m}{\Delta}\right) + 1}, \quad (3.25)$$

where p is the applied pressure. The parameters p_m and Δ are the pressure at which 50% of the compression is reached and the width of the transition regime describing the onset of aggregate restructuring, respectively. The aggregate has an initial volume-filling factor ϕ_1 and saturates at a maximum volume-filling factor of ϕ_2 for $p \rightarrow \infty$.

Compression can be either unidirectional or omnidirectional. Unidirectional compression applies pressure from one side allowing the aggregate to flow and expand into the other directions, while omnidirectional compression applies pressure from all sides. For this reason, the maximum volume-filling factor is higher for omnidirectional compression ($\phi_2 \approx 0.6$) than for unidirectional compression ($\phi_2 \approx 0.3$).

The collective effect of bouncing collisions between porous aggregates should be omnidirectional compression, because the stochastic coagulation process randomises the impact directions. Furthermore, bouncing collisions only compress the outer rim of an aggregate leaving the inner core porous and reducing the volume-filling factor by a factor 0.79 (Weidling et al. 2009; G uttler et al. 2010).

For static omnidirectional compression, the parameter p_m is found to have a value of $p_m = 1.3 \times 10^5 \text{ dyn cm}^{-2}$ (G uttler et al. 2009). However, comparing the measurements to smoothed-particle hydrodynamic (SPH) simulations, G uttler et al. (2009) constrain this value to $p_m = 1.3 \times 10^4 \text{ dyn cm}^{-2}$ to match the experimental results. To also describe compression of aggregates with $\phi < \phi_1$, G uttler et al. (2010) extrapolate Eq. 3.25 to lower volume-filling factors with a power law function for $p < p_m$

$$\phi(p) = \frac{\phi_1 + \phi_2}{2} \cdot \left(\frac{p}{p_m}\right)^{\frac{\phi_2 - \phi_1}{\phi_2 + \phi_1} \cdot \frac{1}{2\Delta \ln 10}}. \quad (3.26)$$

Drop-tower experiments with millimetre-sized porous dust aggregates produced by random-ballistic deposition showed bouncing (Landeck 2016). The number of contacts between neighbouring monomers (coordination number) in these porous aggregates is

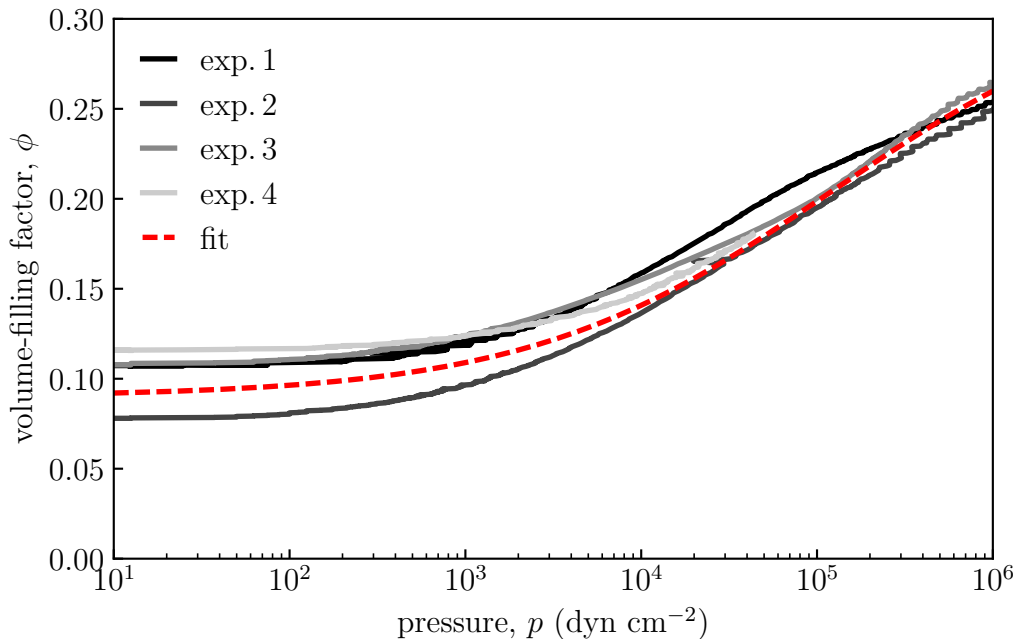


Figure 3.1: Compression curve of granular water ice from laboratory experiments. The experiments were conducted by B. Gundlach, IGEP, TU Braunschweig. Solid and dashed curves show the results from four different measurements and the best fit according to Eq. 3.25. (Credit: Lorek et al., *A&A*, 587, A128, 2016, reproduced with permission ©ESO)

2. According to numerical studies, aggregates with coordination number $\lesssim 6$ should not bounce (Wada et al. 2011; Seizinger and Kley 2013). The experimental results, however, disprove this. Porous aggregates with coordination number of 2 bounce at velocities higher $0.13 - 0.23 \text{ m s}^{-1}$ (Landeck 2016).

Compression experiments with granular water ice

While dust has been studied in the laboratory for a long time, (water) ice has not. However, laboratory experiments measuring the compression curve of granular water ice conducted by B. Gundlach from the Institut für Geophysik und extraterrestrische Physik (IGEP) of TU Braunschweig are available (Lorek et al. 2016).

Droplets of liquid water that were sprinkled into the cold environment of a chamber filled with nitrogen gas produced spherical micrometre-sized water ice grains with a mean radius of $1.45 \mu\text{m}$ (Gundlach et al. 2011a; Jost et al. 2013). The ice grains sedimented to the bottom of the chamber where they formed a porous water ice aggregate. The resulting aggregates had an initial volume-filling factor of 0.1.

The compressive strength was measured in a similar manner as for dust aggregates. The sample was positioned on a scale and slowly compressed with a cooled piston (temperatures kept to 125 K) with the sample being free to flow into non-compressed volumes (unidirectional compression). As in the case of dust aggregates, the compression curve of the granular water ice sample can be fitted with Eq. 3.25 as shown in Fig. 3.1.

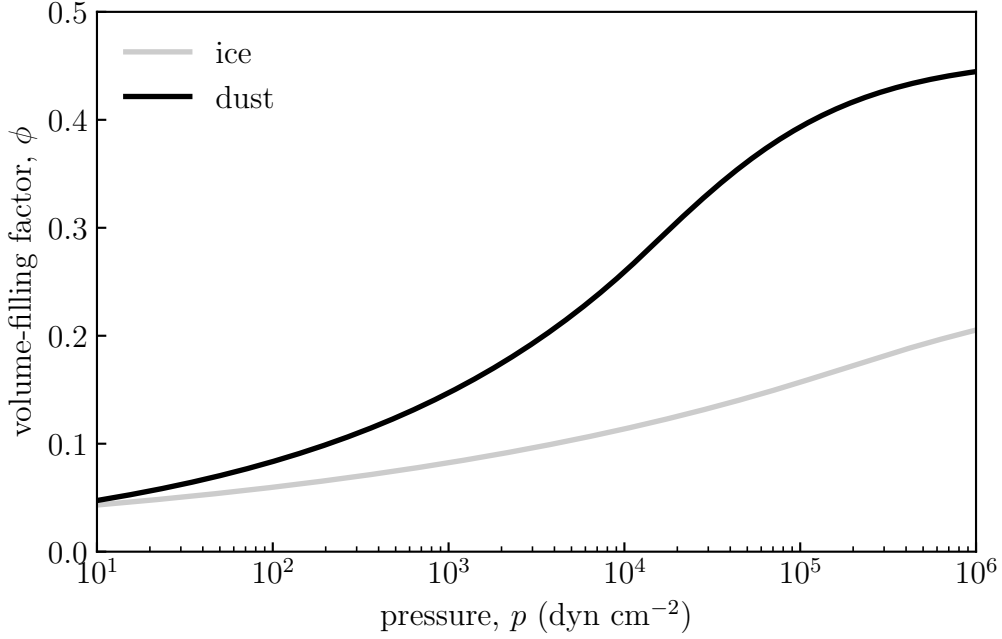


Figure 3.2: Compression curve for dust and ice aggregates. The lines show the compression curve according to Eq. 3.27 with the parameters given in Table 3.1. The volume-filling factor is multiplied with a factor 0.79 to account for the compression of the outer rim (Weidling et al. 2009; Güttler et al. 2010).

The results show that compression of water ice requires a higher pressure compared to silica dust, which agrees with the higher rolling energy of water ice (Gundlach et al. 2011a).

Compression curve for dust aggregates

With Eqs. 3.25 and 3.26, the functional form of the full compression curve is hence given for all values of the volume-filling factor as

$$\phi(p) = \begin{cases} \frac{\phi_1 + \phi_2}{2} \cdot \left(\frac{p}{p_m}\right)^{\frac{\phi_2 - \phi_1}{\phi_1 + \phi_2} \cdot \frac{1}{2\Delta \log_{10}}} & (p < p_m) \\ \phi_2 - \frac{\phi_2 - \phi_1}{\exp\left(\frac{\log_{10} p - \log_{10} p_m}{\Delta}\right) + 1} & (p \geq p_m) \end{cases}. \quad (3.27)$$

The parameters ϕ_1 , ϕ_2 , Δ , and p_m for dust and water ice are summarised in Table 3.1.

Figure 3.2 shows the compression curves for silicate dust and water ice according to Eq. 3.27 with the parameters given in Table 3.1, respectively. The volume-filling factor is multiplied with a factor 0.79 to account for the compression of the outer rim (Weidling et al. 2009; Güttler et al. 2010), which is why the compression curves saturate at values lower than ϕ_2 .

Table 3.1: Parameters for the dust and ice compression curves.

Material	ϕ_1	ϕ_2	p_m (dyn cm ⁻²)	Δ (dex)
Dust ^a	0.12	0.58	1.3×10^4	0.58
Ice ^b	0.09	0.32	12.5×10^4	0.87

Notes. ^(a) Dust value taken from Table 1 in Güttler et al. (2009) ^(b) Ice value taken from Table 1 in Lorek et al. (2016) .

3.4.3 Porosity change in fragmentation, erosion, and mass transfer

When collision velocities are high enough for aggregates to erode or fragment, the fragments that split from either target or projectile have the same fractal dimension as the progenitor aggregate (Krijt et al. 2015). From the fractal relation ($N \propto a^{D_f}$, Eq. 3.2) and the volume-filling factor ($\phi = Na_0^3/a^3$) the fractal dimension is calculated as

$$D_f = 3 \left[1 - \frac{\log_{10} \phi}{\log_{10} N} \right]^{-1} \quad (3.28)$$

(Krijt et al. 2015). The new radius of the fragment can be calculated via the mass-radius relation for fractal aggregates (Eq. 3.2). A constant fractal dimension preserves the internal structure of fragments. Because D_f is constant, the volume-filling factor of the fragment is lower than that of the progenitor aggregate. A higher volume-filling factor reflects that destructive collisions are energetic enough to compress the fragments.

3.4.4 Non-collisional compression of porous aggregates

Kataoka et al. (2013a) introduced a static compression mechanism for porous aggregates. An aggregate of density ρ is able to withstand a maximum pressure of

$$p_{\max} = \frac{E_{\text{roll}}}{a_0^3} \left(\frac{\rho}{\rho_0} \right)^3, \quad (3.29)$$

before being compressed. Here, ρ_0 is the monomer density.

Hence, for a given pressure, $p \geq p_{\max}$, the aggregate is compressed until $p = p_{\max}$ is obtained for an equilibrium density

$$\rho_{\text{eq}} = \frac{\rho_0 a_0}{(E_{\text{roll}} p)^{1/3}}. \quad (3.30)$$

Static compression is the result of non-collisional compression mechanisms that do not result from the collision of two aggregates. One source is the ram-pressure of the gas in the protoplanetary disk, $p_{\text{ram}} = m \Delta v \Omega_K / (\pi a^2 \text{St})$. Another source is self-gravity of the aggregate $p_{\text{grav}} = Gm^2 / (\pi a^4)$. Therefore accounting for these two sources, the

total pressure (p) entering Eq. 3.30 is the sum of p_{ram} and p_{grav} . While ram-pressure plays a role for low aggregate masses, self-gravity becomes important only for aggregate masses $\gtrsim 10^{10}$ g (Kataoka et al. 2013b).

3.5 Aggregates of mixed composition

While sublimation of volatile ices inside the ice line leaves behind the bare refractory silicate grains, condensation of ices on silicate cores forms icy grains outside the ice line.

Crystalline silicate dust grains which could only have formed close to the Sun were found in comet 81P/Wild 2 (McKeegan et al. 2006; Zolensky et al. 2006). These grains must have been transported to the comet forming region via radial mixing processes in the solar nebula where they were incorporated into comets (Gail 2001; Bockelée-Morvan et al. 2002; Hanner and Bradley 2004; Cuzzi and Weidenschilling 2006).

Sunshine et al. (2007) detected water absorption in the infrared spectra of the material excavated from comet 9P/Tempel 1 during the Deep Impact mission which implied micrometre-sized water ice grains being present in the deep interior of the comet. Furthermore, the radial brightness profiles of dust jets emitted from comet 67P can be reproduced using a model of “dirty aggregates” (mixture of dust and ice grains) with radii between $5\ \mu\text{m}$ and $50\ \mu\text{m}$ (Gicquel et al. 2016).

Taking into account that water ice provides the major part of cometary volatiles, this evidence indicates that comets form in a region where two components are available: silicate dust and water ice. It is thus necessary to introduce the concept of mixed composition aggregates as homogeneous mixtures of silicate and water ice monomers. This differs from the core-mantle grains (Greenberg 1989) for aggregates larger than a single monomer, because an ice monomer can still be pictured as water ice that condensed on a small silicate grain whose contribution to the bulk density of the grain is negligible.

It is hence a valid assumption that the solar nebula is radially mixed and that the comet-forming region harbours (sub)micrometre-sized silicate and ice grains emanating from their respective formation region inside and outside the ice line. Aggregates of mixed composition form through collision and coalescence of these grains. There are no experimental or numerical studies with dust/ice-mixed aggregates. However, the collision behaviour of silicate dust and water ice are the limiting cases and an aggregate of mixed composition will presumably lie in between, depending on the relative content of dust and ice. A simple interpolation scheme based on the abundances of dust and ice monomers relative to the total number of monomers within the aggregate should capture this concept.

3.5.1 Composition and density

An aggregate of mass m is an agglomerate of N_d dust monomers with mass $m_{0,d}$ and N_i ice monomers with mass $m_{0,i}$ with $N = N_d + N_i$. The ratio of total dust and ice mass of

the aggregate is the dust-to-ice ratio and gives the composition of the aggregate

$$\xi = \frac{m_d}{m_i} = \frac{N_d m_{0,d}}{N_i m_{0,i}}. \quad (3.31)$$

In this definition, the dust-to-ice ratio is a mass ratio and not the volumetric ratio. Furthermore, other volatile species, such as CO, CO₂, CH₄, or NH₄, that might be present are not considered.

The density of the aggregate depends on the dust-to-ice ratio. For fixed ξ , the total mass of the aggregate is the sum of the dust and ice components,

$$m = m_d + m_i = \rho_d V_d + \rho_i V_i. \quad (3.32)$$

Here, $V_{d,i} = N_{d,i} V_0$ are the volumes filled with dust and ice monomers of densities $\rho_{d,i}$, respectively.

For a porous aggregate with volume-filling factor ϕ , the mass is also given by

$$m = \frac{\rho_\bullet (V_d + V_i)}{\phi}, \quad (3.33)$$

where ρ_\bullet is the density of the aggregate. ρ_\bullet is the actual (porous) density and it is therefore necessary to account for porosity in Eq. 3.33 by including ϕ in the denominator, which simply reflects the definition of the volume-filling factor.

Introducing the total volume $V = V_d + V_i$ and defining the volume fractions $v_{d,i} = V_{d,i}/V$ gives the constraint

$$v_d + v_i = 1. \quad (3.34)$$

From Eqs. 3.31, 3.32, 3.33, and 3.34, the density of the aggregate can be calculated as

$$\rho_\bullet = \phi \frac{\rho_d \rho_i (1 + \xi)}{\xi \rho_i + \rho_d}, \quad (3.35)$$

which depends only on the composition (dust-to-ice ratio), the density of the components (ice and dust monomers), and the porosity (volume-filling factor). In the limiting cases $\xi \rightarrow 0$ (no dust), the density of a porous ice aggregate, $\rho_\bullet = \phi \rho_i$, is recovered and vice versa for $\xi \rightarrow \infty$ (no ice), the density is $\rho_\bullet = \phi \rho_d$.

3.5.2 Collision model for aggregates of mixed composition

The parameter used for interpolation is the abundance of dust monomers $x = N_d/N$, which is linked to the dust-to-ice ratio (see Eq. 3.31). The collision outcome in general depends on the ability to create, restructure, or break contacts between the constituent monomers of the aggregate motivating this choice (Dominik and Tielens 1995, 1997; Blum and Wurm 2000).

Typically, the number of contacts between the monomers is of the order of the number of monomers. More dust makes the aggregate behave more like pure silicate dust, while more ice shifts the collision properties towards pure ice. The threshold

velocities, for example the sticking threshold, for an aggregate of mixed composition are then found from the simple interpolation scheme

$$\Delta v_{\text{stick}}^{\text{mixed}} = x \Delta v_{\text{stick}}^{\text{dust}} + (1 - x) \Delta v_{\text{stick}}^{\text{ice}} \quad (3.36)$$

The same scheme is used for the fragmentation and bouncing thresholds, respectively.

By keeping track of the number of dust and ice monomers that are added (removed) in every single collision, the evolution of the composition of the aggregates can be followed. However, the stochastic nature of coagulation results in aggregates with the same dust-to-ice ratio as the formation location.

To explicitly account for the mixed composition in the porosity evolution, the compression curve and the rolling energy have to be changed to

$$\phi^{\text{mixed}}(p) = x \cdot \phi^{\text{dust}}(p) + (1 - x) \cdot \phi^{\text{ice}}(p), \quad (3.37)$$

$$E_{\text{roll}}^{\text{mixed}} = x \cdot E_{\text{roll}}^{\text{dust}} + (1 - x) \cdot E_{\text{roll}}^{\text{ice}}. \quad (3.38)$$

With the assumption that all monomers have the same size, the monomer density used in the static compression of aggregates can be calculated as $\rho_0^{\text{mixed}} = x \cdot \rho_d + (1 - x) \cdot \rho_i$.

A remark on the abundance of dust monomers. Whenever target and projectile are necessarily treated together, being the case for the sticking and bouncing threshold velocities and the rolling energy in Eqs. 3.24, $x = (N_d^t + N_d^p)/(N^t + N^p)$. On the other hand, when target and projectile are treated separately, being the case for the fragmentation threshold velocity, the compression curve, and E_{roll} in Eq. 3.30, $x = N_d^{t,p}/N^{t,p}$, respectively for target and projectile.

The collisional outcome space

Figure 3.3 shows the typical outcome for collisions between compact aggregates ($\phi = 0.4$) with dust-to-ice ratio of 5 at 30 au. Collision between aggregates of radii $\lesssim 10 \mu\text{m}$ result in sticking due to the low collision velocities of $\lesssim \text{cm s}^{-1}$. For larger aggregate radii, sticking is gradually replaced by bouncing and 100% bouncing is reached for aggregates in the range 0.1 mm–1 mm colliding with velocities between 1 m s^{-1} – 5 m s^{-1} with similar-sized objects. Above this size, collisions between similar-sized aggregates result in fragmentation. If the projectile is smaller than the target, collision velocities increase up to $\sim 60 \text{ m s}^{-1}$ due to relative drift motion. The target can grow due to mass transfer up to $\sim 1 \text{ dm}$ before erosion sets in. Further growth due to mass transfer would require projectiles $\lesssim 10^{-3} \text{ cm}$.

In contrast to Fig. 3.3, Fig. 3.4 shows the collision outcome for porous aggregates ($\phi = 10^{-3}$) with dust-to-ice ratio of 5 at 30 au. Although porosity is not an explicit input parameter for the collision model, it strongly affects the outcome because a high porosity reduces m/A which lowers the Stokes number. The aerodynamic coupling to the solar nebula gas increases and hence the collision velocities decrease. As consequence, aggregates can grow to larger sizes than in the compact case. The bouncing regime starts at $\sim 1 \text{ cm}$ and fragmentation at $\sim 1 \text{ dm}$ for similar-sized aggregates. Boulders of 1 m – 10 m can form due to mass transfer before erosion sets in.

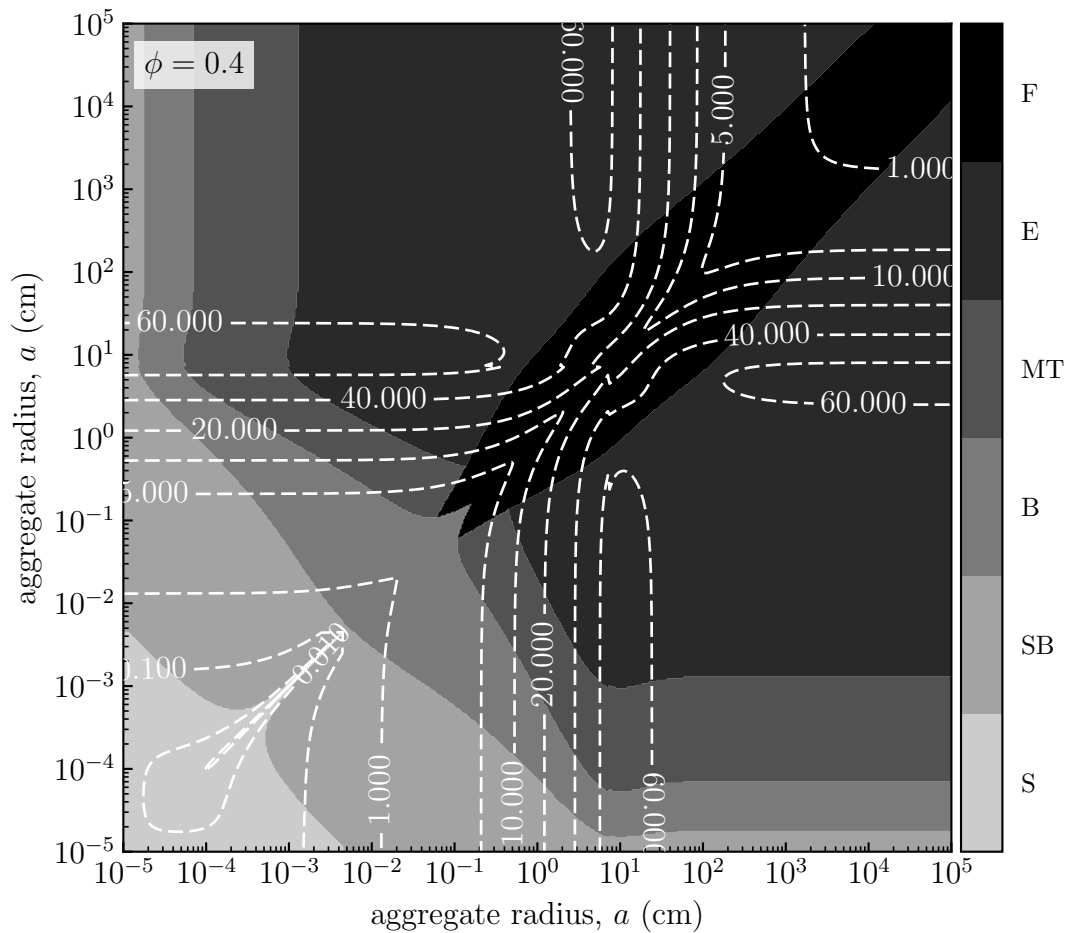


Figure 3.3: Collision outcome map for aggregate collisions. Heliocentric distance is 30 au, monomer radius is $0.1 \mu\text{m}$, and the dust-to-ice-ratio of aggregates is 5. Aggregates are compact with volume-filling factor 0.4. Depending on the size of the colliding aggregates, the outcome is sticking (S), sticking or bouncing with a certain transition probability (SB), bouncing (B), mass transfer (MT), erosion (E), or fragmentation (F). The contours show collision velocities in m s^{-1} .

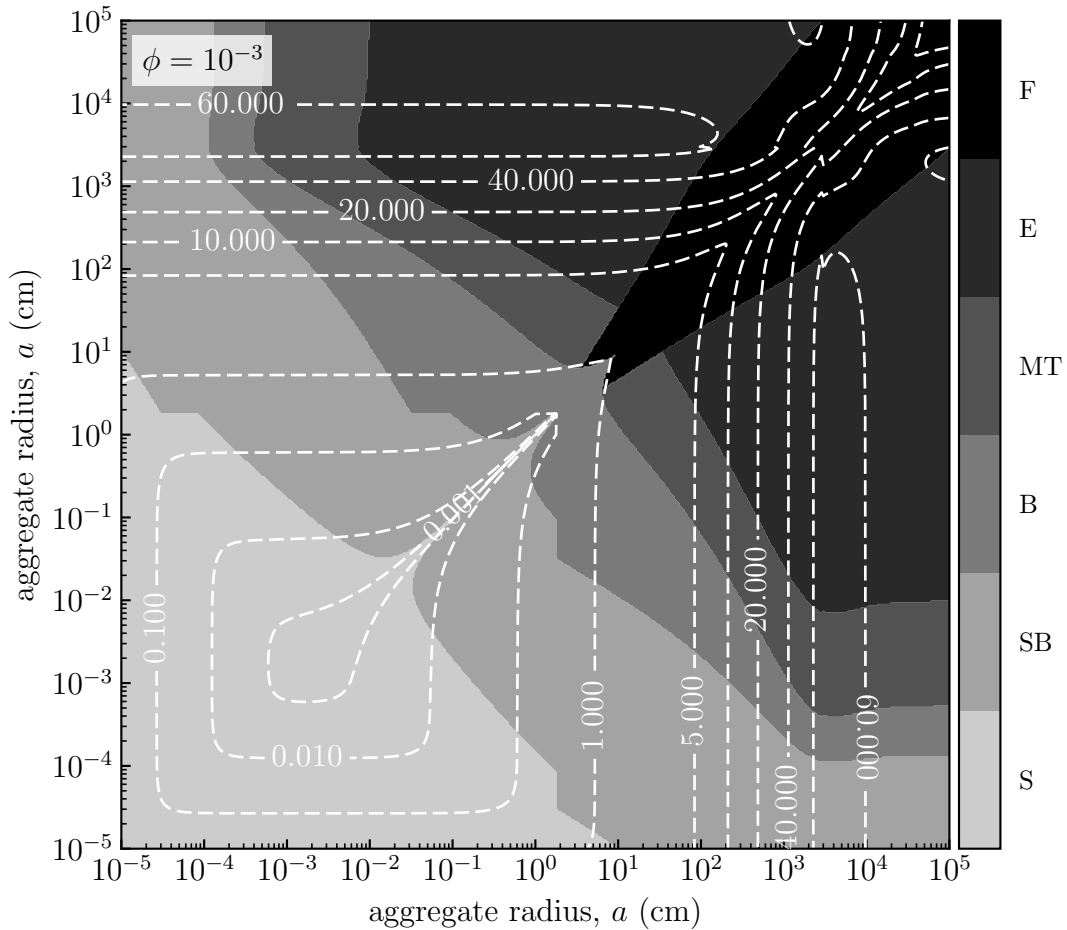


Figure 3.4: Collision outcome map for aggregate collisions. Heliocentric distance is 30 au, monomer radius is $0.1 \mu\text{m}$, and the dust-to-ice-ratio of aggregates is 5. Aggregates are porous with volume-filling factor 10^{-3} . Depending on the size of the colliding aggregates, the outcome is sticking (S), sticking or bouncing with a certain transition probability (SB), bouncing (B), mass transfer (MT), erosion (E), or fragmentation (F). The contours show collision velocities in m s^{-1} .

3.6 Caveats of the collision model

Although the collision model proposed for aggregates of mixed composition is a plausible approach, the underlying assumptions must be kept in mind when making use of it.

3.6.1 Homogeneously mixed aggregates

Condensation of ice on silicate grains with negligible contribution to the bulk density and radial mixing of silicate grains to the outer solar system produces a two-component system from which aggregates as a homogeneous mixture of dust and ice monomers form. This is a reasonable assumption backed up by observational evidence of the composition of cometary grains and modelling of radial transport processes in protoplanetary disks.

However, it only holds true if either all ices have already condensed on silicates or the condensation timescale is longer than the radial mixing and coagulation timescales, respectively. Otherwise, the silicate grains would acquire ice mantles. For this sort of core-mantle grains (Greenberg 1989), the sticking properties would be given by the mantle material, while the mass would be determined by the refractory core. In this case, interpolation between the two materials becomes unnecessary.

3.6.2 Combining collision outcome with porosity

Another caveat concerns the porosity model. Porosity affects the collision outcome only indirectly via the collision velocity, because the coupling to the nebula gas is different from that of compact aggregates. Güttler et al. (2010) include porosity directly in the collision model and distinguish between porous and compact based on a critical volume-filling factor (ϕ_c). Below $\phi_c = 0.4$ aggregates are considered “porous”, while “compact” above ϕ_c . Although Güttler et al. (2010) see different behaviour of porous and compact aggregates, their choice of $\phi_c = 0.4$ is reasonable but not entirely backed up by observation. Furthermore, Güttler et al. (2010) explicitly distinguish between equal-sized and different-sized collisions based on a critical mass ratio in the range 10 – 1000, while the transition might be more smooth.

The collision model of Windmark et al. (2012a) identifies the most important collision types of the Güttler et al. (2010) model and include additional experimental results to construct a smooth collision model for compact aggregates, but not considering porosity. On the other hand, the porosity model is based on numerical experiments for hit-and-stick collisions and sticking with compression (Wada et al. 2008; Suyama et al. 2008; Okuzumi et al. 2009, 2012; Suyama et al. 2012) and laboratory experiments on the compression of porous ($\phi \approx 0.1$) aggregates (Weidling et al. 2009; Güttler et al. 2009; Landeck 2016).

Thus, combining the most important collision types with a porosity model found by other means is a valid first step in understanding collisions of aggregates. A denser coverage of collision outcome space taking the combined effects of collision type, mass ratio, and porosity into account is necessary to further improve the collision model.

3.6.3 Bouncing of porous aggregates

The bouncing behaviour of porous aggregates is not clear, because collision energy needs to be transformed into elastic energy and back to get rebound. The fragile nature of porous-sized aggregates, however, would favour efficient dissipation of the collision energy due to restructuring or breaking of contacts resulting in sticking or fragmentation. While numerical simulations with molecular dynamics codes indeed do not show bouncing unless the coordination number is $\gtrsim 6$ (volume-filling factors $\gtrsim 0.4$) (Wada et al. 2011; Seizinger and Kley 2013), experiments with dust aggregates in the laboratory frequently show bouncing also for porous aggregates (Blum and Münch 1993; Langkowski et al. 2008; Heißelmann et al. 2010; Weidling et al. 2012; Kothe et al. 2013; Weidling and Blum 2015; Landeck 2016).

Most recent results show bouncing also for aggregates with coordination number of 2 (Landeck 2016). The reason why numerical simulations and laboratory experiments deviate is unclear; sample preparation effects have been excluded (Kothe et al. 2013). However, the laboratory experiments indicate that bouncing is a common phenomenon. Therefore, including bouncing in the collision model is reasonable, but extrapolating bouncing behaviour to very low volume-filling factors ($\phi \ll 1$, coordination number of 2) is uncertain, although it is backed up by observation (Landeck 2016). More laboratory work is needed to shed light on this topic in the future.

4 Monte Carlo modelling of dust coagulation

The very first step of comet formation – and planet formation in general – is the growth from (sub)micrometre-sized monomers to larger aggregates in the protoplanetary disk. In this chapter the basic concepts of particle aggregation and how to model it are described.

4.1 The Smoluchowski equation for coagulation

The process of collision and coalescence into larger aggregates is called coagulation. As a direct application for his theory of Brownian motion, Smoluchowski (1916) developed the mathematical framework. The time evolution of the number density $g(m, t)$ of particles with mass m_i is given by the following equation:

$$\begin{aligned} \frac{\partial g(m_i, t)}{\partial t} = & \frac{1}{2} \sum_{j=1}^{i-1} K(m_i - m_j, m_j) g(m_i - m_j, t) g(m_j, t) \\ & - \sum_{j=1}^{\infty} K(m_i, m_j) g(m_i, t) g(m_j, t), \end{aligned} \quad (4.1)$$

where $K(m_i, m_j)$ is the so-called collision kernel containing the physics of the collision, namely the rate at which the particles coagulate.

The Smoluchowski equation is a rate equation describing the time evolution of a certain quantity, here the mass of the particles, by evaluating the gain and loss terms. The first term of Eq. 4.1 is the gain term. It sums up all the combinations of particles with mass $m < m_i$ leading to a particle with mass m_i . The factor 1/2 takes the symmetry of the collision kernel with respect to m_i and m_j into account. The second term in Eq. 4.1 is the loss term and describes the loss of particles with mass m_i by collisions with other particles.

The coagulation equation can also be written in continuous form by replacing the sum with an integration over mass:

$$\begin{aligned} \frac{\partial g(m, t)}{\partial t} = & \frac{1}{2} \int_0^m K(m - m', m') g(m - m', t) g(m', t) dm' \\ & - \int_0^{\infty} K(m, m') g(m, t) g(m', t) dm'. \end{aligned} \quad (4.2)$$

Analytic solutions of the Smoluchowski equation exist for three different collision kernels. These are the constant kernel, $K = \text{const.}$, the linear kernel, $K = m_i + m_j$, and the product kernel, $K = m_i \times m_j$. However, for more realistic collision kernels no analytic solutions exist and for solving Eq. 4.1 one has to resort to numerical methods. The analytic solutions provide a benchmark for the validity of any numerical method of coagulation.

4.2 Numerically solving the Smoluchowski equation

4.2.1 Direct numerical integration

The classical approach for solving the Smoluchowski equation is the numerical integration of Eq. 4.2 (for example Dullemond and Dominik 2005; Brauer et al. 2008; Birnstiel et al. 2010, and many more). While numerical integration is considerably fast and easily allows for modelling protoplanetary disks on a global scale, the method has certain disadvantages. Discretisation of mass, near cancellation of gain and loss terms, mass conservation, and very short time steps for numerical integration render the solution of the Smoluchowski equation numerically challenging (Dullemond and Dominik 2005; Ormel et al. 2007; Zsom and Dullemond 2008; Drążkowska et al. 2014). Furthermore, adding particle properties other than mass (for example porosity) increases the dimensionality of the Smoluchowski equation, which drastically increases the complexity of the numerical integration (Okuzumi et al. 2009).

4.2.2 Monte Carlo methods

A different approach is to use a particle-based Monte Carlo method, which simulates the time evolution of \mathcal{N} particles (for example Gillespie 1975; Ormel et al. 2007; Zsom and Dullemond 2008). Instead of numerically integrating Eq. 4.2, the procedure is to use random numbers to determine the time of the next collision and the colliding particles (Ormel et al. 2007). The outcome of the collision is then calculated based on the underlying collision model. The old particles are removed and a new particle is inserted. Thus, the number of particles decreases as time proceeds.

Ormel et al. (2007) summarise advantages and limitations of the Monte Carlo method: A big advantage is that the Monte Carlo technique conserves the physical character of the growth process, because it traces the time evolution of individual particles and does not use the distribution function directly. This also means that the method is exact, because the time step is determined by the collision rates of the particles, that is the stochastic coagulation process itself. Furthermore, it is easy to account for additional particle properties without complicating the numerical scheme.

However, there are also drawbacks of the Monte Carlo method. The noise scales as $\propto \mathcal{N}^{-1/2}$. If the number of particles, that is the resolution, becomes too small, the results will have a large uncertainty. A computational problem is the calculation of the collision rates. In Monte Carlo methods, each particle is allowed to collide with any other particle. Hence, the calculation of the collision rates is a \mathcal{N}^2 -process. Especially

when many particles are required for a good sampling of the underlying distribution function, calculating and updating the collision rates is a bottleneck.

Ormel et al. (2007) solved the aforementioned problem that the number of particles decreases over time, which increases the noise, by adding duplicates of already existing particles to the simulation. With the assumption that the coagulation process outside the considered volume is the same as inside the volume, adding new particles is equivalent to expanding the volume. Zsom and Dullemond (2008) pointed out that this is not well-suitable for simulating spatially well-defined problems. Thus, Zsom and Dullemond (2008) developed a different Monte Carlo method, which holds the number of computational particles as well as the volume constant.

4.3 The representative particle method

Following the description in Zsom and Dullemond (2008) closely, the basic idea of the representative particle method is to select a number of n so-called representative particles from the ensemble of \mathcal{N} physical particles of the system. It is assumed that the n particles represent the underlying distribution function and that the time evolution of the n particles is representative of the time evolution of the whole system. The total mass of the system is M and the particles are homogeneously distributed within a volume V . Each representative particle represents a fixed fraction of the total mass, the swarm mass $M_{\text{swm}} = M/n$. This means that each representative particle i with mass m_i carries along a swarm of $\mathcal{N}_i = M_{\text{swm}}/m_i$ particles identical to the representative particle. Representative particles are allowed to collide with swarm particles of other representative particles (including their own swarm), but not with other representative particles. This can be assured if $n \ll \mathcal{N}$, because in this case the probability for two representative particles to collide is negligible compared to the probability of a collision between a representative particle and a swarm particle.

4.3.1 Collision rates and time of the next collision

The probability for a representative particle i to collide with a swarm particle j is based on their collision rate

$$C_{ij} = \mathcal{N}_j A_{ij} \Delta v_{ij} / V, \quad (4.3)$$

where A_{ij} is the collision cross-section and Δv_{ij} the collision velocity of both particles. Equation 4.3 is the particle-in-a-box approximation. Within a short time interval Δt , particle i sweeps up the cylindrical volume $V_{\text{cyl}} = A_{ij} \Delta v_{ij} \Delta t$. The number of particles j particle i encounters within this volume is $\Delta \mathcal{N} = V_{\text{cyl}} \cdot \mathcal{N}_j / V$. The collision rate is then $\Delta \mathcal{N} / \Delta t$.

Because there are n different swarm particles, summing Eq. 4.3 over all swarm particles j gives the collision rate between a representative particle i and any other swarm particle $C_i = \sum_{j=1}^n C_{ij}$. The total collision rate is obtained by summing C_i over all representative particles i , $C = \sum_{i=1}^n C_i$. The total collision rate (C) determines the time step for the next collision. Let t be the current time of the system, the next collision occurs at $t + \delta t$, where the time step δt is given by $\delta t = -\log(u) / C$, where

u is a random number in the range $(0, 1)$ drawn from a uniform distribution (Gillespie 1975; Zsom and Dullemond 2008).

4.3.2 Particles involved in the collision

The next step is to determine which particles are involved in the collision. The probability for representative particle i to undergo a collision is $P_i = C_i/C$. The index i of the representative particle can be found by drawing a new random number u in the range between 0 and 1. The random number can be interpreted as the cumulative probability $P_{\leq i} = \sum_{k=1}^i P_k$. The index i of the representative particle is then simply found by the condition $P_{\leq i} \leq u < P_{\leq i+1}$. For given representative particle i , the probability that swarm particle j is involved in the collision is given by the conditional probability $P_{j|i} = C_{ij}/C_i$. The index of swarm j can be found in the same way as before.

4.3.3 Change of particle properties

Having determined the time of the next collision and the involved particles, the representative particle changes its properties based on the underlying collision model. It is important to mention that in the representative particle method only the representative particle changes its properties, while the swarm particle is unaffected. The reason for this is that the method follows the evolution of only the representative particles while the representative particle of the swarm particle is not involved in the collision. As long as the number of representative particles is $n \gg 1$, this asymmetry is lifted in a statistical sense, because the reverse process can also occur, that is representative particle j collides with swarm particle i (Zsom and Dullemond 2008).

In a sticking collision, the representative particle changes its mass according to

$$m_i \leftarrow m_i + m_j \quad (4.4)$$

and the number of swarm particles i needs to be updated to $\mathcal{N}_i = M_{\text{swm}}/m_i$, because M_{swm} is constant.

In case the collision leads to fragmentation, it is more elaborate to find the new mass of the representative particle, because disruptive collisions produce a distribution of fragments. The basic idea for finding the new mass of the representative particle method again follows Zsom and Dullemond (2008). Let $f(m)$ be the mass distribution function of fragments, normalised such that

$$\int_0^{\infty} m f(m) dm = m_i + m_j \quad (4.5)$$

gives the total mass of the involved particles. The new mass of the representative particle can be found once again by drawing a random number $u \in (0, 1)$ from a uniform distribution. The new mass is then given by solving

$$\frac{\int_0^{m'} m f(m) dm}{m_i + m_j} = u \quad (4.6)$$

for m' . Instead of a single distribution of fragments, the collision could also lead to partial fragmentation or erosion, where only a certain amount of mass is being excavated from the particle and a remnant body remains such that $m_i + m_j = m_{\text{rem}} + m_{\text{frag}}$. In this case, it is not *a priori* clear whether the representative particle is part of the remnant or of the fragments. However, the representative particle can be considered as one “monomer” of the entire particle. The probability of finding the monomer in the remnant is then

$$P_{\text{rem}} = \frac{m_{\text{rem}}}{m_i + m_j}, \quad (4.7)$$

where m_{rem} is the mass of the remnant. A random number $u \in (0, 1)$ determines the final outcome: remnant for $u \in (0, P_{\text{rem}})$ and fragment otherwise. When the representative particle is the remnant, the new mass is m_{rem} , otherwise the mass is determined as above, but replacing $m_i + m_j$ with m_{frag} .

5 Local growth of aggregates in the solar nebula

Growth of aggregates takes place over several orders of magnitude in size ranging from submicrometre-sized monomers to centimetre-sized aggregates and larger. Because of the aerodynamic coupling between the aggregates and the gas of the solar nebula, the aggregates drift radially towards to Sun. As long as the growth timescale of the aggregates is shorter than the timescale associated with radial drift, the growth process can be considered local and the maximum size is limited by bouncing or destructive collisions. On the other hand, when radial drift is fast, aggregates move significant distances in the disk during which collisional evolution of the aggregates is still possible. However, the growth process is no longer local.

For a local process, aggregate growth is confined to a specific location in the disk and formation of planetesimals through streaming instability is possible when a metallicity-dependent minimum Stokes number (St_{\min}), that is a minimum size or mass, is reached (Drażkowska and Dullemond 2014). Carrera et al. (2015) and Yang et al. (2017) conducted numerical simulation of streaming instability and found a relation between the metallicity of the disk and the range of Stokes numbers that leads to efficient streaming instability given by

$$\log_{10} Z = \begin{cases} 0.3 (\log_{10} St)^2 + 0.59 \log_{10} St - 1.57 & St > 0.1 \\ 0.1 (\log_{10} St)^2 + 0.20 \log_{10} St - 1.76 & St < 0.1 \end{cases} \quad (5.1)$$

A higher metallicity allows streaming instability for lower Stokes numbers. On the other hand, the lowest metallicity for which streaming instability is observed is $Z \approx 1.5\%$. This is higher than the nominal value of 1% (MMSN) and needs aggregates with $St \approx 0.1$.

As radial drift carries dust inwards, its St decreases because of the increasing surface density of the gas. Unless aggregates pile up, thereby increasing the metallicity, or grow to significantly larger sizes while drifting, streaming instability becomes more and more unlikely. Accordingly, a fast local growth of aggregates up to St_{\min} is strongly desirable for streaming instability as a mechanism for planetesimal formation.

This chapter studies the feasibility of this process using numerical simulations of aggregate growth in the MMSN. To be able to apply the results to comets, the simulations are placed in the outer solar system ($\gtrsim 5$ au), where comets formed as icy planetesimals.

5.1 Initial conditions for the simulations

Table 5.1 summarises the initial conditions described below for the nominal run which is the working model for the study of aggregate growth. Parameter studies are conducted with respect to this model (Sect. 5.2.2).

Table 5.1: Simulation parameters used in the nominal run.

Parameter	Symbol	Value
stellar mass	M_*	$1 M_\odot$
heliocentric distance	r	30 au
metallicity	Z	0.03
dust-to-ice ratio	ξ	1, 5, 10
surface density gas at 1 au	Σ_0	1700 g cm^{-2}
temperature gas at 1 au	T	280 K
mean molecular weight	μ	2.34
molecular cross section	A_{mol}	$2 \times 10^{-15} \text{ cm}^2$
turbulence	α	10^{-3}
monomer radius	a_0	$0.1 \mu\text{m}, 1 \mu\text{m}$
number of representative particles	n	2000

Notes. (Credit: Lorek et al., *A&A*, 611, A18, 2018, reproduced with permission ©ESO)

5.1.1 Coagulation model

Comets consist of refractory dust and ices of different volatiles, mainly H_2O (Mumma and Charnley 2011). The formation region of comets is therefore outside the ice line. The nominal simulations are located at heliocentric distance of $r = 30$ au, which agrees with the typical formation region of comets as has been estimated from cometary D/H-ratios and the detection of N_2 in the coma of comet 67P (Altwegg et al. 2015; Rubin et al. 2015). Additional simulations were conducted at 5 au, 15 au, and 50 au to sample other locations within the comet forming region.

Simulation domain and collision rate

Figure 5.1 shows a sketch of the simulation domain. The simulation domain is an annulus of width $2h_g$ which is centred at r . The surface area is $\mathcal{S} = 4\pi r h_g$. The simulation is collapsed to the midplane of the disk by integrating the collision rates from $z = -\infty$ to $z = +\infty$ taking the St dependent scale height of the aggregates (h_d) into account (that is settling of aggregates).

The collision rate of two aggregates i and j , both with Gaussian vertical density distributions with scale heights $h_{d,i}$ and $h_{d,j}$, respectively, that is used in the representative

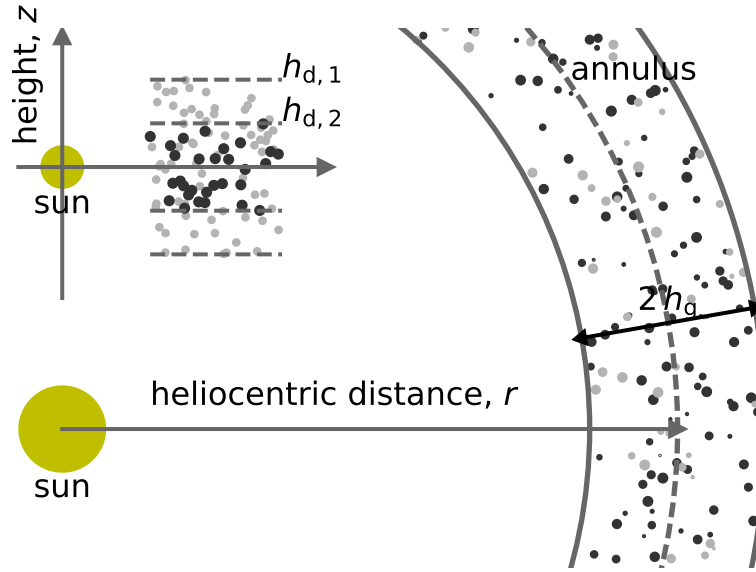


Figure 5.1: Sketch of the simulation domain. The simulation domain is an annulus of width $2h_g$ which is centred at r . The St dependent scale height of the aggregates (h_d) (that is settling of aggregates) is illustrated in the upper left corner.

particle method (see Eq. 4.3 in Sect. 4.3) is

$$C_{ij} = \frac{\mathcal{N}_j A_{ij} \Delta v_{ij}}{\mathcal{S} \sqrt{2\pi (h_{d,i}^2 + h_{d,j}^2)}} \quad (5.2)$$

(Okuzumi et al. 2012; Krijt et al. 2015).

Total dust mass and monomer size

A total dust mass of $M = Z \Sigma_g \mathcal{S}$ is distributed equally over $n = 2000$ representative particles. The metallicity $Z = 0.03$ is a factor of 3 higher than in the MMSN ($Z = 0.01$). For this metallicity, the minimum Stokes number is $St_{\min} = 1.5 \times 10^{-3}$ (Eq. 5.1).

All aggregates start as monomers of either $0.1 \mu\text{m}$ or $1 \mu\text{m}$ radius. Two material types are included: silicate dust and water ice. This allows the formation of aggregates of mixed composition. The ice monomers can be pictured as water ice condensed on small silicate grains whose contribution to the bulk density is negligible.

The dust-to-ice ratio

The dust-to-ice ratio $\xi = M_d/M_i$ (with $M = M_d + M_i$) sets the respective amounts of water ice (of total mass M_i) and silicate dust (of total mass M_d). Because the growth process is a stochastic process, the composition of the aggregates reflects the initial ratio of dust and ice.

Comets were considered as dirty snowballs (Whipple 1950, 1951) until the Giotto mission to comet 1P/Halley in 1986 changed the picture to comets being dirtballs

instead (Keller 1989). Observations of cometary trails, of the material excavated and investigated during the Deep Impact mission to comet 9P/Tempel 1, and recently of comet 67P by the Rosetta mission confirmed this picture (Sykes and Walker 1992; Küppers et al. 2005; Rotundi et al. 2015; Fulle 2017): the dust-to-ice ratio is $\gtrsim 1$ in general and ~ 5 for 67P in particular.

The observation that cometary activity persists over many perihelion passages can only be explained if the active areas on the nucleus surface are not covered by thick dry layers of dust quenching activity (Gundlach et al. 2011b). The high porosity and volatile content of cometary nuclei indicate that they have preserved their pristine properties since formation 4.6 Gyr ago. Thus, the dust-to-ice ratio derived from emitted dust and gas (sublimated ice) must be similar to the internal dust-to-ice ratio of the nucleus, which is an imprint of formation (Keller 1989).

In the simulations, the dust-to-ice ratio is varied between 1 (equal mass in dust and ice) and 10 (dust dominated) to account for cometary dust-to-ice ratios.

Strength of turbulence in the solar nebula

Turbulence strongly affects the collision speeds of aggregates. Numerical simulations of protoplanetary disk turbulence including MRI, VSI, or SBI predict values of $\alpha \approx 10^{-3}$ (see Sect. 2.2). A similar value can be derived from mass accretion rates in protoplanetary disks around T Tauri stars (Hartmann et al. 1998; Cuzzi et al. 2005). However, to account for the fact that the strength of the turbulence is not well constrained, lower or higher values are possible as well. In the nominal simulations $\alpha = 10^{-3}$ is used, but simulations with $\alpha = 10^{-2}$ (strong turbulence) and $\alpha = 10^{-4}$ (weak turbulence) are conducted as a parameter study.

5.1.2 Collision model

The nominal run as the working model uses the collision model introduced in Chapter 3. The collision model is based on the results from laboratory experiments providing the most realistic picture of aggregate collisions (Windmark et al. 2012a). The various collision types include sticking, bouncing, fragmentation, erosion, and mass transfer.

Given that comets are highly porous objects, porosity is followed for aggregate collisions. While sticking collisions build up highly porous aggregates through hit-and-stick collisions for low collision velocities, sticking collisions also result in compression if the collision energy exceeds the rolling energy marking the onset of restructuring within the newly formed aggregate. Recent laboratory experiments have revealed that aggregates with coordination number of 2 bounce (Landeck 2016), being in contrast to numerical simulations (Wada et al. 2011; Seizinger and Kley 2013). Here, bouncing is included for all porosities resulting in compression of the aggregates according to the compression curve. However, it is important to realise that although the bouncing aggregates are highly porous, they are not fractals, for which bouncing has never been observed in the laboratory. A simulation with bouncing included only for aggregates with volume-filling factor $\gtrsim 0.1$ is conducted as a parameter study.

The collision model treats aggregates as homogeneous mixtures of dust and ice monomers which is a good assumption for the reasons outlined in Sect. 3.5 (crystalline

silicates, ice grains, dust jet brightness profiles). The two components differ in sticking properties with ice being 10 times stickier than silicate dust (Gundlach et al. 2011a; Gundlach and Blum 2015). This is reflected in the threshold velocities as well as in the compression curve. Additional compounds, for example organic material, could change the sticking properties. Simulations with different sticking properties are conducted as a parameter study.

5.2 Results of aggregate growth simulations

Growth of aggregates is simulated for $5000 P$, where $P = 2\pi\Omega_K^{-1}$ is the orbital period. Knowing the properties of the representative particles at all times allows following the time evolution of the mass distribution function (mdf) per logarithmic mass bin (Ormel and Spaans 2008). The mass-weighted averages of variables, for example mass or volume-filling factor, characterising the peak of the mdf, are calculated according to

$$m = \frac{\sum_i m_i^2 \mathcal{N}_i}{\sum_i m_i \mathcal{N}_i}, \quad \phi = \frac{\sum_i m_i \phi_i \mathcal{N}_i}{\sum_i m_i \mathcal{N}_i}, \quad \dots, \quad (5.3)$$

to study the properties of the mass-dominating aggregate of the system. Here, m_i and ϕ_i are mass and volume-filling factor of the individual representative particles and \mathcal{N}_i is the number of swarm particles of representative particle i .

The growth timescale is defined as $t_{\text{grow}} = m/(dm/dt)$ and the drift timescale as $t_{\text{drift}} = r/|\Delta v_r|$ (with radial drift velocity according to Eq. 2.13). Aggregate growth is drift limited if $t_{\text{grow}} > t_{\text{drift}}/30$ (Okuzumi et al. 2012). For slower growth timescales, aggregates would rapidly drift towards the Sun rendering the local approach invalid. In the classical picture of coagulation, this effect gives rise to the so-called “metre-size barrier” because at 1 au aggregates with a diameter of 1 m would drift into the Sun within $\sim 100 P$ (Weidenschilling 1977a). Aggregates stop growing when $dm/dt \leq 0$ indicating either bouncing ($= 0$) or fragmentation (< 0). Because bouncing sets in before fragmentation, aggregate growth is bouncing dominated when $dm/dt = 0$. The mdf reaches a steady state for a bouncing-dominated system, whereas the mdf of a drift-limited system is still changing, which means aggregates are still growing.

When the mass-dominating aggregate reaches St_{min} , one important condition for streaming instability is fulfilled. Streaming instability requires a mass loading of $\rho_d/\rho_g \gtrsim 1$ locally. The simulation is vertically integrated and hence collapsed to the disk midplane. The effect of dust settling is taken into account in the collision rate (Eq. 5.2) due to the St dependent scale height of the dust. However, settling alone does not produce a dense midplane layer with $\rho_d/\rho_g \gtrsim 1$ because vertical diffusion due to turbulence opposes settling and puffs up the dust disk (Dubrulle et al. 1995; Dullemond and Dominik 2004; Youdin and Lithwick 2007). A dense midplane layer would only be produced for $St \gg \alpha$ (see Sect. 2.3). However, the turbulent motion of the disk gas itself might still be able to locally increase the mass loading by concentrating aggregates in local pressure maxima thereby setting the prerequisite for streaming instability (Johansen et al. 2014). The question of dust concentration will be discussed more in Sect. 5.2.3.

With the plausible assumption that the limiting factor is St_{\min} , there are two possible pathways. Aggregate growth becomes:

- drift limited before St_{\min} is reached, or
- bouncing dominated before growth becomes drift limited.

In the first case, aggregates remain too small to trigger the streaming instability and local formation of planetesimal is not possible. In the second case, compression of porous aggregates can push aggregates to St_{\min} . This opens the possibility to trigger streaming instability. For the limitations of the present study, only the second case is of interest.

5.2.1 Nominal case: aggregate growth at 30 au

General evolution of aggregate properties

Figure 5.2 shows aggregate properties as functions of time in orbital periods for $0.1 \mu\text{m}$ and $1 \mu\text{m}$ sized monomers at 30 au. The mass distribution functions at different times during the evolution are shown in Figs. 5.3 and 5.4.

The aggregates start as monomers with very low mass and $\phi = 1$. Within about the first $100 P$, the low collision velocity due to Brownian motion favours a phase of hit-and-stick growth in which first monomers and later aggregates stick at the contact point without restructuring. Collisions take place between approximately equal-sized aggregates (ballistic cluster-cluster aggregation, BCCA) which leads to highly porous ($\phi \sim 10^{-4}$) fractal aggregates of fractal dimension $D_f \sim 2$ (Kempf et al. 1999; Blum and Wurm 2008). The mdf during this phase remains relatively narrow peaked.

The mass increases with time $m \propto (t/t_{\text{grow}} + 1)^2$ with growth timescale

$$t_{\text{grow}} = \frac{2^{3/2} m_0^{3/2}}{16 \sqrt{\mu m_H} a_0^2 Z \Sigma_g \Omega_K}, \quad (5.4)$$

where collisions between equal-mass aggregates and a fractal dimension of 2 were assumed. It can be seen that the growth timescale depends on the monomer radius $t_{\text{grow}} \propto a_0^{5/2}$. This means that $t_{\text{grow}} \approx 1 P$ and $t_{\text{grow}} \approx 100 P$ for $0.1 \mu\text{m}$ and $1 \mu\text{m}$ sized monomers, respectively. This difference in timescales due to the lower cross section for aggregates with larger monomers explains why the aggregate mass increases by a factor $\sim 10^4$ within the first $100 P$ for $0.1 \mu\text{m}$ sized monomers, while it is only a factor ~ 3 for $1 \mu\text{m}$ sized monomers.

At roughly $100 P$, turbulence replaces Brownian motion as the dominant source of collision velocities. Because Stokes numbers are lower than $Re_t^{-1/2} \approx 6 \times 10^{-4}$, the first turbulent regime for strongly coupled aggregates of Eq. 3.8 applies.

In this regime, turbulence affects only aggregates that have different Stokes numbers and the larger aggregates grow by sweeping up the smaller ones. Growth is exponential in time $m(t) \propto \exp(t/t_{\text{grow}})$ which explains the steepening of the mass curve in Fig. 5.2. The growth timescale is

$$t_{\text{grow}} = \frac{8 \sqrt{2}}{3 \sqrt{\pi}} \frac{Re_t^{-1/4}}{\sqrt{\alpha} (1 - \beta^{-1})}, \quad (5.5)$$

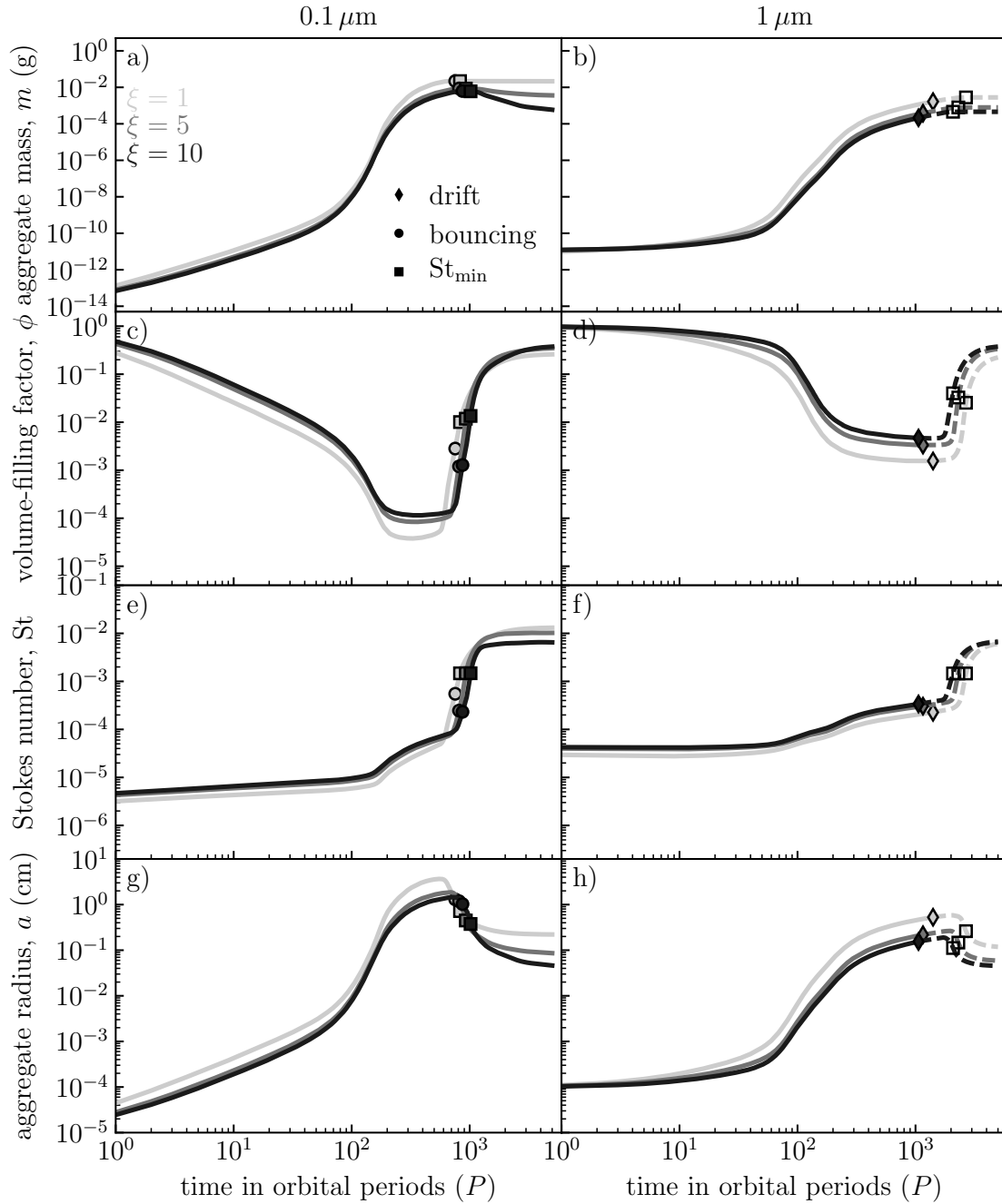


Figure 5.2: Aggregate properties as function of time in the nominal case. *Left*: $0.1 \mu\text{m}$ sized monomers. *Right*: $1 \mu\text{m}$ sized monomers. The rows show aggregate mass, volume-filling factor, Stokes number, and aggregate radius (from top to bottom). The symbols mark the time when aggregate growth becomes drift limited (◆), bouncing dominated (●), and when aggregates reach St_{\min} (■). The local approximation breaks down if growth is drift limited. To indicate this, the lines are continued as dashed lines and an open symbol is used for St_{\min} . (Credit: Lorek et al., A&A, 611, A18, 2018, reproduced with permission ©ESO)

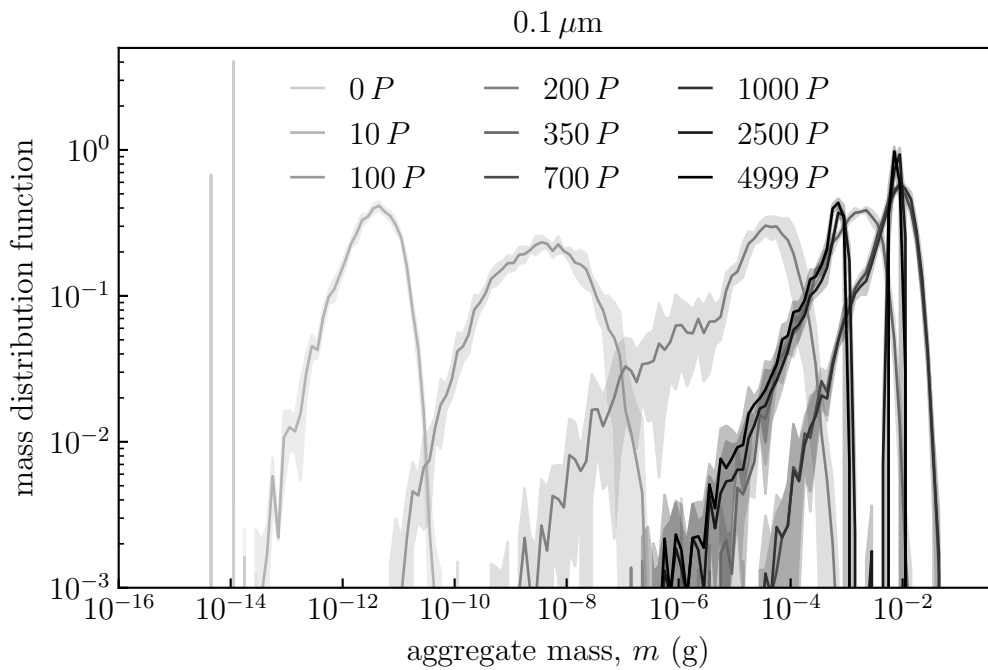


Figure 5.3: Mass distribution function of aggregates in the nominal case for $0.1 \mu\text{m}$ sized monomers and dust-to-ice ratio of 5. The different lines show the mdf with its uncertainty at different times in units of the orbital period (P).

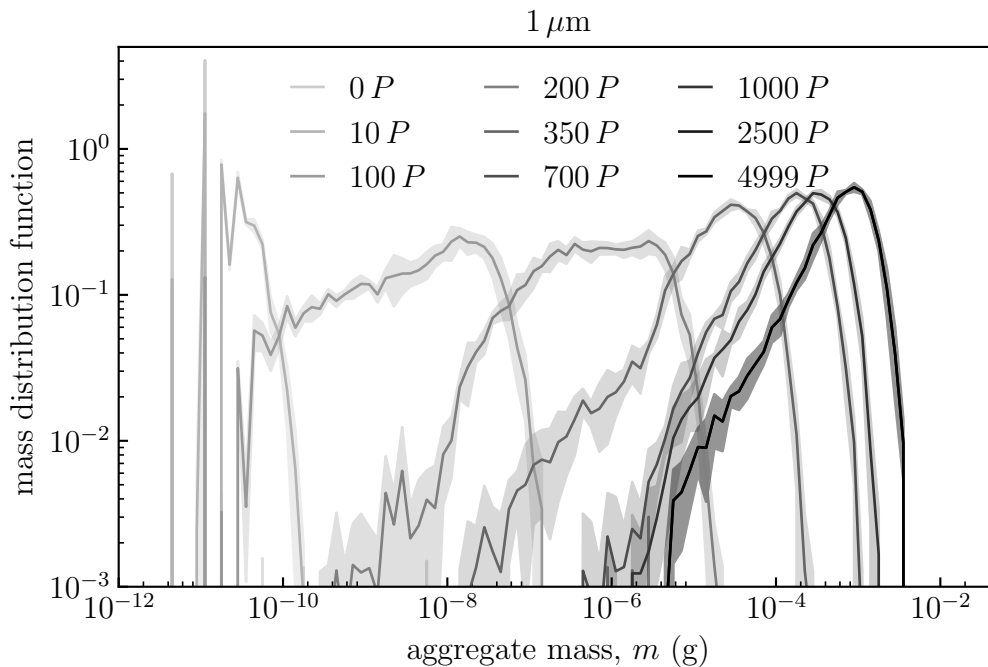


Figure 5.4: Mass distribution function of aggregates in the nominal case for $1 \mu\text{m}$ sized monomers and dust-to-ice ratio of 5. The different lines show the mdf with its uncertainty at different times in units of the orbital period (P).

where Re_t is the turbulent Reynolds number, α is the turbulent strength, and $\beta = St_1/St_2$ is the ratio of Stokes numbers of the two aggregates. In numbers, the growth timescale is $t_{\text{grow}} \approx 10P - 100P$ for $\beta^{-1} = 0.1 - 0.9$. This means that the aggregate mass increases by roughly a factor of 10^4 in $\sim 100P$ due to the accretion of smaller aggregates with lower Stokes numbers. As a consequence, the mass distribution function widens significantly.

When the higher collision velocities exceed the rolling energy of the monomers, restructuring and compression of the colliding aggregates sets in. The mass (m_{roll}) at which this occurs can be calculated from $\Delta E = E_{\text{roll}}$ using the following assumption: collisions are between roughly equal-mass aggregates (BCCA) and the collision velocity is given by the first turbulent regime. The rolling mass is then

$$m_{\text{roll}} = \frac{32\sqrt{2}}{3\pi^2} \frac{E_{\text{roll}}}{c_s^2 \alpha^{3/2}} \left(\frac{\mu m_{\text{H}}}{\Sigma_{\text{g}} A_{\text{mol}}} \right)^{1/2} \left(\frac{\Sigma_{\text{g}}}{\rho_0 a_0} \right)^2 \quad (5.6)$$

(Okuzumi et al. 2012). The corresponding volume-filling factor (ϕ_{roll}) follows from the definition of the volume-filling factor (Eq. 3.3), the mass-radius relation (Eq. 3.2), and the fact that the fractal dimension of the aggregates is $D_f \approx 2$ as $\phi_{\text{roll}} = (m_{\text{roll}}/m_0)^{-1/2}$. According to this estimate, rolling starts at masses of $\sim 1 \times 10^{-7}$ g and $\sim 5 \times 10^{-8}$ g for $0.1 \mu\text{m}$ and $1 \mu\text{m}$ sized monomers, respectively. This corresponds to the flattening seen in the volume-filling factor at $\sim 200P$.

The volume-filling factor stays approximately constant for a few $100P$ because the increase in porosity due to sticking is largely compensated by compression (Okuzumi et al. 2012). Furthermore, aggregate growth is no longer fractal and the fractal dimension increases to $D_f \gtrsim 2$.

At 30 au, compression due to the ram-pressure of the gas is unimportant because the aggregates already have densities higher than the equilibrium density (Eq. 3.30 in Sect. 3.4.4). Assuming that turbulent stirring is the dominant source for the ram-pressure of the gas (Kataoka et al. 2013b), the volume-filling factor below which ram-pressure becomes important can be calculated from $p_{\text{ram}} = p_{\text{max}}$ (see Eq. 3.29 in Sect. 3.4.4) as

$$\phi_{\text{ram}} = \left[\frac{4\rho_0 a_0^4 \alpha^{3/4} c_s \Omega_{\text{K}}}{E_{\text{roll}}} \left(\frac{\Sigma_{\text{g}} A_{\text{mol}}}{2\mu m_{\text{H}}} \right)^{1/4} \right]^{1/3}. \quad (5.7)$$

To derive this expression it was assumed that turbulent stirring causes a relative velocity between the aggregate and the gas of $\Delta v = \sqrt{\alpha} c_s Re_t^{1/4} St$ (Eq. 2.15 in the limit $Re_t^{-1/2} \ll 1$ and $St < Re_t^{-1/2}$) and that the aggregates have a fractal dimension of $D_f = 2$. For $0.1 \mu\text{m}$ sized monomers, the ram-pressure of the gas compresses aggregates with a volume-filling factor lower than $\phi_{\text{ram}} \approx 1 \times 10^{-5}$, which is lower than the volume-filling factor the aggregates have in the simulations ($\phi \approx 10^{-4}$). For $1 \mu\text{m}$ sized monomers, $\phi_{\text{ram}} \approx 6 \times 10^{-5}$, whereas in the simulation $\phi \approx 10^{-2}$.

While aggregates grow larger, their Stokes number increases and the transition to the second turbulent regime occurs at $St \approx 6 \times 10^{-4}$. This results in even higher collision velocities and eventually in bouncing. Because bouncing does not result in any growth of the aggregates, the small aggregates which are still growing eventually

catch up with or are accreted by the aggregates stuck in the bouncing regime. The mass distribution function reaches a steady state and the peak is getting narrow again (Windmark et al. 2012a). This happens in $\lesssim 10^3 P$. Because of bouncing, the volume-filling factor increases sharply from $\phi \ll 1$ to $0.1 \lesssim \phi \lesssim 0.4$ with the maximum value given by the compression curve.

The compression reduces the geometrical cross section of the aggregates and St increases sharply because of the proportionality to the mass-to-surface area ratio ($St \propto m/A$). Higher collision velocities are again the consequence. For dust-to-ice ratios $\gtrsim 5$ and $0.1 \mu\text{m}$ sized monomers, aggregates fragment significantly starting at $\gtrsim 10^3 P$ until a growth-fragmentation equilibrium is attained. Because bouncing collisions compress the aggregates to a maximum extent, fragmentation does not significantly affect the volume-filling factor. For $1 \mu\text{m}$ sized monomers, fragmentation does not occur because aggregates are significantly smaller and therefore have lower collision velocities. The better sticking properties of water ice make aggregates more resistant against fragmentation, but also more resistant against compression. Therefore, fragmentation, if at all, occurs only for a high dust-to-ice ratio.

Aggregate growth: drift limited and bouncing dominated

There is a significant difference between the time evolution of a system of $0.1 \mu\text{m}$ or of $1 \mu\text{m}$ sized monomers that has not been discussed in Sect. 5.2.1.

Aggregate growth is drift limited for $1 \mu\text{m}$ sized monomers, as indicated in Fig. 5.2. After $\sim 10^3 P$, growth has significantly slowed down due to the reduced sticking probability in the transition region from sticking to bouncing (see Sect. 3.3.1). As a consequence, aggregates drift faster than they grow, which renders the local approximation invalid. This happens at $St \approx 3 \times 10^{-4}$, which is approximately one order of magnitude lower than St_{min} . The maximum mass that aggregates can reach up to this point is hence limited by radial drift and streaming instability is prevented.

On the other hand for $0.1 \mu\text{m}$ sized monomers, aggregates rapidly grow into a bouncing-dominated state due to porosity accelerated growth (Okuzumi et al. 2012). The maximum mass of the aggregates is controlled by bouncing collisions. The subsequent evolution is limited by radial drift of the bouncing aggregates. Compression of the porous aggregates due to bouncing pushes the Stokes number towards St_{min} on timescales $\Delta t_{\text{St}} \approx 10 P - 1500 P$, approximately 70 – 1000 times faster than t_{drift} . This renders it possible for streaming instability to set in locally. Aggregates would be concentrated and planetesimal formation through gravitational collapse of the collected material would be the possible outcome.

Investigating the mdf of the aggregates which can be seen in Figs. 5.5 and 5.6 confirms this behaviour. For $0.1 \mu\text{m}$ sized monomers (Fig. 5.5) the mdfs at the estimated times when growth becomes drift limited and bouncing dominated, respectively, are nearly identical indicating that a steady state has already been reached. The peak changes by $\lesssim 2\%$ between drift and bouncing and the two mdfs differ by $\lesssim 5\%$ in the mass interval around the peak that contributes 95% to it. This is not the case for $1 \mu\text{m}$ sized monomers (see Fig. 5.6).

The monomer size-related difference in porosity explains this contrasting behaviour. Despite the collisional compression, sticking collisions produce highly porous aggregates

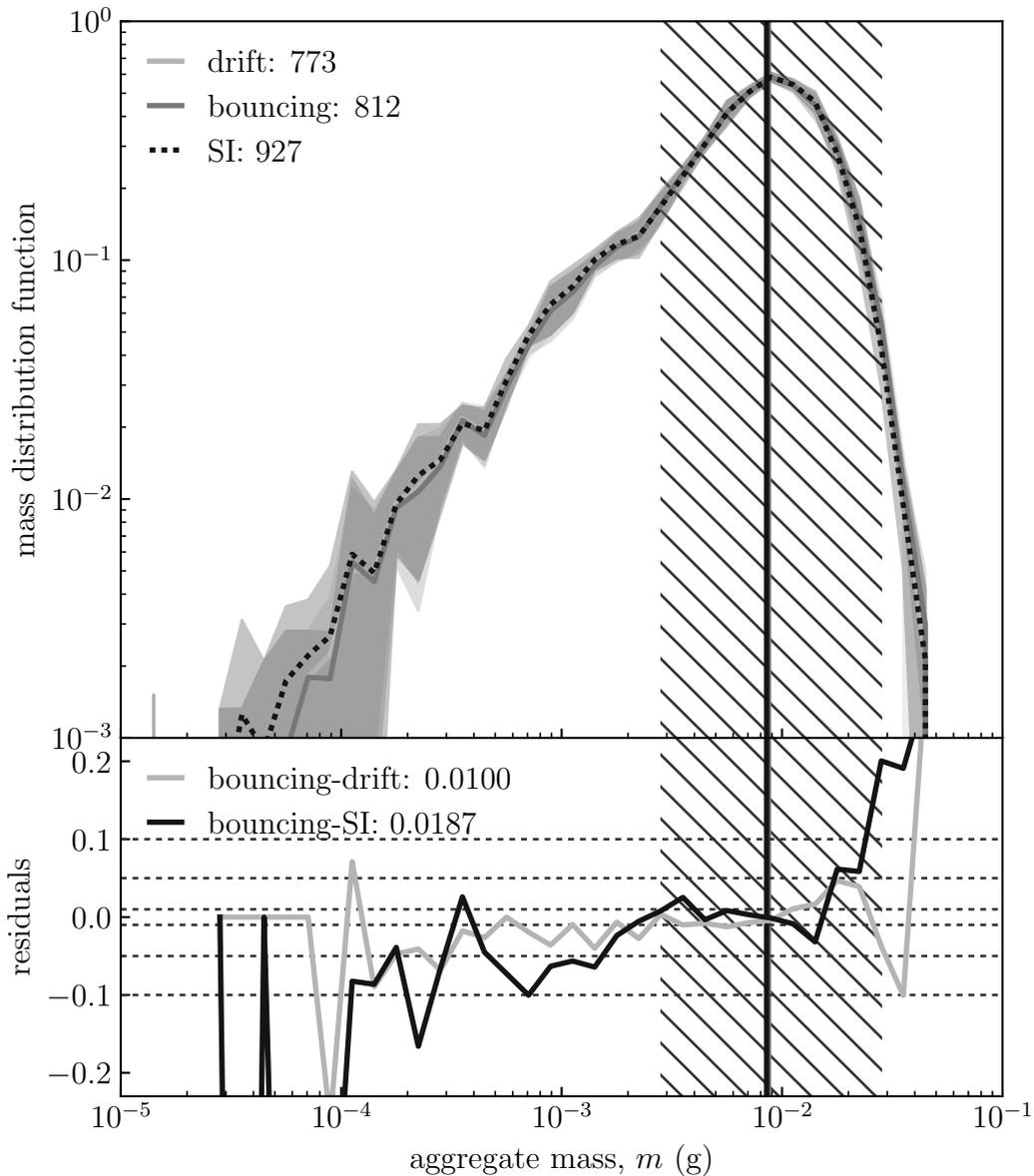


Figure 5.5: Mass distribution function and residuals in the nominal case for $0.1 \mu\text{m}$ sized monomers. For each figure: *top*) mdf at times when the system is drift limited (drift), bouncing dominated (bouncing), and when the aggregates reach St_{min} (SI). Numbers next to the labels are the times in orbital periods. *bottom*) Difference between the mdf for drift and bouncing and for SI and bouncing relative to bouncing, taken as reference. Dotted lines show 0.01, 0.05, and 0.1 levels. Number next to the labels show the relative change of the peak mass between drift or SI and bouncing. In both panels, vertical lines show the peak of the mdf and the hatched area is the mass interval around the peak that contributes 95% to the total mass. The large uncertainties at the low- and high-mass tails of the mdfs are due to the low resolution of the representative particle method. (Credit: Lorek et al., *A&A*, 611, A18, 2018, reproduced with permission ©ESO)

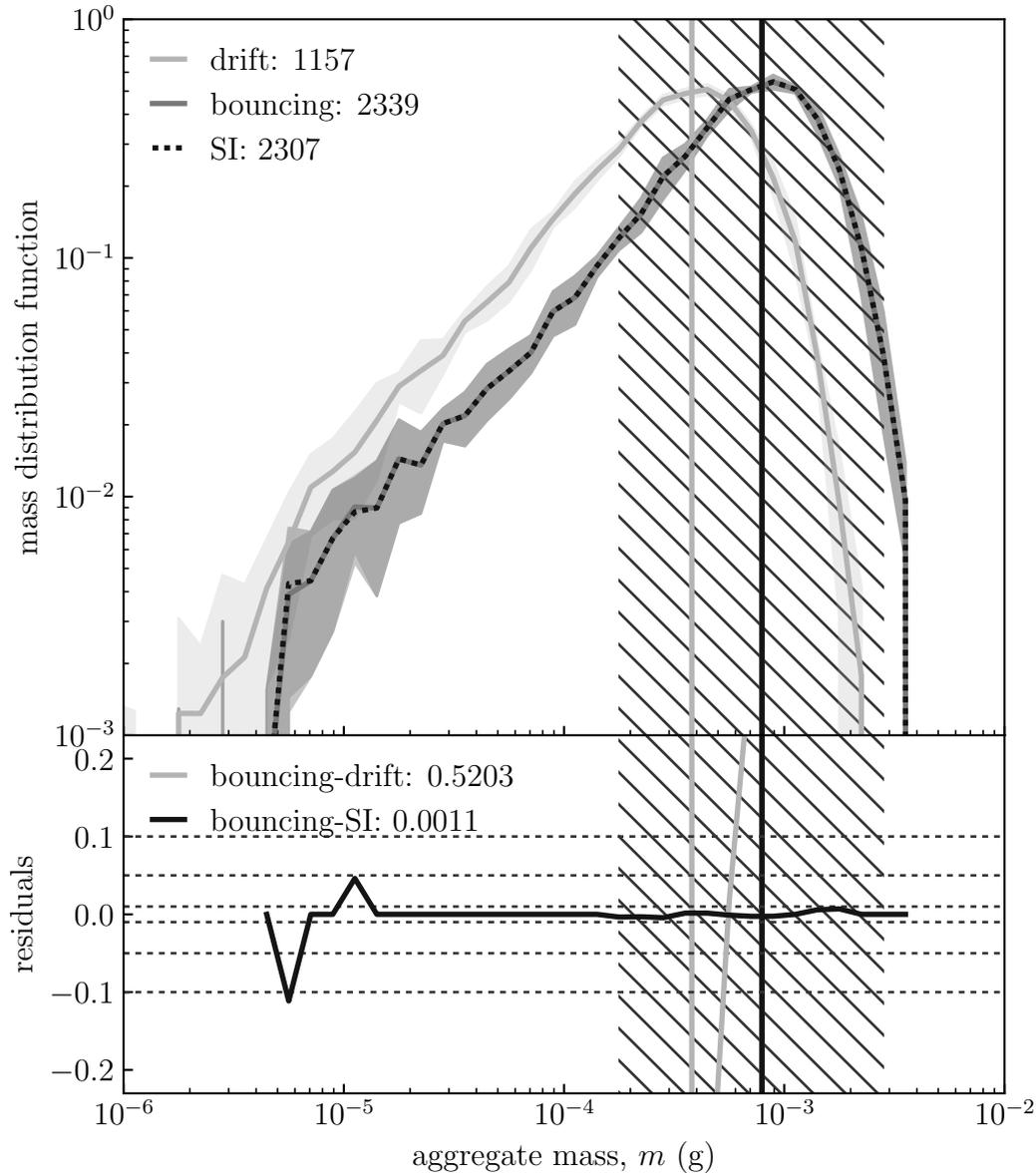


Figure 5.6: Mass distribution function and residuals in the nominal case for $1 \mu\text{m}$ sized monomers. For each figure: *top*) mdf at times when the system is drift limited (drift), bouncing dominated (bouncing), and when the aggregates reach St_{\min} (SI). Numbers next to the labels are the times in orbital periods. *bottom*) Difference between the mdf for drift and bouncing and for SI and bouncing relative to bouncing, taken as reference. Dotted lines show 0.01, 0.05, and 0.1 levels. Number next to the labels show the relative change of the peak mass between drift or SI and bouncing. In both panels, vertical lines show the peak of the mdf and the hatched area is the mass interval around the peak that contributes 95% to the total mass. The large uncertainties at the low- and high-mass tails of the mdfs are due to the low resolution of the representative particle method. (Credit: Lorek et al., *A&A*, 611, A18, 2018, reproduced with permission ©ESO)

with $\phi \ll 1$. The high porosity slows down radial drift significantly because the mass-to-surface area ratio is small, and so is the Stokes number. Additionally, the increased collisional cross section accelerates growth (Okuzumi et al. 2012; Kataoka et al. 2013b). The porosity that builds up during the sticking phase depends on the ratio of collision energy and rolling energy ($\propto (\Delta E/E_{\text{roll}})^{3/10}$). This ratio is also approximately the number of contacts that can be restructured resulting in compression of the aggregate. Because the rolling energy depends not only on the material (higher for ice than for silicate), but also on the monomer size (higher for smaller monomer size due to an increased contact area-to-surface area ratio), $0.1 \mu\text{m}$ sized monomers grow into aggregates with higher porosity than $1 \mu\text{m}$ sized monomers. This also fits quantitatively when working out the scaling of the volume-filling factor with monomer size from the porosity model. The volume of the new aggregate is $V \propto m^{1.2} a_0^{-1}$ resulting in $\phi \propto m^{-0.2} a_0$. A factor of 10 increase in monomer size increases the volume-filling factor by the same factor. This is seen in the simulations in which aggregates of $1 \mu\text{m}$ sized monomers have more than 10 times higher volume-filling factors (Fig. 5.2). The additional deviation comes from the fact that aggregates have significantly lower mass for $1 \mu\text{m}$ sized monomers, in which case more energy is available for restructuring and compression.

5.2.2 Parameter study for aggregate growth

To understand how sensitive the observed behaviour of aggregate growth (St_{min} , aggregate mass, drift limited, bouncing dominated) is to the physical conditions in the disk and the collision physics, a parameter study is conducted with respect to the nominal case. The individual changes are summarised in Table 5.2.

Variation of the heliocentric distance

In addition to the nominal case at 30 au, simulations at 5 au, 15 au, and 50 au were considered to sample different locations in the comet forming region. The results are shown in Fig. 5.7. Aggregate growth is bouncing dominated and St_{min} is reached at all distances for $0.1 \mu\text{m}$ sized monomers. Streaming instability and the formation of planetesimals should thus be possible locally at distances $\lesssim 50$ au.

The picture changes, however, for $1 \mu\text{m}$ sized monomers. Growth is bouncing dominated at 5 au, but drift limited for larger heliocentric distances in which case aggregates fail to reach St_{min} preventing streaming instability. Varying the heliocentric distance affects the maximum mass of the aggregates. This mass decreases from $\sim 10^{-1}$ g at 5 au to $\sim 10^{-4}$ g at 50 au as shown in Fig. 5.13.

The kink and subsequent increase of volume-filling factor seen in Fig. 5.7c for 5 au is due to compression by the ram-pressure of the gas. It is the only case in which this effect plays a role.

Variation of the turbulent strength

Figure 5.8 shows the results of the simulations with different turbulent strengths. Stronger turbulence leads to less porous (before bouncing) and significantly less

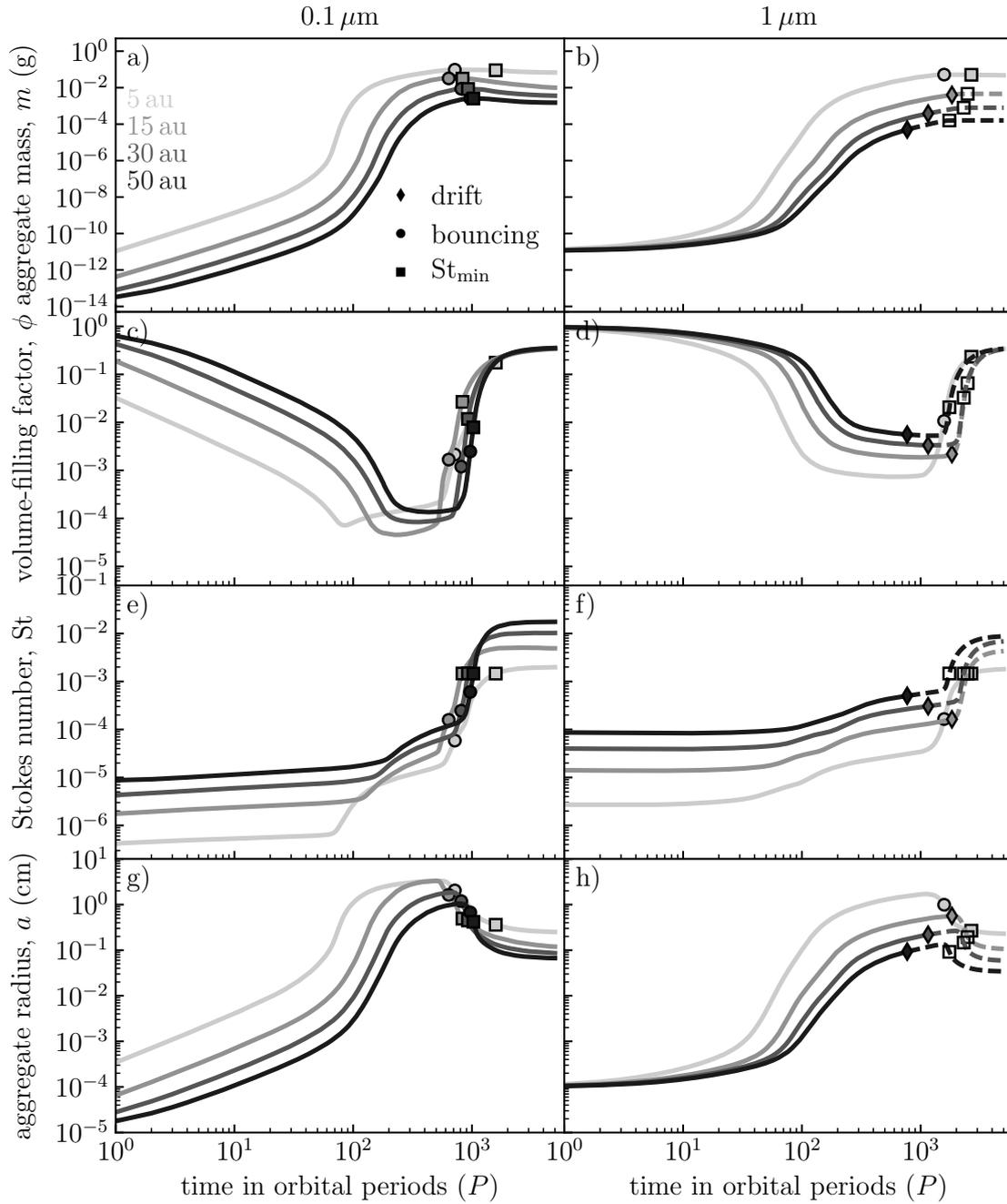


Figure 5.7: Aggregate properties as function of time for different heliocentric distances. *Left:* $0.1 \mu\text{m}$ sized monomers. *Right:* $1 \mu\text{m}$ sized monomers. The rows show aggregate mass, volume-filling factor, Stokes number, and aggregate radius (from top to bottom). The symbols mark the time when aggregate growth becomes drift limited (\blacklozenge), bouncing dominated (\bullet), and when aggregates reach St_{\min} (\blacksquare). The local approximation breaks down if growth is drift-limited. To indicate this, the lines are continued as dashed lines and an open symbol is used for St_{\min} .

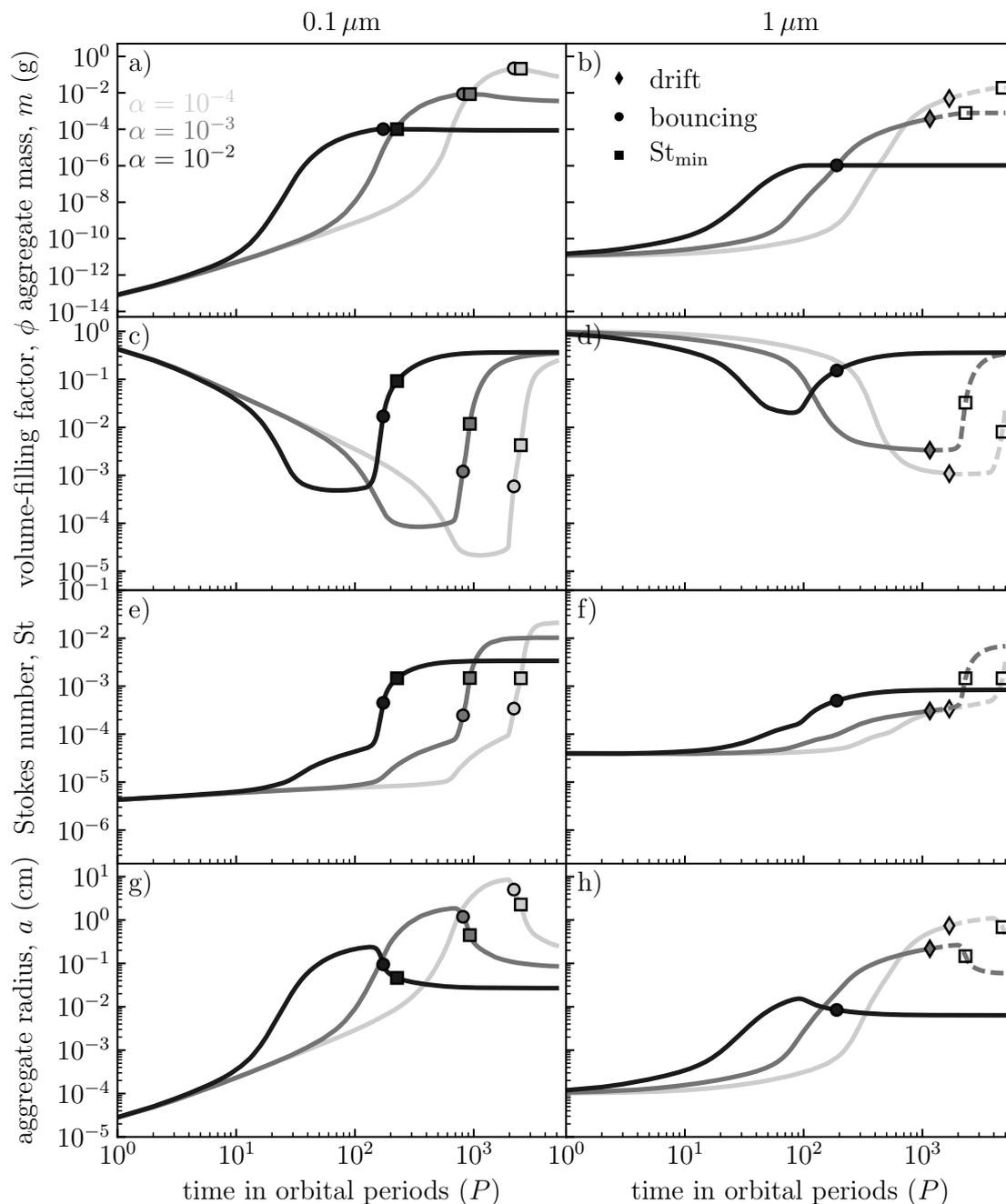


Figure 5.8: Aggregate properties as function of time for weaker and stronger turbulence. *Left:* $0.1 \mu\text{m}$ sized monomers. *Right:* $1 \mu\text{m}$ sized monomers. The rows show aggregate mass, volume-filling factor, Stokes number, and aggregate radius (from top to bottom). The symbols mark the time when aggregate growth becomes drift limited (\blacklozenge), bouncing dominated (\bullet), and when aggregates reach St_{\min} (\blacksquare). The local approximation breaks down if growth is drift limited. To indicate this, the lines are continued as dashed lines and an open symbol is used for St_{\min} . (Credit: Lorek et al., A&A, 611, A18, 2018, reproduced with permission $\text{\textcircled{C}}\text{ESO}$)

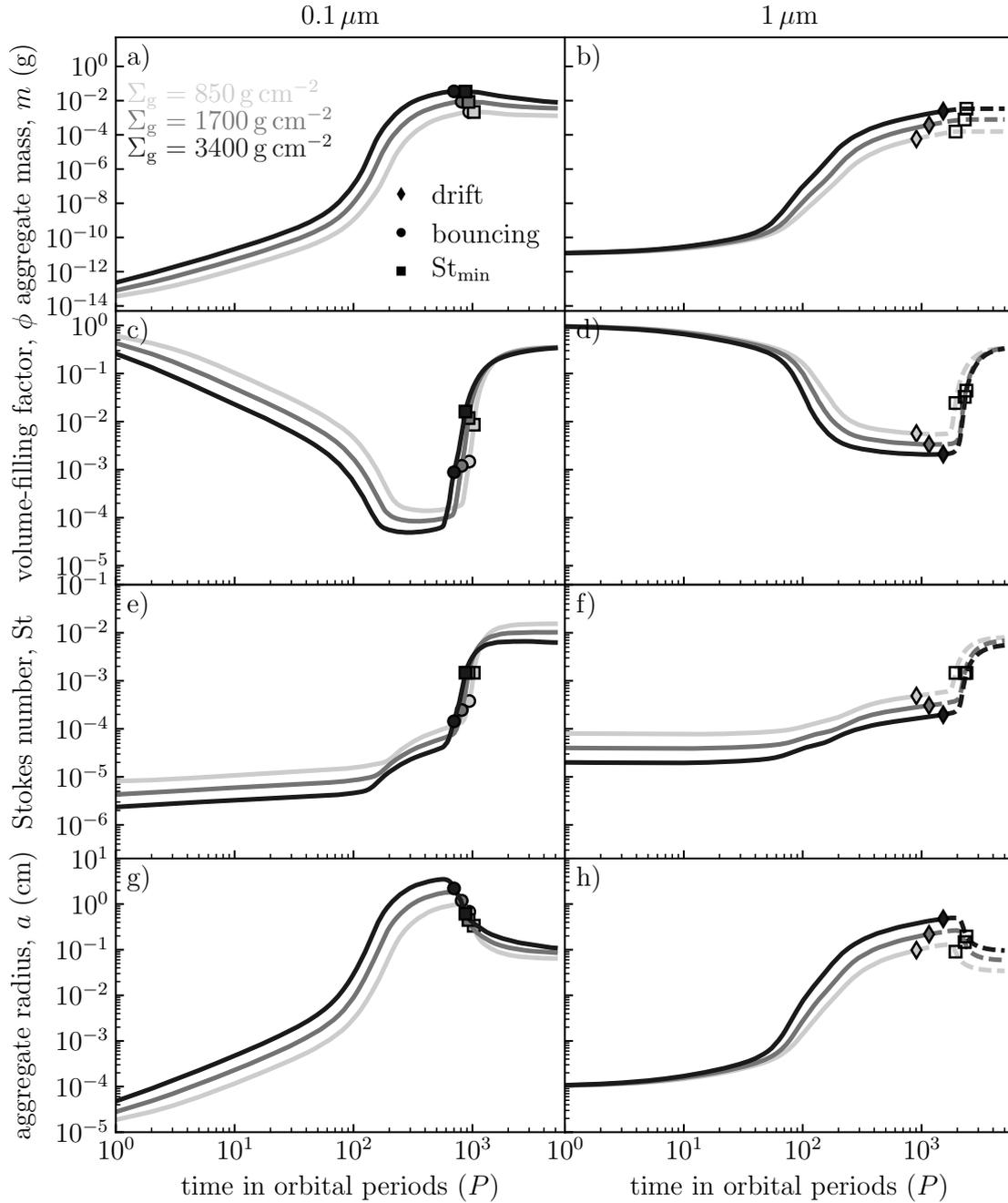


Figure 5.9: Aggregate properties as function of time for varying the surface density of the solar nebula. *Left:* $0.1 \mu\text{m}$ sized monomers. *Right:* $1 \mu\text{m}$ sized monomers. The rows show aggregate mass, volume-filling factor, Stokes number, and aggregate radius (from top to bottom). The symbols mark the time when aggregate growth becomes drift limited (◆), bouncing dominated (●), and when aggregates reach St_{\min} (■). The local approximation breaks down if growth is drift limited. To indicate this, the lines are continued as dashed lines and an open symbol is used for St_{\min} . (Credit: Lorek et al., A&A, 611, A18, 2018, reproduced with permission ©ESO)

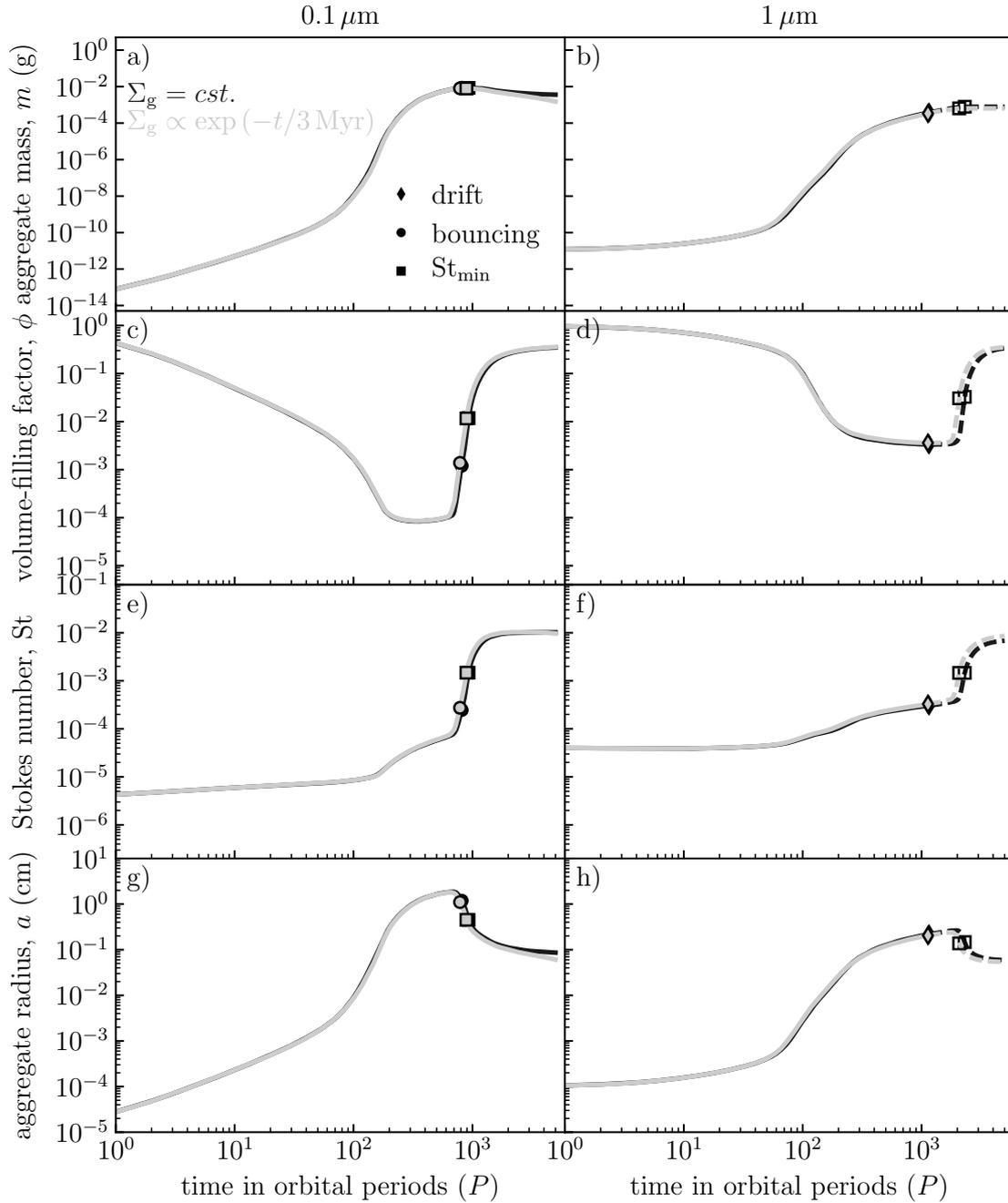


Figure 5.10: Aggregate properties as function of time for a dispersing solar nebula. *Left*: $0.1 \mu\text{m}$ sized monomers. *Right*: $1 \mu\text{m}$ sized monomers. The rows show aggregate mass, volume-filling factor, Stokes number, and aggregate radius (from top to bottom). The symbols mark the time when aggregate growth becomes drift limited (\blacklozenge), bouncing dominated (\bullet), and when aggregates reach St_{\min} (\blacksquare). The local approximation breaks down if growth is drift limited. To indicate this, the lines are continued as dashed lines and an open symbol is used for St_{\min} . (Credit: Lorek et al., A&A, 611, A18, 2018, reproduced with permission $\text{\textcircled{C}}\text{ESO}$)

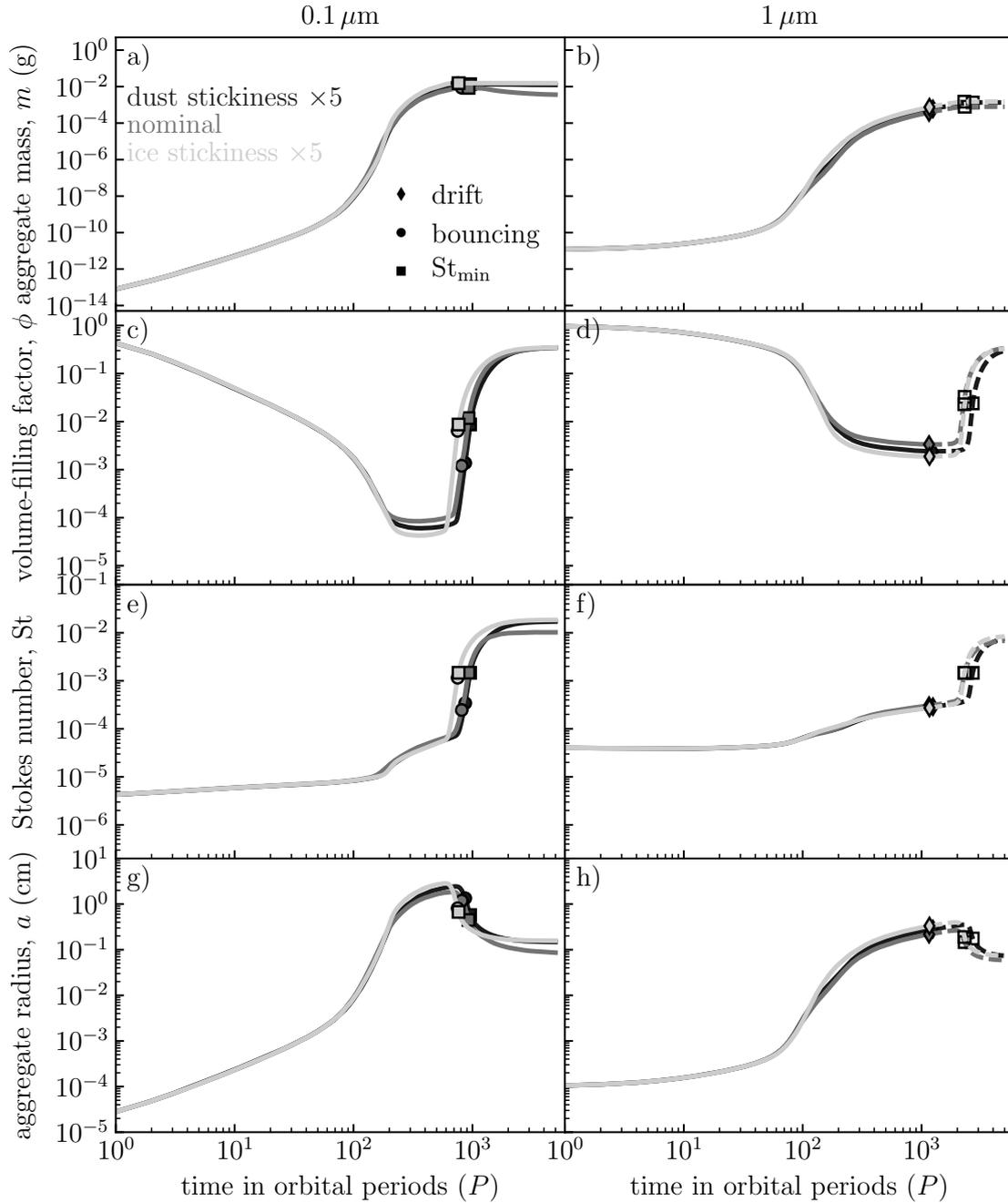


Figure 5.11: Aggregate properties as function of time for varying the sticking properties. *Left*: $0.1 \mu\text{m}$ sized monomers. *Right*: $1 \mu\text{m}$ sized monomers. The rows show aggregate mass, volume-filling factor, Stokes number, and aggregate radius (from top to bottom). The symbols mark the time when aggregate growth becomes drift limited (\blacklozenge), bouncing dominated (\bullet), and when aggregates reach St_{\min} (\blacksquare). The local approximation breaks down if growth is drift limited. To indicate this, the lines are continued as dashed lines and an open symbol is used for St_{\min} . (Credit: Lorek et al., *A&A*, 611, A18, 2018, reproduced with permission $\text{\textcircled{C}}\text{ESO}$)

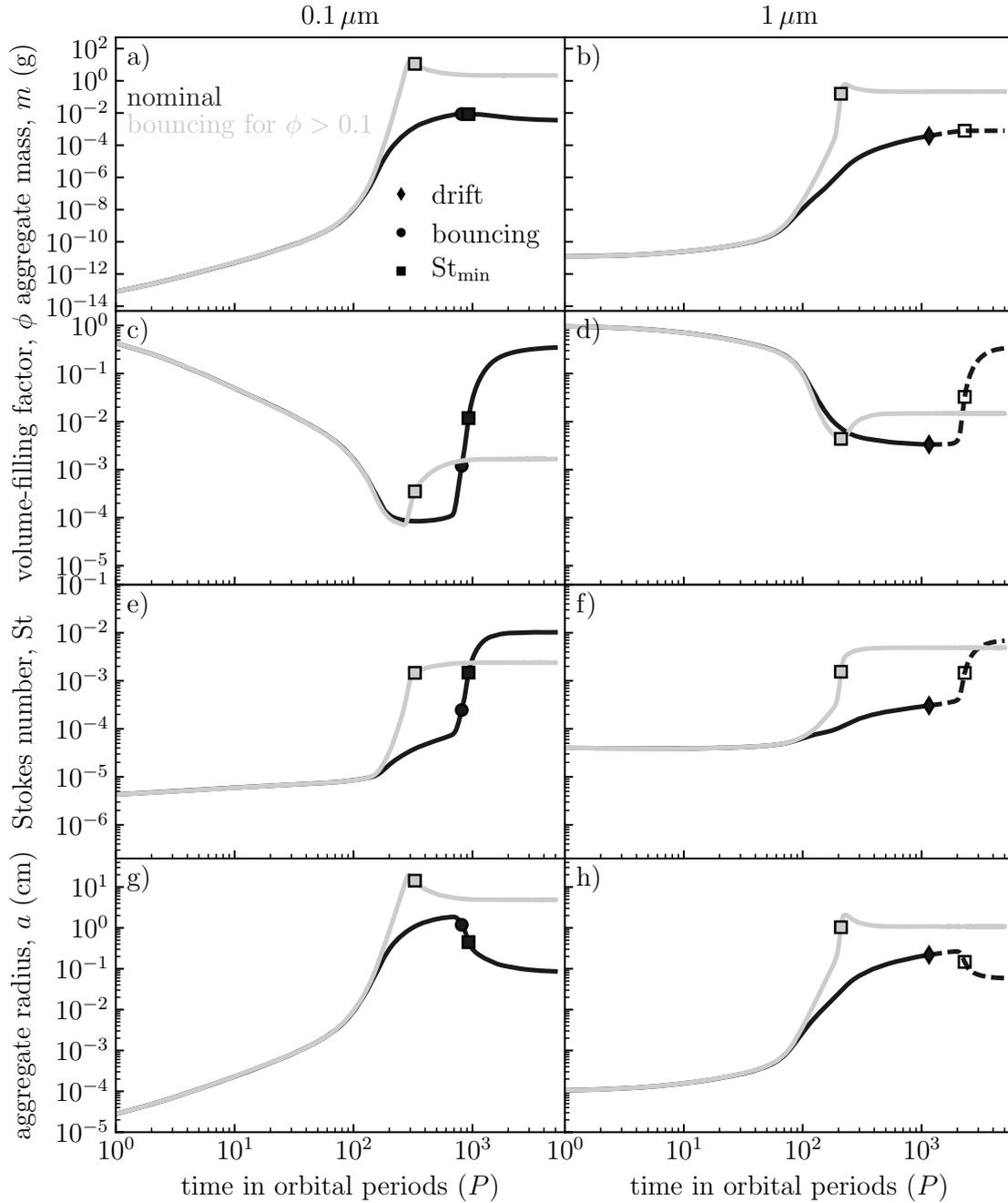


Figure 5.12: Aggregate properties as function of time with bouncing permitted only for compact aggregates. *Left*: $0.1 \mu\text{m}$ sized monomers. *Right*: $1 \mu\text{m}$ sized monomers. The rows show aggregate mass, volume-filling factor, Stokes number, and aggregate radius (from top to bottom). The symbols mark the time when aggregate growth becomes drift limited (\blacklozenge), bouncing dominated (\bullet), and when aggregates reach St_{\min} (\blacksquare). The local approximation breaks down if growth is drift limited. To indicate this, the lines are continued as dashed lines and an open symbol is used for St_{\min} . (Credit: Lorek et al., A&A, 611, A18, 2018, reproduced with permission $\text{\textcircled{C}}\text{ESO}$)

Table 5.2: Overview of model designs used in parameter study.

Simulation	Description
5au	heliocentric distance of 5 au
15au	heliocentric distance of 15 au
50au	heliocentric distance of 50 au
dSN	disk dispersal with mean lifetime of 3 Myr
iSd	5 times higher stickiness of dust
iSi	5 times higher stickiness of ice
nB	no bouncing for $\phi \leq 0.1$
α_{x10}	strong turbulence, $\alpha = 10^{-2}$
$\alpha_{_10}$	weak turbulence, $\alpha = 10^{-4}$
$\Sigma_g \times 2$	high gas surface density, $\Sigma_0 = 3400 \text{ g cm}^{-2}$
$\Sigma_g \text{ _}2$	low gas surface density, $\Sigma_0 = 850 \text{ g cm}^{-2}$

Notes. All parameters and model designs are varied with respect to the nominal case at 30 au heliocentric distance and MMSN initial conditions (see Table 5.1). (Credit: Lorek et al., A&A, 611, A18, 2018, reproduced with permission ©ESO)

massive aggregates, whereas weaker turbulence has the opposite effect. Because the collision velocities due to turbulence scale as $\Delta v \propto \sqrt{\alpha}$, threshold velocities leading to bouncing or fragmentation are reached at lower Stokes numbers that is for smaller and less massive aggregates.

Growth is bouncing dominated for $0.1 \mu\text{m}$ sized monomers for $\alpha = 10^{-4}$ and $\alpha = 10^{-2}$ with maximum aggregate masses of $\sim 2 \times 10^{-1} \text{ g}$ and $\sim 1 \times 10^{-4} \text{ g}$, respectively. Growth is drift limited for $1 \mu\text{m}$ sized monomers and $\alpha = 10^{-4}$ at a mass of $\sim 5 \times 10^{-3} \text{ g}$, whereas growth is bouncing dominated for $\alpha = 10^{-2}$. However, the maximum mass in the latter case, $\sim 1 \times 10^{-6} \text{ g}$, is too low for aggregates to eventually reach St_{\min} .

Variation of the gas surface density

An increase of the gas surface density to twice the MMSN value while keeping the metallicity fixed leads to more massive aggregates, as shown in Fig. 5.9. Because $\text{St} \propto \Sigma_g^{-1}$, a higher Σ_g results in a lower St . This decreases the collision velocities allowing aggregates to grow more massive before bouncing or fragmentation sets in.

For $0.1 \mu\text{m}$ sized monomers, growth is bouncing dominated for $\Sigma_0 = 850 \text{ g cm}^{-2}$ and $\Sigma_0 = 3400 \text{ g cm}^{-2}$ (Σ_0 is the gas surface density at 1 au) limiting the maximum mass to $\sim 2 \times 10^{-3} \text{ g}$ and $\sim 4 \times 10^{-2} \text{ g}$, respectively. For $1 \mu\text{m}$ sized monomers, radial drift terminates local growth at a maximum mass of $\sim 6 \times 10^{-5} \text{ g}$ and $\sim 2 \times 10^{-3} \text{ g}$ for low and high surface density, respectively.

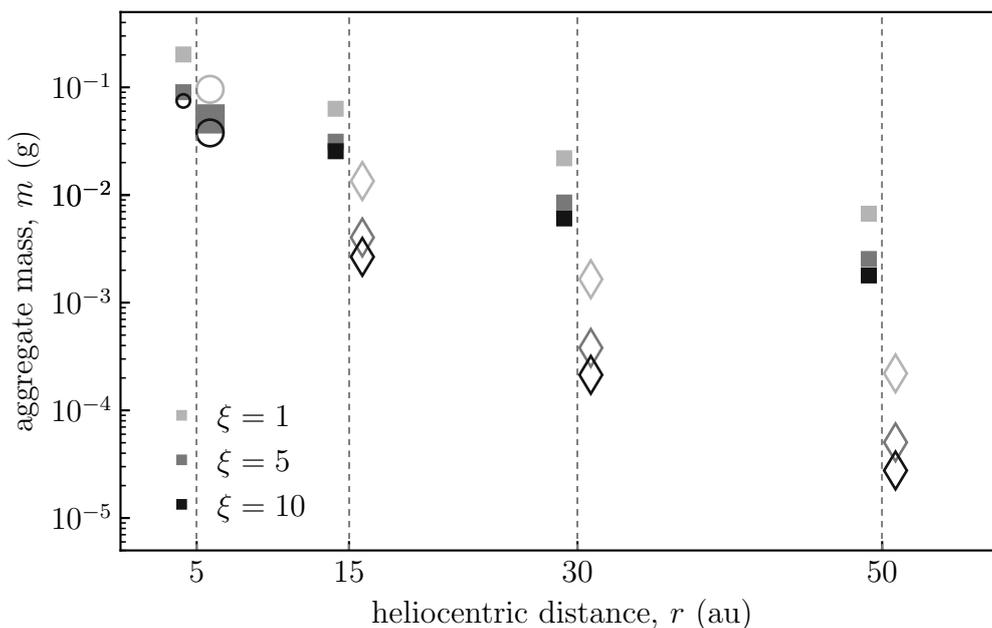


Figure 5.13: Aggregate mass versus heliocentric distance. Small symbols (left) and large symbols (right) are used for $0.1 \mu\text{m}$ and $1 \mu\text{m}$ sized monomers, respectively. A vertical dotted line is used to guide the eye. A filled square (■) shows the mass of aggregates which reached St_{min} . If St_{min} is not reached, the maximum mass to which aggregates can locally grow due to drift (◆) or bouncing (●) is shown with an open symbol instead. (Credit: Lorek et al., *A&A*, 611, A18, 2018, reproduced with permission ©ESO)

Dispersal of the solar nebula gas

It is known from observations that protoplanetary disks disperse over time with mean lifetime of $\tau \approx 3 \text{ Myr}$ (Haisch et al. 2001; Fedele et al. 2010). Physical processes that make the disk disappear are, for example, accretion onto the central star due to the viscous evolution of the disk or photoevaporation of the gas due to UV irradiation by the central star (Lynden-Bell and Pringle 1974; Hartmann et al. 1998; Alexander et al. 2014).

To study the effect of disk dispersal on aggregate growth, a simulation in which the gas density decays exponentially with time as $\propto \exp(-t/\tau)$ with $\tau = 3 \text{ Myr}$ is conducted. The results are shown in Fig. 5.10. Because aggregate growth up to the bouncing regime is fast ($\lesssim 10^3 P \approx 10^5 \text{ yr}$ at 30 au) compared to the mean lifetime of the disk, this modification has only minor influence. The two main differences are that aggregate masses decrease by $\sim 10\%$, and that fragmentation is stronger at later times ($t \gtrsim 10^3 P$). Both effects are linked to the higher collision velocities due to slightly higher Stokes numbers because of the gradually decreasing surface density of gas.

Variation of the sticking properties

The sticking property of ice is already ten times enhanced compared to silicate. Sticky organic compound could result in an increase of the sticking properties of ice or dust, respectively.

Figure 5.11 shows the results of artificially increasing the stickiness of ice or dust, respectively, by an additional factor of 5. This is done by increasing the threshold velocities, rolling energy, and the parameter p_m of the compression curve by the same factor.

There is no significant change of the growth process. Growth is bouncing dominated for $0.1 \mu\text{m}$ sized monomers at $\sim 1 \times 10^{-4} \text{ g}$ and drift limited for $1 \mu\text{m}$ sized monomers at $\sim 7 \times 10^{-4} \text{ g}$. The maximum mass of the aggregates is at most a factor of 2 higher than in the nominal case. Towards later times ($\gtrsim 10^3 P$), aggregate fragmentation is prevented in both cases, because 5 times higher collision velocities would be necessary to cause fragmentation. These high velocities are, however, not reached.

Bouncing only for compact aggregates

Figure 5.12 shows the effect of modifying the collision model to permit only bouncing for aggregates with volume-filling factors $\phi > 0.1$. This model prevents bouncing entirely because porous growth produces aggregates with volume-filling factors of $\phi \approx 10^{-4} - 10^{-2}$ depending on monomer size even if restructuring is taken into account.

While growing, the collision velocities increase due to higher Stokes numbers and the aggregates start to fragment when the velocities exceed the fragmentation threshold. Fragmentation creates a population of small fragments which grow again to larger aggregates and eventually a steady state between growth and fragmentation is reached.

Without bouncing, radial drift of the aggregates is slow due to the high porosity and the maximum size of the aggregates is limited by fragmentation, which sets in at masses of $\sim 2 \times 10^1 \text{ g}$ and $6 \times 10^{-1} \text{ g}$ for $0.1 \mu\text{m}$ and $1 \mu\text{m}$ sized monomers, respectively.

5.2.3 Caveats

Local approximation of aggregate growth

In Sect. 5.2 it was argued that the local approach breaks down when radial drift is faster than aggregate growth: $t_{\text{grow}} > t_{\text{drift}}/30$ (Okuzumi et al. 2012).

A different approach to this complication is to calculate the total distance aggregates would drift (Δr_{drift}) before growth becomes bouncing-dominated and compare it to the orbital distance at which the simulation is located. The local approach is justified if $\Delta r_{\text{drift}}/r \ll 1$ (Ormel et al. 2008).

The total distance aggregates would drift can be obtained by integrating the radial drift velocity Eq. 2.13 over time:

$$\Delta r_{\text{drift}} = \int_0^{t_{\text{bouncing}}} \Delta v_r dt, \quad (5.8)$$

where t_{bouncing} is the time at which growth would be bouncing dominated.

At 5 au, $\Delta r_{\text{drift}}/r \approx 10^{-3}$ for $0.1 \mu\text{m}$ and $1 \mu\text{m}$ sized monomers. Aggregates would drift only insignificant distances before reaching the bouncing-dominated regime.

For increasing heliocentric distance, it changes. At 15 au and 30 au, $\Delta r_{\text{drift}}/r \approx 10^{-3}$ for $0.1 \mu\text{m}$ sized monomers, whereas $\Delta r_{\text{drift}}/r \approx 10^{-2} - 10^{-1}$ for $1 \mu\text{m}$ sized monomers. The latter case means that aggregates would drift 1% – 10% closer to the Sun, which are a few au in absolute numbers.

Finally at 50 au, $\Delta r_{\text{drift}} \approx 10^{-2}$ for $0.1 \mu\text{m}$ sized monomers and $\Delta r_{\text{drift}} \gtrsim 10^{-1}$ for $1 \mu\text{m}$ sized monomers. While the submicrometre case still agrees with a local approximation ($\Delta r_{\text{drift}} \lesssim 1$ au), the micrometre case clearly does not fulfil this criterion.

Trapping of dust aggregates

It is important to notice that reaching St_{min} is not the only condition for streaming instability to set in. A mass loading $\rho_{\text{d}}/\rho_{\text{g}} \gtrsim 1$ is furthermore necessary because the active feedback of the dust on the gas is important. In a smooth disk without pressure bumps or other preferred locations of dust accumulation, a mass loading $\gtrsim 1$ is not easily reached.

Assuming that the vertical dust density profile is given by Eq. 2.5, the mass loading in the midplane of the disk can be estimated as

$$\frac{\rho_{\text{d}}}{\rho_{\text{g}}} = \frac{\Sigma_{\text{d}} h_{\text{g}}}{\Sigma_{\text{g}} h_{\text{d}}} \approx Z \sqrt{\frac{\text{St}}{\alpha}}, \quad (5.9)$$

with metallicity Z , turbulence parameter α , and Stokes number St (see Sect. 2.3).

For the values used in the nominal simulation (Table 5.1) and a minimum value $\text{St}_{\text{min}} = 1.5 \times 10^{-3}$, the mass loading that is achieved due to settling of dust to the midplane is $\rho_{\text{d}}/\rho_{\text{g}} \approx 0.02 \ll 1$. The reason is that at these low Stokes numbers the dust is tightly coupled to the gas and turbulent diffusion prevents efficient settling to the midplane. This caveat could pose a severe problem to streaming instability (Estrada et al. 2016; Ida and Guillot 2016; Krijt et al. 2016).

However, disks are not smooth in general and the turbulent motion of the gas favours the concentration of dust aggregates. Johansen et al. (2014) summarise the most important dust trapping mechanisms:

Aggregates with low Stokes numbers ($\text{St} \approx 10^{-5} - 10^{-4}$) can be trapped in high-pressure regions between turbulent eddies of typical scale ($\sim \text{km}$). The aggregates couple to the gas on a timescale comparable to the eddy overturn time, which is the typical decay time of a turbulent eddy. They are expelled from the eddy and concentrated in the high pressure region between the eddies. Aggregates with lower or higher Stokes number either move with the gas flow or experience only random kicks from the eddy (see Sect. 2.3.3) and are less efficiently concentrated. Because of that, aggregate trapping depends on the scale of the turbulence.

Aggregates with higher Stokes numbers ($\text{St} \approx 0.1 - 10$) can be trapped in rotating vortices and pressure bumps which form on larger scales ($1 h_{\text{g}} - 10 h_{\text{g}}$) due to Keplerian shear and Coriolis forces.

The resulting force on an aggregate in a vortex depends on the pressure gradient inside the vortex. If pressure decreases outwards, the aggregate is accelerated to

the centre of the eddy. Therefore, aggregates are trapped in high pressure regions. Low-pressure regions, in contrast, expel aggregates.

A pressure bump is surrounded by sub- and super-Keplerian flow. Aggregates are trapped because the headwind velocity Δv_{hw} that controls the direction of the radial drift is now determined by the local pressure gradient of the pressure bump. At the maximum of the bump, $\Delta v_{\text{hw}} = 0$ and aggregates do not drift. Aggregates drifting into the pressure bump from larger heliocentric distance are therefore stopped. On the other hand, inside the bump where the gas is super-Keplerian, aggregates are accelerated outwards towards the pressure maximum. Pressure bumps might form due to zonal flows in MRI turbulent disks (Johansen et al. 2009; Pinilla et al. 2012) or due to a drop of ionisation fraction of the gas at the outer edges of dead zones (Kretke and Lin 2007; Drażkowska et al. 2013).

5.2.4 Summary of aggregate properties

Tables 5.3 and 5.4 give a summary of the maximum mass of the aggregates together with the corresponding volume-filling factor and the Stokes number. Furthermore, the mass and the volume-filling factor at St_{min} are given. However, for drift-limited growth St_{min} is essentially not reached and the values given serve only for the sake of completeness.

The model for aggregate growth is successful if growth is not drift limited, aggregates reach St_{min} , and Δt_{St} is shorter than t_{drift} in the bouncing-dominated case. Table 5.5 gives a summary of the various model designs which are successful and produce aggregates which could eventually cause streaming instability leading to the formation of planetesimals.

Table 5.3: Maximum mass and mass at St_{\min} with corresponding volume-filling factor and Stokes number for all simulations with $0.1 \mu\text{m}$ sized monomers.

Simulation	ξ	maximum			St_{\min}		Growth Limit
		m (g)	ϕ	St	m (g)	ϕ	
nominal	1	2.2×10^{-2}	2.8×10^{-3}	5.5×10^{-4}	2.2×10^{-2}	1.0×10^{-2}	bouncing
	5	8.7×10^{-3}	1.2×10^{-3}	2.5×10^{-4}	8.5×10^{-3}	1.2×10^{-2}	bouncing
	10	6.3×10^{-3}	1.3×10^{-3}	2.3×10^{-4}	6.1×10^{-3}	1.4×10^{-2}	bouncing
5au	1	2.0×10^{-1}	5.2×10^{-3}	1.3×10^{-4}	2.0×10^{-1}	1.7×10^{-1}	bouncing
	5	9.7×10^{-2}	2.1×10^{-3}	5.9×10^{-5}	9.0×10^{-2}	1.8×10^{-1}	bouncing
	10	7.5×10^{-2}	3.2×10^{-3}	6.7×10^{-5}	bouncing
15au	1	6.3×10^{-2}	3.5×10^{-3}	3.3×10^{-4}	6.3×10^{-2}	2.6×10^{-2}	bouncing
	5	3.2×10^{-2}	1.7×10^{-3}	1.6×10^{-4}	3.1×10^{-2}	2.7×10^{-2}	bouncing
	10	2.8×10^{-2}	1.3×10^{-3}	1.2×10^{-4}	2.5×10^{-2}	2.8×10^{-2}	bouncing
50au	1	6.7×10^{-3}	3.0×10^{-3}	8.6×10^{-4}	6.7×10^{-3}	6.1×10^{-3}	bouncing
	5	2.6×10^{-3}	2.5×10^{-3}	6.1×10^{-4}	2.5×10^{-3}	7.9×10^{-3}	bouncing
	10	1.8×10^{-3}	1.9×10^{-3}	4.5×10^{-4}	1.8×10^{-3}	8.4×10^{-3}	bouncing
dSN	5	8.0×10^{-3}	1.4×10^{-3}	2.7×10^{-4}	7.9×10^{-3}	1.2×10^{-2}	bouncing
iSd	5	1.4×10^{-2}	1.4×10^{-3}	3.4×10^{-4}	1.4×10^{-2}	8.7×10^{-3}	bouncing
iSi	5	1.6×10^{-2}	6.4×10^{-3}	1.2×10^{-3}	1.6×10^{-2}	8.7×10^{-3}	bouncing
nB	5	1.6×10^1	1.9×10^{-4}	1.1×10^{-3}	1.1×10^1	3.5×10^{-4}	fragmentation
α_{10}	5	2.2×10^{-1}	5.9×10^{-4}	3.4×10^{-4}	2.1×10^{-1}	4.2×10^{-3}	bouncing
α_{x10}	5	1.0×10^{-4}	1.7×10^{-2}	4.5×10^{-4}	1.0×10^{-4}	9.2×10^{-2}	bouncing
Σ_{g_2}	5	2.2×10^{-3}	1.5×10^{-3}	3.8×10^{-4}	2.2×10^{-3}	8.6×10^{-3}	bouncing
Σ_{g_x2}	5	3.5×10^{-2}	8.8×10^{-4}	1.4×10^{-4}	3.4×10^{-2}	1.6×10^{-2}	bouncing

Table 5.4: Maximum mass and mass at St_{\min} with corresponding volume-filling factor and Stokes number for all simulations with $1 \mu\text{m}$ sized monomers.

Simulation	ξ	maximum			St_{\min}		Growth Limit
		m (g)	ϕ	St	m (g)	ϕ	
nominal	1	1.7×10^{-3}	1.6×10^{-3}	2.3×10^{-4}	2.8×10^{-3}	2.5×10^{-2}	drift
	5	3.8×10^{-4}	3.3×10^{-3}	3.1×10^{-4}	7.9×10^{-4}	3.3×10^{-2}	drift
	10	2.1×10^{-4}	4.7×10^{-3}	3.4×10^{-4}	4.6×10^{-4}	4.0×10^{-2}	drift
5au	1	9.6×10^{-2}	1.1×10^{-2}	1.7×10^{-4}	bouncing
	5	5.2×10^{-2}	1.1×10^{-2}	1.6×10^{-4}	5.1×10^{-2}	2.3×10^{-1}	bouncing
	10	3.8×10^{-2}	5.9×10^{-3}	1.0×10^{-4}	bouncing
15au	1	1.3×10^{-2}	1.4×10^{-4}	1.3×10^{-4}	1.4×10^{-2}	5.4×10^{-2}	drift
	5	4.0×10^{-3}	2.2×10^{-3}	1.6×10^{-4}	3.0×10^{-3}	7.1×10^{-2}	drift
	10	2.7×10^{-3}	2.9×10^{-3}	1.8×10^{-4}	3.0×10^{-3}	7.1×10^{-2}	drift
50au	1	2.2×10^{-4}	2.4×10^{-3}	3.6×10^{-4}	7.8×10^{-4}	1.5×10^{-2}	drift
	5	5.0×10^{-5}	5.6×10^{-3}	5.0×10^{-4}	1.6×10^{-4}	2.1×10^{-2}	drift
	10	2.8×10^{-5}	8.0×10^{-3}	5.6×10^{-4}	7.0×10^{-5}	2.7×10^{-2}	drift
dSN	5	3.4×10^{-4}	3.6×10^{-3}	3.3×10^{-4}	6.4×10^{-4}	3.0×10^{-2}	drift
iSd	5	6.0×10^{-4}	2.4×10^{-3}	2.9×10^{-4}	1.3×10^{-3}	2.4×10^{-2}	drift
iSi	5	7.5×10^{-4}	1.9×10^{-3}	2.7×10^{-4}	1.5×10^{-3}	2.3×10^{-2}	drift
nB	5	6.0×10^{-1}	5.0×10^{-3}	3.3×10^{-3}	1.6×10^{-1}	4.4×10^{-3}	fragmentation
α_{10}	5	4.9×10^{-3}	1.1×10^{-3}	3.4×10^{-4}	1.9×10^{-2}	8.1×10^{-3}	drift
α_{x10}	5	1.0×10^{-6}	1.5×10^{-1}	5.0×10^{-4}	bouncing
Σ_{g_2}	5	5.8×10^{-5}	5.6×10^{-3}	4.8×10^{-4}	1.6×10^{-4}	2.4×10^{-2}	drift
Σ_{g_x2}	5	2.4×10^{-3}	2.1×10^{-3}	2.0×10^{-4}	3.4×10^{-3}	4.4×10^{-2}	drift

Notes. The mass at St_{\min} has no actual physical meaning in the drift-limited cases and is only mentioned for the sake of completeness.

Table 5.5: Aggregate growth for different model settings.

Simulation	ξ^a	growth limit ^b		$\Delta t_{\text{St}} \lesssim t_{\text{drift}}^c$		St_{min}^d		SI^e	
		0.1 μm	1 μm	0.1 μm	1 μm	0.1 μm	1 μm	0.1 μm	1 μm
nominal	1	B	D	✓	✓	✓	✓	✓	✗
	5	B	D	✓	✓	✓	✓	✓	✗
	10	B	D	✓	✓	✓	✓	✓	✗
5au	1	B	B	✓	✗	✓	✗	✓	✗
	5	B	B	✓	✓	✓	✓	✓	✓
	10	B	B	✗	✗	✗	✗	✗	✗
15au	1	B	D	✓	✓	✓	✓	✓	✗
	5	B	D	✓	✓	✓	✓	✓	✗
	10	B	D	✓	✓	✓	✓	✓	✗
50au	1	B	D	✓	✓	✓	✓	✓	✗
	5	B	D	✓	✓	✓	✓	✓	✗
	10	B	D	✓	✓	✓	✓	✓	✗
dSN	5	B	D	✓	✓	✓	✓	✓	✗
iSd	5	B	D	✓	✓	✓	✓	✓	✗
iSi	5	B	D	✓	✓	✓	✓	✓	✗
nB [*]	5	F	F	✓	✓	✓	✓
α_{10}	5	B	D	✓	✓	✓	✓	✓	✗
α_{x10}	5	B	B	✓	✗	✓	✗	✓	✗
Σ_g_{2}	5	B	D	✓	✓	✓	✓	✓	✗
Σ_g_{x2}	5	B	D	✓	✓	✓	✓	✓	✗

Notes. The symbols indicate whether a criterion is fulfilled (✓) or not (✗), unless mentioned otherwise.

^(a) dust-to-ice ratio. ^(b) Growth is drift limited (D), bouncing dominated (B), or fragmentation limited (F). ^(c) Compression is faster than radial drift of bouncing aggregates. ^(d) Aggregates reach St_{min} . ^(e) Aggregates potentially trigger streaming instability if conditions *c* and *d* are fulfilled and growth is not drift limited (*b*).

^(*) Without bouncing, aggregates easily grow to St_{min} , but further growth is limited by fragmentation.

(Credit: Lorek et al., A&A, 611, A18, 2018, reproduced with permission ©ESO)

6 Aggregate compression during the gravitational collapse of pebble clouds

The density of a planetesimal formed through gravitational collapse of a cloud of aggregates collected through streaming instability depends on the properties of the aggregates, in particular porosity and dust-to-ice ratio, and the arrangement of the aggregates within the planetesimal.

In the previous chapter, the properties of aggregates as they grow through coagulation up until they can trigger the streaming instability were investigated. The gravitational collapse of a cloud of this sort of aggregates will further modify their structure. Whether a planetesimal has comet-like properties (see Sect. 1.2) depends thus on the evolution of the aggregates during the collapse.

The typical collision velocities of the aggregates are of the order of the virial velocity $v_{\text{vir}} = \sqrt{3GM/5R}$, where M and R are cloud mass and radius, respectively, ranging from cm s^{-1} to m s^{-1} for clouds corresponding to planetesimals of diameters $\lesssim 100$ km. In this velocity range, millimetre- to decimetre-sized aggregates preferably bounce. Thus, compression is the most important modification aggregates are expected to experience.

The aim of this chapter is to investigate the compression of aggregates during the collapse of the cloud and to relate the results to observed properties of comets.

6.1 Gravitational collapse of a pebble cloud

Wahlberg Jansson and Johansen (2014) developed a simple energy-based model for simulating the gravitational collapse of a cloud of millimetre- to decimetre-sized aggregates (hereafter pebble cloud). The pebble cloud is assumed to be gas-free. A lower limit for the mass loading of a pebble cloud assuming a MMSN is given by comparing Hill density, at which the pebble cloud becomes gravitationally bound, to the midplane gas density and results in $\rho_{\text{d}}/\rho_{\text{g}} = 316 (r/\text{au})^{-1/4}$ (Johansen et al. 2014). Typical values found in numerical simulations of streaming instability are of the order $10^2 - 10^3$ (Johansen et al. 2007). The solid material should therefore dominate the collapse dynamics.

The pebble cloud is initially in virial equilibrium with the random motion of the

aggregates providing the pressure to balance gravity

$$2U + W = 0. \quad (6.1)$$

$U = \sum_{i=1}^N (1/2) m_i v_i^2$ and $W = -3GM^2/(5R)$ are the total internal and gravitational energies of the pebble cloud, respectively. The internal energy is also written as $U = 1/2 M v_{\text{vir}}^2$ with v_{vir} being the virial velocity. The virial velocity is the mass-weighted root mean square velocity and a measure for the typical velocity of the aggregates. The total energy of the cloud is the sum of internal and potential energy, $E = U + W$, which is negative ($E < 0$) for a gravitationally bound system.

Unless energy is dissipated the pebble cloud remains in equilibrium without collapsing, comparable to a globular star cluster. Fully elastic collisions (coefficient of restitution $\varepsilon = 1$) only redistribute the orbital planes of the aggregates. On the other hand, inelastic collisions between the aggregates (coefficient of restitution $\varepsilon < 1$) dissipate energy. Using the virial theorem and the fact that the gravitational energy is $\propto R^{-1}$ easily shows that energy dissipation must lead to cloud collapse, similar to the gravitational contraction of a pre-main sequence T Tauri star, where energy is lost by being radiated from the stellar surface.

For known energy dissipation $\delta E (< 0)$ it is straight forward to calculate the gravitational collapse. For this, Wahlberg Jansson and Johansen (2014) introduced non-dimensional energies to parameterise the pebble cloud. The subscript 0 refers to initial values before contraction. The radius of the cloud is given by the ratio of potential energies

$$\eta = \frac{W_0}{W} = \frac{R}{R_0}. \quad (6.2)$$

The initial radius of the cloud is the Hill radius $R_{\text{H}} = r (M/3M_{\odot})^{1/3}$, where M_{\odot} is the mass of the Sun, and which depends on pebble cloud mass (M) and heliocentric distance (r). The Hill radius defines that the cloud is gravitationally bound, because if the total mass of the aggregates is confined within a sphere of radius R_{H} , self-gravity of the pebble cloud is stronger than tidal forces due to the Sun and Keplerian shear of the disk rotation. The aforementioned Hill density is associated to the Hill radius by requiring $R = R_{\text{H}}$ and solving for the density. The second parameter is the ratio of internal energies

$$\eta_{\text{K}} = \frac{U_0}{U}, \quad (6.3)$$

which quantifies how much internal energy the aggregates lose through dissipation in collisions and gain through the release of potential energy during collapse. The last parameter is the total energy

$$\eta_{\text{eq}} = \frac{E_0}{E}, \quad (6.4)$$

which changes due to energy dissipation in pebble collisions.

The pebble-cloud collapse is then modelled by following the changes of the three η -parameters. Dissipation of energy δE leads to a change of η_{eq} . The cloud strives to

reach virial equilibrium on the free-fall timescale (τ_{ff}) and hence the desired change of cloud radius is $\delta\eta = \eta_{\text{eq}} - \eta$. However, the cloud cannot contract faster than in free fall. Thus, the maximum radius change of the cloud from R_0 to current radius R within the timestep δt is given by

$$\delta\eta_{\text{max}} = -\frac{\pi}{2} \frac{1}{\tau_{\text{ff},0}} \sqrt{\frac{1-\eta}{\eta}} \delta t \quad (6.5)$$

(Wahlberg Jansson and Johansen 2014). Combining both results gives the radius change of the pebble cloud as $\delta\eta = \min(|\eta_{\text{eq}} - \eta|, |\delta\eta_{\text{max}}|)$ and the new radius of the cloud as $\eta + \delta\eta$. Energy dissipation and radius change can be combined to calculate the change of internal energy of the aggregates $\delta\eta_{\text{K}} = \eta_{\text{K}}^2 (\delta E/E_0 + 2\delta\eta/\eta^2)$ (Wahlberg Jansson and Johansen 2014). The first term in brackets is the energy dissipated in aggregate collisions and the second term is the potential energy released during collapse. If the gravitational collapse cannot keep up with the energy dissipated in collisions, that is $\delta\eta_{\text{K}} > 0$, the aggregates slow down and acquire subvirial velocities. The collapse proceeds in free-fall, like the gravitational collapse of a $T = 0$ K gas cloud in star formation.

How much energy is dissipated in a single collision follows from the collision model and is given by the collision energy, $\Delta E = 1/2 (1 - \varepsilon^2) m_{\text{red}} \Delta v^2$, where $m_{\text{red}}^{-1} = m_1^{-1} + m_2^{-1}$ is the reduced mass of the two aggregates (see Eq. 3.12). For sticking or fragmentation, the collision is fully inelastic with coefficient of restitution $\varepsilon = 0$. Therefore, the entire energy of the relative motion of the two aggregates is dissipated. Bouncing collisions, on the other hand, dissipate only a fraction $(1 - \varepsilon^2)$ of this energy, given by a coefficient of restitution $0 < \varepsilon < 1$.

Collapse stops when the cloud reaches the desired planetesimal size R_c at $\eta = \eta_c$. Because the cloud's initial radius is R_{H} , the collapse essentially stops when the density of the desired planetesimal ρ_c is reached at $\eta_c = (9M_{\odot}/4\pi\rho_c r^3)^{1/3}$. In the case of a typical comet, it is $\rho_c = 0.5 \text{ g cm}^{-3}$ (for example Sierks et al. 2015) and $\eta_c \approx 10^{-4}$ at 30 au. From its initial size to planetesimal size, the pebble cloud hence shrinks by a factor $\sim 10^4$.

6.2 Initial conditions for the simulations

6.2.1 Pebble cloud model and collision model

Numerical simulations of streaming instability produce a mass distribution of pebble clouds with a typical mass equivalent to ~ 100 km-diameter planetesimals (Schäfer et al. 2017).

To study the compression of aggregates, the gravitational collapse of four different pebble clouds with masses equivalent to planetesimal radii of $R_c = 0.5 \text{ km}, 5 \text{ km}, 50 \text{ km},$ and 500 km , respectively, and density of $\rho_{c,\text{typ}} = 0.5 \text{ g cm}^{-3}$ is simulated. These objects span a range from comet- to roughly Ceres-sized bodies.

For each cloud mass, a parameter study is conducted varying the initial porosity and the dust-to-ice ratio of the aggregates. The compact size of the aggregates is 1 cm. The volume-filling factors range from 10^{-3} (very porous) to 0.4 (compact). This

represents the large range of aggregate porosities found in planet formation studies: from very porous as formed through hit-and-stick collisions with negligible collisional compression (for example Okuzumi et al. 2012) to strongly compressed in bouncing collisions (for example Zsom et al. 2010). The dust-to-ice ratios of the pebbles span a range from 0 (only ice) to 10 (dust dominated) and, additionally, the extreme case ∞ (only dust).

Wahlberg Jansson and Johansen (2014) use a simple collision model for compact silicate particles neglecting porosity. This is a valid approach for the formation of rocky planetesimals, but not for comet-like objects, for which ice and porosity play a crucial role. To apply this model to comet formation, water ice and porosity are included by using the collision model of Chapter 3 and the representative particle method of Chapter 4.3.

6.2.2 Coefficient of restitution of aggregates

The coefficient of restitution controls the energy dissipation in bouncing collisions which affects the gravitational collapse of the pebble cloud. The gravitational collapse is prolonged for a high value of ϵ because less energy is dissipated per collision (Wahlberg Jansson and Johansen 2014).

Theoretical considerations for grazing collisions of spherical dust aggregates give a value of $\epsilon \approx 0.7$ for the coefficient of restitution (Blum and Münch 1993). Microgravity experiments with millimetre-sized dust aggregates give values uniformly distributed between $0.29 \lesssim \epsilon \lesssim 0.81$ (Weidling et al. 2012), while similar experiments with millimetre- to centimetre-sized solid ice particles give values in the ranges $0.06 \lesssim \epsilon \lesssim 0.84$ (Heißelmann et al. 2010) and $0.08 \lesssim \epsilon \lesssim 0.65$ (Hill et al. 2015), respectively. The coefficient of restitution is therefore only loosely constrained and a constant value of $\epsilon = 0.7$ agrees with theoretical considerations and laboratory experiments is chosen.

6.2.3 Summary of the initial conditions

The initial conditions for the collapse simulations and the nomenclature for the different pebble cloud masses are summarised in Table 6.1.

Table 6.1: Initial conditions for simulations of pebble cloud collapse.

Parameter	Symbol	Value	Remarks
pebble cloud mass	M	2.6×10^{14} g	very low-mass
		2.6×10^{17} g	low-mass
		2.6×10^{20} g	intermediate-mass
		2.6×10^{23} g	high-mass
initial volume-filling factor	ϕ_0	0.001	
		0.01	
		0.05 – 0.4	in steps of 0.05
dust-to-ice ratio	ξ	0	only ice
		0.5 – 10	cometary
		∞	only dust
initial pebble radius	a	1 cm	compact radius
coefficient of restitution	ε	0.7	
representative particles	n	100	
heliocentric distance	r	40 au	comet-forming region

6.3 Results of pebble cloud collapse simulations

The quantity of interest is the volume-weighted mean volume-filling factor of the pebbles at the end of collapse (that is at the desired planetesimal density) calculated as

$$\phi_V = \frac{\sum_{i=1}^n \mathcal{N}_i V_i \phi_i}{\sum_{i=1}^n \mathcal{N}_i V_i}, \quad (6.6)$$

because large and porous pebbles are expected to contribute most to the overall porosity of the planetesimal. The reason for this is that for a random packing of a size distribution of approximately spherical aggregates it cannot be generally assumed that the small aggregates end up filling the void space between the larger ones (Fulle and Blum 2017). Here, $\mathcal{N}_i = M / (n m_i)$ is the number of swarm particles of a representative particle, V_i and ϕ_i are volume and volume-filling factor of the aggregates, respectively.

The collapse is visualised as a function of the pebble cloud density, which is also the planetesimal density. The density is calculated from the non-dimensional cloud radius η as

$$\rho_c = \frac{9M_\odot}{4\pi(\eta r)^3} \quad (6.7)$$

and allows for studying a range of planetesimal densities.

6.3.1 Collision types during collapse

A general result regardless of cloud mass and initial aggregate properties is that $\sim 100\%$ of the collisions during the collapse result in bouncing.

The typical collision velocity of the aggregates

$$v_{\text{vir}} = 2.5 \text{ cm s}^{-1} \left(\frac{r}{40 \text{ au}} \right)^{-1/2} \left(\frac{\rho_c}{0.5 \text{ g cm}^{-3}} \right)^{1/3} \left(\frac{R_c}{5 \text{ km}} \right) \eta^{-1/2} \quad (6.8)$$

is of the order of cm s^{-1} to m s^{-1} towards the end of the collapse for typical values of the parameters.

The virial velocity is in fact an upper limit to the collision velocities of aggregates, because efficient cooling due to fragmentation (for higher cloud masses) and a high frequency of bouncing collisions dynamically cools the cloud resulting in subvirial velocities and a cold collapse (Wahlberg Jansson and Johansen 2014). Aggregates colliding at these velocities will bounce off each other (Güttler et al. 2010; Windmark et al. 2012a; Landeck 2016).

For this reason, the collapse is indeed a sequence of bouncing collisions forming a randomly packed planetesimal (Blum et al. 2014). As collapse proceeds, aggregates may change their properties (volume-filling factor, mass) depending on the initial pebble cloud mass.

Collision velocities of the aggregates

Figure 6.1 shows the typical collision velocities of aggregates during collapse for aggregates with an initial volume-filling factor of 10^{-2} and dust-to-ice ratio of 5.

In the very low-mass pebble cloud, collision velocities are of the order of cm s^{-1} , well above the sticking threshold and very close to the bouncing threshold. Because the sticking probability decreases towards Δv_{bounce} , sticking is not expected to play a crucial role.

The collision velocities of aggregates in the low-mass pebble cloud are within cm s^{-1} to $\sim 10 \text{ cm s}^{-1}$ above the bouncing threshold and below the fragmentation threshold. Bouncing is hence the only collision type to be expected. Processes other than compression of porous aggregates are not expected.

Collision velocities shift closer to the fragmentation threshold for higher cloud masses. While aggregate fragmentation starts to occur when the maximum velocity reaches $\sim 20 \text{ cm s}^{-1}$ in the intermediate-mass pebble cloud, fragmentation dominates at the beginning of the collapse of the high-mass pebble cloud when collision velocities are $\gtrsim 1 \text{ m s}^{-1}$. However, as collapse proceeds and collision velocities decrease, the aggregates evolve into a bouncing-dominated population in all pebble clouds. Because the collision velocity is independent of the aggregate properties and only determined by the gravitational collapse, the results shown should hold for all other cases of volume-filling factor and dust-to-ice ratio.

Collision types

Figure 6.2 shows the fraction of the different collision types during collapse for aggregates with an initial volume-filling factor of 10^{-2} and dust-to-ice ratio of 5 and illustrates the point made seen in Fig. 6.1.

In very low-mass pebble clouds, sticking velocities occur as already expected from Fig. 6.1a. However, the fraction is $\lesssim 1\%$, decreases rapidly as collapse proceeds,

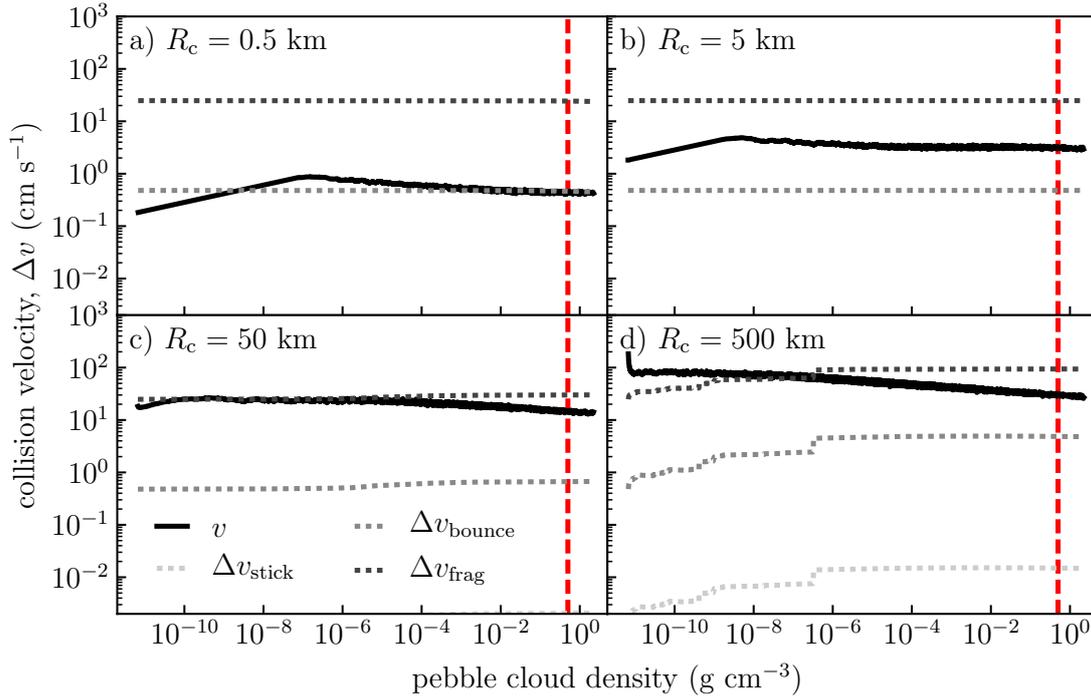


Figure 6.1: Collision velocity as function of pebble cloud density for aggregates with an initial volume-filling factor of 10^{-2} and dust-to-ice ratio of 5. a) Very low-mass pebble cloud. b) Low-mass pebble cloud. c) Intermediate-mass pebble cloud. d) High-mass pebble cloud. Solid lines show the actual collision velocity of the aggregates during collapse. Dotted lines represent the sticking, bouncing, and fragmentation threshold velocities. The vertical dashed line indicates a pebble cloud density of 0.5 g cm^{-3} which equals the typical density of a comet.

and bouncing collisions dominate again. For low mass pebble clouds, the fraction of bouncing collisions is 100%. In the intermediate mass pebble cloud, the fraction of destructive collisions is $\lesssim 1\%$, decreasing rapidly. In the pebble cloud with highest mass, however, fragmentation dominates at the beginning accounting for $\sim 100\%$ of the collisions, but quickly changes into a bouncing-dominated population of aggregates.

Mass distribution function of aggregates

Figure 6.3 shows the mass distribution function (mdf) for the four cloud masses for aggregates with initial volume-filling factor of 10^{-2} and dust-to-ice ratio of 5. The initial mass of the aggregates is the same for all four pebble clouds.

While the presence of sticking collisions in the very low-mass pebble cloud does not affect the mass distribution significantly, fragmentation does for higher cloud masses. The mdf is shown early in the collapse at a density of $10^{-9} \text{ g cm}^{-3}$, towards the end at a density of $10^{-3} \text{ g cm}^{-3}$, and at the end at a density of 0.5 g cm^{-3} .

Very low- and low-mass clouds preserve the mass distribution, because of bouncing collisions resulting only in compression. For the intermediate-mass cloud the mdf shows two populations of aggregates, a narrow peak around the initial aggregate mass

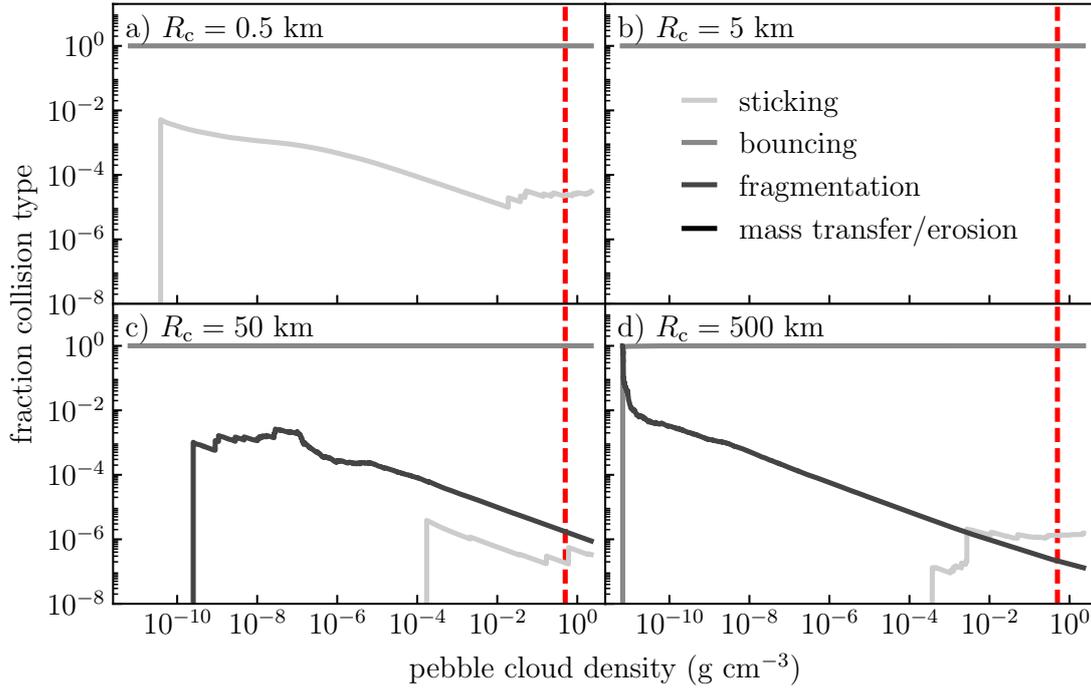


Figure 6.2: Collision types as a function of planetesimal density for aggregates with an initial volume-filling factor of 10^{-2} and dust-to-ice ratio of 5. *a)* Very low-mass pebble cloud. *b)* Low-mass pebble cloud. *c)* Intermediate-mass pebble cloud. *d)* High-mass pebble cloud. The different lines represent the different collision types: sticking, bouncing, fragmentation, and mass transfer respectively erosion. The vertical dashed line indicates a pebble cloud density of 0.5 g cm^{-3} which equals the typical density of a comet.

and a wider second peak with power law tail at lower masses corresponding to the fragments. The mean mass is roughly a factor 2 lower than the initial mass. In the high-mass cloud, however, fragmentation results in a significant decrease of the mass of the aggregates by about a factor of 10^4 .

Therefore, clouds with masses corresponding to planetesimals $\lesssim 50 \text{ km}$ are expected to preserve all or a part of the initial aggregates, while the heavier clouds do not. Despite the simpler collision model, this result of aggregate fragmentation agrees with Wahlberg Jansson and Johansen (2014), who expressed it in terms of pebble fraction (aggregates with sizes $> 1 \text{ mm}$) found to be a decreasing function of pebble cloud mass.

6.3.2 Compression of aggregates

Keeping the mass of the pebble cloud fixed, a higher dust-to-ice ratio results in stronger compression of the aggregates. This can be seen in Fig. 6.4 showing the volume-filling factors of the aggregates when the planetesimal has reached a density of 0.5 g cm^{-3} as a function of initial volume-filling factor.

Ice is harder to compress than silicate dust, which is visible in the compression curves (Fig. 3.2), because the rolling friction force of two ice grains in contact is roughly

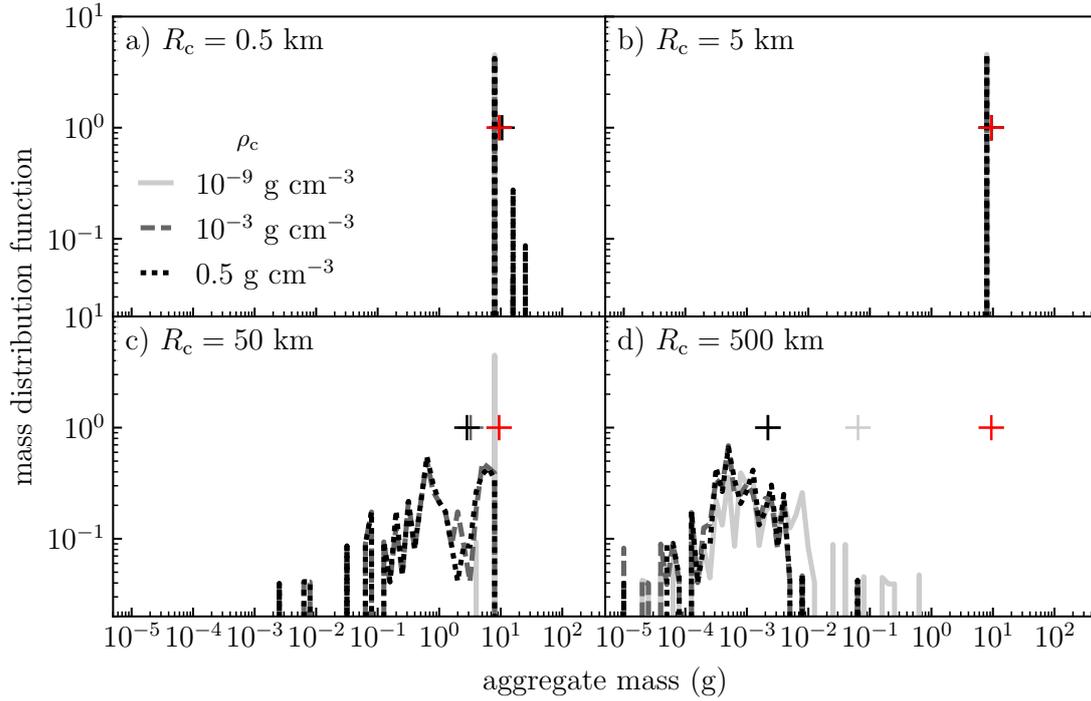


Figure 6.3: Mass distribution function of aggregates during pebble cloud collapse for aggregates with an initial volume-filling factor of 10^{-2} and dust-to-ice ratio of 5. *a)* Very low-mass pebble cloud. *b)* Low-mass pebble cloud. *c)* Intermediate-mass pebble cloud. *d)* High-mass pebble cloud. Different lines correspond to different times in the collapse: very early when the density is 10^{-9} g cm $^{-3}$ (solid), towards the end when the cloud has collapsed to a density of 10^{-3} g cm $^{-3}$ (dashed), and at the end of the collapse at a density of 0.5 g cm $^{-3}$ (dotted). The symbols (+) indicate the initial mass (red) and the mass-weighted average mass (grey). Lines overlap in panels *a)*, *b)*, and *c)* which shows that there is either little change (*a* and *b*) or a steady state is quickly established (*c*).

ten times higher than for two silica grains (Gundlach et al. 2011a). An aggregate of mixed composition ($0 < \xi < \infty$) is expected to have compressional properties in between the cases of pure dust ($\xi = \infty$) and pure ice ($\xi = 0$). For the same amount of energy available due to the collision, more dust than ice contacts are restructured resulting in stronger compression for higher dust-to-ice ratio. The extreme cases are pure dust and pure ice for which the highest and lowest volume-filling factors are obtained, respectively.

Figure 6.5 shows the compression of aggregates with dust-to-ice ratios of 0 and ∞ and with initial volume-filling factors down to $\phi_0 = 10^{-3}$.

Compression of pure dust aggregates is negligible in very low-mass pebble clouds. The aggregates mostly retain their initial volume-filling factor, although occasional sticking collisions decrease ϕ_v by a small amount. Higher pebble cloud masses lead to significant compression of the aggregates to volume-filling factors $0.22 \lesssim \phi_v \lesssim 0.43$, but only if $M \geq 2.6 \times 10^{20}$ g (intermediate- and high-mass pebble clouds) aggregates approach their maximum volume-filling factor of ≈ 0.46 (Weidling et al. 2009; Güttler

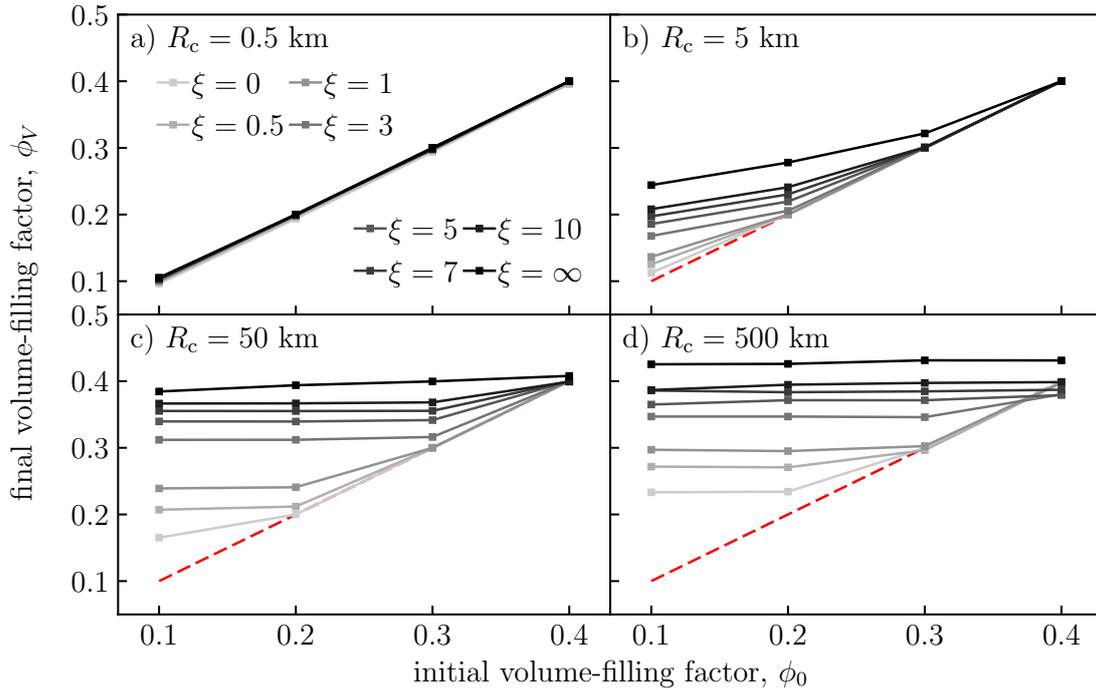


Figure 6.4: Volume-filling factor of aggregates as a function of initial volume-filling factor. a) Very low-mass pebble cloud. b) Low-mass pebble cloud. c) Intermediate-mass pebble cloud. d) High-mass pebble cloud. Different lines (solid) are for different dust-to-ice ratio of the aggregates ($0 \leq \xi \leq \infty$). Along the red dashed diagonal line $\phi_V = \phi_0$. Above the line aggregates experienced compression, whereas below the line aggregates gained porosity. (Credit: Lorek et al., *A&A*, 587, A128, 2016, reproduced with permission (©ESO))

et al. 2010).

As it is the case for silicate aggregates, pure ice aggregates experience only negligible compression in very low-mass pebble clouds. For higher pebble cloud masses, the aggregates are compressed up to a certain value. In the low-mass pebble cloud, this value is $\phi_V \approx 0.11$ and in the intermediate-mass pebble cloud, aggregates reach $\phi_V \approx 0.16$. Only in the high-mass pebble cloud the volume-filling factor approaches the maximum value of $\phi_V \approx 0.23$.

6.3.3 Formation of comet-like planetesimal

With the volume-filling factor of the aggregates as a function of dust-to-ice ratio, initial volume-filling factor, and pebble cloud mass, it is possible to constrain conditions for comet formation.

Observations and modelling have shown that cometary densities are in the range $0.1 \text{ g cm}^{-3} \lesssim \rho_c \lesssim 1 \text{ g cm}^{-3}$ (Blum et al. 2006; A'Hearn 2011) with a typical value of $\rho_{c,\text{typ}} = 0.5 \text{ g cm}^{-3}$ (comet 67P, see Preusker et al. 2015; Sierks et al. 2015; Jorda et al. 2016; Pätzold et al. 2016). By applying this density range to the (constant) pebble cloud masses used in this model, strictly speaking, the planetesimal radii are 70%

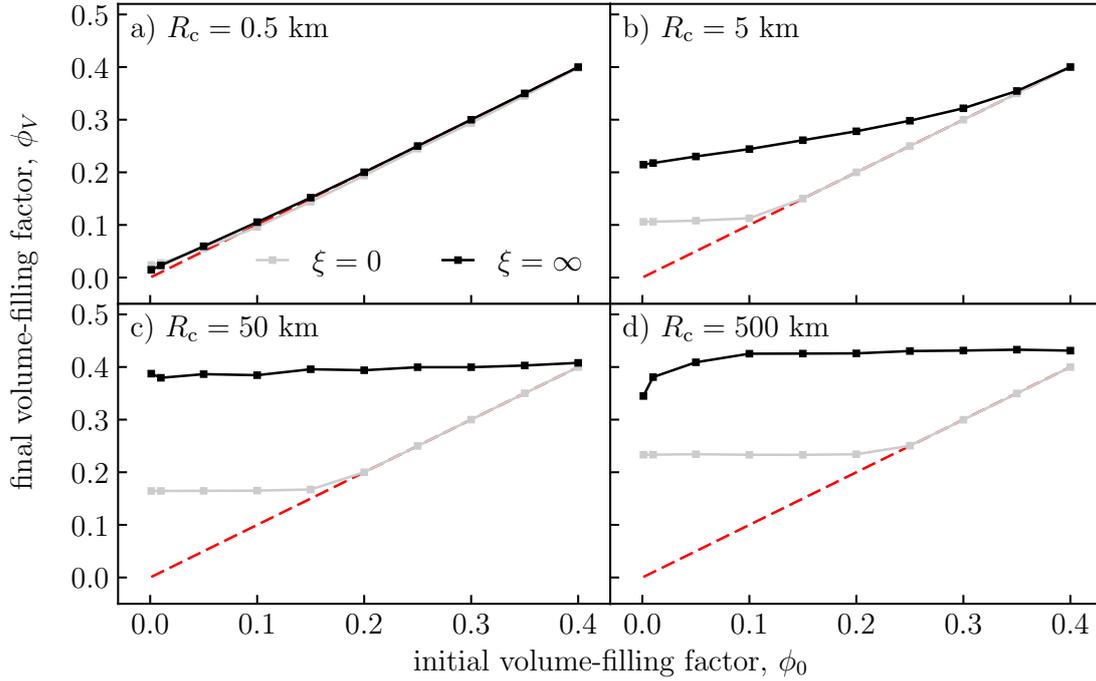


Figure 6.5: Volume-filling factor of aggregates as a function of initial volume-filling factor for pure dust and ice aggregates and initial volume-filling factors down to 10^{-3} . a) Very low-mass pebble cloud. b) Low-mass pebble cloud. c) Intermediate-mass pebble cloud. d) High-mass pebble cloud. Along the red dashed diagonal line $\phi_V = \phi_0$. Above the line aggregates experienced compression, whereas below the line aggregates gained porosity. (Credit: Lorek et al., *A&A*, 587, A128, 2016, reproduced with permission ©ESO)

larger for 0.1 g cm^{-3} and 20% smaller for 1 g cm^{-3} compared to the reference radius R_c , respectively.

In addition to Eq. 6.7, the density of the planetesimal is given directly from the material properties as the product of the bulk density of the aggregate, depending on dust-to-ice ratio and volume-filling factor, and the volume-filling factor of the aggregate packing (ϕ_p),

$$\rho_c = \rho_*^* \phi_V \phi_p. \quad (6.9)$$

Here, $\rho_*^* = \rho_d \rho_i (1 + \xi) / (\xi \rho_i + \rho_d)$ is the density of the aggregate if there is no void space (compact bulk density, see Eq. 3.35). The volume-filling factor of the aggregate packing is $\phi_p \approx 0.6$. This is in between the values obtained for a random loose packing (RLP) of spheres which has $\phi_p = 0.55$ and a random close packing (RCP) which has $\phi_p = 0.64$ (Skorov and Blum 2012; Fulle and Blum 2017). A packing structure with $\phi_p > 0.64$ or $\phi < 0.55$ would imply processes that either crush void space between aggregates or that create a packing of aggregates with large voids, respectively. Both cases are not consistent with the random process of deposition of approximately spherical aggregates.

The product $\phi_V \phi_p$ is the total volume-filling factor of the planetesimal, that is

Table 6.2: Volume-weighted mean filling factor of aggregates for all simulations.

M (g)	ξ	ρ_* (g cm ⁻³)	ϕ_0									
			0.001	0.01	0.05	0.10	0.15	0.20	0.25	0.30	0.35	0.40
2.6×10^{14}	0	1.00	0.024	0.028	0.056	0.096	0.144	0.194	0.245	0.294	0.345	0.399
	0.5	1.29	0.099	...	0.197	...	0.297	...	0.396
	1.0	1.50	0.100	...	0.200	...	0.297	...	0.400
	3.0	2.00	0.101	...	0.200	...	0.299	...	0.400
	5.0	2.25	0.103	...	0.200	...	0.300	...	0.400
	7.0	2.40	0.103	...	0.199	...	0.300	...	0.400
	10.0	2.54	0.104	...	0.200	...	0.298	...	0.400
	∞	3.00	0.015	0.023	0.060	0.105	0.152	0.200	0.250	0.300	0.350	0.400
2.6×10^{17}	0	1.00	0.106	0.106	0.108	0.113	0.150	0.200	0.250	0.300	0.350	0.400
	0.5	1.29	0.125	...	0.200	...	0.300	...	0.400
	1.0	1.50	0.136	...	0.200	...	0.300	...	0.400
	3.0	2.00	0.168	...	0.206	...	0.300	...	0.400
	5.0	2.25	0.186	...	0.219	...	0.300	...	0.400
	7.0	2.40	0.197	...	0.230	...	0.300	...	0.400
	10.0	2.54	0.208	...	0.241	...	0.301	...	0.400
	∞	3.00	0.215	0.217	0.230	0.244	0.261	0.278	0.298	0.322	0.355	0.400
2.6×10^{20}	0	1.00	0.164	0.164	0.165	0.165	0.167	0.200	0.250	0.300	0.350	0.400
	0.5	1.29	0.207	...	0.212	...	0.300	...	0.400
	1.0	1.50	0.239	...	0.241	...	0.300	...	0.400
	3.0	2.00	0.312	...	0.312	...	0.316	...	0.400
	5.0	2.25	0.340	...	0.339	...	0.342	...	0.400
	7.0	2.40	0.355	...	0.355	...	0.356	...	0.400
	10.0	2.54	0.366	...	0.367	...	0.368	...	0.399
	∞	3.00	0.388	0.380	0.386	0.385	0.395	0.394	0.400	0.400	0.403	0.408
2.6×10^{23}	0	1.00	0.233	0.233	0.234	0.233	0.233	0.234	0.250	0.300	0.350	0.400
	0.5	1.29	0.272	...	0.271	...	0.296	...	0.398
	1.0	1.50	0.297	...	0.295	...	0.303	...	0.398
	3.0	2.00	0.347	...	0.347	...	0.346	...	0.380
	5.0	2.25	0.365	...	0.371	...	0.372	...	0.379
	7.0	2.40	0.386	...	0.383	...	0.385	...	0.387
	10.0	2.54	0.387	...	0.395	...	0.397	...	0.399
	∞	3.00	0.345	0.382	0.408	0.425	0.426	0.428	0.429	0.431	0.432	0.432

Notes. Columns from left to right: mass of the pebble cloud, dust-to-ice ratio (0 for pure dust and ∞ for pure ice), bulk density of the aggregate, and final volume-filling factors at planetesimal density of 0.5 g cm^{-3} . The initial compact aggregate size is 1 cm in each simulation. 100 representative particles were used. The typical uncertainties of the final volume-filling factors are $\lesssim 15\%$. The individual uncertainties can reach 50% in the high-mass cloud for pure dust aggregates with $\phi_0 = 10^3$, because of the presence of barely compressed pebbles. (Credit: Lorek et al., *A&A*, 587, A128, 2016, reproduced with permission ©ESO)

$1 - \mathcal{P}$ with \mathcal{P} being the porosity of the planetesimal. In this model of planetesimal formation through gravitational collapse of pebble clouds, porosity hence is separated into two contributions: porosity of aggregates (micro-porosity) and aggregate packing (macro-porosity). For comets with a typical density of 0.5 g cm^{-3} , depending on the compact bulk density of the aggregates, the porosity is hence expected to be in the range $\mathcal{P} \approx 50\% - 83\%$. Consequently, a lower comet density results in a higher porosity, and vice versa. An object with density 0.1 g cm^{-3} would have a porosity in the range $90\% - 97\%$, while an object with 1 g cm^{-3} would have $\lesssim 33\%$.

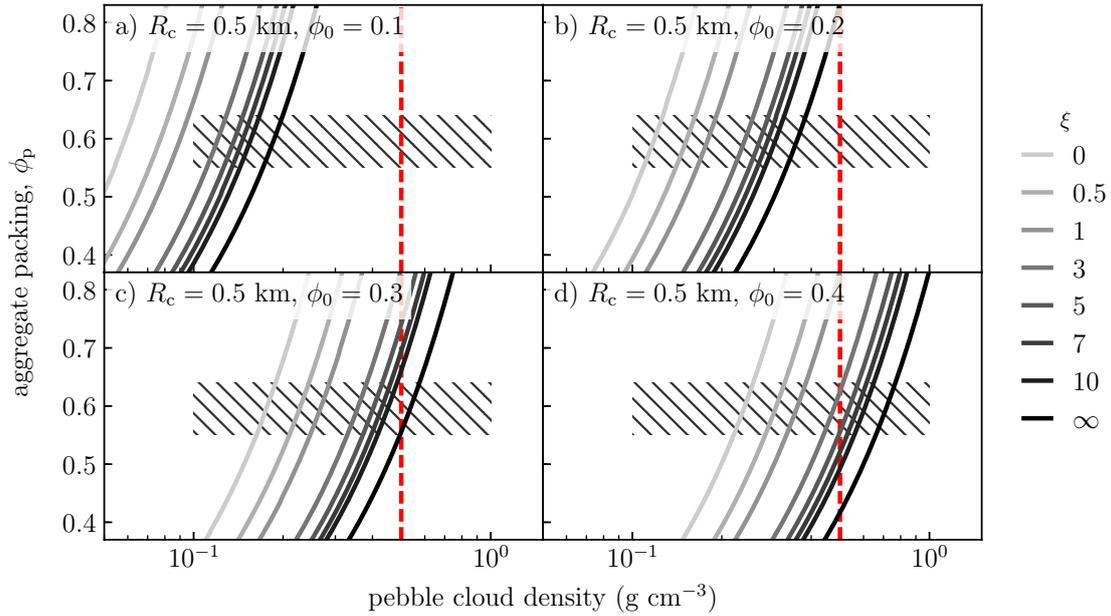


Figure 6.6: Aggregate packing as function of pebble cloud density in a very low-mass pebble cloud. *a)* Porous aggregates with initial volume-filling factor $\phi_0 = 0.1$. *b)* Initial volume-filling factor $\phi_0 = 0.2$. *c)* Initial volume-filling factor $\phi_0 = 0.3$. *d)* Compact aggregates with initial volume-filling factor $\phi_0 = 0.4$. The hatched area indicates the region where the resulting planetesimal has comet-like properties: a density in the range $0.1 \text{ g cm}^{-3} \leq \rho_c \leq 1 \text{ g cm}^{-3}$ and an aggregate packing in the range $0.55 \leq \phi_p \leq 0.64$. The solid lines show $\phi_p(\rho_c)$ (see text for details) for different dust-to-ice ratios. The typical comet density of 0.5 g cm^{-3} is indicated with a vertical dashed line. The planetesimal is considered comet-like if the line crosses the hatched area.

To finally link the pebble cloud collapse to comet formation, Eq. 6.9 is used to calculate ϕ_p as a function of ρ_c . A comparison with the permitted range $0.55 \leq \phi_p \leq 0.64$ allows to constrain pebble cloud mass, dust-to-ice ratio, and initial volume-filling factor of the aggregates that result in a comet-like planetesimal.

A comet-like planetesimal is therefore defined as a planetesimal with density in the range $0.1 \text{ g cm}^{-3} \leq \rho_c \leq 1 \text{ g cm}^{-3}$ and aggregate packing in the range $0.55 \leq \phi_p \leq 0.64$. Because comets have typically sizes in the range 1 km – 10 km (A’Hearn 2011; Kokotanekova et al. 2017) but pebble clouds with masses up to 500 km-radius objects are studied, the term comet-like addresses only the material properties. A more detailed discussion of this topic will be given in Chapter 7.

Very low-mass pebble cloud

Figure 6.6 shows aggregate packing as a function of planetesimal density for the very low-mass pebble cloud.

Initially porous aggregates with $\phi_0 = 0.1$ are not significantly compressed during the collapse and the formation of comet-like planetesimals requires dust-to-ice ratios

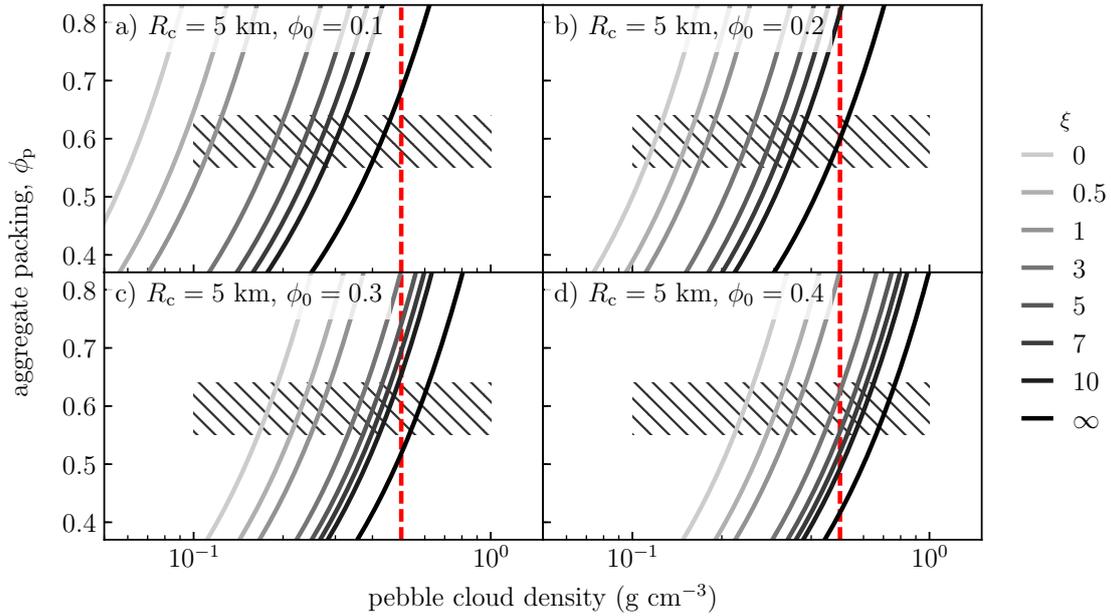


Figure 6.7: Aggregate packing as function of pebble cloud density in a low-mass pebble cloud. *a)* Porous aggregates with initial volume-filling factor $\phi_0 = 0.1$. *b)* Initial volume-filling factor $\phi_0 = 0.2$. *c)* Initial volume-filling factor $\phi_0 = 0.3$. *d)* Compact aggregates with initial volume-filling factor $\phi_0 = 0.4$. The hatched area indicates the region where the resulting planetesimal has comet-like properties: a density in the range $0.1 \text{ g cm}^{-3} \leq \rho_c \leq 1 \text{ g cm}^{-3}$ and an aggregate packing in the range $0.55 \leq \phi_p \leq 0.64$. The solid lines show $\phi_p(\rho_c)$ (see text for details) for different dust-to-ice ratios. The typical comet density of 0.5 g cm^{-3} is indicated with a vertical dashed line. The planetesimal is considered comet-like if the line crosses the hatched area.

$\gtrsim 3$, because of the higher compact bulk density of the aggregates. However, densities are significantly lower than $\rho_{c,\text{typ}}$ and even a planetesimal made of dust would have a density of only $\sim 0.2 \text{ g cm}^{-3}$, rendering the object highly porous with $\mathcal{P} \approx 93\%$.

For increasing initial volume-filling factor, comet-like planetesimals form regardless of dust-to-ice ratio. The density approaches $\rho_{c,\text{typ}}$ for $\phi_0 = 0.3$ and $\xi \gtrsim 10$. However, the dust-to-ice ratios of volatile-rich comets (~ 5) are significantly lower than this (for example Rotundi et al. 2015, for comet 67P).

Initially compact aggregates with $\phi_0 = 0.4$ and dust-to-ice ratios in the range $3 \lesssim \xi \lesssim 5$ form comet-like planetesimals with $\rho_{c,\text{typ}}$. The formation of compact aggregates is predicted in the inner solar system at 1 au by models of aggregate growth that include bouncing collisions (Zsom et al. 2010). However, farther out in the disk, aggregates remain porous (see the results presented in Chapter 5).

Low-mass pebble cloud

Figure 6.7 shows aggregate packing as a function of planetesimal density for the low-mass pebble cloud.

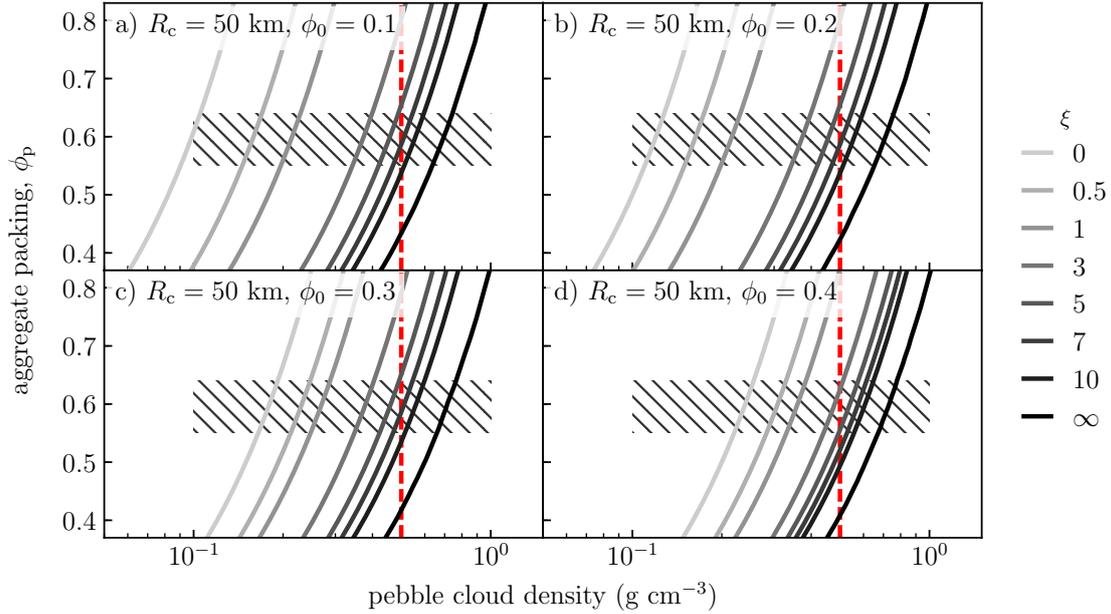


Figure 6.8: Aggregate packing as function of pebble cloud density in an intermediate-mass pebble cloud. a) Porous aggregates with initial volume-filling factor $\phi_0 = 0.1$. b) Initial volume-filling factor $\phi_0 = 0.2$. c) Initial volume-filling factor $\phi_0 = 0.3$. d) Compact aggregates with initial volume-filling factor $\phi_0 = 0.4$. The hatched area indicates the region where the resulting planetesimal has comet-like properties: a density in the range $0.1 \text{ g cm}^{-3} \leq \rho_c \leq 1 \text{ g cm}^{-3}$ and an aggregate packing in the range $0.55 \leq \phi_p \leq 0.64$. The solid lines show $\phi_p(\rho_c)$ (see text for details) for different dust-to-ice ratios. The typical comet density of 0.5 g cm^{-3} is indicated with a vertical dashed line. The planetesimal is considered comet-like if the line crosses the hatched area.

Because of the higher mass of the pebble cloud, initially porous aggregates are compressed to a greater extent during collapse (see Fig. 6.4). The formation of comet-like planetesimals requires dust-to-ice ratios $\gtrsim 0.5$. Because of the compression of aggregates, densities of comet-like planetesimals can be higher than in the previous case for the very low-mass pebble cloud. The reason is that for a given density, more compact aggregates require a less dense packing, which is closer to random packing. However, also here comet-like planetesimals with density $\rho_{c,\text{typ}}$ form only for $\phi_0 = 0.4$ and $3 \lesssim \xi \lesssim 5$, unless the dust-to-ice ratio is $\gtrsim 10$.

Intermediate-mass pebble cloud

The collapse of an intermediate-mass pebble cloud sufficiently compresses the aggregates so that comet-like planetesimals very generally form regardless of the dust-to-ice ratio and initial volume-filling factor of the aggregates. Densities of $\rho_{c,\text{typ}}$ are possible for all initial volume-filling factors, as shown in Fig. 6.8.

However, while aggregates with $\phi_0 < 0.4$ require dust-to-ice ratios in the range $5 \lesssim \xi \lesssim 10$, compact aggregates require $3 \lesssim \xi \lesssim 5$ as in the previous cases. Numeri-

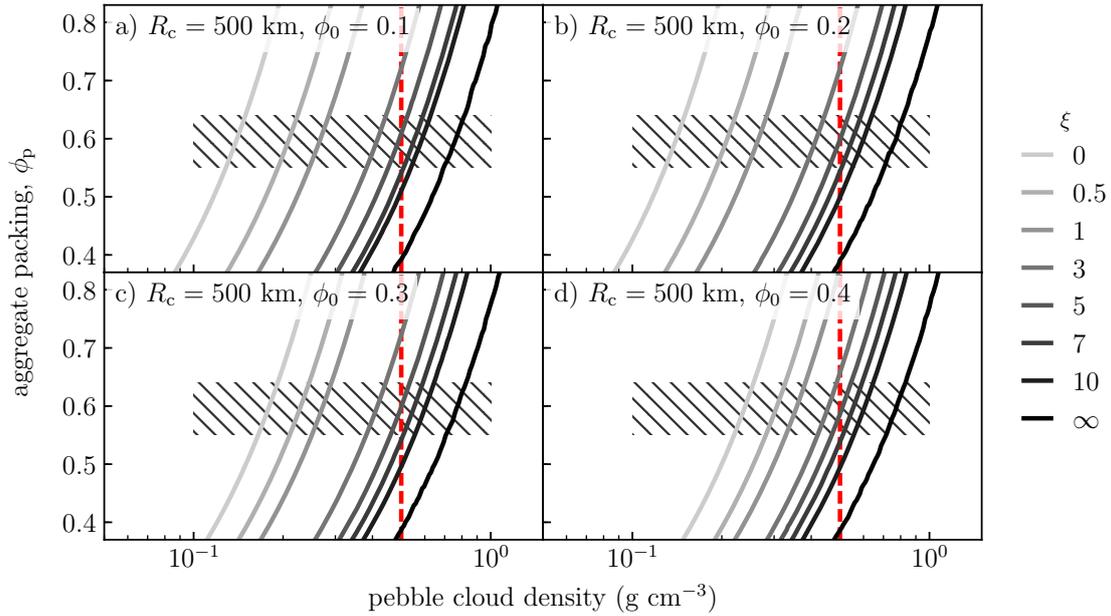


Figure 6.9: Aggregate packing as function of pebble cloud density in a high-mass pebble cloud. *a)* Porous aggregates with initial volume-filling factor $\phi_0 = 0.1$. *b)* Initial volume-filling factor $\phi_0 = 0.2$. *c)* Initial volume-filling factor $\phi_0 = 0.3$. *d)* Compact aggregates with initial volume-filling factor $\phi_0 = 0.4$. The hatched area indicates the region where the resulting planetesimal has comet-like properties: a density in the range $0.1 \text{ g cm}^{-3} \leq \rho_c \leq 1 \text{ g cm}^{-3}$ and an aggregate packing in the range $0.55 \leq \phi_p \leq 0.64$. The solid lines show $\phi_p(\rho_c)$ (see text for details) for different dust-to-ice ratios. The typical comet density of 0.5 g cm^{-3} is indicated with a vertical dashed line. The planetesimal is considered comet-like if the line crosses the hatched area.

cal studies of planetesimal formation through streaming instability predict a typical planetesimal size of $\sim 100 \text{ km}$ (Schäfer et al. 2017). Accordingly, this case should be representative of the majority of icy planetesimals.

High-mass pebble cloud

Finally, Fig. 6.9 shows the case of a high-mass pebble cloud.

The formation of comet-like planetesimals is possible for any values of the dust-to-ice ratio and the initial volume-filling factor. But as in the previous case, the formation of a comet-like planetesimal with $\rho_{c,\text{typ}}$ only occurs for certain combinations of ϕ_0 and ξ . While aggregates with $\phi_0 < 0.4$ require $5 \lesssim \xi \lesssim 7$, aggregates with $\phi_0 = 0.4$ require $3 \lesssim \xi \lesssim 7$.

Objects forming from pebble clouds this heavy ($2.6 \times 10^{23} \text{ g}$) have approximately the size of Ceres (mean radius 473 km), an icy dwarf planet in the asteroid belt orbiting the Sun at a distance of 2.8 au. In addition to the compression of aggregates during collapse, self-gravity is no longer negligible resulting in additional compression of the material and changes in the internal structure (differentiation). Furthermore as shown

in Fig. 6.3, the mass distribution function changes significantly due to fragmentation. It is hence very unlikely that a planetesimal of this size would retain comet-like properties. However, it is also not clear how the collapse of such a massive pebble cloud proceeds. Fragmentation of the pebble cloud as a possible mechanism is discussed in Chapter 7.

Summary of the formation of comet-like planetesimals

The formation of a comet-like planetesimal with typical density of 0.5 g cm^{-3} requires in all four pebble clouds studied here a dust-to-ice ratio of the aggregates in the range $3 \lesssim \xi \lesssim 10$. Because of the assumption that the pebble cloud collapses into a single planetesimal, the resulting planetesimal has the same dust-to-ice ratio as the aggregates.

Heating of aggregates due to energy dissipation in bouncing collisions is not enough to sublimate volatile ices which would change the dust-to-ice ratio. This can be shown with a quick estimate of the maximum temperature increase due to collisions. The maximum energy that is dissipated is the kinetic energy of an aggregate approaching the planetesimal from infinity, $\Delta E_{\text{kin,max}} = GMm/R$, where M is the mass of the planetesimal, R is the radius of the planetesimal, and m is the mass of the aggregate. Water ice at -100°C has a specific heat of $c_V = 1.389 \times 10^7 \text{ erg g}^{-1} \text{ K}^{-1}$. The temperature change associated to the dissipation of $\Delta E_{\text{kin,max}}$ is $\Delta T = GM/c_V R$. For a planetesimal with density of 0.5 g cm^{-3} , the temperature of the aggregates increases by $\Delta T \lesssim 1 \text{ K}$ if the radius is $\lesssim 100 \text{ km}$. The temperature changes by up to a few 10 K for larger planetesimal radii due to their deeper potential well. Because ices are expected to have very low temperatures (water ice condenses at $\sim 180 \text{ K}$ for solar nebula conditions), it is not expected that this temperature changes results in vaporisation of volatiles.

Therefore, the model constrains the dust-to-ice ratio of comet-like planetesimals to be in the range 3 – 10, which is consistent with observations of comets. The particles of cometary dust trails have a dust-to-volatile ratio of ~ 3 (Sykes and Walker 1992). Küppers et al. (2005) estimated from ejecta material produced during the Deep Impact mission that the nucleus of comet 9P/Tempel has a dust-to-ice ratio $\gtrsim 1$. From data obtained during the Rosetta mission to comet 67P/Churyumov-Gerasimenko, Rotundi et al. (2015) found a dust-to-gas ratio of 6 ± 2 , if only water ice, and 4 ± 2 , if water ice, CO, CO₂, are considered, respectively. Fulle et al. (2016a) and Fulle et al. (2017) derived the dust-to-ice ratio of 67P from the density of dust aggregates measured with the Grain Impactor Analyser and Dust Accumulator (GIADA) on board Rosetta and constraints on the composition from solar system elemental abundances (Lodders 2003). This gives a value of $\xi = 7.5$ inside the nucleus of 67P (Fulle et al. 2017). For this reason, very high ($\gtrsim 10$) as well as very low dust-to-ice ratios ($\lesssim 3$) can be excluded for volatile-rich comets. With respect to the dust-to-ice ratio, the predictions of the simulations for comet-like planetesimals are consistent with observations.

However, the model calculations do not allow to constrain pebble cloud mass and initial volume-filling factor of the aggregates independently. Pebble clouds with masses $M \lesssim 2.6 \times 10^{20} \text{ g}$ in combination with aggregates of initial $\phi \gtrsim 0.4$ produce comet-like planetesimals; but so do pebble clouds with masses $M \gtrsim 2.6 \times 10^{20} \text{ g}$ and any initial volume-filling factor of the aggregates. One therefore has to resort to models of aggregate growth as done in Chapter 5 to distinguish both cases. This difference is

important because the mass of the pebble cloud is related to the size of planetesimal that forms. While the comet-like planetesimals emerging from the low mass pebble clouds already have sizes consistent with comets (~ 1 km to few tens of kilometres), higher mass pebble clouds form larger objects. Only in the first case, comet-like planetesimals are also comets. In the latter case, however, additional processes are necessary to form comets. This complication is further addressed in Chapter 7.

7 Implications for the formation of comets

In this chapter, the results from modelling aggregate growth in the solar nebula and aggregate compression during the gravitational collapse of a pebble cloud are combined to place constraints on the gravitational instability model for comet formation.

The growth process of aggregates in the solar nebula allows conclusions on whether or not in situ comet formation through streaming instability is possible. The initial porosity of the aggregates that form in the solar nebula allows confining the pebble cloud mass, comparing it to predictions made by numerical simulations of streaming instability, and comparing it to the sizes of comets.

As building blocks of the comet-like planetesimals, the aggregates from the simulations are compared to the pebbles observed on comet 67P which sets constraints on the conditions in the solar nebula favouring comet formation. At the end, this leads to a more complete picture of comet formation.

7.1 Local formation of comets at large heliocentric distance

Porous growth of aggregates in the solar nebula is sensitive to the monomer size (see Chapter 5). Aggregate growth is bouncing dominated for $0.1 \mu\text{m}$ sized monomers and drift limited for $1 \mu\text{m}$ sized monomers. The latter case prevents streaming instability to set in, because aggregates do not locally reach St_{min} . On the other hand, compression of porous aggregates in the bouncing-dominated case pushes aggregates towards St_{min} faster than radial drift removes the bouncing aggregates.

This result is important in two ways. Firstly, it allows comet formation to be a local process if monomers are submicrometre in size. The presence of highly volatile species in comets (for example N_2) argues for a cold formation region where these volatiles were present as ice and that the nucleus was never heated above a certain temperature ($\lesssim 40 \text{ K}$) (Rubin et al. 2015; Davidsson et al. 2016). Radial drift, however, transports material over significant radial distances thereby crossing ice lines which results in the sublimation of volatile ices. In this case, it is difficult to incorporate these species into the nucleus during formation either in solid form as ice or in gaseous form trapped in amorphous ice or clathrates (Bar-Nun et al. 2007; Rubin et al. 2015; Mousis et al. 2016), a problem that is not encountered if comets form in situ at heliocentric distances in the range 5 au to 50 au.

Secondly, submicrometre-sized monomers are commonly predicted to dominate cometary matter. The Micro-Imaging Dust Analysis System (MIDAS) on board the Rosetta spacecraft showed that even micrometre-sized cometary grains show substructure of submicrometre in size (Bentley et al. 2016). This is strong indication that monomers are submicrometre in size. Furthermore, submicrometre-sized monomers are consistent with experimental studies on dust condensation (Toppani et al. 2006; Kimura et al. 2008, 2011), grain size distributions in the ISM (Mathis et al. 1977; Weingartner and Draine 2001; Kimura et al. 2003; Ormel et al. 2009), crystalline silicates in chondritic-porous interstellar dust particles (CP IDPs) (Bradley 2003), glasses with embedded metals and sulphides (GEMS) in IDPs (Draine 2003), and optical and infrared spectroscopy of dust in the coma of comets (Min et al. 2005; Kimura et al. 2003; Kelley and Wooden 2009).

7.2 Implications from the comparison with observations of cometary pebbles

The Comet Infrared and Visible Analyser (CIVA) camera on board the Philae lander of the Rosetta spacecraft obtained high-resolution images of an exposed bare wall (not covered by dust) which the lander was facing after reaching its final landing site. On these images, granular structures embedded in a fine-grained unresolved material were found.

Poulet et al. (2016) argue that these structures (pebbles) cannot have formed recently because their size distribution differs significantly from young cometary material (dust in the coma, boulders on the surface). Instead, the observed pebbles are most likely the building blocks from which the comet once formed. The pebbles have diameters in the range 3 mm to 1.6 cm. Towards smaller diameters (< 5 mm) the cumulative size-frequency distribution of the pebbles reaches a plateau, which is partly attributed to the spatial resolution of ~ 1 mm of the CIVA images (Poulet et al. 2016).

7.2.1 Compression of millimetre-sized aggregates

The simulations of aggregate growth presented in Chapter 5 have shown that aggregates with St_{\min} are millimetre in size with volume-filling factors in the range $0.1 - 10^{-2}$, depending on dust-to-ice ratio and heliocentric distance. Taking these aggregate properties as initial conditions, gravitational collapse simulations were conducted to refine the picture of formation of comet-like planetesimals obtained for centimetre-sized aggregates. With bouncing being the dominant collision type, compression depends only on the initial volume-filling factor, but not on the size of the aggregates. Thus, the results found in Chapter 6 should remain valid.

Heliocentric distance 30 au

At 30 au, aggregates with St_{\min} have radii of $a = 0.72$ cm, 0.45 cm, and 0.38 cm with volume-filling factors of $\phi = 1.0 \times 10^{-2}$, 1.2×10^{-2} , and 1.4×10^{-2} for dust-to-ice ratios of $\xi = 1, 5,$ and 10, respectively.

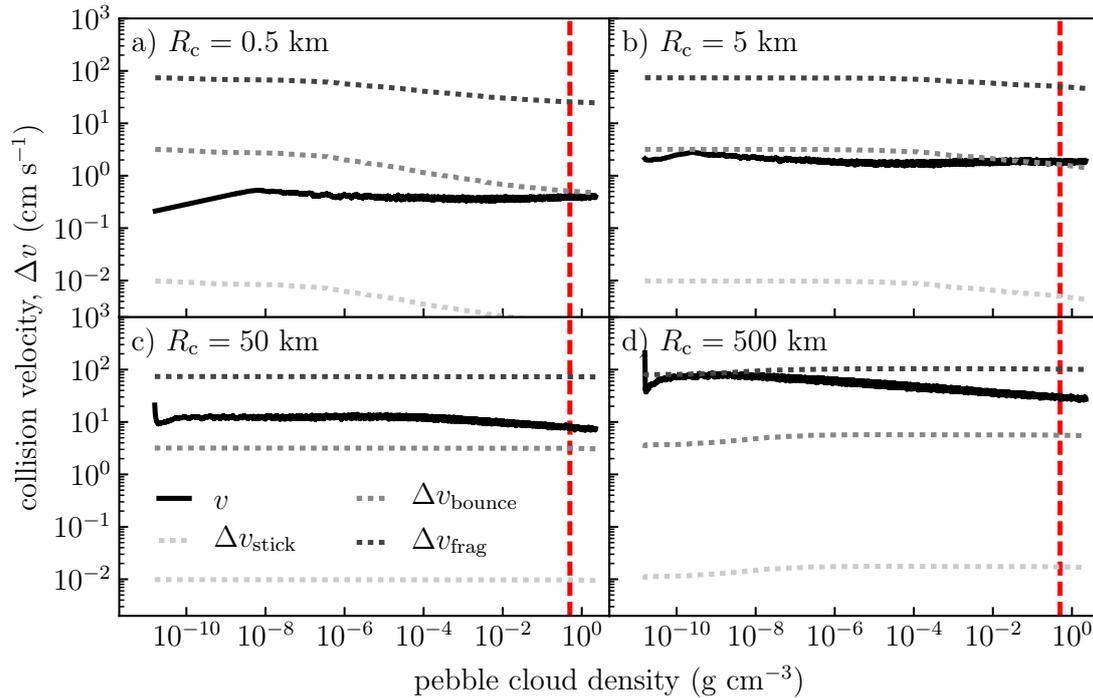


Figure 7.1: Collision velocity as function of pebble cloud density for aggregates with radius 0.45 mm, 0.1 μm monomers, initial volume-filling factor of 1.2×10^{-2} , and dust-to-ice ratio of 5 at 30 au. *a)* Very low-mass pebble cloud. *b)* Low-mass pebble cloud. *c)* Intermediate-mass pebble cloud. *d)* High-mass pebble cloud. Solid lines show the actual collision velocity of the aggregates during collapse. Dotted lines represent the sticking, bouncing, and fragmentation threshold velocities. The vertical dashed line indicates a pebble cloud density of 0.5 g cm⁻³ which equals the typical density of a comet.

The threshold velocities depend on the projectile mass and shift to higher velocities for lower mass. This affects the collisions of aggregates during the collapse. Figure 7.1 shows the collision velocities of aggregates during the collapse.

For the very low-mass pebble cloud, collision velocities are above the sticking threshold and below the bouncing threshold. For these velocities, aggregates stick with a certain sticking probability. In contrast to the centimetre-sized aggregates shown in Fig. 6.1, sticking collisions account for a significant fraction of up to 10% of all collisions between the millimetre-sized aggregates.

Collision velocities in the low-mass pebble cloud are closer to the bouncing threshold, but still lower.

The intermediate-mass pebble cloud for millimetre-sized aggregates behaves like the low-mass pebble cloud for centimetre-sized aggregates. Collision velocities are above the bouncing threshold, but below the fragmentation threshold, and only bouncing collisions occur.

In the high-mass pebble cloud, collision velocities are initially high enough for millimetre-sized aggregates to fragment significantly. However, collision velocities quickly drop below the fragmentation threshold and bouncing becomes dominant.

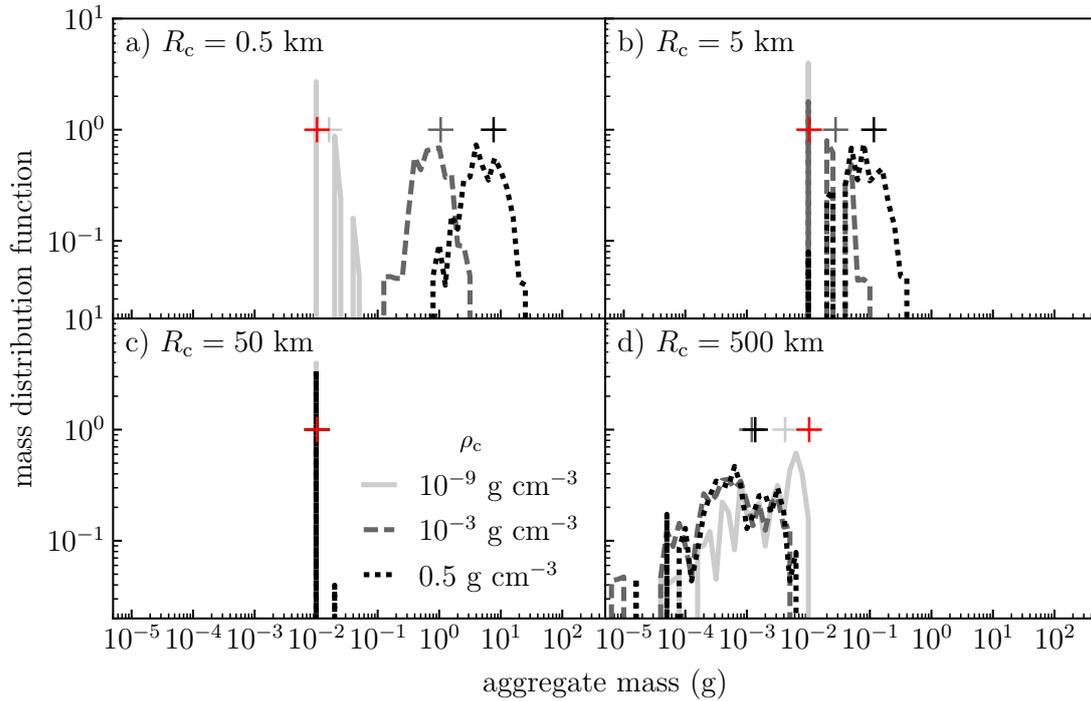


Figure 7.2: Mass distribution function of aggregates during pebble cloud collapse for aggregates with radius 0.45 mm, $0.1 \mu\text{m}$ monomers, initial volume-filling factor of 1.2×10^{-2} , and dust-to-ice ratio of 5 at 30 au. *a)* Very low-mass pebble cloud. *b)* Low-mass pebble cloud. *c)* Intermediate-mass pebble cloud. *d)* High-mass pebble cloud. Different lines correspond to different times in the collapse: very early when the density is $10^{-9} \text{ g cm}^{-3}$ (solid), towards the end when the cloud has collapsed to a density of $10^{-3} \text{ g cm}^{-3}$ (dashed), and at the end of the collapse at a density of 0.5 g cm^{-3} (dotted). The symbols (+) indicate the initial mass (red) and the mass-weighted average mass (grey). Lines overlap in panels *b)*, *c)*, and *d)* which shows that there is either little change (*b* and *c*) or a steady state is quickly established (*d*).

Figure 7.2 shows the mass distribution function for the millimetre-sized aggregates. Table 7.1 gives an overview of mass, size, and volume-filling factors obtained at planetesimal densities of 0.1 g cm^{-3} , 0.5 g cm^{-3} , and 1 g cm^{-3} .

The sticking collisions in the very low- and low-mass pebble clouds increases the peak mass from initially 10^{-2} g to $\sim 10^1 \text{ g}$ and 10^{-1} g , respectively. Because of this, the volume-filling factor of the aggregates increases at first before being compressed when the fraction of sticking collisions drops below 1.4% – 2.7%. The aggregate mass does not change in the intermediate mass pebble cloud, but the bouncing collisions compress the aggregates to volume-filling factors of $\sim 0.18 - 0.34$ depending on dust-to-ice ratio. In the high-mass pebble cloud, aggregates fragment. The peak mass decreases by roughly a factor of 10, which is lower than for centimetre-sized aggregates. Unless the fragments have masses $m \ll m_{\text{initial}}$, their volume-filling factor does not change significantly during fragmentation ($\phi \propto (m/m_{\text{initial}})^{-0.5 \dots 0} \lesssim 10$ for $2 \lesssim D_f \lesssim 3$ and $m \approx 10^{-2} m_{\text{initial}}$) and bouncing collisions compress the aggregates to volume-filling factors in the range 0.25 – 0.38 for dust-to-ice ratios of 1 – 10.

7.2 Implications from the comparison with observations of cometary pebbles

Table 7.1: Aggregate properties at different planetesimal densities at 30 au.

(a) Very low-mass pebble cloud.					(b) Low-mass pebble cloud.				
ρ_c (g cm ⁻³)	ξ	m (g)	a (cm)	ϕ	ρ_c (g cm ⁻³)	ξ	m (g)	a (cm)	ϕ
0.1	1	7.3×10^0	4.8×10^0	9.5×10^{-3}	0.1	1	1.1×10^{-1}	5.6×10^{-1}	8.4×10^{-2}
	5	5.1×10^0	3.6×10^0	1.0×10^{-2}		5	8.1×10^{-2}	4.0×10^{-1}	1.2×10^{-1}
	10	4.4×10^0	3.3×10^0	1.1×10^{-2}		10	6.0×10^{-2}	3.3×10^{-1}	1.4×10^{-1}
0.5	1	1.1×10^1	4.9×10^0	1.4×10^{-2}	0.5	1	1.7×10^{-1}	6.5×10^{-1}	9.2×10^{-2}
	5	7.7×10^0	3.7×10^0	1.5×10^{-2}		5	1.2×10^{-1}	4.3×10^{-1}	1.4×10^{-1}
	10	6.1×10^0	3.2×10^0	1.6×10^{-2}		10	8.8×10^{-2}	3.6×10^{-1}	1.6×10^{-1}
1.0	1	1.3×10^1	4.8×10^0	1.6×10^{-2}	1.0	1	2.1×10^{-1}	6.8×10^{-1}	9.6×10^{-2}
	5	8.6×10^0	3.6×10^0	1.8×10^{-2}		5	1.4×10^{-1}	4.5×10^{-1}	1.5×10^{-1}
	10	7.2×10^0	3.2×10^0	1.9×10^{-2}		10	1.0×10^{-1}	3.7×10^{-1}	1.7×10^{-1}

(c) Intermediate-mass pebble cloud.					(d) High-mass pebble cloud.				
ρ_c (g cm ⁻³)	ξ	m (g)	a (cm)	ϕ	ρ_c (g cm ⁻³)	ξ	m (g)	a (cm)	ϕ
0.1	1	2.4×10^{-2}	2.7×10^{-1}	1.8×10^{-1}	0.1	1	1.8×10^{-2}	2.1×10^{-1}	2.5×10^{-1}
	5	1.0×10^{-2}	1.5×10^{-1}	3.0×10^{-1}		5	1.3×10^{-3}	6.4×10^{-2}	3.5×10^{-1}
	10	8.4×10^{-3}	1.3×10^{-1}	3.4×10^{-1}		10	3.8×10^{-4}	4.1×10^{-2}	3.9×10^{-1}
0.5	1	2.4×10^{-2}	2.8×10^{-1}	1.8×10^{-1}	0.5	1	1.8×10^{-2}	2.1×10^{-1}	2.5×10^{-1}
	5	1.0×10^{-2}	1.5×10^{-1}	3.0×10^{-1}		5	1.4×10^{-3}	6.6×10^{-2}	3.5×10^{-1}
	10	8.7×10^{-3}	1.3×10^{-1}	3.4×10^{-1}		10	4.6×10^{-4}	4.5×10^{-2}	3.8×10^{-1}
1.0	1	2.4×10^{-2}	2.8×10^{-1}	1.8×10^{-1}	1.0	1	1.8×10^{-2}	2.1×10^{-1}	2.5×10^{-1}
	5	1.1×10^{-2}	1.6×10^{-1}	3.0×10^{-1}		5	1.4×10^{-3}	6.7×10^{-2}	3.5×10^{-1}
	10	9.2×10^{-3}	1.4×10^{-1}	3.4×10^{-1}		10	4.9×10^{-4}	4.6×10^{-2}	3.8×10^{-1}

Notes. Initial aggregate masses and volume-filling factors are 2.3×10^{-2} g and 1.0×10^{-2} for $\xi = 1$, 1.0×10^{-2} g and 1.2×10^{-2} for $\xi = 5$, and 8.2×10^{-3} g and 1.4^{-2} for $\xi = 10$. Monomer size is $0.1 \mu\text{m}$.

Figure 7.3 shows the packing fraction as a function of planetesimal density for pebble clouds at 30 au. Comet-like planetesimals cannot form in very low-mass pebble clouds. The high porosity and insignificant compression due to low collision velocities would require an aggregate packing $\phi_p \gg 1$. For this reason, planetesimal densities remain $\ll 0.1 \text{ g cm}^{-3}$ and the objects are highly porous. The bulk density of aggregates with $1 \lesssim \xi \lesssim 10$ is not high enough to increase the density to comet-like values.

For increasing pebble-cloud mass, however, the porous aggregates are more strongly compressed, which makes it possible for comet-like planetesimals to form. While for a low-mass pebble cloud this requires a dust-to-ice ratio $\gtrsim 1$, higher pebble-cloud masses form somewhat low density comet-like planetesimals. Objects with typical density of $\rho_{c,\text{typ}} = 0.5 \text{ g cm}^{-3}$ require aggregates with dust-to-ice ratios $5 \lesssim \xi \lesssim 10$ and pebble clouds with masses equivalent to $R_c \lesssim 50 \text{ km}$.

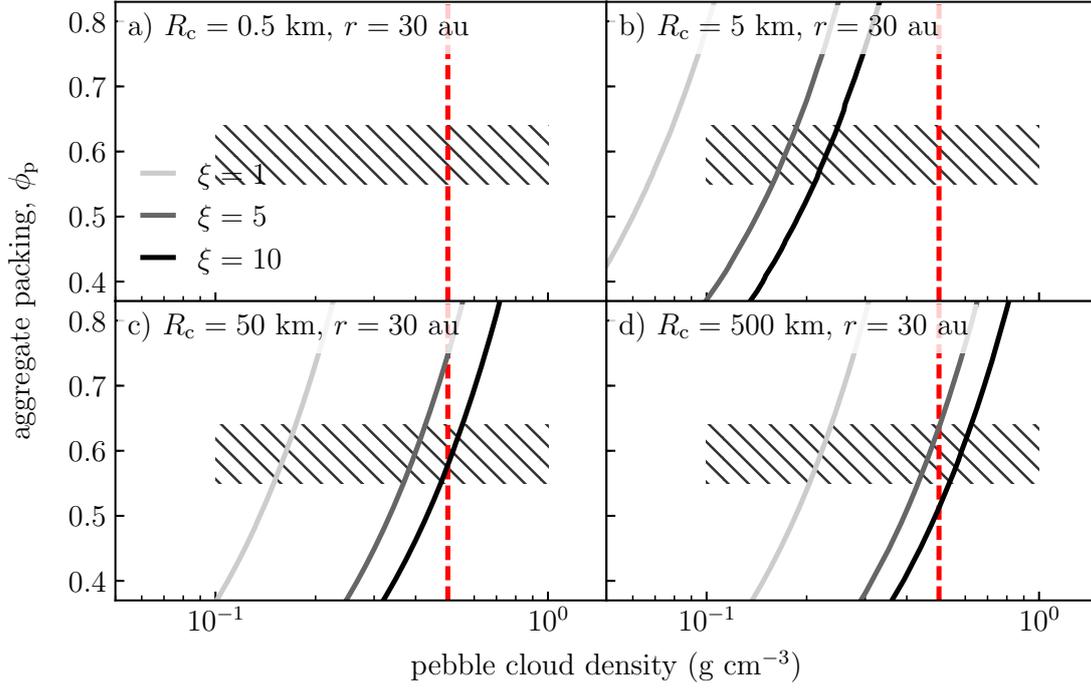


Figure 7.3: Aggregate packing as function of pebble cloud density for aggregates with radius 0.45 mm, $0.1 \mu\text{m}$ monomers, initial volume-filling factor of 1.2×10^{-2} , and dust-to-ice ratio of 5 at 30 au. *a)* Very low-mass pebble cloud. *b)* Low-mass pebble cloud. *c)* Intermediate-mass pebble cloud. *d)* High-mass pebble cloud. The hatched area indicates the region where the resulting planetesimal has comet-like properties: a density in the range $0.1 \text{ g cm}^{-3} \leq \rho_c \leq 1 \text{ g cm}^{-3}$ and an aggregate packing in the range $0.55 \leq \phi_p \leq 0.64$. The solid lines show $\phi_p(\rho_c)$ (see text for details) for different dust-to-ice ratios. The typical comet density of 0.5 g cm^{-3} is indicated with a vertical dashed line. The planetesimal is considered comet-like if the line crosses the hatched area.

Heliocentric distance 5 au

At a heliocentric of 5 au, simulations of aggregate growth produce aggregates with St_{\min} that are millimetre in size. The aggregates have $a = 0.55 \text{ cm}$ and $\phi = 0.17$ for a dust-to-ice ratio of $\xi = 1$, and $a = 0.36 \text{ cm}$ and $\phi = 0.18$ for $\xi = 5$. A higher dust-to-ice ratio was not able to produce aggregates with St_{\min} .

Because the typical collision velocity depends on heliocentric distance as $\Delta v \propto r^{-1/2}$ (see Eq. 6.8), collision types and aggregate evolution during collapse should be affected. Figure 7.4 shows the mass distribution function for millimetre-sized aggregates, initial volume-filling factor of $\sim 10^{-1}$, and dust-to-ice ratio of 5. The main difference to pebble cloud collapse at 30 au is that because of the higher collision velocities the fraction of sticking collisions is lower in the very low- and low-mass pebble clouds, but fragmentation is stronger in the high-mass pebble cloud. However, the properties of the fragmented aggregates are very similar to the values found at 30 au. Table 7.2 summarises the aggregate properties.

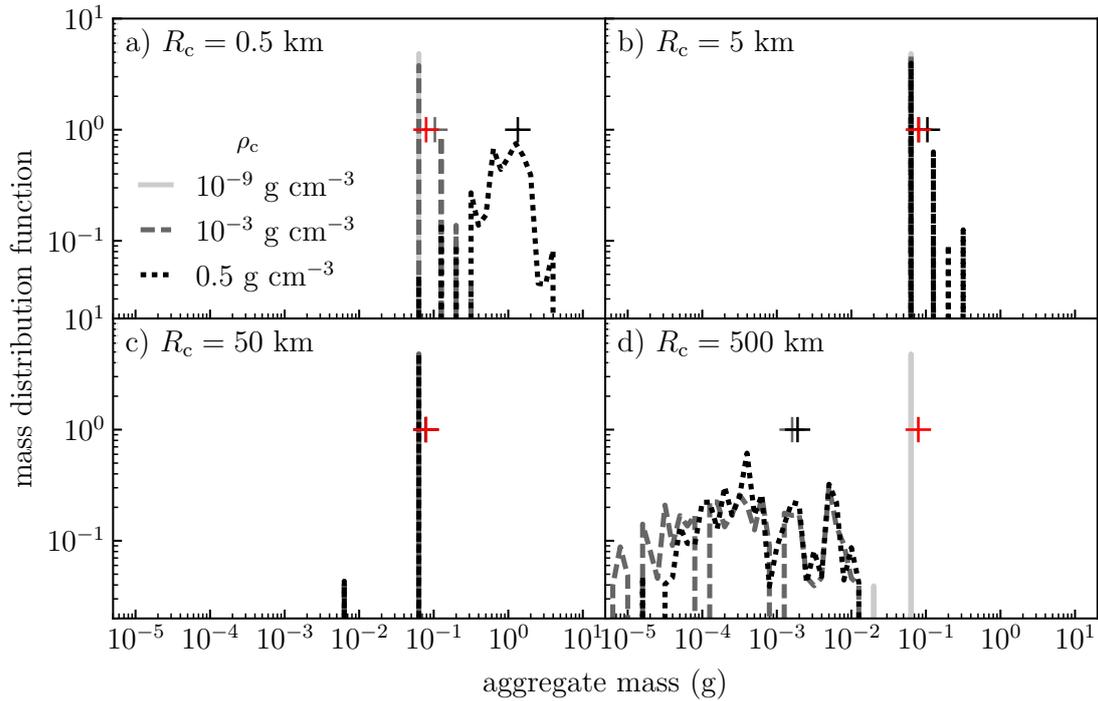


Figure 7.4: Mass distribution function of aggregates during pebble cloud collapse for aggregates with radius 0.36 mm , $0.1 \mu\text{m}$ monomers, initial volume-filling factor of 1.8×10^{-1} , and dust-to-ice ratio of 5 at 5 au. *a)* Very low-mass pebble cloud. *b)* Low-mass pebble cloud. *c)* Intermediate-mass pebble cloud. *d)* High-mass pebble cloud. Different lines correspond to different times in the collapse: very early when the density is $10^{-9} \text{ g cm}^{-3}$ (solid), towards the end when the cloud has collapsed to a density of $10^{-3} \text{ g cm}^{-3}$ (dashed), and at the end of the collapse at a density of 0.5 g cm^{-3} (dotted). The symbols (+) indicate the initial mass (red) and the mass-weighted average mass (grey). Lines overlap in all panels which shows that there is either little change (*b* and *c*) or a steady state is quickly established (*d*).

Figure 7.5 shows the packing fraction as a function of planetesimal density for the pebble clouds at 5 au. Comet-like planetesimals form for all pebble cloud masses. However, the densities are $\lesssim 0.3 \text{ g cm}^{-3}$ for the very low- and low-mass pebble clouds. Intermediate- and high-mass pebble clouds have densities $\sim 0.5 \text{ g cm}^{-3}$ only for dust-to-ice ratios $\gtrsim 5$, very similar to the case at 30 au.

Summary of the compression of millimetre-sized aggregates

The collapse of very-low and low-mass pebble clouds produces different aggregate properties at 5 au and 30 au. Because millimetre-sized pebbles undergo only bouncing collisions in the intermediate-mass pebble cloud and because fragmentation of aggregates produces fragments of similar mass, the collapse of these pebble clouds is similar at 5 au and 30 au. As it was the case already for the centimetre-sized aggregates, high-mass pebble clouds do not preserve the mass of aggregates. Additionally, sticking collisions in very low- and low-mass pebble clouds also change aggregate

Table 7.2: Aggregate properties at different planetesimal densities at 5 au.

(a) Very low-mass pebble cloud.					(b) Low-mass pebble cloud.				
ρ_c (g cm ⁻³)	ξ	m (g)	a (cm)	ϕ	ρ_c (g cm ⁻³)	ξ	m (g)	a (cm)	ϕ
0.1	1	9.8×10^{-1}	1.0×10^0	1.3×10^{-1}	0.1	1	1.9×10^{-1}	5.6×10^{-1}	1.7×10^{-1}
	5	5.9×10^{-1}	7.6×10^{-1}	1.3×10^{-1}		5	8.5×10^{-2}	3.6×10^{-1}	1.9×10^{-1}
0.5	1	1.7×10^0	1.3×10^0	1.1×10^{-1}	0.5	1	1.9×10^{-1}	5.6×10^{-1}	1.7×10^{-1}
	5	1.3×10^0	1.1×10^0	1.1×10^{-1}		5	1.0×10^{-1}	3.9×10^{-1}	1.8×10^{-1}
1.0	1	2.3×10^0	1.5×10^0	1.5×10^{-1}	1.0	1	2.0×10^{-1}	5.7×10^{-1}	1.7×10^{-1}
	5	2.0×10^0	1.2×10^0	1.0×10^{-1}		5	1.2×10^{-1}	4.1×10^{-1}	1.8×10^{-1}

(c) Intermediate-mass pebble cloud.					(d) High-mass pebble cloud.				
ρ_c (g cm ⁻³)	ξ	m (g)	a (cm)	ϕ	ρ_c (g cm ⁻³)	ξ	m (g)	a (cm)	ϕ
0.1	1	1.8×10^{-1}	5.3×10^{-1}	1.9×10^{-1}	0.1	1	1.4×10^{-2}	1.4×10^{-1}	2.5×10^{-1}
	5	7.8×10^{-2}	3.0×10^{-1}	3.1×10^{-1}		5	1.7×10^{-3}	6.2×10^{-2}	3.5×10^{-1}
0.5	1	1.8×10^{-1}	5.3×10^{-1}	1.9×10^{-1}	0.5	1	1.4×10^{-2}	1.5×10^{-1}	2.5×10^{-1}
	5	7.8×10^{-2}	3.0×10^{-1}	3.1×10^{-1}		5	1.9×10^{-3}	6.6×10^{-2}	3.5×10^{-1}
1.0	1	1.8×10^{-1}	5.3×10^{-1}	1.9×10^{-1}	1.0	1	1.5×10^{-2}	1.5×10^{-1}	2.5×10^{-1}
	5	7.8×10^{-2}	3.0×10^{-1}	3.1×10^{-1}		5	2.0×10^{-3}	6.8×10^{-2}	3.5×10^{-1}

Notes. Initial aggregate masses and volume-filling factors are 1.8×10^{-1} g and 1.7×10^{-1} for $\xi = 1$ and 7.9×10^{-2} g and 1.8×10^{-1} for $\xi = 5$. A dust-to-ice ratio of 10 failed to produce aggregates with St_{\min} . Monomer size is $0.1 \mu\text{m}$.

mass. Therefore, only intermediate-mass pebble clouds would preserve the mass of the aggregates.

7.2.2 Post-collapse aggregate sizes in the nominal case

In the simulations presented in Chapter 5, aggregates with St_{\min} have masses in the range 0.1 mg to 100 mg and volume-filling factors in the range 10^{-2} to 0.1.

The high porosity implies that for a planetesimal with density of $\rho_{c,\text{typ}} = 0.5 \text{ g cm}^{-3}$ to be formed, the aggregates need to be significantly compressed during the collapse requiring pebble cloud masses equivalent to planetesimal diameters ~ 100 km. However, the cloud mass should not be significantly higher, because that would lead to aggregate fragmentation during collapse (see also Wahlberg Jansson and Johansen 2014). The collapse simulations have shown that the maximum volume-filling factor of aggregates (ϕ_{\max}) for a 100 km planetesimal is in the range between 0.24 and 0.37 for dust-to-ice ratio between 1 and 10, respectively (see Table 6.2). Simulations with millimetre-sized aggregates confirm this picture.

Assuming that bouncing is the dominant compression type and fragmentation does not occur, the post-collapse aggregate radius is $a_{\text{pc}} = a \cdot (\phi / \phi_{\max})^{1/3}$. Applying this formula to the aggregates found in the simulations of aggregate growth allows direct comparison between the modelled aggregates and the pebbles observed on 67P. Because

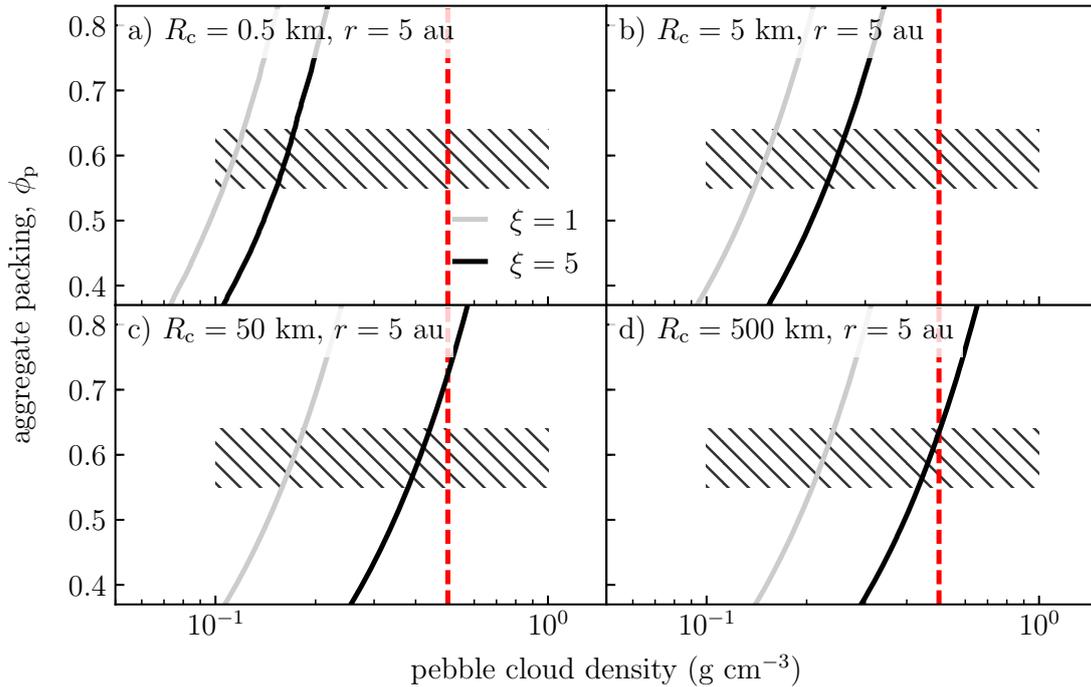


Figure 7.5: Aggregate packing as function of pebble cloud density for aggregates with radius 0.36 mm , $0.1 \mu\text{m}$ monomers, initial volume-filling factor of 1.8×10^{-1} , and dust-to-ice ratio of 5 at 5 au. a) Very low-mass pebble cloud. b) Low-mass pebble cloud. c) Intermediate-mass pebble cloud. d) High-mass pebble cloud. The hatched area indicates the region where the resulting planetesimal has comet-like properties: a density in the range $0.1 \text{ g cm}^{-3} \leq \rho_c \leq 1 \text{ g cm}^{-3}$ and an aggregate packing in the range $0.55 \leq \phi_p \leq 0.64$. The solid lines show $\phi_p(\rho_c)$ (see text for details) for different dust-to-ice ratios. The typical comet density of 0.5 g cm^{-3} is indicated with a vertical dashed line. The planetesimal is considered comet-like if the line crosses the hatched area.

the final volume-filling factor enters only as $\phi^{1/3}$, the lower volume-filling factors of the millimetre-sized aggregates do not change the result significantly.

Figure 7.6 show that the post-collapse aggregate sizes agree well with what is seen on 67P if comets form locally between 5 au and 15 au. At the nominal distance of 30 au and beyond, modelled aggregates are typically 1 mm, and hence slightly smaller than on 67P, unless the dust-to-ice ratio is unity. However, a dust-to-ice ratio of 1 does not agree with measurements which show dust-to-ice ratio $\gtrsim 1$. 67P has a measured dust-to-ice ratio of ~ 5 . Furthermore, the collapse simulations also require a higher dust-to-ice ratio in the range $3 \lesssim \xi \lesssim 10$.

7.2.3 Post-collapse aggregate sizes in the parameter study

Varying the parameters of the growth model affects the maximum mass of the aggregates in different ways as can be seen in Fig. 7.7

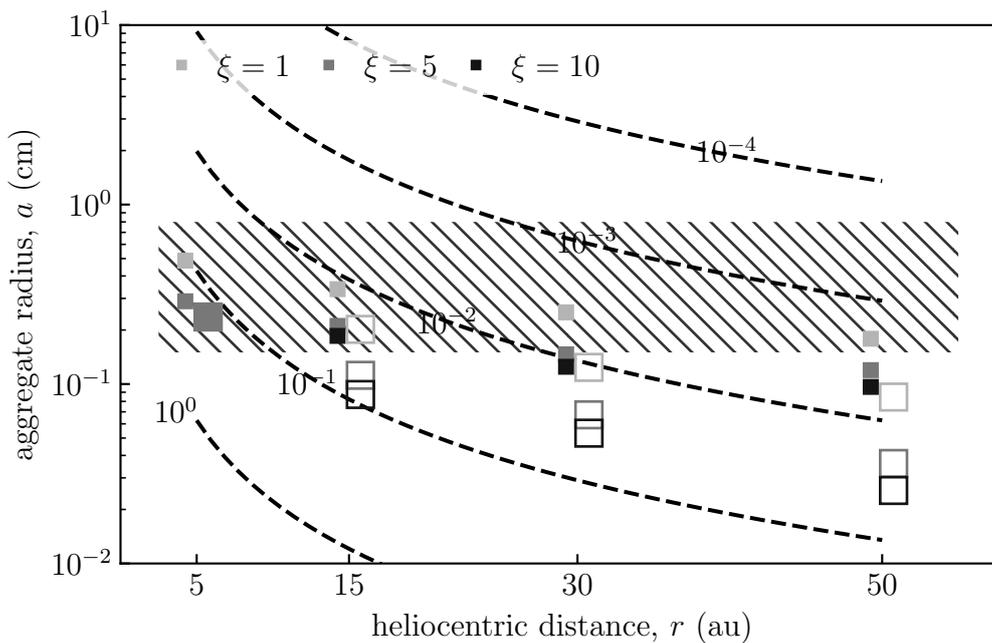


Figure 7.6: Post-collapse aggregate radius versus heliocentric distance. Symbols (■) show aggregate size at St_{\min} . Small and large symbols are for $0.1 \mu\text{m}$ and $1 \mu\text{m}$ sized monomers, respectively. Symbols are filled for aggregates potentially triggering streaming instability. Dashed lines indicate the minimum size for aggregates with given volume-filling factor to have St_{\min} (assuming Epstein drag); ϕ_0 refers to the initial volume-filling factor before compression. The hatched area marks the range of pebble sizes measured on 67P by the CIVA camera on board Rosetta/Philae (Poulet et al. 2016). (Credit: Lorek et al., *A&A*, 611, A18, 2018, reproduced with permission ©ESO)

Dispersal of the solar nebula gas

While disk dispersal becomes important at later stages of aggregate growth ($t > 10^3 P \approx 0.16 \text{ Myr}$) when the reduced gas density increases St thereby increasing collision velocities and promoting fragmentation, it is unimportant for growth up to St_{\min} . Post-collapse aggregate sizes are the same as in the nominal case ($\sim 1.5 \text{ mm}$).

Variation of the sticking properties

Compared to silicates, ice has better sticking properties. A higher surface energy and a higher rolling friction force allows ice aggregates to stick at velocities ~ 10 times higher than silicate aggregates would stick and renders them more resistant to fragmentation (Gundlach et al. 2011a; Gundlach and Blum 2015).

Increasing the stickiness of either component mimicking, for example, organic compounds which are believed to have better sticking properties than silicates, leads to the formation of aggregates slightly larger ($1.7 \text{ mm} - 2.0 \text{ mm}$) than in the nominal case (1.5 mm), but still of the order of 1 mm .

However, the sticking properties of organics are temperature dependent with sticking threshold velocities $> 2 \text{ m s}^{-1}$ in the asteroid belt region at $\sim 3 \text{ au}$; closer in and

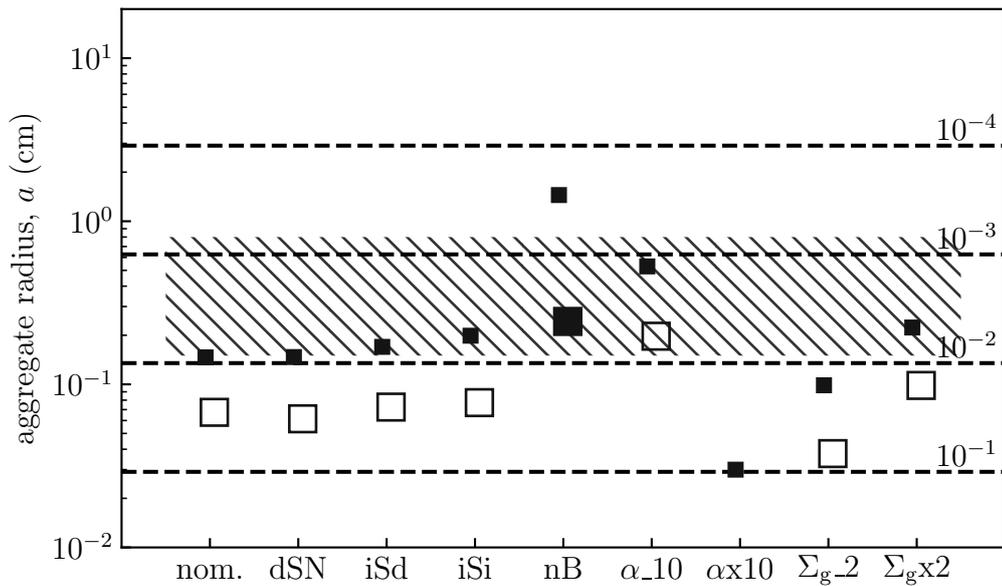


Figure 7.7: Post-collapse aggregate radius for parameter study at 30 au. Symbols (■) show aggregate size at St_{\min} . Small and large symbols are for $0.1 \mu\text{m}$ and $1 \mu\text{m}$ sized monomers, respectively. Symbols are filled for aggregates potentially triggering streaming instability. Dashed lines indicate the minimum size for aggregates with given volume-filling factor to have St_{\min} (assuming Epstein drag); ϕ_0 refers to the initial volume-filling factor before compression. The hatched area marks the range of pebble sizes measured on 67P by the CIVA camera on board Rosetta/Philae (Poulet et al. 2016). The abbreviations for the different models are in shown in Table 5.2. (Credit: Lorek et al., *A&A*, 611, A18, 2018, reproduced with permission ©ESO)

farther out, organics do not enhance sticking (Kudo et al. 2002). Accordingly, for aggregates growing in the cold part of the disk, organics should be of only minor importance for the growth process.

Variation of the gas surface density

Increasing the surface density of the gas while keeping the metallicity constant, increases the mass of the aggregates (and vice versa). However, with post-collapse aggregate sizes of $\sim 1 \text{ mm}$ and $\sim 2 \text{ mm}$ for lower and higher Σ_g , respectively, the changes are small compared to the nominal case.

The MMSN gas surface density $\Sigma_g = 1700 \text{ g cm}^{-2}$ is derived from the assumption that the planets accreted all solid material. From observations of protoplanetary disks around other stars, the derived gas masses are in the range $5 \times 10^{-4} M_\odot$ to $5 \times 10^{-2} M_\odot$ (Williams and Best 2014). Assuming the same extent of the disk as in the MMSN (0.35 au–36 au), surface densities at 1 au are in the range 65 g cm^{-2} – 6500 g cm^{-2} and the variation by a factor of 2 is well within these limits. Revision of the MMSN based on the more compact starting configuration and radial migration of the planets in the Nice model (Gomes et al. 2005; Morbidelli et al. 2005; Tsiganis et al. 2005) implies a

denser solar nebula by roughly a factor 4 (Desch 2007). Growth of aggregates in a nebula denser than MMSN is thus likely.

Variation of the turbulent strength

With strong turbulence ($\alpha = 10^{-2}$) collision velocities are high preventing aggregates from growing to sizes larger than ~ 0.3 mm, well outside the observed size range of pebbles on 67P (Poulet et al. 2016, bearing in mind the resolution limit of ~ 1 mm). On the other hand, a less turbulent environment ($\alpha = 10^{-4}$) promotes the growth of larger aggregates (~ 5 mm) because the lower collision velocities prevent fragmentation. The post-collapse sizes agree well with the observed size range.

However, this requires mechanisms to suppress turbulence. Dead zones in which MRI-driven turbulence is effectively suppressed due to insufficient ionisation of the disk gas are candidates for low-turbulence environments (Gammie 1996). The dead zone typically extends from 0.5 au to 30 au for nominal disk conditions (see Fig. 7 in Johansen et al. 2014). Thus, low turbulence might indeed be present if comets form in the dead zone well within 30 au. At the outer edge, however, hydrostatic equilibrium is prone to break into vortices through Rossby wave instability increasing turbulence again (Johansen et al. 2014).

Bouncing only for compact aggregates

The highest impact on aggregate growth is modifying the collision model to allow bouncing only for aggregates with volume-filling factors > 0.1 . Because aggregates remain highly porous ($\phi \approx 3 \times 10^{-4} - 3 \times 10^{-3}$) throughout the growth process, they never reach a bouncing regime. Furthermore, the high porosity significantly slows down radial drift. The maximum mass of the aggregate is limited by fragmentation and is 200 – 1300 times higher than in the nominal case. The post-collapse aggregate sizes are ~ 1.4 cm and ~ 0.2 mm for $0.1 \mu\text{m}$ and $1 \mu\text{m}$ sized monomers, respectively. While aggregates of $0.1 \mu\text{m}$ monomers are roughly twice as large as the largest pebbles on 67P, they fit well in the measured size range for larger monomers. Thus, aggregates would be expected to be bigger than cometary pebbles as inferred from Rosetta data (Poulet et al. 2016).

7.2.4 Preferred solar nebula conditions for comet formation

In summary, based on the properties of the aggregates that form in the solar nebula and the different growth behaviour (drift limited versus bouncing dominated), comet-like planetesimals should have formed at heliocentric distances $\lesssim 30$ au. The high porosity of the aggregates demands additional compression during gravitational collapse of the pebble clouds imposing that the pebble clouds should have masses equivalent to planetesimals of diameters $\gtrsim 100$ km. However, not significantly higher to avoid fragmentation of the aggregates during collapse. Comparison of post-collapse aggregate sizes with measured pebbles on 67P suggests that the aggregates formed in an environment with lower turbulence than nominal ($\alpha \lesssim 10^{-3}$) and higher gas surface density than MMSN ($\Sigma_g \gtrsim 1700 \text{ g cm}^{-2}$) from submicrometre-sized monomers.

Table 7.3: Pre- and post-collapse aggregate radii.

Simulation	ξ	0.1 μm monomers		1 μm monomers	
		pre-collapse a (cm)	post-collapse a_{pc} (cm)	pre-collapse a (cm)	post-collapse a_{pc} (cm)
nominal	1	7.2×10^{-1}	2.5×10^{-1}	2.6×10^{-1}	1.2×10^{-1}
	5	4.5×10^{-1}	1.5×10^{-1}	1.5×10^{-1}	6.7×10^{-2}
	10	3.8×10^{-1}	1.2×10^{-1}	1.1×10^{-1}	5.3×10^{-2}
5au	1	5.5×10^{-1}	4.9×10^{-1}
	5	3.6×10^{-1}	2.9×10^{-1}	2.7×10^{-1}	2.4×10^{-1}
	10
15au	1	7.1×10^{-1}	3.4×10^{-1}	3.3×10^{-1}	2.0×10^{-1}
	5	4.9×10^{-1}	2.1×10^{-1}	1.9×10^{-1}	1.1×10^{-1}
	10	4.4×10^{-1}	1.9×10^{-1}	1.5×10^{-1}	8.7×10^{-2}
50au	1	6.1×10^{-1}	1.8×10^{-1}	2.1×10^{-1}	8.5×10^{-2}
	5	4.2×10^{-1}	1.2×10^{-1}	9.2×10^{-1}	3.6×10^{-2}
	10	3.4×10^{-1}	9.6×10^{-2}	6.1×10^{-2}	2.6×10^{-2}
dSN	5	4.5×10^{-1}	1.5×10^{-1}	1.4×10^{-1}	6.1×10^{-2}
iSd	5	5.8×10^{-1}	1.7×10^{-1}	1.8×10^{-1}	7.3×10^{-2}
iSi	5	6.7×10^{-1}	2.0×10^{-1}	1.9×10^{-1}	7.7×10^{-2}
nB	5	1.4×10^1	1.4×10^0	1.0×10^0	2.4×10^{-1}
α_{10}	5	2.3×10^1	5.3×10^{-1}	6.9×10^{-1}	2.0×10^{-1}
α_{x10}	5	4.6×10^{-2}	3.0×10^{-2}
Σ_{g_2}	5	3.4×10^{-1}	9.9×10^{-2}	9.1×10^{-2}	3.8×10^{-2}
Σ_{g_x2}	5	6.2×10^{-1}	2.2×10^{-1}	1.9×10^{-1}	9.8×10^{-2}

Notes. The calculation of the post-collapse aggregate radii assumes maximum volume-filling factors of 0.24, 0.34, and 0.37 for dust-to-ice ratios 1, 5, and 10, respectively. These volume-filling factors correspond to the compressions obtained in intermediate-mass pebble clouds.

Table 7.3 summarises the pre- and post-collapse aggregate radii found in the simulations.

7.3 Formation of comets from comet-like planetesimals

Cometary nuclei have typical sizes in the range 1 km–10 km (Lamy et al. 2004; A’Hearn 2011; Kokotanekova et al. 2017). This is much smaller than the typical planetesimal sizes (~ 100 km) found in numerical studies of the initial mass function of planetesimals formed through streaming instability (Schäfer et al. 2017). It is also smaller than the sizes required by the model presented here for the planetesimals to have comet-like density when the building blocks are porous. Furthermore, many cometary nuclei visited by spacecraft show a bilobed structure (see Fig. 1.2).

The formation of large planetesimals through streaming instability poses the question of how do comets form. Comets as fragments of collisions between large planetesimals (Morbidelli and Rickman 2015; Rickman et al. 2015) are ruled out because the fractal aggregates found by GIADA and MIDAS in cometary dust of 67P would not survive the high impact pressures producing stresses higher than the tensile strengths of fractal aggregates (Fulle et al. 2015, 2016b,a; Mannel et al. 2016; Fulle and Blum 2017).

7.3.1 Formation of substructure by clustering of aggregates

The possibility remains that the pebble cloud itself fragments into a size distribution of objects during collapse, in which case comets would correspond to the small bodies in the distribution. This mechanism would not only be able to explain the formation of binaries as frequently observed in the Kuiper belt (Nesvorný et al. 2010; Fraser et al. 2017), but also the formation of bilobed structures of cometary nuclei from contact binaries.

It is worthwhile to speculate on how fragmentation of pebble clouds could actually be achieved:

Because of the high mass loading and the high frequency of bouncing collisions, a pebble cloud shows similarities to a granular gas. A granular gas is a system of macroscopic particles whose evolution is driven by inelastic collisions, in contrast to an ideal gas whose evolution is driven by elastic collisions. The dissipative nature of the inelastic collision gives rise to clustering of particles, which is known as the clustering instability in dissipative gases (Goldhirsch and Zanetti 1993).

In regions of the granular gas where the density is higher due to fluctuations of the system, the collision rates are also higher. More energy is dissipated which decreases the pressure in this region. Pressure can be understood in terms of the random motion of the particles. Particles move from the low density region to the high density region due to the pressure gradient which enhances the clustering even more (Goldhirsch and Zanetti 1993).

Similar processes resulting in clustering and the formation of substructure could take place in pebble clouds. While Goldhirsch and Zanetti (1993) studied a granular gas not subject to external forces, gravity has to be taken into account for pebble clouds. It is hence desirable to study granular gases under the effect of gravity to better understand the internal dynamics of the gravitational collapse of pebble clouds.

7.3.2 Rotation of pebble clouds

The model for the gravitational collapse of a pebble cloud (Wahlberg Jansson and Johansen 2014) does not include rotation.

Johansen and Lacerda (2010) showed that the accretion of millimetre- to metre-sized aggregates onto protoplanets embedded in the solar nebula increased the rotation velocity of the protoplanet close to the rotational breakup velocity. At the breakup velocity, gravity balances the centrifugal acceleration of a test particle located at the equator of the rotating body. The breakup velocity of a body of mass M and radius R is hence $\Omega_{\text{bu}} = \sqrt{GM/R^3}$. For $\Omega > \Omega_{\text{bu}}$, the centrifugal force would disrupt the body.

Angular momentum should be conserved for a pebble cloud in a similar fashion when aggregates fall into the potential well of the already accumulated aggregates. Furthermore, the differential rotation of the disk should introduce mild rotation because the angular velocity difference between the cloud centre at heliocentric distance r and the outskirts at $r \pm R_H$ is $\Delta\Omega = |(3/2)\Omega_K R_H/r| \approx 5 \times 10^{-5}\Omega_K$ for a pebble cloud of mass 2.6×10^{20} g at 30 au.

Nesvorný et al. (2010) studied the gravitational collapse of pebble clouds using N-body simulations and a simple collision model in which bodies merged when they collided. They included rotation and found that this resulted in the formation of binaries. In approximately 80% of the binaries that formed in their simulations, the two bodies had similar sizes which means that the ratio of their radii was > 0.7 . Faster initial cloud rotation resulted in smaller objects because most of the material was dispersed due to excess angular momentum.

Interesting for comet formation is the growth history of the bodies shown by Nesvorný et al. (2010). Bodies grow by accretion to sizes of ~ 20 km. When reaching this size, the largest bodies grow faster than the smaller ones because gravitational focusing increases their collisional cross section. However, according to Fig. 6 of Nesvorný et al. (2010), there is still a large number of objects with radii $\lesssim 20$ km left. Those bodies are not part of binary system but must be ejected from the cloud, forming comets.

The results of Nesvorný et al. (2010) are encouraging because they show that angular momentum could indeed produce km-sized comets from high-mass pebble clouds that would otherwise collapse into a single $\gtrsim 100$ km planetesimal.

7.3.3 Presence of fractal aggregates

The presence of fractal aggregates in cometary dust is puzzling (Fulle et al. 2015; Mannel et al. 2016).

Firstly, from the hierarchical growth process in the solar nebula, it is not expected that these aggregates survive because they should have collided with other aggregates leading to compression and destruction of the fractal structure.

Secondly, streaming instability filters a specific aggregate size, namely those with St_{\min} . Fractal aggregates are tightly coupled to the gas and should not be collected.

However, the gas dynamics during the gravitational collapse of a pebble cloud is poorly understood. Although the mass loading is very high ($\rho_d/\rho_g \gtrsim 10^2$), the gas might still play a role. Fractal aggregates suspended in the gas could thereby enter the planetesimal filling the voids between the randomly packed intact aggregates (Fulle and Blum 2017).

8 Conclusion

In this thesis, the origin of comets in the framework of planetesimal formation through streaming instability was investigated. The growth of aggregates of mixed composition (ice and silicate dust) was modelled to find the specific properties of the aggregates that participate in the streaming instability. With a model for the gravitational collapse of a pebble cloud based on energy dissipation due to aggregate collisions, the compression of aggregates during collapse was studied to constrain their composition and initial porosity, and the pebble-cloud mass that lead to comet-like planetesimals. The main conclusions of this work are:

- Aggregate growth is sensitive to the monomer size when porosity is taken into account in the collision model. With $0.1 \mu\text{m}$ sized monomers, aggregates are highly porous ($\phi \sim 10^{-4}$) which slows down radial drift towards the Sun and accelerates growth such that aggregates reach a bouncing-dominated state before they drift significant distances in the disk. On the other hand, with $1 \mu\text{m}$ sized monomers, aggregates are more compact ($\phi \sim 10^{-3} - 10^{-2}$) and the maximum mass that aggregates can locally grow to is limited by radial drift.
- A disk-metallicity dependent minimum value of the Stokes number (St_{min}) necessary for streaming instability can be reached in a bouncing-dominated population of porous aggregates due to compression in bouncing collisions. At St_{min} , aggregates are porous with volume-filling factors $\phi \lesssim 0.1$ and masses $m \lesssim 0.1 \text{ g}$; aggregate radii are in the range millimetres to centimetres.
- Formation of planetesimals with comet-like density ($0.1 \text{ g cm}^{-3} \lesssim \rho_c \lesssim 1 \text{ g cm}^{-3}$) depends on the mass of the pebble cloud, the initial porosity of the aggregates collected by the streaming instability, and the composition in terms of the dust-to-ice ratio of the aggregates. Comet-like planetesimal would only form for certain combinations of these variables:
 - if the pebbles are initially compact ($\phi \gtrsim 0.4$), regardless of the pebble-cloud mass.
 - if the pebbles are initially porous ($\phi \lesssim 0.4$), only in pebble clouds with a mass $\gtrsim 2.6 \times 10^{20} \text{ g}$ (equivalent to planetesimals of diameters $\gtrsim 100 \text{ km}$).

In any case, formation of comet-like planetesimals with density $\rho_{\text{c,typ}} \approx 0.5 \text{ g cm}^{-3}$ requires a dust-to-ice ratio $3 \lesssim \xi \lesssim 10$. This means that at least 75% of the mass must be in silicate dust to ensure aggregates are soft enough for significant compression to occur during collapse, or to compensate for the lack of compression due to the increased bulk density of the material.

- The highly porous aggregates with St_{\min} require significant compression during collapse and thus pebble-cloud masses equivalent to planetesimals of diameters $\gtrsim 100$ km. However, aggregates fragment for significantly higher masses (that is for planetesimal diameters of ~ 1000 km) and collapse into large planetesimals is very unlikely to preserve comet-like properties due to self-gravity.
- Taking the compression during gravitational collapse into account, the aggregates that would constitute the building blocks of comets would have radii in the range ~ 1 mm – 4 mm comparable to the radii of pebbles found on 67P which are in the range 1.5 mm – 8 mm.

The findings of the numerical study of aggregate growth and pebble-cloud collapse agree well with cometary properties which renders streaming instability as a viable mechanism for comet formation. The preferred pebble cloud mass corresponds to planetesimals of diameters ~ 100 km, much larger than typical comet nuclei. The process by which these massive clouds produce kilometre-sized comets needs more investigation. Catastrophic collisions between large planetesimals can be ruled out based on the survival of fractal aggregates from the growth phase in the solar nebula in cometary dust (Fulle and Blum 2017). A possible alternative scenario is the fragmentation of the pebble cloud during collapse into a size distribution of objects, in which case comets would be identified as the small bodies in this distribution. Additionally, fragmentation of the pebble cloud could lead to the formation of binaries explaining the large binary fraction in the Kuiper belt as well as the bilobed structure of many cometary nuclei as the result of gentle low-velocity collisions or contact binaries.

Bibliography

- I. Adachi, C. Hayashi, and K. Nakazawa. The gas drag effect on the elliptical motion of a solid body in the primordial solar nebula. *Progress of Theoretical Physics*, 56: 1756–1771, December 1976. doi: 10.1143/PTP56.1756.
- M. F. A'Hearn. Comets as Building Blocks. *ARA&A*, 49:281–299, September 2011. doi: 10.1146/annurev-astro-081710-102506.
- M. F. A'Hearn, M. J. S. Belton, W. A. Delamere, L. M. Feaga, D. Hampton, J. Kissel, K. P. Klaasen, L. A. McFadden, K. J. Meech, H. J. Melosh, P. H. Schultz, J. M. Sunshine, P. C. Thomas, J. Veverka, D. D. Wellnitz, D. K. Yeomans, S. Besse, D. Bodewits, T. J. Bowling, B. T. Carcich, S. M. Collins, T. L. Farnham, O. Groussin, B. Hermalyn, M. S. Kelley, M. S. Kelley, J.-Y. Li, D. J. Lindler, C. M. Lisse, S. A. McLaughlin, F. Merlin, S. Protopapa, J. E. Richardson, and J. L. Williams. EPOXI at Comet Hartley 2. *Science*, 332:1396, June 2011. doi: 10.1126/science.1204054.
- R. Alexander, I. Pascucci, S. Andrews, P. Armitage, and L. Cieza. The Dispersal of Protoplanetary Disks. *Protostars and Planets VI*, pages 475–496, 2014. doi: 10.2458/azu_uapress_9780816531240-ch021.
- K. Altwegg, H. Balsiger, A. Bar-Nun, J. J. Berthelier, A. Bieler, P. Bochslers, C. Briois, U. Calmonte, M. Combi, J. De Keyser, P. Eberhardt, B. Fiethe, S. Fuselier, S. Gasc, T. I. Gombosi, K. C. Hansen, M. Hässig, A. Jäckel, E. Kopp, A. Korth, L. LeRoy, U. Mall, B. Marty, O. Mousis, E. Neefs, T. Owen, H. Rème, M. Rubin, T. Sémon, C.-Y. Tzou, H. Waite, and P. Wurz. 67P/Churyumov-Gerasimenko, a Jupiter family comet with a high D/H ratio. *Science*, 347(27):1261952, January 2015. doi: 10.1126/science.1261952.
- P. J. Armitage. *Astrophysics of Planet Formation*. 2010.
- P. J. Armitage. Physical processes in protoplanetary disks. *ArXiv e-prints*, September 2015.
- G. Aumatell and G. Wurm. Ice aggregate contacts at the nm-scale. *MNRAS*, 437: 690–702, January 2014. doi: 10.1093/mnras/stt1921.
- S. A. Balbus and J. F. Hawley. A powerful local shear instability in weakly magnetized disks. I - Linear analysis. II - Nonlinear evolution. *ApJ*, 376:214–233, July 1991. doi: 10.1086/170270.

- A. Bar-Nun, G. Notesco, and T. Owen. Trapping of N₂, CO and Ar in amorphous ice—Application to comets. *Icarus*, 190:655–659, October 2007. doi: 10.1016/j.icarus.2007.03.021.
- E. Beitz, C. Güttler, J. Blum, T. Meisner, J. Teiser, and G. Wurm. Low-velocity Collisions of Centimeter-sized Dust Aggregates. *ApJ*, 736:34, July 2011. doi: 10.1088/0004-637X/736/1/34.
- M. S. Bentley, R. Schmied, T. Mannel, K. Torkar, H. Jeszenszky, J. Romstedt, A.-C. Levasseur-Regourd, I. Weber, E. K. Jessberger, P. Ehrenfreund, C. Koeberl, and O. Havnes. Aggregate dust particles at comet 67P/Churyumov-Gerasimenko. *Nature*, 537:73–75, September 2016. doi: 10.1038/nature19091.
- L. Biermann. Kometenschweife und solare Korpuskularstrahlung. *ZAp*, 29:274, 1951.
- T. Birnstiel, C. P. Dullemond, and F. Brauer. Gas- and dust evolution in protoplanetary disks. *A&A*, 513:A79, April 2010. doi: 10.1051/0004-6361/200913731.
- J. Blum. Dust agglomeration. *Advances in Physics*, 55:881–947, December 2006. doi: 10.1080/00018730601095039.
- J. Blum and M. Münch. Experimental investigations on aggregate-aggregate collisions in the early solar nebula. *Icarus*, 106:151, November 1993. doi: 10.1006/icar.1993.1163.
- J. Blum and R. Schräpler. Structure and Mechanical Properties of High-Porosity Macroscopic Agglomerates Formed by Random Ballistic Deposition. *Physical Review Letters*, 93(11):115503, September 2004. doi: 10.1103/PhysRevLett.93.115503.
- J. Blum and G. Wurm. Experiments on Sticking, Restructuring, and Fragmentation of Preplanetary Dust Aggregates. *Icarus*, 143:138–146, January 2000. doi: 10.1006/icar.1999.6234.
- J. Blum and G. Wurm. The Growth Mechanisms of Macroscopic Bodies in Protoplanetary Disks. *ARA&A*, 46:21–56, September 2008. doi: 10.1146/annurev.astro.46.060407.145152.
- J. Blum, R. Schräpler, B. J. R. Davidsson, and J. M. Trigo-Rodríguez. The Physics of Protoplanetary Dust Agglomerates. I. Mechanical Properties and Relations to Primitive Bodies in the Solar System. *ApJ*, 652:1768–1781, December 2006. doi: 10.1086/508017.
- J. Blum, B. Gundlach, S. Mühle, and J. M. Trigo-Rodríguez. Comets formed in solar-nebula instabilities! - An experimental and modeling attempt to relate the activity of comets to their formation process. *Icarus*, 235:156–169, June 2014. doi: 10.1016/j.icarus.2014.03.016.
- D. Bockelée-Morvan, D. Gautier, F. Hersant, J.-M. Huré, and F. Robert. Turbulent radial mixing in the solar nebula as the source of crystalline silicates in comets. *A&A*, 384:1107–1118, March 2002. doi: 10.1051/0004-6361:20020086.

- H. Boehnhardt. *Split comets*, pages 301–316. 2004.
- J. Bradley. The Astromineralogy of Interplanetary Dust Particles. In T. K. Henning, editor, *Astromineralogy*, volume 609 of *Lecture Notes in Physics*, Berlin Springer Verlag, pages 217–235, 2003.
- F. Brauer, C. P. Dullemond, and T. Henning. Coagulation, fragmentation and radial motion of solid particles in protoplanetary disks. *A&A*, 480:859–877, March 2008. doi: 10.1051/0004-6361:20077759.
- F. Capaccioni, A. Coradini, G. Filacchione, S. Erard, G. Arnold, P. Drossart, M. C. De Sanctis, D. Bockelee-Morvan, M. T. Capria, F. Tosi, C. Leyrat, B. Schmitt, E. Quirico, P. Cerroni, V. Mennella, A. Raponi, M. Ciarniello, T. McCord, L. Moroz, E. Palomba, E. Ammannito, M. A. Barucci, G. Bellucci, J. Benkhoff, J. P. Bibring, A. Blanco, M. Blecka, R. Carlson, U. Carsenty, L. Colangeli, M. Combes, M. Combi, J. Crovisier, T. Encrenaz, C. Federico, U. Fink, S. Fonti, W. H. Ip, P. Irwin, R. Jaumann, E. Kuehrt, Y. Langevin, G. Magni, S. Mottola, V. Orofino, P. Palumbo, G. Piccioni, U. Schade, F. Taylor, D. Tiphene, G. P. Tozzi, P. Beck, N. Biver, L. Bonal, J.-P. Combe, D. Despan, E. Flamini, S. Fornasier, A. Frigeri, D. Grassi, M. Gudipati, A. Longobardo, K. Markus, F. Merlin, R. Orosei, G. Rinaldi, K. Stephan, M. Cartacci, A. Cicchetti, S. Giuppi, Y. Hello, F. Henry, S. Jacquino, R. Noschese, G. Peter, R. Politi, J. M. Reess, and A. Semery. The organic-rich surface of comet 67P/Churyumov-Gerasimenko as seen by VIRTIS/Rosetta. *Science*, 347(1):aaa0628, January 2015. doi: 10.1126/science.aaa0628.
- A. Carballido, S. Fromang, and J. Papaloizou. Mid-plane sedimentation of large solid bodies in turbulent protoplanetary discs. *MNRAS*, 373:1633–1640, December 2006. doi: 10.1111/j.1365-2966.2006.11118.x.
- D. Carrera, A. Johansen, and M. B. Davies. How to form planetesimals from mm-sized chondrules and chondrule aggregates. *A&A*, 579:A43, July 2015. doi: 10.1051/0004-6361/201425120.
- E. I. Chiang and P. Goldreich. Spectral Energy Distributions of T Tauri Stars with Passive Circumstellar Disks. *ApJ*, 490:368–376, November 1997. doi: 10.1086/304869.
- J. N. Cuzzi and R. C. Hogan. Blowing in the wind. I. Velocities of chondrule-sized particles in a turbulent protoplanetary nebula. *Icarus*, 164:127–138, July 2003. doi: 10.1016/S0019-1035(03)00104-0.
- J. N. Cuzzi and S. J. Weidenschilling. *Particle-Gas Dynamics and Primary Accretion*, pages 353–381. 2006.
- J. N. Cuzzi, F. J. Ciesla, M. I. Petaev, A. N. Krot, E. R. D. Scott, and S. J. Weidenschilling. Nebula Evolution of Thermally Processed Solids: Reconciling Models and Meteorites. In A. N. Krot, E. R. D. Scott, and B. Reipurth, editors, *Chondrites and the Protoplanetary Disk*, volume 341 of *Astronomical Society of the Pacific Conference Series*, page 732, December 2005.

- B. J. R. Davidsson, H. Sierks, C. Güttler, F. Marzari, M. Pajola, H. Rickman, M. F. A'Hearn, A.-T. Auger, M. R. El-Maarry, S. Fornasier, P. J. Gutiérrez, H. U. Keller, M. Massironi, C. Snodgrass, J.-B. Vincent, C. Barbieri, P. L. Lamy, R. Rodrigo, D. Koschny, M. A. Barucci, J.-L. Bertaux, I. Bertini, G. Cremonese, V. Da Deppo, S. Debei, M. De Cecco, C. Feller, M. Fulle, O. Groussin, S. F. Hviid, S. Höfner, W.-H. Ip, L. Jorda, J. Knollenberg, G. Kovacs, J.-R. Kramm, E. Kührt, M. Küppers, F. La Forgia, L. M. Lara, M. Lazzarin, J. J. Lopez Moreno, R. Moissl-Fraund, S. Mottola, G. Naletto, N. Oklay, N. Thomas, and C. Tubiana. The primordial nucleus of comet 67P/Churyumov-Gerasimenko. *A&A*, 592:A63, July 2016. doi: 10.1051/0004-6361/201526968.
- S. J. Desch. Mass Distribution and Planet Formation in the Solar Nebula. *ApJ*, 671: 878–893, December 2007. doi: 10.1086/522825.
- C. Dominik and A. G. G. M. Tielens. Resistance to rolling in the adhesive contact of two elastic spheres. *Philosophical Magazine, Part A*, 72:783–803, September 1995. doi: 10.1080/01418619508243800.
- C. Dominik and A. G. G. M. Tielens. The Physics of Dust Coagulation and the Structure of Dust Aggregates in Space. *ApJ*, 480:647–673, May 1997.
- B. T. Draine. Interstellar Dust Grains. *ARA&A*, 41:241–289, 2003. doi: 10.1146/annurev.astro.41.011802.094840.
- J. Drażkowska and C. P. Dullemond. Can dust coagulation trigger streaming instability? *A&A*, 572:A78, December 2014. doi: 10.1051/0004-6361/201424809.
- J. Drażkowska, F. Windmark, and C. P. Dullemond. Planetesimal formation via sweep-up growth at the inner edge of dead zones. *A&A*, 556:A37, August 2013. doi: 10.1051/0004-6361/201321566.
- J. Drażkowska, F. Windmark, and C. P. Dullemond. Modeling dust growth in protoplanetary disks: The breakthrough case. *A&A*, 567:A38, July 2014. doi: 10.1051/0004-6361/201423708.
- B. Dubrulle, G. Morfill, and M. Sterzik. The dust subdisk in the protoplanetary nebula. *Icarus*, 114:237–246, April 1995. doi: 10.1006/icar.1995.1058.
- C. P. Dullemond and C. Dominik. The effect of dust settling on the appearance of protoplanetary disks. *A&A*, 421:1075–1086, July 2004. doi: 10.1051/0004-6361:20040284.
- C. P. Dullemond and C. Dominik. Dust coagulation in protoplanetary disks: A rapid depletion of small grains. *A&A*, 434:971–986, May 2005. doi: 10.1051/0004-6361:20042080.
- A. Dutrey, D. Semenov, E. Chapillon, U. Gorti, S. Guilloteau, F. Hersant, M. Hogerheijde, M. Hughes, G. Meeus, H. Nomura, V. Piétu, C. Qi, and V. Wakelam. Physical and Chemical Structure of Planet-Forming Disks Probed by Millimeter Observations and Modeling. *Protostars and Planets VI*, pages 317–338, 2014. doi: 10.2458/azu_uapress_9780816531240-ch014.

- K. E. Edgeworth. The origin and evolution of the Solar System. *MNRAS*, 109:600–609, 1949. doi: 10.1093/mnras/109.5.600.
- P. S. Epstein. On the Resistance Experienced by Spheres in their Motion through Gases. *Physical Review*, 23:710–733, June 1924. doi: 10.1103/PhysRev.23.710.
- P. R. Estrada, J. N. Cuzzi, and D. A. Morgan. Global Modeling of Nebulae with Particle Growth, Drift, and Evaporation Fronts. I. Methodology and Typical Results. *ApJ*, 818: 200, February 2016. doi: 10.3847/0004-637X/818/2/200.
- D. Fedele, M. E. van den Ancker, T. Henning, R. Jayawardhana, and J. M. Oliveira. Timescale of mass accretion in pre-main-sequence stars. *A&A*, 510:A72, February 2010. doi: 10.1051/0004-6361/200912810.
- J. A. Fernandez and K. Jockers. REVIEW ARTICLE: Nature and origin of comets. *Reports on Progress in Physics*, 46:665–772, June 1983. doi: 10.1088/0034-4885/46/6/001.
- M. C. Festou, H. U. Keller, and H. A. Weaver. *A brief conceptual history of cometary science*, pages 3–16. 2004.
- M. J. Finson and R. F. Probst. A theory of dust comets. I. Model and equations. *ApJ*, 154:327–352, October 1968. doi: 10.1086/149761.
- W. C. Fraser, M. T. Bannister, R. E. Pike, M. Marsset, M. E. Schwamb, J. J. Kavelaars, P. Lacerda, D. Nesvorný, K. Volk, A. Delsanti, S. Benecchi, M. J. Lehner, K. Noll, B. Gladman, J.-M. Petit, S. Gwyn, Y.-T. Chen, S.-Y. Wang, M. Alexandersen, T. Burdullis, S. Sheppard, and C. Trujillo. All planetesimals born near the Kuiper belt formed as binaries. *Nature Astronomy*, 1:0088, April 2017. doi: 10.1038/s41550-017-0088.
- M. Fulle. *Motion of cometary dust*, pages 565–575. 2004.
- M. Fulle. The ice content of Kuiper belt objects. *Nature Astronomy*, 1:0018, January 2017. doi: 10.1038/s41550-016-0018.
- M. Fulle and J. Blum. Fractal dust constrains the collisional history of comets. *MNRAS*, 469:S39–S44, July 2017. doi: 10.1093/mnras/stx971.
- M. Fulle, V. Della Corte, A. Rotundi, P. Weissman, A. Juhasz, K. Szego, R. Sordini, M. Ferrari, S. Ivanovski, F. Lucarelli, M. Accolla, S. Merouane, V. Zakharov, E. Mazzotta Epifani, J. J. López-Moreno, J. Rodríguez, L. Colangeli, P. Palumbo, E. Grün, M. Hilchenbach, E. Bussoletti, F. Esposito, S. F. Green, P. L. Lamy, J. A. M. McDonnell, V. Mennella, A. Molina, R. Morales, F. Moreno, J. L. Ortiz, E. Palomba, R. Rodrigo, J. C. Zarnecki, M. Cusi, F. Giovane, B. Gustafson, M. L. Herranz, J. M. Jerónimo, M. R. Leese, A. C. López-Jiménez, and N. Altobelli. Density and Charge of Pristine Fluffy Particles from Comet 67P/Churyumov-Gerasimenko. *ApJ*, 802:L12, March 2015. doi: 10.1088/2041-8205/802/1/L12.
- M. Fulle, V. Della Corte, A. Rotundi, F. J. M. Rietmeijer, S. F. Green, P. Weissman, M. Accolla, L. Colangeli, M. Ferrari, S. Ivanovski, J. J. Lopez-Moreno, E. M. Epifani, R. Morales, J. L. Ortiz, E. Palomba, P. Palumbo, J. Rodriguez, R. Sordini,

- and V. Zakharov. Comet 67P/Churyumov-Gerasimenko preserved the pebbles that formed planetesimals. *MNRAS*, 462:S132–S137, November 2016a. doi: 10.1093/mnras/stw2299.
- M. Fulle, F. Marzari, V. Della Corte, S. Fornasier, H. Sierks, A. Rotundi, C. Barbieri, P. L. Lamy, R. Rodrigo, D. Koschny, H. Rickman, H. U. Keller, J. J. López-Moreno, M. Accolla, J. Agarwal, M. F. A'Hearn, N. Altobelli, M. A. Barucci, J.-L. Bertaux, I. Bertini, D. Bodewits, E. Bussoletti, L. Colangeli, M. Cosi, G. Cremonese, J.-F. Crifo, V. Da Deppo, B. Davidsson, S. Debei, M. De Cecco, F. Esposito, M. Ferrari, F. Giovane, B. Gustafson, S. F. Green, O. Groussin, E. Grün, P. Gutierrez, C. Güttler, M. L. Herranz, S. F. Hviid, W. Ip, S. L. Ivanovski, J. M. Jerónimo, L. Jorda, J. Knollenberg, R. Kramm, E. Kührt, M. Küppers, L. Lara, M. Lazzarin, M. R. Leese, A. C. López-Jiménez, F. Lucarelli, E. Mazzotta Epifani, J. A. M. McDonnell, V. Mennella, A. Molina, R. Morales, F. Moreno, S. Mottola, G. Naletto, N. Oklay, J. L. Ortiz, E. Palomba, P. Palumbo, J.-M. Perrin, F. J. M. Rietmeijer, J. Rodríguez, R. Sordini, N. Thomas, C. Tubiana, J.-B. Vincent, P. Weissman, K.-P. Wenzel, V. Zakharov, and J. C. Zarnecki. Evolution of the Dust Size Distribution of Comet 67P/Churyumov-Gerasimenko from 2.2 au to Perihelion. *ApJ*, 821:19, April 2016b. doi: 10.3847/0004-637X/821/1/19.
- M. Fulle, V. Della Corte, A. Rotundi, S. F. Green, M. Accolla, L. Colangeli, M. Ferrari, S. Ivanovski, R. Sordini, and V. Zakharov. The dust-to-ices ratio in comets and Kuiper belt objects. *MNRAS*, 469:S45–S49, July 2017. doi: 10.1093/mnras/stx983.
- H.-P. Gail. Radial mixing in protoplanetary accretion disks. I. Stationary disc models with annealing and carbon combustion. *A&A*, 378:192–213, October 2001. doi: 10.1051/0004-6361:20011130.
- C. F. Gammie. Layered Accretion in T Tauri Disks. *ApJ*, 457:355, January 1996. doi: 10.1086/176735.
- A. Gicquel, J.-B. Vincent, J. Agarwal, M. F. A'Hearn, I. Bertini, D. Bodewits, H. Sierks, Z.-Y. Lin, C. Barbieri, P. L. Lamy, R. Rodrigo, D. Koschny, H. Rickman, H. U. Keller, M. A. Barucci, J.-L. Bertaux, S. Besse, G. Cremonese, V. Da Deppo, B. Davidsson, S. Debei, J. Deller, M. De Cecco, E. Frattin, M. R. El-Maarry, S. Fornasier, M. Fulle, O. Groussin, P. J. Gutiérrez, P. Gutiérrez-Marquez, C. Güttler, S. Höfner, M. Hofmann, X. Hu, S. F. Hviid, W.-H. Ip, L. Jorda, J. Knollenberg, G. Kovacs, J.-R. Kramm, E. Kührt, M. Küppers, L. M. Lara, M. Lazzarin, J. J. L. Moreno, S. Lowry, F. Marzari, N. Masoumzadeh, M. Massironi, F. Moreno, S. Mottola, G. Naletto, N. Oklay, M. Pajola, A. Pommerol, F. Preusker, F. Scholten, X. Shi, N. Thomas, I. Toth, and C. Tubiana. Sublimation of icy aggregates in the coma of comet 67P/Churyumov-Gerasimenko detected with the OSIRIS cameras on board Rosetta. *MNRAS*, 462:S57–S66, November 2016. doi: 10.1093/mnras/stw2117.
- D. T. Gillespie. An Exact Method for Numerically Simulating the Stochastic Coalescence Process in a Cloud. *Journal of Atmospheric Sciences*, 32:1977–1989, October 1975. doi: 10.1175/1520-0469(1975)032<1977:AEMFNS>2.0.CO;2.
- I. Goldhirsch and G. Zanetti. Clustering instability in dissipative gases. *Physical Review Letters*, 70:1619–1622, March 1993. doi: 10.1103/PhysRevLett.70.1619.

- R. Gomes, H. F. Levison, K. Tsiganis, and A. Morbidelli. Origin of the cataclysmic Late Heavy Bombardment period of the terrestrial planets. *Nature*, 435:466–469, May 2005. doi: 10.1038/nature03676.
- J. Greenberg. The Core-Mantle Model of Interstellar Grains and the Cosmic Dust Connection. In L. J. Allamandola and A. G. G. M. Tielens, editors, *Interstellar Dust*, volume 135 of *IAU Symposium*, page 345, 1989.
- K. I. Gringauz, T. I. Gombosi, A. P. Remizov, I. Apathy, I. Szemerey, M. I. Verigin, L. I. Denchikova, A. V. Dyachkov, E. Keppler, I. N. Klimenko, A. K. Richter, A. J. Somogyi, K. Szego, S. Szendro, M. Tatrallyay, A. Varga, and G. A. Vladimirova. First in situ plasma and neutral gas measurements at comet Halley. *Nature*, 321:282–285, May 1986. doi: 10.1038/321282a0.
- O. Groussin, L. Jorda, A.-T. Auger, E. Kührt, R. Gaskell, C. Capanna, F. Scholten, F. Preusker, P. Lamy, S. Hviid, J. Knollenberg, U. Keller, C. Huettig, H. Sierks, C. Barbieri, R. Rodrigo, D. Koschny, H. Rickman, M. F. A'Hearn, J. Agarwal, M. A. Barucci, J.-L. Bertaux, I. Bertini, S. Boudreault, G. Cremonese, V. Da Deppo, B. Davidsson, S. Debei, M. De Cecco, M. R. El-Maarry, S. Fornasier, M. Fulle, P. J. Gutiérrez, C. Güttler, W.-H. Ip, J.-R. Kramm, M. Küppers, M. Lazzarin, L. M. Lara, J. J. Lopez Moreno, S. Marchi, F. Marzari, M. Massironi, H. Michalik, G. Naletto, N. Oklay, A. Pommerol, M. Pajola, N. Thomas, I. Toth, C. Tubiana, and J.-B. Vincent. Gravitational slopes, geomorphology, and material strengths of the nucleus of comet 67P/Churyumov-Gerasimenko from OSIRIS observations. *A&A*, 583:A32, November 2015. doi: 10.1051/0004-6361/201526379.
- S. Gulikis, M. Allen, P. von Allmen, G. Beaudin, N. Biver, D. Bockelée-Morvan, M. Choukroun, J. Crovisier, B. J. R. Davidsson, P. Encrenaz, T. Encrenaz, M. Frerking, P. Hartogh, M. Hofstadter, W.-H. Ip, M. Janssen, C. Jarchow, S. Keihm, S. Lee, E. Lellouch, C. Leyrat, L. Rezac, F. P. Schloerb, and T. Spilker. Subsurface properties and early activity of comet 67P/Churyumov-Gerasimenko. *Science*, 347(1):aaa0709, January 2015. doi: 10.1126/science.aaa0709.
- B. Gundlach and J. Blum. The Stickiness of Micrometer-sized Water-ice Particles. *ApJ*, 798:34, January 2015. doi: 10.1088/0004-637X/798/1/34.
- B. Gundlach, S. Kiliyas, E. Beitz, and J. Blum. Micrometer-sized ice particles for planetary-science experiments - I. Preparation, critical rolling friction force, and specific surface energy. *Icarus*, 214:717–723, August 2011a. doi: 10.1016/j.icarus.2011.05.005.
- B. Gundlach, Y. V. Skorov, and J. Blum. Outgassing of icy bodies in the Solar System - I. The sublimation of hexagonal water ice through dust layers. *Icarus*, 213:710–719, June 2011b. doi: 10.1016/j.icarus.2011.03.022.
- C. Güttler, M. Krause, R. J. Geretschauser, R. Speith, and J. Blum. The Physics of Protoplanetary Dust Agglomerates. IV. Toward a Dynamical Collision Model. *ApJ*, 701:130–141, August 2009. doi: 10.1088/0004-637X/701/1/130.

- C. Güttler, J. Blum, A. Zsom, C. W. Ormel, and C. P. Dullemond. The outcome of protoplanetary dust growth: pebbles, boulders, or planetesimals?. I. Mapping the zoo of laboratory collision experiments. *A&A*, 513:A56, April 2010. doi: 10.1051/0004-6361/200912852.
- K. E. Haisch, Jr., E. A. Lada, and C. J. Lada. Disk Frequencies and Lifetimes in Young Clusters. *ApJ*, 553:L153–L156, June 2001. doi: 10.1086/320685.
- M. S. Hanner and J. P. Bradley. *Composition and mineralogy of cometary dust*, pages 555–564. 2004.
- L. Hartmann, N. Calvet, E. Gullbring, and P. D’Alessio. Accretion and the Evolution of T Tauri Disks. *ApJ*, 495:385–400, March 1998. doi: 10.1086/305277.
- C. Hayashi. Structure of the Solar Nebula, Growth and Decay of Magnetic Fields and Effects of Magnetic and Turbulent Viscosities on the Nebula. *Progress of Theoretical Physics Supplement*, 70:35–53, 1981. doi: 10.1143/PTPS.70.35.
- L.-O. Heim, J. Blum, M. Preuss, and H.-J. Butt. Adhesion and Friction Forces between Spherical Micrometer-Sized Particles. *Physical Review Letters*, 83:3328–3331, October 1999. doi: 10.1103/PhysRevLett.83.3328.
- D. Heißelmann, J. Blum, H. J. Fraser, and K. Wolling. Microgravity experiments on the collisional behavior of saturnian ring particles. *Icarus*, 206:424–430, April 2010. doi: 10.1016/j.icarus.2009.08.009.
- C. R. Hill, D. Heißelmann, J. Blum, and H. J. Fraser. Collisions of small ice particles under microgravity conditions. *A&A*, 573:A49, January 2015. doi: 10.1051/0004-6361/201424069.
- S. Ida and T. Guillot. Formation of dust-rich planetesimals from sublimated pebbles inside of the snow line. *A&A*, 596:L3, November 2016. doi: 10.1051/0004-6361/201629680.
- D. Jewitt and J. Luu. Discovery of the candidate Kuiper belt object 1992 QB1. *Nature*, 362:730–732, April 1993. doi: 10.1038/362730a0.
- A. Johansen and P. Lacerda. Prograde rotation of protoplanets by accretion of pebbles in a gaseous environment. *MNRAS*, 404:475–485, May 2010. doi: 10.1111/j.1365-2966.2010.16309.x.
- A. Johansen, J. S. Oishi, M.-M. Mac Low, H. Klahr, T. Henning, and A. Youdin. Rapid planetesimal formation in turbulent circumstellar disks. *Nature*, 448:1022–1025, August 2007. doi: 10.1038/nature06086.
- A. Johansen, A. Youdin, and H. Klahr. Zonal Flows and Long-lived Axisymmetric Pressure Bumps in Magnetorotational Turbulence. *ApJ*, 697:1269–1289, June 2009. doi: 10.1088/0004-637X/697/2/1269.

- A. Johansen, J. Blum, H. Tanaka, C. Ormel, M. Bizzarro, and H. Rickman. The Multifaceted Planetesimal Formation Process. *Protostars and Planets VI*, pages 547–570, 2014. doi: 10.2458/azu_uapress_9780816531240-ch024.
- K. L. Johnson, K. Kendall, and A. D. Roberts. Surface Energy and the Contact of Elastic Solids. *Proceedings of the Royal Society of London Series A*, 324:301–313, September 1971. doi: 10.1098/rspa.1971.0141.
- L. Jorda, R. Gaskell, C. Capanna, S. Hviid, P. Lamy, J. Ďurech, G. Faury, O. Groussin, P. Gutiérrez, C. Jackman, S. J. Keihm, H. U. Keller, J. Knollenberg, E. Kührt, S. Marchi, S. Mottola, E. Palmer, F. P. Schloerb, H. Sierks, J.-B. Vincent, M. F. A'Hearn, C. Barbieri, R. Rodrigo, D. Koschny, H. Rickman, M. A. Barucci, J. L. Bertaux, I. Bertini, G. Cremonese, V. Da Deppo, B. Davidsson, S. Debei, M. De Cecco, S. Fornasier, M. Fulle, C. Güttler, W.-H. Ip, J. R. Kramm, M. Küppers, L. M. Lara, M. Lazzarin, J. J. Lopez Moreno, F. Marzari, G. Naletto, N. Oklay, N. Thomas, C. Tubiana, and K.-P. Wenzel. The global shape, density and rotation of Comet 67P/Churyumov-Gerasimenko from preperihelion Rosetta/OSIRIS observations. *Icarus*, 277:257–278, October 2016. doi: 10.1016/j.icarus.2016.05.002.
- B. Jost, B. Gundlach, A. Pommerol, J. Oesert, S. N. Gorb, J. Blum, and N. Thomas. Micrometer-sized ice particles for planetary-science experiments - II. Bidirectional reflectance. *Icarus*, 225:352–366, July 2013. doi: 10.1016/j.icarus.2013.04.007.
- A. Kataoka, H. Tanaka, S. Okuzumi, and K. Wada. Static compression of porous dust aggregates. *A&A*, 554:A4, June 2013a. doi: 10.1051/0004-6361/201321325.
- A. Kataoka, H. Tanaka, S. Okuzumi, and K. Wada. Fluffy dust forms icy planetesimals by static compression. *A&A*, 557:L4, September 2013b. doi: 10.1051/0004-6361/201322151.
- H. U. Keller. Comets: Dirty snowballs or icy dirtballs. In J. J. Hunt and T. D. Guyenne, editors, *Physics and Mechanics of Cometary Materials*, volume 302 of *ESA Special Publication*, December 1989.
- H. U. Keller, C. Arpigny, C. Barbieri, R. M. Bonnet, S. Cazes, M. Coradini, C. B. Cosmovici, W. A. Delamere, W. F. Huebner, D. W. Hughes, C. Jamar, D. Malaise, H. J. Reitsema, H. U. Schmidt, W. K. H. Schmidt, P. Seige, F. L. Whipple, and K. Wilhelm. First Halley multicolour camera imaging results from Giotto. *Nature*, 321:320–326, May 1986. doi: 10.1038/321320a0.
- H. U. Keller, R. Kramm, and N. Thomas. Surface features on the nucleus of Comet Halley. *Nature*, 331:227–231, January 1988. doi: 10.1038/331227a0.
- M. S. Kelley and D. H. Wooden. The composition of dust in Jupiter-family comets inferred from infrared spectroscopy. *Planet. Space Sci.*, 57:1133–1145, August 2009. doi: 10.1016/j.pss.2008.11.017.
- S. Kempf, S. Pfalzner, and T. K. Henning. N-Particle-Simulations of Dust Growth. I. Growth Driven by Brownian Motion. *Icarus*, 141:388–398, October 1999. doi: 10.1006/icar.1999.6171.

- H. Kimura, L. Kolokolova, and I. Mann. Optical properties of cometary dust. Constraints from numerical studies on light scattering by aggregate particles. *A&A*, 407:L5–L8, August 2003. doi: 10.1051/0004-6361:20030967.
- Y. Kimura, S. Sasaki, H. Suzuki, A. Kumamoto, M. Saito, and C. Kaito. Experimental Demonstration of Condensation of Mg-bearing Silicate Grains around Evolved Stars. *ApJ*, 684:1496–1501, September 2008. doi: 10.1086/589966.
- Y. Kimura, J. A. Nuth, III, K. Tsukamoto, and C. Kaito. Laboratory annealing experiments of refractory silicate grain analogs using differential scanning calorimetry. *Meteoritics and Planetary Science*, 46:92–102, January 2011. doi: 10.1111/j.1945-5100.2010.01143.x.
- J. Kissel, D. E. Brownlee, K. Buchler, B. C. Clark, H. Fechtig, E. Grun, K. Hornung, E. B. Igenbergs, E. K. Jessberger, F. R. Krueger, H. Kuczera, J. A. M. McDonnell, G. M. Morfill, J. Rahe, G. H. Schwehm, Z. Sekanina, N. G. Utterback, H. J. Volk, and H. A. Zook. Composition of comet Halley dust particles from Giotto observations. *Nature*, 321:336, May 1986a. doi: 10.1038/321336a0.
- J. Kissel, R. Z. Sagdeev, J. L. Bertaux, V. N. Angarov, J. Audouze, J. E. Blamont, K. Buchler, E. N. Evlanov, H. Fechtig, M. N. Fomenkova, H. von Hoerner, N. A. Inogamov, V. N. Khromov, W. Knabe, F. R. Krueger, Y. Langevin, B. Leonasv, A. C. Levasseur-Regourd, G. G. Managadze, S. N. Podkolzin, V. D. Shapiro, S. R. Tabaldyev, and B. V. Zubkov. Composition of comet Halley dust particles from VEGA observations. *Nature*, 321:280–282, May 1986b. doi: 10.1038/321280a0.
- W. Kofman, A. Herique, Y. Barbin, J.-P. Barriot, V. Ciarletti, S. Clifford, P. Edenhofer, C. Elachi, C. Eyraud, J.-P. Goutail, E. Heggy, L. Jorda, J. Lasue, A.-C. Levasseur-Regourd, E. Nielsen, P. Pasquero, F. Preusker, P. Puget, D. Plettemeier, Y. Rogez, H. Sierks, C. Statz, H. Svedhem, I. Williams, S. Zine, and J. Van Zyl. Properties of the 67P/Churyumov-Gerasimenko interior revealed by CONSERT radar. *Science*, 349 (2), July 2015. doi: 10.1126/science.aab0639.
- R. Kokotanekova, C. Snodgrass, P. Lacerda, S. F. Green, S. C. Lowry, Y. R. Fernandez, C. Tubiana, A. Fitzsimmons, and H. H. Hsieh. Rotation of Cometary Nuclei: New Lightcurves and an Update of the Ensemble Properties of Jupiter-Family Comets. *ArXiv e-prints*, July 2017.
- S. Kothe, J. Blum, R. Weidling, and C. Güttler. Free collisions in a microgravity many-particle experiment. III. The collision behavior of sub-millimeter-sized dust aggregates. *Icarus*, 225:75–85, July 2013. doi: 10.1016/j.icarus.2013.02.034.
- T. Kozasa, J. Blum, H. Okamoto, and T. Mukai. Optical properties of dust aggregates. 11. Angular dependence of scattered light. *A&A*, 276:278, September 1993.
- D. Krankowsky, P. Lammerzahl, I. Herrwerth, J. Woweries, P. Eberhardt, U. Dolder, U. Herrmann, W. Schulte, J. J. Berthelier, J. M. Illiano, R. R. Hodges, and J. H. Hoffman. In situ gas and ion measurements at comet Halley. *Nature*, 321:326–329, May 1986. doi: 10.1038/321326a0.

- K. A. Kretke and D. N. C. Lin. Grain Retention and Formation of Planetesimals near the Snow Line in MRI-driven Turbulent Protoplanetary Disks. *ApJ*, 664:L55–L58, July 2007. doi: 10.1086/520718.
- S. Krijt, C. Dominik, and A. G. G. M. Tielens. Rolling friction of adhesive microspheres. *Journal of Physics D Applied Physics*, 47(17):175302, April 2014. doi: 10.1088/0022-3727/47/17/175302.
- S. Krijt, C. W. Ormel, C. Dominik, and A. G. G. M. Tielens. Erosion and the limits to planetesimal growth. *A&A*, 574:A83, February 2015. doi: 10.1051/0004-6361/201425222.
- S. Krijt, C. W. Ormel, C. Dominik, and A. G. G. M. Tielens. A panoptic model for planetesimal formation and pebble delivery. *A&A*, 586:A20, February 2016. doi: 10.1051/0004-6361/201527533.
- T. Kudo, A. Kouchi, M. Arakawa, and H. Nakano. The role of sticky interstellar organic material in the formation of asteroids. *Meteoritics and Planetary Science*, 37:1975–1983, December 2002. doi: 10.1111/j.1945-5100.2002.tb01178.x.
- G. P. Kuiper. On the Origin of the Solar System. *Proceedings of the National Academy of Science*, 37:1–14, January 1951. doi: 10.1073/pnas.37.1.1.
- M. Küppers, I. Bertini, S. Fornasier, P. J. Gutierrez, S. F. Hviid, L. Jorda, H. U. Keller, J. Knollenberg, D. Koschny, R. Kramm, L.-M. Lara, H. Sierks, N. Thomas, C. Barbieri, P. Lamy, H. Rickman, R. Rodrigo, M. F. A'Hearn, F. Angrilli, M. Bailey, P. Barthol, M. A. Barucci, J.-L. Bertaux, J. A. Burns, G. Cremonese, W. Curdt, M. De Cecco, S. Debei, M. Fulle, F. Gliem, W. H. Ip, E. Huhrt, A. Llebaria, J. J. Lopez Moreno, F. Marzari, G. Naletto, L. Sabau, A. Sanz Andres, J. P. Sivan, G. Tondello, and K.-P. Wenzel. A large dust/ice ratio in the nucleus of comet 9P/Tempel 1. *Nature*, 437:987–990, October 2005. doi: 10.1038/nature04236.
- P. L. Lamy, I. Toth, Y. R. Fernandez, and H. A. Weaver. *The sizes, shapes, albedos, and colors of cometary nuclei*, pages 223–264. 2004.
- W. A. Landeck. Stöße zwischen hochporösen Staubagglomeraten im Laborfallturm, 2016. Bachelor Thesis, Technische Universität Braunschweig.
- D. Langkowski, J. Teiser, and J. Blum. The Physics of Protoplanetary Dust Agglomerates. II. Low-Velocity Collision Properties. *ApJ*, 675:764–776, March 2008. doi: 10.1086/525841.
- H. F. Levison. Comet Taxonomy. In T. Rettig and J. M. Hahn, editors, *Completing the Inventory of the Solar System*, volume 107 of *Astronomical Society of the Pacific Conference Series*, pages 173–191, 1996.
- K. Lodders. Solar System Abundances and Condensation Temperatures of the Elements. *ApJ*, 591:1220–1247, July 2003. doi: 10.1086/375492.

- S. Lorek, B. Gundlach, P. Lacerda, and J. Blum. Comet formation in collapsing pebble clouds. What cometary bulk density implies for the cloud mass and dust-to-ice ratio. *A&A*, 587:A128, March 2016. doi: 10.1051/0004-6361/201526565.
- S. Lorek, P. Lacerda, and J. Blum. Local growth of dust- and ice-mixed aggregates as cometary building blocks in the solar nebula. *A&A*, 611:A18, March 2018. doi: 10.1051/0004-6361/201630175.
- D. Lynden-Bell and J. E. Pringle. The evolution of viscous discs and the origin of the nebular variables. *MNRAS*, 168:603–637, September 1974. doi: 10.1093/mnras/168.3.603.
- T. Mannel, M. S. Bentley, R. Schmied, H. Jeszyszky, A. C. Levasseur-Regourd, J. Romstedt, and K. Torkar. Fractal cometary dust - a window into the early Solar system. *MNRAS*, 462:S304–S311, November 2016. doi: 10.1093/mnras/stw2898.
- J. S. Mathis, W. Rumpl, and K. H. Nordsieck. The size distribution of interstellar grains. *ApJ*, 217:425–433, October 1977. doi: 10.1086/155591.
- J. A. M. McDonnell, W. M. Alexander, W. M. Burton, E. Bussoletti, D. H. Clark, J. L. Grard, E. Gruen, M. S. Hanner, Z. Sekanina, and D. W. Hughes. Dust density and mass distribution near comet Halley from Giotto observations. *Nature*, 321:338–341, May 1986. doi: 10.1038/321338a0.
- KevinDD. McKeegan, Jerome Aléon, Jhn Bradley, Donald Brownlee, Henner Busemann, Anna Butterworth, Mrrc Chaussidon, Stewrrt Fallon, Christine Floss, Jamie Gilmour, Mattheeu Gounelle, Giles Graham, Yunbin Guan, Philipp R. Heck, Peter Hoppe, Ian D. Hutcheon, Joacimm Huth, Hppe Ishii, Motoo Ito, SteinBB. Jacobsen, Anton Kearsley, Laurie A. Leshin, Ming-Chang Liu, ann Lyon, Kuljett Marhas, Bernrdd Marty, Gracilla Matrajt, Anders Meibom, Scott Messenger, Smail Mostefaoui, Sujoy Mukhopadhyay, Keiko Nakamura-Messenger, Larry Nittler, Rsss Palma, Robert O. Pepin, Dimitri A. Papanastassiou, François Robert, Dennis Schlutter, Christopher J. Snead, FrankJJ. Stadermann, Rhonda Stroud, Peter Tsou, Andrew Westphal, Edward D. Young, Karen Ziegler, Laurntt Zimmermann, and E. Zinner. Isotopic Compositions of Cometary Matter Returned by Stardust. *Science*, 314:1724–, December 2006. doi: 10.1126/science.1135992.
- M. Min, J. W. Hovenier, A. de Koter, L. B. F. M. Waters, and C. Dominik. The composition and size distribution of the dust in the coma of Comet Hale Bopp. *Icarus*, 179:158–173, December 2005. doi: 10.1016/j.icarus.2005.05.015.
- T. Minato, M. Köhler, H. Kimura, I. Mann, and T. Yamamoto. Momentum transfer to fluffy dust aggregates from stellar winds. *A&A*, 452:701–707, June 2006. doi: 10.1051/0004-6361:20054774.
- A. Morbidelli and H. Rickman. Comets as collisional fragments of a primordial planetesimal disk. *A&A*, 583:A43, November 2015. doi: 10.1051/0004-6361/201526116.

- A. Morbidelli, H. F. Levison, K. Tsiganis, and R. Gomes. Chaotic capture of Jupiter's Trojan asteroids in the early Solar System. *Nature*, 435:462–465, May 2005. doi: 10.1038/nature03540.
- O. Mousis, J. I. Lunine, A. Luspai-Kuti, T. Guillot, B. Marty, M. Ali-Dib, P. Wurz, K. Altwegg, A. Bieler, M. Hässig, M. Rubin, P. Vernazza, and J. H. Waite. A Protosolar Nebula Origin for the Ices Agglomerated by Comet 67P/Churyumov-Gerasimenko. *ApJ*, 819:L33, March 2016. doi: 10.3847/2041-8205/819/2/L33.
- T. Mukai, H. Ishimoto, T. Kozasa, J. Blum, and J. M. Greenberg. Radiation pressure forces of fluffy porous grains. *A&A*, 262:315–320, August 1992.
- M. J. Mumma and S. B. Charnley. The Chemical Composition of Comets—Emerging Taxonomies and Natal Heritage. *ARA&A*, 49:471–524, September 2011. doi: 10.1146/annurev-astro-081309-130811.
- Y. Nakagawa, M. Sekiya, and C. Hayashi. Settling and growth of dust particles in a laminar phase of a low-mass solar nebula. *Icarus*, 67:375–390, September 1986. doi: 10.1016/0019-1035(86)90121-1.
- D. Nesvorný, A. N. Youdin, and D. C. Richardson. Formation of Kuiper Belt Binaries by Gravitational Collapse. *AJ*, 140:785–793, September 2010. doi: 10.1088/0004-6256/140/3/785.
- S. Okuzumi, H. Tanaka, and M.-a. Sakagami. Numerical Modeling of the Coagulation and Porosity Evolution of Dust Aggregates. *ApJ*, 707:1247–1263, December 2009. doi: 10.1088/0004-637X/707/2/1247.
- S. Okuzumi, H. Tanaka, H. Kobayashi, and K. Wada. Rapid Coagulation of Porous Dust Aggregates outside the Snow Line: A Pathway to Successful Icy Planetesimal Formation. *ApJ*, 752:106, June 2012. doi: 10.1088/0004-637X/752/2/106.
- J. H. Oort. The structure of the cloud of comets surrounding the Solar System and a hypothesis concerning its origin. *Bull. Astron. Inst. Netherlands*, 11:91–110, January 1950.
- C. W. Ormel and J. N. Cuzzi. Closed-form expressions for particle relative velocities induced by turbulence. *A&A*, 466:413–420, May 2007. doi: 10.1051/0004-6361:20066899.
- C. W. Ormel and M. Spaans. Monte Carlo Simulation of Particle Interactions at High Dynamic Range: Advancing beyond the Googol. *ApJ*, 684:1291-1309, September 2008. doi: 10.1086/590052.
- C. W. Ormel, M. Spaans, and A. G. G. M. Tielens. Dust coagulation in protoplanetary disks: porosity matters. *A&A*, 461:215–232, January 2007. doi: 10.1051/0004-6361:20065949.
- C. W. Ormel, J. N. Cuzzi, and A. G. G. M. Tielens. Co-Accretion of Chondrules and Dust in the Solar Nebula. *ApJ*, 679:1588-1610, June 2008. doi: 10.1086/587836.

- C. W. Ormel, D. Paszun, C. Dominik, and A. G. G. M. Tielens. Dust coagulation and fragmentation in molecular clouds. I. How collisions between dust aggregates alter the dust size distribution. *A&A*, 502:845–869, August 2009. doi: 10.1051/0004-6361/200811158.
- V. Ossenkopf. Dust coagulation in dense molecular clouds: The formation of fluffy aggregates. *A&A*, 280:617–646, December 1993.
- M. Pätzold, T. Andert, M. Hahn, S. W. Asmar, J.-P. Barriot, M. K. Bird, B. Häusler, K. Peter, S. Tellmann, E. Grün, P. R. Weissman, H. Sierks, L. Jorda, R. Gaskell, F. Preusker, and F. Scholten. A homogeneous nucleus for comet 67P/Churyumov-Gerasimenko from its gravity field. *Nature*, 530:63–65, February 2016. doi: 10.1038/nature16535.
- P. Pinilla, T. Birnstiel, L. Ricci, C. P. Dullemond, A. L. Uribe, L. Testi, and A. Natta. Trapping dust particles in the outer regions of protoplanetary disks. *A&A*, 538:A114, February 2012. doi: 10.1051/0004-6361/201118204.
- F. Poulet, A. Lucchetti, J.-P. Bibring, J. Carter, B. Gondet, L. Jorda, Y. Langevin, C. Pilorget, C. Capanna, and G. Cremonese. Origin of the local structures at the Philae landing site and possible implications on the formation and evolution of 67P/Churyumov-Gerasimenko. *MNRAS*, 462:S23–S32, November 2016. doi: 10.1093/mnras/stw1959.
- F. Preusker, F. Scholten, K.-D. Matz, T. Roatsch, K. Willner, S. F. Hviid, J. Knollenberg, L. Jorda, P. J. Gutiérrez, E. Kührt, S. Mottola, M. F. A'Hearn, N. Thomas, H. Sierks, C. Barbieri, P. Lamy, R. Rodrigo, D. Koschny, H. Rickman, H. U. Keller, J. Agarwal, M. A. Barucci, J.-L. Bertaux, I. Bertini, G. Cremonese, V. Da Deppo, B. Davidsson, S. Debei, M. De Cecco, S. Fornasier, M. Fulle, O. Groussin, C. Güttler, W.-H. Ip, J. R. Kramm, M. Küppers, L. M. Lara, M. Lazzarin, J. J. Lopez Moreno, F. Marzari, H. Michalik, G. Naletto, N. Ockay, C. Tubiana, and J.-B. Vincent. Shape model, reference system definition, and cartographic mapping standards for comet 67P/Churyumov-Gerasimenko - Stereo-photogrammetric analysis of Rosetta/OSIRIS image data. *A&A*, 583:A33, November 2015. doi: 10.1051/0004-6361/201526349.
- H. Rickman, S. Marchi, M. F. A'Hearn, C. Barbieri, M. R. El-Maarry, C. Güttler, W.-H. Ip, H. U. Keller, P. Lamy, F. Marzari, M. Massironi, G. Naletto, M. Pajola, H. Sierks, D. Koschny, R. Rodrigo, M. A. Barucci, J.-L. Bertaux, I. Bertini, G. Cremonese, V. Da Deppo, S. Debei, M. De Cecco, S. Fornasier, M. Fulle, O. Groussin, P. J. Gutiérrez, S. F. Hviid, L. Jorda, J. Knollenberg, J.-R. Kramm, E. Kührt, M. Küppers, L. M. Lara, M. Lazzarin, J. J. Lopez Moreno, H. Michalik, L. Sabau, N. Thomas, J.-B. Vincent, and K.-P. Wenzel. Comet 67P/Churyumov-Gerasimenko: Constraints on its origin from OSIRIS observations. *A&A*, 583:A44, November 2015. doi: 10.1051/0004-6361/201526093.
- A. Rotundi, H. Sierks, V. Della Corte, M. Fulle, P. J. Gutierrez, L. Lara, C. Barbieri, P. L. Lamy, R. Rodrigo, D. Koschny, H. Rickman, H. U. Keller, J. J. López-Moreno, M. Accolla, J. Agarwal, M. F. A'Hearn, N. Altobelli, F. Angrilli, M. A. Barucci, J.-L. Bertaux, I. Bertini, D. Bodewits, E. Bussoletti, L. Colangeli, M. Cosi, G. Cremonese,

- J.-F. Crifo, V. Da Deppo, B. Davidsson, S. Debei, M. De Cecco, F. Esposito, M. Ferrari, S. Fornasier, F. Giovane, B. Gustafson, S. F. Green, O. Groussin, E. Grün, C. Güttler, M. L. Herranz, S. F. Hviid, W. Ip, S. Ivanovski, J. M. Jerónimo, L. Jorda, J. Knollenberg, R. Kramm, E. Kührt, M. Küppers, M. Lazzarin, M. R. Leese, A. C. López-Jiménez, F. Lucarelli, S. C. Lowry, F. Marzari, E. M. Epifani, J. A. M. McDonnell, V. Mennella, H. Michalik, A. Molina, R. Morales, F. Moreno, S. Mottola, G. Naletto, N. Oklay, J. L. Ortiz, E. Palomba, P. Palumbo, J.-M. Perrin, J. Rodríguez, L. Sabau, C. Snodgrass, R. Sordini, N. Thomas, C. Tubiana, J.-B. Vincent, P. Weissman, K.-P. Wenzel, V. Zakharov, and J. C. Zarnecki. Dust measurements in the coma of comet 67P/Churyumov-Gerasimenko inbound to the Sun. *Science*, 347:aaa3905, January 2015. doi: 10.1126/science.aaa3905.
- M. Rubin, K. Altwegg, H. Balsiger, A. Bar-Nun, J.-J. Berthelier, A. Bieler, P. Bochslers, C. Briois, U. Calmonte, M. Combi, J. De Keyser, F. Dhooghe, P. Eberhardt, B. Fiethe, S. A. Fuselier, S. Gasc, T. I. Gombosi, K. C. Hansen, M. Hässig, A. Jäckel, E. Kopp, A. Korth, L. Le Roy, U. Mall, B. Marty, O. Mousis, T. Owen, H. Rème, T. Sémon, C.-Y. Tzou, J. H. Waite, and P. Würz. Molecular nitrogen in comet 67P/Churyumov-Gerasimenko indicates a low formation temperature. *Science*, 348:232–235, April 2015. doi: 10.1126/science.aaa6100.
- U. Schäfer, C.-C. Yang, and A. Johansen. Initial mass function of planetesimals formed by the streaming instability. *A&A*, 597:A69, January 2017. doi: 10.1051/0004-6361/201629561.
- R. Schräpler and J. Blum. The Physics of Protoplanetary Dust Agglomerates. VI. Erosion of Large Aggregates as a Source of Micrometer-sized Particles. *ApJ*, 734:108, June 2011. doi: 10.1088/0004-637X/734/2/108.
- A. Seizinger and W. Kley. Bouncing behavior of microscopic dust aggregates. *A&A*, 551:A65, March 2013. doi: 10.1051/0004-6361/201220946.
- N. I. Shakura and R. A. Sunyaev. Black holes in binary systems. Observational appearance. *A&A*, 24:337–355, 1973.
- F. H. Shu, F. C. Adams, and S. Lizano. Star formation in molecular clouds - Observation and theory. *ARA&A*, 25:23–81, 1987. doi: 10.1146/annurev.aa.25.090187.000323.
- H. Sierks, C. Barbieri, P. L. Lamy, R. Rodrigo, D. Koschny, H. Rickman, H. U. Keller, J. Agarwal, M. F. A'Hearn, F. Angrilli, A.-T. Auger, M. A. Barucci, J.-L. Bertaux, I. Bertini, S. Besse, D. Bodewits, C. Capanna, G. Cremonese, V. Da Deppo, B. Davidsson, S. Debei, M. De Cecco, F. Ferri, S. Fornasier, M. Fulle, R. Gaskell, L. Giacomini, O. Groussin, P. Gutierrez-Marques, P. J. Gutiérrez, C. Güttler, N. Hoekzema, S. F. Hviid, W.-H. Ip, L. Jorda, J. Knollenberg, G. Kovacs, J. R. Kramm, E. Kührt, M. Küppers, F. La Forgia, L. M. Lara, M. Lazzarin, C. Leyrat, J. J. Lopez Moreno, S. Magrin, S. Marchi, F. Marzari, M. Massironi, H. Michalik, R. Moissl, S. Mottola, G. Naletto, N. Oklay, M. Pajola, M. Pertile, F. Preusker, L. Sabau, F. Scholten, C. Snodgrass, N. Thomas, C. Tubiana, J.-B. Vincent, K.-P. Wenzel, M. Zaccariotto, and M. Pätzold. On the nucleus structure and activity of comet 67P/Churyumov-Gerasimenko. *Science*, 347:aaa1044, January 2015. doi: 10.1126/science.aaa1044.

- Y. Skorov and J. Blum. Dust release and tensile strength of the non-volatile layer of cometary nuclei. *Icarus*, 221:1–11, September 2012. doi: 10.1016/j.icarus.2012.01.012.
- M. V. Smoluchowski. Drei Vorträge über Diffusion, Brownsche Bewegung und Koagulation von Kolloidteilchen. *Zeitschrift für Physik*, 17:557–585, 1916.
- J. M. Sunshine, O. Groussin, P. H. Schultz, M. F. A'Hearn, L. M. Feaga, T. L. Farnham, and K. P. Klaasen. The distribution of water ice in the interior of Comet Tempel 1. *Icarus*, 191:73–83, 2007. doi: 10.1016/j.icarus.2007.04.037.
- T. Suyama, K. Wada, and H. Tanaka. Numerical Simulation of Density Evolution of Dust Aggregates in Protoplanetary Disks. I. Head-on Collisions. *ApJ*, 684:1310–1322, September 2008. doi: 10.1086/590143.
- T. Suyama, K. Wada, H. Tanaka, and S. Okuzumi. Geometric Cross Sections of Dust Aggregates and a Compression Model for Aggregate Collisions. *ApJ*, 753:115, July 2012. doi: 10.1088/0004-637X/753/2/115.
- M. V. Sykes and R. G. Walker. Cometary dust trails. I - Survey. *Icarus*, 95:180–210, February 1992. doi: 10.1016/0019-1035(92)90037-8.
- J. Teiser and G. Wurm. High-velocity dust collisions: forming planetesimals in a fragmentation cascade with final accretion. *MNRAS*, 393:1584–1594, March 2009. doi: 10.1111/j.1365-2966.2008.14289.x.
- N. Thomas, H. Sierks, C. Barbieri, P. L. Lamy, R. Rodrigo, H. Rickman, D. Koschny, H. U. Keller, J. Agarwal, M. F. A'Hearn, F. Angrilli, A.-T. Auger, M. A. Barucci, J.-L. Bertaux, I. Bertini, S. Besse, D. Bodewits, G. Cremonese, V. Da Deppo, B. Davidsson, M. De Cecco, S. Debei, M. R. El-Maarry, F. Ferri, S. Fornasier, M. Fulle, L. Giacomini, O. Groussin, P. J. Gutierrez, C. Güttler, S. F. Hviid, W.-H. Ip, L. Jorda, J. Knollenberg, J.-R. Kramm, E. Kührt, M. Küppers, F. La Forgia, L. M. Lara, M. Lazzarin, J. J. L. Moreno, S. Magrin, S. Marchi, F. Marzari, M. Massironi, H. Michalik, R. Moissl, S. Mottola, G. Naletto, N. Oklay, M. Pajola, A. Pommerol, F. Preusker, L. Sabau, F. Scholten, C. Snodgrass, C. Tubiana, J.-B. Vincent, and K.-P. Wenzel. The morphological diversity of comet 67P/Churyumov-Gerasimenko. *Science*, 347(1):aaa0440, January 2015. doi: 10.1126/science.aaa0440.
- Colin Thornton and Zemin Ning. A theoretical model for the stick/bounce behaviour of adhesive, elastic-plastic spheres. *Powder Technology*, 99(2):154 – 162, 1998. ISSN 0032-5910. doi: [http://dx.doi.org/10.1016/S0032-5910\(98\)00099-0](http://dx.doi.org/10.1016/S0032-5910(98)00099-0). URL <http://www.sciencedirect.com/science/article/pii/S0032591098000990>.
- A. Toppani, G. Libourel, F. Robert, and J. Ghanbaja. Laboratory condensation of refractory dust in protosolar and circumstellar conditions. *Geochim. Cosmochim. Acta*, 70:5035–5060, October 2006. doi: 10.1016/j.gca.2006.05.020.
- S. Tremaine. The distribution of comets around stars. In J. A. Phillips, S. E. Thorsett, and S. R. Kulkarni, editors, *Planets Around Pulsars*, volume 36 of *Astronomical Society of the Pacific Conference Series*, pages 335–344, January 1993.

- K. Tsiganis, R. Gomes, A. Morbidelli, and H. F. Levison. Origin of the orbital architecture of the giant planets of the Solar System. *Nature*, 435:459–461, May 2005. doi: 10.1038/nature03539.
- K. Wada, H. Tanaka, T. Suyama, H. Kimura, and T. Yamamoto. Numerical Simulation of Dust Aggregate Collisions. I. Compression and Disruption of Two-Dimensional Aggregates. *ApJ*, 661:320–333, May 2007. doi: 10.1086/514332.
- K. Wada, H. Tanaka, T. Suyama, H. Kimura, and T. Yamamoto. Numerical Simulation of Dust Aggregate Collisions. II. Compression and Disruption of Three-Dimensional Aggregates in Head-on Collisions. *ApJ*, 677:1296–1308, April 2008. doi: 10.1086/529511.
- K. Wada, H. Tanaka, T. Suyama, H. Kimura, and T. Yamamoto. The Rebound Condition of Dust Aggregates Revealed by Numerical Simulation of Their Collisions. *ApJ*, 737:36, August 2011. doi: 10.1088/0004-637X/737/1/36.
- K. Wada, H. Tanaka, S. Okuzumi, H. Kobayashi, T. Suyama, H. Kimura, and T. Yamamoto. Growth efficiency of dust aggregates through collisions with high mass ratios. *A&A*, 559:A62, November 2013. doi: 10.1051/0004-6361/201322259.
- K. Wahlberg Jansson and A. Johansen. Formation of pebble-pile planetesimals. *A&A*, 570:A47, October 2014. doi: 10.1051/0004-6361/201424369.
- S. J. Weidenschilling. Aerodynamics of solid bodies in the solar nebula. *MNRAS*, 180:57–70, July 1977a.
- S. J. Weidenschilling. The distribution of mass in the planetary system and solar nebula. *Ap&SS*, 51:153–158, September 1977b. doi: 10.1007/BF00642464.
- S. J. Weidenschilling. The Origin of Comets in the Solar Nebula: A Unified Model. *Icarus*, 127:290–306, June 1997. doi: 10.1006/icar.1997.5712.
- R. Weidling and J. Blum. Free collisions in a microgravity many-particle experiment. IV. - Three-dimensional analysis of collision properties. *Icarus*, 253:31–39, June 2015. doi: 10.1016/j.icarus.2014.12.010.
- R. Weidling, C. Güttler, J. Blum, and F. Brauer. The Physics of Protoplanetary Dust Agglomerates. III. Compaction in Multiple Collisions. *ApJ*, 696:2036–2043, May 2009. doi: 10.1088/0004-637X/696/2/2036.
- R. Weidling, C. Güttler, and J. Blum. Free collisions in a microgravity many-particle experiment. I. Dust aggregate sticking at low velocities. *Icarus*, 218:688–700, March 2012. doi: 10.1016/j.icarus.2011.10.002.
- J. C. Weingartner and B. T. Draine. Dust Grain-Size Distributions and Extinction in the Milky Way, Large Magellanic Cloud, and Small Magellanic Cloud. *ApJ*, 548:296–309, February 2001. doi: 10.1086/318651.
- F. L. Whipple. A comet model. I. The acceleration of Comet Encke. *ApJ*, 111:375–394, March 1950. doi: 10.1086/145272.

- F. L. Whipple. A Comet Model. II. Physical Relations for Comets and Meteors. *ApJ*, 113: 464, May 1951. doi: 10.1086/145416.
- J. P. Williams and W. M. J. Best. A Parametric Modeling Approach to Measuring the Gas Masses of Circumstellar Disks. *ApJ*, 788:59, June 2014. doi: 10.1088/0004-637X/788/1/59.
- F. Windmark, T. Birnstiel, C. Güttler, J. Blum, C. P. Dullemond, and T. Henning. Planetesimal formation by sweep-up: how the bouncing barrier can be beneficial to growth. *A&A*, 540:A73, April 2012a. doi: 10.1051/0004-6361/201118475.
- F. Windmark, T. Birnstiel, C. W. Ormel, and C. P. Dullemond. Breaking through: The effects of a velocity distribution on barriers to dust growth. *A&A*, 544:L16, August 2012b. doi: 10.1051/0004-6361/201220004.
- C.-C. Yang, A. Johansen, and D. Carrera. Concentrating small particles in protoplanetary disks through the streaming instability. *A&A*, 606:A80, October 2017. doi: 10.1051/0004-6361/201630106.
- A. N. Youdin and J. Goodman. Streaming Instabilities in Protoplanetary Disks. *ApJ*, 620:459–469, February 2005. doi: 10.1086/426895.
- A. N. Youdin and Y. Lithwick. Particle stirring in turbulent gas disks: Including orbital oscillations. *Icarus*, 192:588–604, December 2007. doi: 10.1016/j.icarus.2007.07.012.
- M. E. Zolensky, T. J. Zega, H. Yano, S. Wirick, A. J. Westphal, M. K. Weisberg, I. Weber, J. L. Warren, M. A. Velbel, A. Tsuchiyama, P. Tsou, A. Toppani, N. Tomioka, K. Tomeoka, N. Teslich, M. Taheri, J. Susini, R. Stroud, T. Stephan, F. J. Stadermann, C. J. Snead, S. B. Simon, A. Simionovici, T. H. See, F. Robert, F. J. M. Rietmeijer, W. Rao, M. C. Perronnet, D. A. Papanastassiou, K. Okudaira, K. Ohsumi, I. Ohnishi, K. Nakamura-Messenger, T. Nakamura, S. Mostefaoui, T. Mikouchi, A. Meibom, G. Matrajt, M. A. Marcus, H. Leroux, L. Lemelle, L. Le, A. Lanzirotti, F. Langenhorst, A. N. Krot, L. P. Keller, A. T. Kearsley, D. Joswiak, D. Jacob, H. Ishii, R. Harvey, K. Hagiya, L. Grossman, J. N. Grossman, G. A. Graham, M. Gounelle, P. Gillet, M. J. Genge, G. Flynn, T. Ferroir, S. Fallon, D. S. Ebel, Z. R. Dai, P. Cordier, B. Clark, M. Chi, A. L. Butterworth, D. E. Brownlee, J. C. Bridges, S. Brennan, A. Brearley, J. P. Bradley, P. Bleuet, P. A. Bland, and R. Bastien. Mineralogy and Petrology of Comet 81P/Wild 2 Nucleus Samples. *Science*, 314:1735, December 2006. doi: 10.1126/science.1135842.
- A. Zsom and C. P. Dullemond. A representative particle approach to coagulation and fragmentation of dust aggregates and fluid droplets. *A&A*, 489:931–941, October 2008. doi: 10.1051/0004-6361:200809921.
- A. Zsom, C. W. Ormel, C. Güttler, J. Blum, and C. P. Dullemond. The outcome of protoplanetary dust growth: pebbles, boulders, or planetesimals? II. Introducing the bouncing barrier. *A&A*, 513:A57, April 2010. doi: 10.1051/0004-6361/200912976.

Publications

Refereed Publications

S. Lorek, P. Lacerda, and J. Blum, *Local growth of dust- and ice-mixed aggregates as cometary building blocks in the solar nebula*, *A&A*, 611, A18, doi: 10.1051/0004-6361/201630175, 2018, March

S. Lorek, B. Gundlach, P. Lacerda, and J. Blum, *Comet formation in collapsing pebble clouds. What cometary bulk density implies for the cloud mass and dust-to-ice ratio*, *A&A*, 587, A128, doi: 10.1051/0004-6361/201526565, 2016, March

Conference Contributions

S. Lorek, P. Lacerda, J. Blum, *Comet formation in collapsing pebble clouds: Pebble formation*, Department of Planetary Science/European Planetary Science Congress Joint Meeting, Pasadena, California, USA, 2016, October (*Poster*)

S. Lorek, P. Lacerda, J. Blum, B. Gundlach, *Size matters? Monomer size and transition from fractal to compact ice aggregates*, Wilhelm und Else Heraeus Seminar *How primitive are comets?*, Bad-Honnef, Germany, 2016, April (*Poster*)

S. Lorek, P. Lacerda, B. Gundlach, and J. Blum, *Compression of Pebbles in Collapsing Pebble Clouds*, Planet Formation and Evolution Workshop, Duisburg-Essen, Germany, 2016, March (*Oral*)

S. Lorek, P. Lacerda, B. Gundlach, and J. Blum, *Compression of Pebbles in Collapsing Pebble Clouds and the Dust-to-Ice ratio*, European Planetary Science Congress (EPSC), Nantes, France, 2015, October (*Oral*)

Seminar Talks

S. Lorek, *Comet Formation in Collapsing Pebble Clouds*, Solar System School (S3) seminar, Max Planck Institute for Solar System Research, Göttingen, Germany, 2017, May

S. Lorek, *Comet Formation in Collapsing Pebble Clouds: Pebble Formation*, Solar System School (S3) seminar, Max Planck Institute for Solar System Research, Göttingen, Germany, 2016, June

S. Lorek, *Comet Formation in Collapsing Pebble Clouds*, Solar System School (S3) seminar, Max Planck Institute for Solar System Research, Göttingen, Germany, 2015, June

Acknowledgements

I would like to thank my supervisors, Pedro Lacerda and Jürgen Blum, for their guidance and their tremendous support during the three years of my PhD. I am especially indebted to Pedro Lacerda for his patience and his thoroughness in proofreading my various manuscripts.

A special thanks to Klaus Jockers and to Uli Christensen for constructive feedback on my thesis draft and to Franziska Zeuner for proofreading my thesis.

Furthermore, I would like to thank my colleagues at the Max Planck Institute for Solar System Research for occasional discussions about the topic.

This PhD thesis was carried out in the framework of the Solar System School, the International Max Planck Research School (IMPRS) for Solar System Science at the Max Planck Institute for Solar System Research, Göttingen.

Curriculum vitae

Personal Information

Name Sebastian Lorek
Date of Birth 2 November 1988
Place of Birth Neumarkt i.d.OPf., Germany
Nationality German

Education

2014 – 2017 PhD in Physics, Solar System School, International Max Planck Research School (IMPRS), Max Planck Institute for Solar System Research, Göttingen
2011 – 2014 Master of Science in Physics, Ruprecht Karls University, Department of Physics and Astronomy, Heidelberg
2008 – 2011 Bachelor of Science in Physics, Ruprecht Karls University, Department of Physics and Astronomy, Heidelberg

Professional Experience

2015 – 2016 Chairperson, Small Bodies Journal Club for Students and Post-Docs, Max Planck Institute for Solar System Research, Göttingen
Winter term 2012/2013 . Tutor, Introduction to Astronomy and Astrophysics I, Ruprecht Karls University, Department of Physics and Astronomy, Heidelberg

Public Outreach

May 2017 Child care, Der Herr der Ringe und Monde - Eine Expedition ins Saturnsystem, public lecture, Max Planck Institute for Solar System Research, Göttingen
January 2017 Child care, Nacht des Wissens, Max Planck Institute for Solar System Research, Göttingen
May 2016 Guide, Büchertag, Max-Planck-Gymnasium, Göttingen
January 2015 Guide, Nacht des Wissens, Max Planck Institute for Solar System Research, Göttingen
November 2014 Guide, Philae landing event, Max Planck Institute for Solar System Research, Göttingen

Research Interests

..... astrophysics of planet formation; dust coagulation; protoplanetary disks; N-body dynamics of planetesimals and planets; collisional evolution of planetesimals; small bodies in the solar system; linking planet formation models to solar system formation and evolution; comets

Computer Skills

..... Fortran, Python, C/C++, IDL, \LaTeX , MS Office and Libre Office, UNIX user level

Language Skills

German..... native
English..... fluent

Memberships

2017 – present Astronomische Gesellschaft (AG)
2008 – present Deutsche Physikalische Gesellschaft (DPG)
2001 – present Bayerische Volkssternwarte Neumarkt i.d.OPf. e.V.